Effects of Complex Heterogeneous Constitutive Properties on the Structural Integrity of a Flawed Weld

Invloed van sterk heterogene constitutieve materiaaleigenschappen op de structurele integriteit van een las met defecten

Sameera Naib

Promotoren: prof. dr. ir. W. De Waele, prof. dr. ir. S. Hertelé
Proefschrift ingediend tot het behalen van de graad van
Doctor in de ingenieurswetenschappen: werktuigkunde-elektrotechniek

UNIVERSITEIT
GENT

Vakgroep Elektromechanica, Systeem- en Metaalengineering
Voorzitter: prof. dr. ir. L. Dupré
Faculteit Ingenieurswetenschappen en Architectuur
Academiejaar 2019 - 2020

ISBN 978-94-6355-349-0
NUR 978
Wettelijk depot: D/2020/10.500/26

Supervisors

Prof. dr. ir. Wim De Waele
Ghent University
Faculty of Engineering and Architecture
Department of Electromechanical, Systems and Metal Engineering

Prof. dr. ir. Stijn Hertelé
Ghent University
Faculty of Engineering and Architecture
Department of Electromechanical, Systems and Metal Engineering

Examination Committee

Prof. Patrick De Baets (Chair)
Ghent University
Faculty of Engineering and Architecture
Department of Electromechanical, Systems and Metal Engineering

Prof. Nenad Gubeljak (Secretary)
University of Maribor
Faculty of Mechanical Engineering
Laboratory for Mechanical Elements and Structures

Prof. Sebastian Münstermann
RWTH Aachen University
Head of group for integrity of materials and structures
IEHK - Institut für Eisenhüttenkunde / Steel Institute

Prof. Roumen Petrov
Ghent University
Faculty of Engineering and Architecture
Department of Electromechanical, Systems and Metal Engineering

Dr. ir. Kaveh Samadian
Ghent University
Faculty of Engineering and Architecture
Department of Electromechanical, Systems and Metal Engineering

Research Institute

Soete Laboratory – Ghent University
Department of Electromechanical, Systems and Metal Engineering
Faculty of Engineering and Architecture

Technologiepark Zwijnaarde 46
B-9052 Zwijnaarde

॥ ॐ नमो भगवते वासुदेवाय ॥

janmādyasya yato'nvayāditarataś cārtheṣvabhijñaḥ svarāṭ
tene brahma hṛdā ya ādikavaye muhyanti yatsūrayaḥ
tejovārimṛdāṁ yathā vinimayo yatra trisargo'mṛṣā
dhāmnā svena sadā nirastakuhakaṁ satyaṁ paraṁ dhīmahi ||

Shrimad Bhagavatam— Canto 1, Chapter 1, Verse 1

The cycle of birth and the death, knowledge and ignorance, creation and destruction are transpiring in this universe because of an eternal entity, which is conscious of all its manifestations. The entity which is the 'Absolute truth', is the reason for humanity to have access to the knowledge about all mechanisms of this universe. This entity has been trying to save n-number of souls from the cycle of birth and death by creating this magnificent universe, though it has no consequence from it. I bow to the entity which can be termed as 'Sriman Narayana'.

Acknowledgements

I express my sincere gratitude to my supervisors Prof. Wim De Waele and Prof. Stijn Hertelé who continually extended their guidance and supervision for successful accomplishment of my doctoral thesis. Without their expertise and competence, this work would not have been possible. I would like to thank the funding organization 'Fonds Wetenschappelijk Onderzoek - Vlaanderen (FWO)' who made this work possible by allocating the funds to undertake this research (grant no. G.0609.15N). I'm highly grateful to our collaborators Prof. Nenad Gubeljak and Mr. Primož Štefane from Maribor University in Slovenia for their contribution towards this project. I am very thankful to the jury members Prof. Patrick de Baets (chair), Prof. Sebastian Münstermann, Prof. Nenad Gubeljak, Prof. Roumen Petrov and Dr. Kaveh Samadian for taking time to examine this work.

I am thankful to Hans Van Severen, Johan Van Den Bossche, Koen van Minnebruggen, Lieven Van West, Wouter Ost, Julien De Meyer, Jonathan Vancoillie, Michel De Waele and Sam de Meester for offering technical support and assistance for conducting experiments during this research. My special acknowledgement to Georgette D'Hondt for her consistent assistance in the administrative aspects during this research. I appreciate the effort of master students Matthijs, Marc and Florence for their contribution towards this dissertation in the form of their thesis.

During the undertaking of this work, I was consistently aided, encouraged and motivated by my experienced colleagues. I'm indebted to Adam 'Hori', Kaveh 'Kavya', Saosometh 'Dr. Sao', Vitor 'Viterrr', Ádám, Levi 'De Pauw', Diego 'DBR', Kannaki 'Kenaaki', Jules, Samir, Jie 'Jeff', three musketeer tambis - Dhanraj, Gopal and Naveen, Nadeem 'bhai', Klari, Hanan, Peter 'Wo tsao' Deng, Yu, Phuc, Jacob and Mojtaba. I also recognize and appreciate the assistance of several anonymous minds and hands behind this success.

I praise my friends - Rahul 'Dadi', Rajesh 'Krishnu' and Pradeep '123' who are more like my brothers, for their consistent support, help and companionship. Long live our brotherhood!

I offer my obeisance to the Almighty for being born on this earth in the form of my parents. I have been trying and will try my best to follow the path which you have laid for me. I salute the supreme for joining me in the journey of this life in the form of my wife. I will do my best to walk in the path of 'Dharma - the righteousness' along with her. I bow to omnipresent, who has bestowed me with amazing grandparents, in-laws, uncles, aunts, cousins, nephews, nieces and friends along with perfect living conditions which made it possible to accomplish this feat.

I show my utmost gratitude towards Śrī Śrī 1008 Śrī Satyātma-tīrtha Swamiji for his blessings and discourses which has been a guide throughout my life.

I dedicate this work to 'Sriman Narayana' upon whom I will meditate to give us all the pertinent energy to achieve ultimate freedom called 'Moksha'.

Sameera Naib *February 2020*

Summary

Flawed welds often require an Engineering Critical Assessment (ECA) to judge on the necessity for weld repair. ECA is a fracture mechanics based prediction of the integrity of structural components with defects under operating conditions. Adding to the complexity of a weld ECA is the occurrence of local strength variations in the weldment ('weld strength heterogeneity'). This thesis is part of a FWO-ARRS funded project involving a collaboration between two universities (Ghent and Maribor). The main objective of this project is to improve the understanding of effects of weld strength heterogeneity on the accuracy of ECA, and to develop engineering guidance to treat weld heterogeneity within established ECA practice (which currently assumes welds to be homogeneous in terms of strength properties).

This work first tackles the challenge to experimentally characterize local strength property variations within welded connections. Hardness measurements allow to quantify weld strength heterogeneity given their theoretical relation with ultimate tensile strength. However, various standards and procedures report a wide variety of relations ('transfer functions') between hardness and both yield and ultimate tensile strength, and recognize substantial scatter in hardness based predictions of strength. To overcome the scatter associated with standardized transfer functions, this thesis suggests an experimental calibration procedure based on all weld metal tensile testing and Vickers hardness mapping. Finite Element (FE) analysis has been conducted on welds originating from steels to simulate their crack driving force response in Single-Edge notched Tension (SE(T)) specimens. Single specimen Single Edge notched Tension (SE(T)) testing has become a mainstream method to characterize the ductile tearing resistance of metals under conditions of low crack tip constraint. Heterogeneous welds in SE(T) specimens have been finite element modelled by assigning local material properties using the developed transfer functions. Simulation results show good agreement with experimental fracture toughness test results, adding confidence to the developed method. Additionally, All Weld Metal Tensile Tests and Miniature Tensile Test (MTT) results were utilized along with hardness results to further evaluate the experimentally calibrated transfer functions.

The post-processing of experimental single specimen SE(T) test results requires calculation of crack driving force and measurement of crack extension as the test progresses. Various methods have been investigated and were shown to be reliable for testing of homogeneous materials. Published data, however, indicate that the accuracy of these methods may degrade when testing welded joints. This thesis reports on an SE(T) test program in which several weld configurations (including severely heterogeneous welds produced at University of Maribor) were tested. The Direct Current Potential Drop (DCPD) method is adopted to assess the crack extension and is compared with the Normalization Data Reduction (NDR) technique and nine point average method for final crack extension. The results show that DCPD is a robust technique to reveal the crack extension in heterogeneous welds (e.g. revealing slope shifts in tearing resistance curves) and is also an effective method to predict final crack extension. The NDR method, albeit more straightforward to apply, does not reveal the potentially irregular shape of tearing resistance curves observed for heterogeneous welds.

In presence of crack path deviation, DCPD analysis is related to crack extension projected in the through-thickness direction, rather than the extension along its actual trajectory.

The variation of constitutive properties within the weld influences the deformation patterns around the crack and, as a consequence, the load bearing capacity of the joint. These deformation patterns are theoretically assessed using concepts of 'slip line field theory' which concentrates plastic deformation along trajectories that follow the direction of maximum shear stresses. This theory is based on severe assumptions which do not necessarily reflect realistic conditions in SE(T) testing. In order to understand the outcome of implementing this theory on actual specimens, paths of maximum equivalent plastic strains and maximum shear stresses were derived from stress and strain contour output in SE(T) simulations. The trajectory of these lines was validated using SE(T) experiments, where the deformations were extracted using Digital image Correlations (DIC). This assessments showed the deviations in the deformation behavior of welds showing material strength heterogeneity, compared to homogeneous specimens.

The engineering critical assessment of a defected welded joint requires quantification of its proximity to fracture, and its proximity to plastic collapse. The former is influenced by the apparent toughness of the material (which, in turn, is influenced by crack tip constraint). The latter is influenced by the limit load of the connection. Effects of weld strength heterogeneity on both aspects have been investigated, making use of the techniques developed in earlier chapters (particularly, slip line analysis).

A first study focuses on the prediction of limit load, which allows to calculate the structure's proximity to plastic collapse. Simplified theorems have been adopted to identify lower and upper bound values of limit load. These theorems are well established for homogeneous continua, but less so for heterogeneous connections. This work develops lower and upper bound limit load equations for heterogeneously welded SE(T) specimens, and explores the predictive accuracy of both methods. A parametric study involves 2D plane strain simulations of single-edge notched tension (SE(T)) specimens. Additional to actual heterogeneous welds, bi-material welds consisting of two regions of different material properties (at the root and at the cap) are introduced within a parametric study. The obtained estimations of limit load are then compared against the simulated limit loads. It turns out that application of the lower bound theorem on heterogeneous welded connections is hampered by the inability to pinpoint the exact location of failure, thus resulting in potentially excessive conservatism. The upper bound theorem, in contrast, provides limit load predictions which are in close agreement with (and generally slightly overestimate) actual limit load values.

Knowledge of crack tip stress fields ('crack tip constraint') plays a major role in assessing the fracture behavior of a weld, as these fields affect the apparent fracture toughness of the weld. Traditional theories of single parameter fracture mechanics assume crack tip stresses in high crack tip constraint conditions, but are in poor agreement with reality for cases involving low crack tip constraint (such as SE(T) specimens). To quantify and address this disagreement, two parameter fracture mechanics (based on J-Q theory) was utilized to assess the effects of strength heterogeneity crack tip constraint. A theoretical relation based on slip line field theory and additional strong assumptions predicts that the Q parameter is linearly related to the angle of the slip line at the crack tip. Understanding of this relation would

conceptually allow to estimate crack tip constraint from an SE(T) specimen's deformation behavior. The developed relation has been scrutinized using SE(T) simulations, and it turns out that the actual relation between crack tip constraint and deformation behavior is more nuanced than predicted. This can be understood from the severity of the assumptions that led to the development of the analytical relation.

Based on the above, the behavior of a defect present in a tension loaded heterogeneous weld is better understood in terms of crack driving force, ductile tearing resistance and trajectory, and limit load. It is envisaged that the obtained insights can lead to a translation of weld heterogeneity effects into established ECA practice, and concrete guidance to achieve this is provided in a concluding chapter.

Samenvatting

De aanwezigheid van lasfouten vereist vaak een kritische ingenieursbeoordeling ('Engineering critical assessment' of ECA) om te beoordelen of lasreparatie al dan niet noodzakelijk is. ECA is een op breukmechanica gebaseerde voorspelling van de integriteit van structurele componenten met defecten met inbegrip van alle omstandigheden (materiaal, geometrie, fout, randvoorwaarden). Het optreden van lokale sterktevariaties in de las ('heterogeniteit van lassterkte') vormt een grote uitdaging binnen ECA, aangezien deze de nauwkeurigheid van de voorspellingen (veelal gebaseerd op de aanname van een homogene las) beïnvloeden.

Dit proefschrift is onderdeel van een door FWO Vlaanderen en ARRS Slovenië gefinancierd project waarbij een samenwerking tussen twee universiteiten (Gent en Maribor) werd opgestart. Het hoofddoel van dit project is het verbeteren van het begrip van de effecten van lassterkte-heterogeniteit op de nauwkeurigheid van ECA, en het ontwikkelen van ingenieursrichtlijnen voor het behandelen van las-heterogeniteit binnen de gevestigde ECA-praktijk (die momenteel veronderstelt dat lassen homogeen zijn in termen van sterkte-eigenschappen) .

Dit werk gaat eerst de uitdaging aan om experimentele lokale eigenschappen van sterkte-eigenschappen binnen gelaste verbindingen experimenteel te karakteriseren. Metingen van Vickers hardheid maken het mogelijk de heterogeniteit van de lassterkte te kwantificeren, gezien hun theoretische relatie met de treksterkte. Verschillende standaarden en procedures rapporteren echter een breed scala van relaties ('overdrachtsfuncties') tussen hardheid en zowel vloeigrens als uiteindelijke treksterkte, en erkennen een aanzienlijke spreiding in hardheidsgebaseerde voorspellingen van sterkte. Om de verspreiding van gestandaardiseerde overdrachtsfuncties te overkomen, ontwikkelt dit proefschrift een experimentele kalibratieprocedure op basis van lasmetaaltrekproeven en Vickers-hardheidsmapping. Eindige elementen analyses worden uitgevoerd op stalen lassen afkomstig zodoende de scheurdrijvende kracht in heterogene lassen te simuleren in eenzijdig gekerfde trekproeven (Single-Edge notched Tension of SE(T) proeven). SE(T) beproeving is een gangbare methode geworden om de ductiele scheuruitbreidingsweerstand van metalen te karakteriseren onder omstandigheden met een lage spanningstriaxialiteit aan de kerftip. Heterogene lasnaden in SE(T)-monsters worden gemodelleerd via eindige elementen door lokale materiaaleigenschappen toe te wijzen met behulp van de hierboven ontwikkelde overdrachtsfuncties. Simulatieresultaten tonen goede overeenstemming met experimentele breuktaaiheidstestresultaten, wat vertrouwen geeft aan de ontwikkelde methode. Bovendien werden resultaten van lasmetaaltrekproeven en miniatuur trekproeven gecombineerd met hardheidsresultaten om de experimenteel gekalibreerde transferfuncties verder te evalueren.

De analyse van experimentele SE(T) testresultaten vereist een berekening van de scheurdrijvende kracht en meting van de scheuruitbreiding naarmate de test vordert. Verschillende methoden zijn onderzocht en bleken betrouwbaar te zijn voor het testen van homogene materialen. Uit gepubliceerde gegevens blijkt echter dat de nauwkeurigheid van deze methoden kan afnemen bij het testen van lasverbindingen. Dit proefschrift rapporteert

over een SE(T)-testprogramma waarin verschillende lasconfiguraties (waaronder zeer heterogene lassen geproduceerd aan de Universiteit van Maribor) werden getest. De gelijkstroom spanningsvalmethode (direct current potential drop; DCPD) wordt gebruikt om de scheuruitbreiding te beoordelen en wordt vergeleken met normaliserings-datareductie (Normalization Data Reduction; NDR) en de negenpunts-gemiddelde (nine point average) methode. De resultaten tonen aan dat DCPD een robuuste techniek is om de scheuruitbreiding in heterogene lassen te onthullen (bijv. hellingverschuivingen in scheurweerstandskrommen kunnen bepaald worden) en ook een effectieve methode is om de uiteindelijke scheuruitbreiding te voorspellen. De NDR-methode, hoewel eenvoudiger toe te passen, onthult niet de potentieel onregelmatige vorm van scheurweerstandscurven waargenomen voor heterogene lassen. In aanwezigheid van scheurpadafwijking is DCPD-analyse gerelateerd aan scheurverlenging geprojecteerd in de dikterichting, eerder dan de extensie langs zijn werkelijke traject.

De variatie van constitutieve eigenschappen binnen een las beïnvloedt de vervormingspatronen rond een lasfout en, bijgevolg, het draagvermogen van de verbinding. Deze vervormingspatronen worden theoretisch beoordeeld met behulp van de concepten van sliplijnveldtheorie ('slip line field theory') die plastische vervorming concentreert langs trajecten die de richting van maximale schuifspanningen volgen. Deze theorie is gebaseerd op ernstige veronderstellingen die niet noodzakelijkerwijs realistische omstandigheden weerspiegelen. Om de uitkomst van de implementatie van deze theorie op werkelijke SE(T) specimens te begrijpen, werden paden van maximum equivalente plastische rek en maximale schuifspanningen afgeleid van rek- en spanningenoutput uit SE(T)-simulaties. Het traject van deze lijnen werd gevalideerd met behulp van SE(T)-experimenten, waarbij de vervormingen werden geëxtraheerd met behulp van digitale beeldcorrelatie (digital image correlation; DIC). Deze beoordelingen toonden sterke afwijkingen in het vervormingsgedrag van heterogene lassen, in vergelijking met homogene SE(T)-monsters.

De ECA van een gelaste verbinding met lasfout vereist kwantificering van zijn nabijheid tot breuk en zijn nabijheid tot plastisch bezwijken. Het eerstgenoemde aspect wordt beïnvloed door de schijnbare taaiheid van het materiaal (die op zijn beurt wordt beïnvloed door de spanningsinperking aan de kerftip). Het laatstgenoemde aspect wordt beïnvloed door de limietbelasting van de verbinding. Effecten van lassterkteheterogeniteit op beide aspecten zijn onderzocht, met behulp van de technieken die in eerdere hoofdstukken zijn ontwikkeld (in het bijzonder, sliplijnanalyse).

Een eerste studie richt zich op de voorspelling van de limietbelasting ('limit load'), waarmee de nabijheid van een constructie/component/proefstuk tot plastisch bezwijken kan worden berekend. Vereenvoudigde stellingen werden ruime tijd geleden ontwikkeld om theoretische onder- en bovengrenswaarden van de limietbelasting te identificeren. Deze stellingen zijn eenvoudig toepasbaar voor homogene continua, maar minder voor heterogene verbindingen. Dit werk ontwikkelt ondergrens- en bovengrensvergelijkingen voor de limietbelasting van heterogene gelaste SE(T)-monsters en onderzoekt het voorspellend vermogen van beide methoden. Een parameterstudie omvat 2D-simulaties (onder vlakvervorming) van SE(T) proeven. Aanvullend op experimenteel gekarakteriseerde heterogene lassen, worden bi-materiaal lassen bestaande uit twee gebieden met verschillende materiaaleigenschappen geïntroduceerd in de parameterstudie. De verkregen schattingen van de limietbelasting worden vervolgens vergeleken met gesimuleerde

limietbelastingen van de heterogene lassen. Het blijkt dat de toepassing van de ondergrensvergelijking op heterogene gelaste verbindingen wordt belemmerd door het onvermogen om de exacte faallocatie te voorspellen, wat resulteert in mogelijk buitensporig conservatisme. De bovengrensstelling biedt daarentegen voorspellingen voor de limietbelasting die in nauwe overeenstemming zijn met (en in het algemeen enigszins overschat worden) de werkelijke limietwaarden.

Kennis van spanningsvelden aan een scheurtip (spanningsinperking of 'crack tip constraint') speelt een belangrijke rol bij het beoordelen van het breukgedrag van een las, aangezien deze velden de schijnbare breuktaaiheid van de las beïnvloeden. Traditionele theorieën van breukmechanica zijn gebaseerd op één enkele bepalende parameter en gaan uit een hoge spanningsinperking aan de scheurtip. Deze theorieën zijn echter in slechte overeenstemming met situaties gekarakteriseerd door een lage spanningsinperking (zoals SE(T)-monsters). Om deze discrepantie te kwantificeren en aan te pakken, werd twee-parameterbreukmechanica (gebaseerd op J-Q-theorie) gebruikt om de effecten van sterkteheterogeniteit op spanningsinperking te beoordelen. Een theoretische relatie gebaseerd op sliplijnveldtheorie en aanvullende grove veronderstellingen voorspelt dat de Q-parameter lineair gerelateerd is aan de hoek van de sliplijn ter hoogte van de scheurtip. Inzicht in deze relatie zou conceptueel toelaten om de spanningsinperking uniek te schatten op basis van het vervormingsgedrag van een SE(T)-monster. De ontwikkelde relatie werd onder de loep genomen met behulp van SE (T)-simulaties, en het blijkt dat de feitelijke relatie tussen spanningsinperking en vervormingsgedrag meer genuanceerd is dan voorspeld. Dit is een gevolg van de ernstige veronderstellingen die noodzakelijk waren voor het afleiden van het analytisch model.

Het uitgevoerde onderzoek laat toe het gedrag van een lasfout in een heterogene las onder trekbelasting beter te begrijpen in termen van scheuraandrijvende kracht, ductiele scheurgroeiweerstand en -traject, en plastische bezwijkbelasting. De verkregen inzichten kunnen leiden tot een vertaling van lasheterogeniteitseffecten in gevestigde ECA-praktijk. Hieromtrent worden in een concluderend hoofdstuk concrete richtlijnen gegeven.

Contents

Nomenclature

a_o	*Initial crack length (mm)*
a_f	*Final crack length (mm)*
a_b	*Blunting corrected crack length (mm)*
$a_{(i)}$	*Length of the crack from each of 9 points, where i = 1,2,….8, 9 (mm)*
a_{pd}	*Crack depth obtained from DCPD measurements (mm)*
a_{NDR}	*Crack depth obtained from NDR measurements (mm)*
A	*Cross-sectional area (mm²)*
b	*Ligament thickness (W-a) (mm)*
b_1	*Cap ligament thickness (mm)*
b_2	*Root ligament thickness (mm)*
B	*Width of the SE(T) specimen (mm)*
B_N	*Net section width (in presence of side grooves) (mm)*
$D_{meas,1}$	*Distance between two measuring points across the crack in DCPD (mm)*
E	*Young's modulus (MPa)*
H	*Half-width of the weld (mm)*
H_r	*Half-width of the root (mm)*
H_c	*Half-width of the cap (mm)*
J	*J – integral (N/mm)*
k	*Critical shear stress (N/mm²)*
L	*Daylight length between the grips of SE(T) specimen (mm)*
M_{eq}	*Mismatch ratio ($M_{eq} = \sigma_{yw} / \sigma_{yb}$)*
M_r	*Mismatch ratio of the root*
M_c	*Mismatch ratio of the cap*
n	*Strain hardening exponent (-)*
P	*Tensile load (kN)*
P_N	*Normalized tensile load (kN)*

$P_{N,F}$	*Normalized load obtained by curve fitting (kN)*
P_{LB}	*Lower bound limit load (kN)*
P_{LBM}	*Mismatch lower bound limit load (kN)*
P_{LBb}	*Base material lower bound limit load (kN)*
P_{UB}	*Upper bound limit load (kN)*
Q	*Constraint parameter (-)*
r	*Radius of the notch tip (mm)*
R_{p02}	*0.2% proof stress (MPa)*
$R_{p02(AWMTT)}$	*0.2% proof stress obtained from all weld metal tensile tests (MPa)*
R_m	*Ultimate tensile strength (MPa)*
$R_{m(AWMTT)}$	*Ultimate tensile strength obtained from all weld metal tensile tests (MPa)*
V	*Measured voltage drop across the crack (V)*
V_{ref}	*Supplied voltage drop considered as a reference (V)*
W	*Width of the SE(T) specimen (mm)*
W_r	*Width of the weld root (mm)*
W_c	*Width of the weld cap (mm)*
Y/T	*Yield to tensile ratio* (R_{p02}/R_m)
α	*Yield offset (-)*
ε_y	*True yield strain (-)*
$\varepsilon_{eq,pl}$	*Equivalent plastic strain (-)*
$\varepsilon_{eq,pl-max}$	*Maximum equivalent plastic strain (-)*
σ	*True stress (N/mm²)*
σ_m	*Mean stress (N/mm²)*
σ_y	*Yield stress (N/mm²)*
σ_{yb}	*Yield stress of base material (N/mm²)*
σ_{ym}	*Yield stress of the mismatched weld (N/mm²)*
$\sigma_{\theta\theta}$	*Crack tip opening stress (N/mm²)*
τ	*True shear stress (N/mm²)*
τ_{max}	*Maximum shear stress (N/mm²)*

SE(T)	*Single Edge notched (Tensile)*
DCPD	*Direct Current Potential Drop*
UC	*Unloading Compliance*
9_{pt}	*Nine point measurements*
NDR	*Normalization data reduction*
CMOD	*Crack Mouth Opening Displacement (mm)*
$CMOD_{pl}$	*Plastic component of CMOD (mm)*
$CMOD_N$	*Normalized Crack Mouth Opening Displacement (mm)*
CTOD	*Crack Tip Opening Displacement (mm)*
AWMTT	*All weld metal tensile test*
ECA	*Engineering critical assessment*
HV	*Vickers hardness*
HV_{AWMTT}	*Vickers hardness obtained by averaging HV from the region of AWMTT extraction*

Prologue to the doctoral dissertation

Background

The integrity assessment of flawed welds requires quantification of fracture toughness and crack driving force under imposed loading conditions. Their comparison allows estimating whether or not catastrophic failure will occur, thus allowing for an 'Engineering Critical Assessment' (ECA) of the weld flaw. Such ECAs are essential with respect to the safety of the welded joint and cost-effectiveness of welding since weld flaws are virtually unavoidable and full repair is extremely costly. An ECA allows for a sound statement on the necessity to repair flaws. For contemporary steel grades, an ECA should allow for (limited) plasticity resulting from stress concentrations near the flaw tip, thus requiring elastic-plastic fracture mechanics theory.

Most ECA procedures assume flaws to be surrounded by homogeneous material (in terms of stress-strain behavior and toughness), as this assumption allows for the application of well-established fracture mechanics procedures. For instance, the concept of a unique path integral (J) to express crack driving force as an energy release rate relies on material homogeneity, as J becomes path-dependent within a heterogeneous environment [1]. Also, the mathematical background of the EPRI framework to estimate J (which is the base for many ECA approaches) assumes non-variable, unique material properties [2].

The assumption of homogeneous material properties becomes questionable for flaws in fusion welds. A widely recognized and studied topic is the heat affected zone (HAZ) with considerably different properties compared to the weld and base metals. These differences affect the toughness as well as the stress-strain behavior. Both softening and hardening of the HAZ have been reported and are known to influence the deformation capacity of the weld joint and the path of ductile crack extension. Also the weld material itself typically comprises a wide variety of microstructures resulting from the complex thermal history. These inhomogeneities may lead to local yield strength variations (e.g. changes up to 100 MPa have been observed in metal arc welded steels within a distance of 5 mm in [3]). This is known to influence crack driving force [4] and crack tip constraint [5] that has a direct influence on fracture toughness. Flaw assessment procedures recognize that local strength variations within the weld may hamper a clear-cut interpretation of the assessment result [6]. Therefore, much effort has been made over the past decades to include effects of weld geometry (bevel, reinforcements and weld fusion line profile) and strength properties into fracture mechanics procedures. Following these efforts, currently established defect assessment procedures can account for weld strength mismatch (weld strength as compared to the base metal) and – to a limited extent – weld geometry.

Despite the efforts of the last decades, the current state of the art regarding weld flaw assessment adopts significant approximations. For instance, limit load

solutions in the flaw assessment standard R6 [7] and fitness-for-purpose procedure FITNET [6] assume 'idealized' welds in which the fusion lines are straight and the weld metal is strength mismatched with respect to the base metal, but homogeneous in itself. Idealized welds have been extensively analyzed on the basis of parametric finite element analyses [8, 9] and fundamental plasticity studies involving slip line field theory [5]. Yet, there is no generic approach to incorporate complex distributions of strength and irregular fusion line profiles into assessment procedures.

In a preliminary attempt to include complex weld heterogeneity in flaw assessments, the Soete Laboratory of Ghent University had developed a theoretical framework for the estimation of crack driving force, taking into account variable stress-strain properties along theoretical slip lines [10]. Promising crack driving force predictions were made for tension loaded flawed welds containing different material properties at the root side and the cap side (a strongly simplified case of weld heterogeneity).

Collaboration

In a project funded by FWO Flanders and ARRS Slovenia, *Soete Laboratory of Ghent University in Belgium* and the *Faculty of Mechanical Engineering at Maribor University in Slovenia* joined forces in the year 2015 to perform research on the effect of weld heterogeneity on structural integrity assessment of flawed welds. The intention was to utilize the specific expertise and facilities of both universities to undertake fundamental research and put forward an understanding and approach to deal with the issue of constitutive property variations in defect assessments in welded connections.

Ghent University has been involved in several national and international projects related to strain-based design and defect tolerance of welded structures. Contributions have been made to various international (pipeline) codes and guidelines. The laboratory was involved in international round-robin programs regarding (a) the design, execution, and analysis of Single Edge notched Tension (SE(T)) tests for quantification of ductile tearing resistance under low constraint levels and (b) curved wide plate tension tests for quantification of strain capacity of pipe girth weldments. Current research is related to weld flaw assessment; material heterogeneity on the crack driving force and ductile tearing resistance; fatigue of offshore structures. The proposed project was a logical extension of the ongoing activities.

Faculty of Mechanical Engineering at Maribor University has vast experience in fracture toughness testing of welded joints and its numerical simulation. Research activities are focused on the study of fracture behavior of weld joints and more specifically the effects of global and local strength mismatch on fracture toughness.

The promotors of this work, **prof. dr. ir. Wim De Waele** and **prof. dr. ir. Stijn Hertelé** of Ghent University started a collaboration with **prof. dr. ir. Nenad Gubeljak** of Maribor University with the project titled "**Effects of complex heterogeneous constitutive properties on the structural integrity of a flawed weld**". Ghent University was awarded a Fonds Wetenschappelijk Onderzoek (FWO) research fund (grant number G.0609.15N) and Maribor University a Slovenian Research Agency (ARRS) research fund. Two doctoral researchers were hired by the respective universities, one from each. The doctoral researchers were *Mr. Primož Štefane* at Maribor University (from January 2015) and *Mr. Sameera Naib* at Ghent University (from October 2015).

Objectives of the research

The research ambition is to achieve a deep understanding of the effects of weld constitutive property variations on weld behavior in the presence of defects. The uncontrolled conservatism of predictions in defect assessment standards (due to uncertainties in accuracy) need to be minimized without compromising the safety of the structure. This will have a direct consequence on the wide range of structures like pipelines, pressure vessels, piping equipment in refineries, etc. by increasing operational efficiency thereby reducing the cost of maintenance and repair.

Starting from the state of the art and aiming towards full understanding, the FWO-ARRS project is translated into four concrete objectives:

1. Judging the applicability of recognized flaw assessment approaches for more complex and, hence, more realistic cases of weld heterogeneity
2. Assessing different loading scenarios (like bending, tension, etc.)
3. Examining the effects of heterogeneity on both crack driving force and crack tip constraint (i.e. fracture toughness)
4. Providing experimental validation of the predictions made by means of theoretical or numerical analyses.

The project is narrowed down to the assessment of surface flaws, which are known to be more critical than embedded flaws in terms of structural integrity.

This research was split between the research groups of Ghent and Maribor. Ghent University (Soete laboratory) focused the research on weld heterogeneity characterization and assessment of defect behavior through crack driving force, limit load and crack tip constraint along with tearing resistance analysis in tension using Single Edge notched Tension (SE(T)) specimens. Maribor University focused research on the effect of weld heterogeneity on defect behavior using constraints and damage mechanics in bending using Single Edge notched Bending specimens (SE(B)).

Organization of the dissertation

This thesis is organized into eight chapters.

Chapter 1 gives a brief background on the influences and treatment of weld strength heterogeneity in Engineering Critical Assessments (ECA). It details hurdles incurred by several researchers and their approach towards finding a solution. Also, this chapter points out the importance of characterizing strength heterogeneity in welds.

Chapter 2 explains the experimental and numerical procedure utilized in this work to assess the behavior of cracks or other sharp defects in heterogeneous welds. The experimental methods to characterize weld strength heterogeneity include Vickers hardness mapping, all weld metal tensile tests and miniature tensile tests. Tearing resistance and crack driving force prediction methods in SE(T) testing is put forward. The numerical model of SE(T) which includes heterogeneity was utilized to validate the transfer functions developed to obtain material properties from experiments.

Chapter 3 employs an experimental procedure to estimate fracture resistance curves of SE(T) specimens having different weld and specimen configurations. Crack growth in heterogeneous regions of the weld is determined by different experimental techniques and the pros and cons of the techniques are explained.

Chapter 4 explains the method to obtain constitutive properties from macro hardness values by calibrating a transfer function between hardness and stress-strain behavior, which is validated using the numerical SE(T) model. The numerical model is further compared with SE(T) experiments to show the robustness of the calibrated transfer function. It is shown that the calibrated transfer function proves to be a better estimation method for obtaining constitutive properties from hardness values compared to standardized equations.

Chapter 5 is used to give background on the deformation behavior of a crack using slip line field theory. The importance of assessing deformations and the influence of material heterogeneity on deformation behavior is demonstrated using numerical simulations of heterogeneous welded SE(T) specimens complemented with experiments using Digital Image Correlation (DIC).

Chapter 6 exploits a 2D Single Edge notched Tension (SE(T)) model to analyze the limit loads of the complex and simplified welded specimens. Bounded limit analysis (i.e. lower and upper bound theorem) is used to predict limit loads of complex welded SE(T) specimens. Additionally, complex welds are simplified into a single weld region in terms of material properties and the limit loads are assessed.

Chapter 7 is a study of the effect of weld strength heterogeneity on the crack tip constraint and its relationship with deformation patterns and slip lines. Using *J-Q* theory, the crack tip stresses are explained in complex welded SE(T) specimens using numerical simulations. The deformations are then assessed for their relation with crack tip stresses through slip line analysis.

Chapter 8 gathers the outcomes of chapters 1 to 7 to provide a concise summary of the effects of weld heterogeneity and to detail a procedure involving heterogeneous aspects in an Engineering Critical Assessment (ECA) procedure. Based on these results, possible extension to this research and recommendations for future work are given.

Chapter 1

Strength heterogeneity in weldments – A perennial challenge for integrity assessment

1.1. Introduction

Engineering structures, which are meant to fulfill the needs of mankind, are established after meticulous examination and detailing of the scenario of purpose. Once a structure is completed and in operation successfully, the reliability and functionality have to be monitored at regular intervals. Even though these structures were efficiently designed and manufactured for a specific application, degradation and deterioration can be observed due to various factors depending on the structural utilization. Failures during the operation of engineering structures may lead to severe damage to the structure and its surroundings, having an impact on human life, environment, and economy. The term '*Structural Integrity Assessment*' is coined for the process that is used to predict the capability of the structure to be in operation for the predicted lifetime.

Anderson [11] explains the two main causes of structural failure, (i) negligence during design, construction or operation, and (ii) application of new design/material which provides unexpected results. He points out that design procedures can be used to prevent failures as per (i) but that it is very difficult to avoid failures mentioned in (ii). If the newly improved design or material has to be implemented for operation, they will be thoroughly analyzed. Even then, failures can just be reduced but cannot be prevented. A typical example of such types of failures that are often discussed in the literature is the case of the Liberty ships during world war II [12], which failed due to design changes. Several examples can be found throughout history for failures due to design and material changes [13]. The structural failures relate to the degrading mechanical functionality and hence it has to be assured that this degradation does not occur. To suffice this criterion, '*Structural Integrity Assessment'* plays a major role, during design, manufacturing, and operation.

Welded structures like pressure vessels, pipelines, fixed off-shore structures, drilling units, etc. are large sized. The safety of these structures must be ensured by having low risk to its users and the surroundings, performing the intended purpose effectively and efficiently. These objectives are achieved by having good design and construction practices, which should prevent most of the structural failures. However, as these huge structures might be subjected to complex and changing load conditions and operate in hostile environments (subsea, underground, extreme weather conditions), they are also susceptible to flaws during the manufacturing stage and damage during service. This is one of the major causes of welded structures to fail.

Among these welded structures, the importance of pipelines (*Figure 1 – network of oil and gas pipeline in France/Belgium region)* transporting oil, natural gas, petrochemicals, and other chemicals have been acknowledged throughout the world. For example, per day, 96.2 million liters of petroleum products and 3.48 trillion cubic meters of natural gas are consumed [14]. In Belgium alone, there is a

network of 4000km of pipelines transporting natural gas, oil, and refined products [15]. All over the world, the network is over 3,000,000 km, thus making the industry a multi-billion dollar worth.

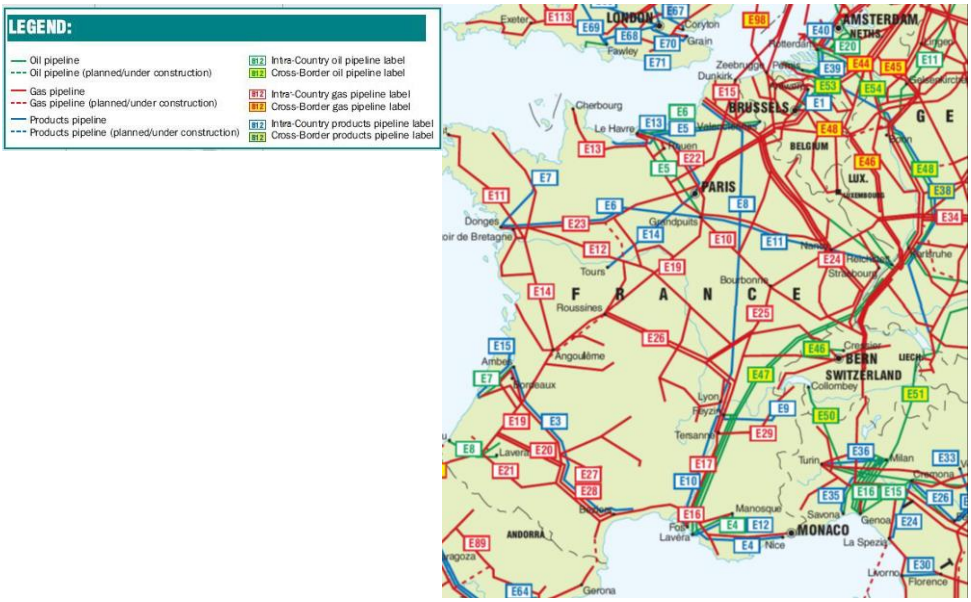

Figure 1: Oil and gas pipeline network in Belgium and neighboring countries [16, 17]

One of the biggest challenges of the pipeline industry is the aging infrastructure. In 2003, 50% of the pipeline network in the US was over 40 years old [18] and the majority of the European pipeline network is over 20 years old. BP's annual report of 2018 estimates that the available oil reserves would be sufficient to meet 50.2 years of requirements [19]. This means the current pipeline infrastructure will need to be operated for a longer duration. At this point, in order to apprehend our aging assets, structural integrity assessment will play a major role. Key elements in ensuring pipeline integrity are highly trained workforce, efficient engineering design and operation, inspection and maintenance, Fitness-For-Service (FFS) assessment and risk management.

1.2. Engineering Critical Assessment (ECA)

Pipeline construction is subjected to quality control, design codes and workmanship standards like BS 4515:2009 or API 1104 [20] in order to ensure the welds are free of potentially dangerous flaws, i.e. flaws that can lead to structural failures. Due to the different manufacturing processes used, sometimes in harsh environmental conditions, the pipes and its welds contain flaws that are of various sizes and shapes. FFS assessments are widely used to check whether the failure condition is reached during the operational life of the pipe. FFS provides an analytical basis for the acceptability of flaws and utilizes techniques based on standardized methods. Once flaws are rejected by workmanship standards, they are termed to be defects.

Additionally, welding which offers high-speed manufacturing and high design flexibility with low costs, involves complexities in metallurgical properties. If the presence of flaws is one aspect of a weld, another important aspect is the presence of inhomogeneous material properties within and around the region of the weld. Because of this, welds act as a major study subject in the field of fracture mechanics.

'*Engineering Critical Assessment*' is a popular fitness-for-service procedure that is widely used in the oil and gas industry to determine defect tolerance of safety-critical systems [18]. *Figure 2* elucidates the manner in which a flaw is analyzed. ECA standards and codes like BS 7910 [21], API 579 [22] or R6 [7, 23] are utilized for this purpose based on preferences, requirements and geographical location.

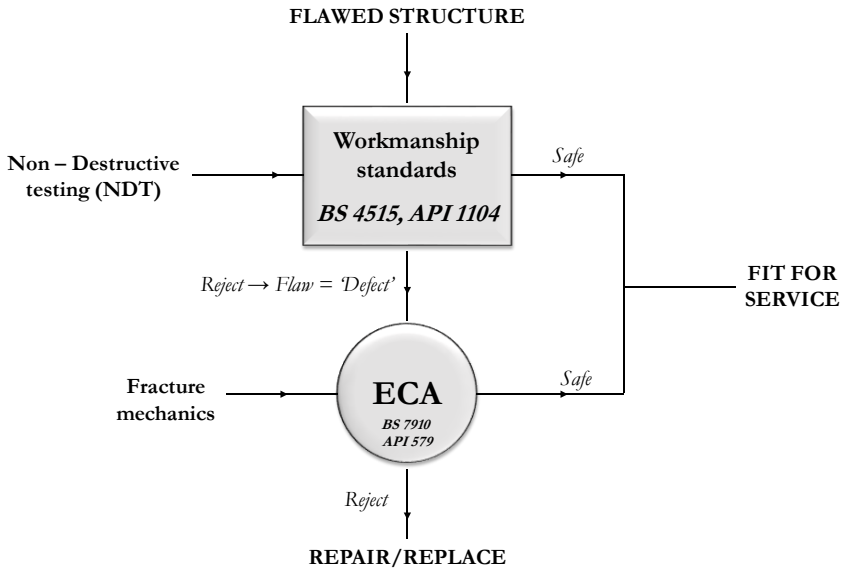

Figure 2: The assessment of a flawed structure through workmanship standards and Engineering Critical Assessment (ECA)

ECA assists in determining the limiting conditions for failure that are "safe", i.e. conservative results can be obtained. ECA standards have been developed for and are being used in the field of oil and gas, nuclear, aeronautics, naval constructions and others. In order to perform an effective ECA of a flawed component, three major types of information are required. This is illustrated in *Figure 3*. The three components, which are mentioned below, help in assessing if the flaws can be retained or a repair/replacement is required.

- The size, position, and orientation of the flaw(s)
- The stresses developed in the material surrounding the flaw(s) during operation
- Toughness and tensile properties of the region surrounding the flaw(s)

In welded structures that are under operation, flaws are usually characterized by Non-Destructive Inspection (NDI) methods. Welds can be subjected to various detection methods like visual inspection [[24] and [25]], liquid penetrant [[26] and [27]], Eddy current [[28] and [29]] and others [21]. ISO 5817:2014 [30] lists and describes up to 26 different types of weld imperfections like cracks, porosities, lack of fusion and others. Cracks and crack-like imperfections, categorized after workmanship procedures can be dangerous to the structure and should be directly subjected to a fracture mechanics assessment [31]. Other imperfections like porosities in low-stress conditions can be neglected to a prescribed extent. It is important to note that these *'cracks'* are generally rejected by workmanship standards and are classified under the category of *'defects'*.

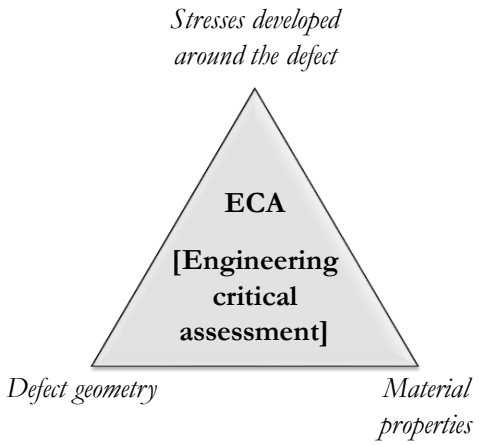

Figure 3: Three required components for Engineering Critical Assessment (ECA) of a defected structure

Stresses originating from internal pressure, thermal or any other type should be determined. For ECA, the stresses determined by the unflawed structure are considered. As mentioned in BS 7910:2015 [21], primary stresses are considered to estimate plastic collapse and fracture. These primary stresses arise from internal pressure and/or external loads. Secondary stresses which are mostly residual stresses are required to satisfy the compatibility/equilibrium conditions of the structure. These can be relieved by local yielding or heat treatment. Secondary stresses contribute to fracture but not to plastic collapse. The tensile and toughness properties of the region surrounding the flaw assist in understanding the fracture behavior of the weld. Tensile properties can be determined by tensile tests for which several standards are available [ASTM E8/E8M [32] etc.] or indirectly through Vickers hardness measurements [ISO 15653:2010 [33] etc.]. Fracture toughness tests can be performed according to several standards like BS 7448 [34], BS EN ISO 15653[33], ASTM E1820 [35] and others.

1.3. Weld heterogeneity

1.3.1. *The background*

Depending on the process and procedure followed for joining two base metals by fusion welding, the cooling of the molten metal occurs diversely forming various microstructures. Thus, a weld is generally classified into three regions: base metal, weld metal and Heat Affected Zones (HAZ). This can be seen in *Figure 4*. If a weld involves multiple passes or regions of repairs, this results in microstructure variations within the weld itself. These variations affect the deformation and fracture behavior of the (flawed) welds. Fracture toughness is affected by the microstructures around the flaw tip while the deformation behavior is influenced by the properties of the larger region of the weldments. In order to construe the fracture toughness of weld metal with heterogeneity, it is first required to understand different features of heterogeneity that contribute to the global fracture toughness behavior.

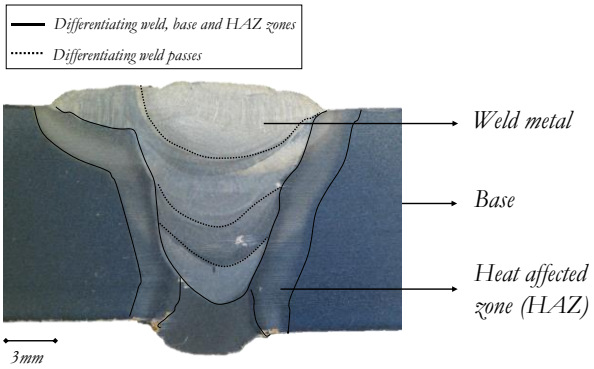

Figure 4: The three regions of the weld – Base, weld and HAZ along with different layers of weld passes

The challenges in structural integrity assessment due to weld strength and toughness heterogeneity have been faced by researchers from the time welding was invented. However extensive research on the effects of property variations in weldments began a couple of decades ago. A brief comprehension of historical developments on strength and toughness heterogeneity aspects in weldments is required for an in-depth understanding of the existing challenges of the methods in use.

Early attempts to study these features of heterogeneity were made by Satoh and Toyoda in 1982 [36]. They raised issues of mechanical heterogeneity in the evaluation of fracture toughness; absorbed energy was obtained with the V-notch Charpy test. They concluded that the absorbed energy makes neither a characteristic nor a qualitative parameter as it is influenced by strength heterogeneity. In continuation

of this outcome, they assessed the effect of mechanical heterogeneity on Crack Opening Displacement (COD) [37]. In 1992, Seo et al. [38] validated the experimental results of Satao et al. [36] showing that the absorbed energy is not only affected by the fracture toughness of the material at the notch tip but also by the mechanical heterogeneity existing in the vicinity of the notch tip.

Vickers hardness has been used by several researchers to estimate local strength properties in weldments. Qiao et al. [39], during their attempt to evaluate residual plastic strain distribution in dissimilar metal welds (DMW's), utilized micro-hardness to characterize residual plasticity in tensile pre-strained steels welded by automated gas tungsten arc welding (GTAW) process with seven passes (*Figure* 5). Additionally, a buttering layer of an alloy is seen on the left side of 7 passes of the weld region. They applied 200g and 1000g of loads which yielded similar hardness values. They obtained the heterogeneous distribution of hardness ranging from 190 HV to 250 HV, which they inferred as the effect of chemistry and plastic strain. *Figure 6* shows an example of a heterogeneous bi-material weld extracted from a pipe during a project at Soete laboratory.

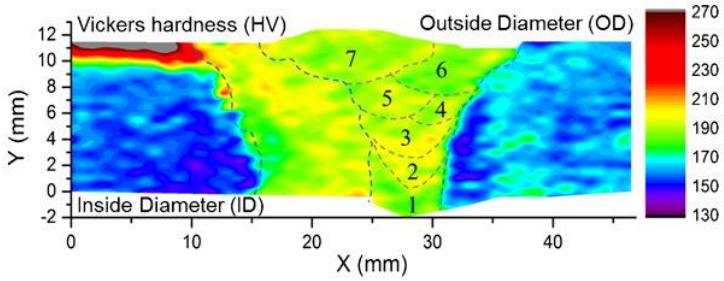

Figure 5: Hardness distribution in dissimilar metal weld [39]

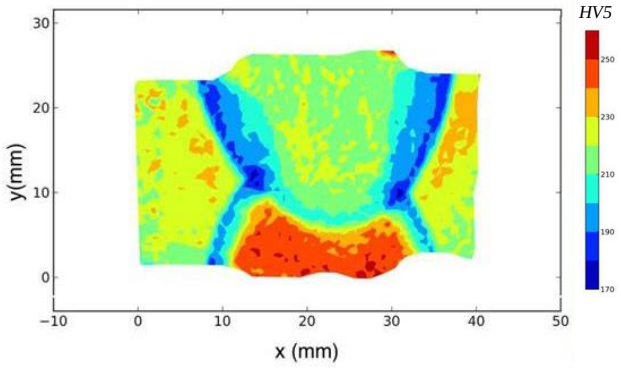

Figure 6: Submerged Arc Weld (SAW) seam of an X80 pipe acquired from a project at Soete laboratory

The variations in the microstructure may lead to loss or gain of yield strength depending on the material being used and the thermo-mechanical treatments subjected to the material. In a master thesis written by Matthijs De Visschere at

Ghent University during the academic year 2015-16, data from several research papers regarding yield strength variations were assessed. The study focused on different weld processes (mostly Shielded Metal Arc Welds (SMAW) and submerged arc welds (SAW)) [40, 41], dissimilar metal welds [42, 43] and other sources where hardness heterogeneity in welds was found [44, 45]. Hardness differences were calculated based on the local maxima and minima. The hardness values in a weldment (involving base, HAZ and weld metal) ranged between 10 HV and 58 HV, which resembles a percentage fluctuation of 5% to 29% with respect to the average hardness. While considering only the weld region, local hardness differences range between 10 HV and 40 HV for SMAW and 10 to 25 HV for SAW.

The strength variations are popularly accounted for by researchers in the form of '*strength mismatch*' in engineering applications [31, 46, 47]. *'Strength mismatch'* is defined between weld and base metal as the ratio of yield strength of the weld metal σ_{yw} to yield strength of the base material σ_{yb}, both of which are often obtained from standardized tensile tests. The relation is shown in *Equation 1.1.*

$$M = \frac{\sigma_{yw}}{\sigma_{yb}} \qquad 1.1$$

This relation is directly related to the mismatch occurring globally in a weldment. Due to strength mismatch the deformation behavior will be affected and different from a material having uniformly distributed strength properties. When strength mismatch is present in a cracked weldment, the plastic strain concentrations around the crack tip will be influenced. As a consequence, the crack driving forces will be affected accordingly. Research in [48] points to a variation of yield strength up to 50% from root and cap regions. Cracks at different locations in a weld would behave differently and this has a huge effect on the fracture behavior of a defect in the weldment. A thorough understanding of the behavior of cracks in a heterogeneous weld region is yet to be understood in detail.

1.3.2. Appraisal of the procedures

Soon after the acknowledgment of the effects on structural integrity due to strength variation in weldments, the need to include mismatch effects in standard ECA procedures arose. As Zerbst et al. [2] point out, there are two different defect assessment methodologies for an elastic-plastic material; the Failure assessment diagram (FAD) and the crack driving force approach (CDF). The choice of two approaches is a matter of convenience as both are equivalent. The CDF approach is similar to an assessment based on a finite element analysis as far as the determination of the crack driving force and its comparison with the material toughness are realized in two separate steps whereas the toughness is a normalizing parameter for the crack driving force in the FAD approach and thus resulting in a failure assessment line.

The earliest analytical defect assessment procedure that included the mismatch effect is the Engineering Treatment Model – Mismatch (ETM-MM) [46, 49] developed in the 1990s by GKSS, Germany. This model helps in estimating CTOD values of bi-material problems such as mismatched welded joints. Welds having a strength mismatch greater than 1.10 (i.e. overmatching by more than 10%) can be analyzed. With is model, the mismatched yield loads can be determined with the information of stress triaxiality and considerations of fracture property transferability.

Following this, in the year 1999, a three-year project undertaken by seventeen institutions from nine European countries was completed. This project aimed at unifying flaw assessment methods. This was termed 'Structural Integrity Assessment Procedures for European Industry (SINTAP)' [47, 50, 51]. During this project, the limitations of all procedures were studied and modifications were made to suit the problems of that time. For mismatch/bi-materials cases, SINTAP allowed users to estimate defect characteristics of a weld with a mismatch lesser or higher than 10%. Also, it provided a procedure to perform *J*-integral analysis. These new aspects were added to SINTAP from the ETM-MM approach. The Fitness-For-Service Network (FITNET) project was launched in the year 2002 by 50 organizations from 17 countries in Europe with contributions from the USA, Japan, and Korea. The objective was to develop and extend fitness for service procedures for welded and non-welded metallic structures. It ran for four years and was completed in the year 2006 [6]. As similar to SINTAP, FITNET also discusses the importance of mismatching in welds (bi-material) and requires limit load solutions for defect assessments. The latest version of BS 7910:2013+A1:2015 [21] has incorporated mismatching effects as mentioned in FITNET [6] and this is the popularly used current standard that discusses mismatching effects. DNV-RP-108 procedures [52] also consider mismatch effects.

BS 7910:2015 [21] standard put forward a procedure to analyze a flawed weld which includes strength mismatching in the weld and HAZ with respect to base material. A general assessment flow chart for assessing fracture is shown in *Figure 7*. The procedure begins with the selection of an assessment option (1, 2 and 3) based on the data availability and lever of conservatism required. This is not detailed in this section. However, the purpose of showing this flow chart is to indicate that options 2 and 3 are advanced procedures in which the weld complexities are considered. The strength mismatches are included in this part of the assessments. *Figure 8* shows the weldment in the form of an idealized two material geometry considered in the standard to assess fracture assessment parameters like limit loads (further explained in *Chapter 6*) which are required for the completion of the procedure. In *Figure 8*, *2a* is the length of the notch and *2H* is the width of the weld. However, the standard does not mention how to obtain an idealized weld from a complex and intricate fusion line and its material properties.

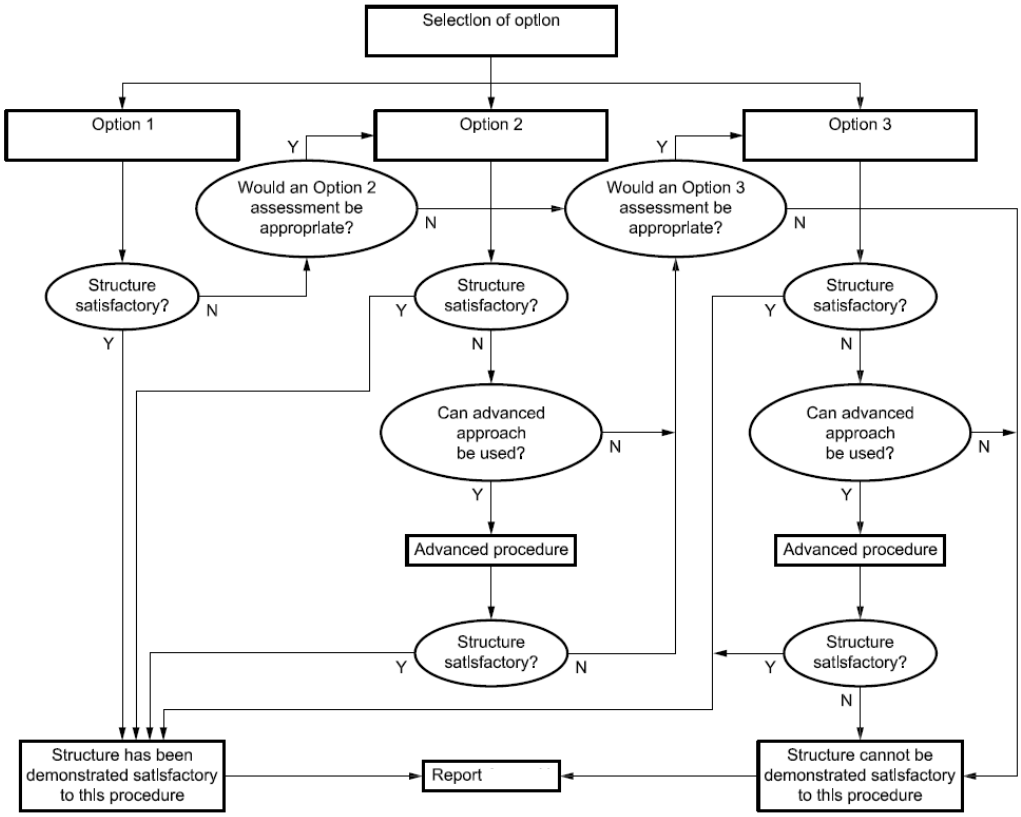

Figure 7: A general flowchart for fracture assessment according to BS 7910 [21]

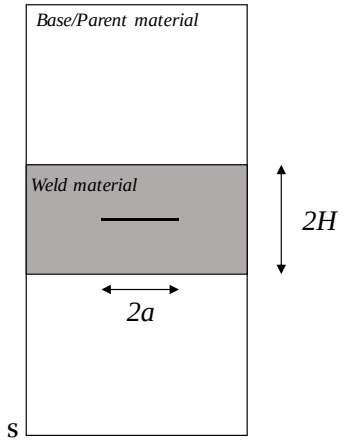

Figure 8: Idealized weldment geometry consisting of two materials, weld and base, as proposed by BS7910

After understanding the current status of weld assessment included in standards, the upcoming section gives a brief literature survey about how researchers dealt with the weld mismatching for fracture assessments.

1.4. Fracture assessments of defects in mismatched welds

In the early 1990s, the study of the effect of strength mismatches in weldments rose to prominence. It was obvious that the weld consumables, which were generally specified at the design stage, incurred higher tensile properties in the weld metal when compared to the base metal. This was performed to avoid the localized accumulation of plastic strains. Several studies on fracture in mismatched welds were made during this period. Crack driving forces (Crack Tip Opening Displacement (CTOD) [53] and *J*-integral [54]) of several weld configurations were estimated for integrity assessments. These estimates showed that the fracture behavior of strength mismatched weldments depends on the various interdependent factors: load, geometry, and location of the crack, local fracture toughness, mismatch ratio, weld geometry, etc. [31]. Full-scale tests of welded pipes prove to be expensive. Hence smaller specimens were extracted from weldments, which replicate the loading conditions on a defect in real size structures. Several test specimens have been standardized to obtain conservative fracture resistance levels like compact tension (C(T)), Single Edge notch Bend (SE(B)) and Single Edge notch Tension (SE(T)) specimens [21, 34, 35, 55].

Schwalbe et al. [56] extended their Engineering Treatment Model (ETM) to involve weld strength mismatch (between two bi-metallic interfaces as in *Figure 8*) for the determination of CTOD [49]. This model required the determination of fracture toughness parameter (stress intensity factor *K*), yield (limit) load, crack driving forces like CTOD and *J*-integral values, and load point displacements which can be used to predict failure in the defected welds. Limit load solutions are important as they are used to estimate the material response in the presence of the defect. Estimation of limit load assists in obtaining crack driving forces through methods like reference stress approach [57] that describe fracture behavior of a defect. This also acts as an important parameter for CDF and FAD approaches of the ECA procedure. The ETM model requires the transition point between the local yielding region and fully plastic region for which limit load solutions are used. Using this point, ETM equations help to obtain CDF curves (CTOD). Zerbst et al. [31] give a detailed review of the importance of limit load estimations for elastic-plastic analysis and show that it is an important input parameter to obtain crack driving forces. They point out that the estimations can be very conservative and that several methods have been used to obtain them.

Miller [58] published an in-depth review of limit load solutions for structures containing defects. Here, he put forward the equations to obtain lower bound (underestimating) and upper bound (overestimating) limit loads for different specimen configurations such as SE(B), SE(T) and M(T). Hao et al. [9] constructed slip line fields that were extracted from numerical simulations of a Center Cracked Tensile (CC(T)) panel having mis-matched weld configuration. This helped in

obtaining limit load solutions for overmatched and undermatched weld configurations. Their work will be detailed in *Chapters 5, 6 and 7.*

Lei et al. [59] used a similar test configuration and proposed a *J*-integral estimation scheme for mismatched welds by defining an equivalent stress-strain relationship of both weld and base material. This relationship was derived based on limit load solutions put forward by Joch et al. [60] as a result of slip line fields determined for the CC(T) specimens. Kim et al. [8, 61] studied mismatch effects on limit loads by simplifying mismatched welds. They utilized yield load solutions to obtain *J*-estimations for CC(T) and SE(B) specimens. Using Engineering Treatment Model (ETM) [49, 56, 62] equations, they modified them to include mismatch effects. All these solutions were validated using elastic-perfectly plastic finite element models. Different mismatch conditions [63] and notch locations [64] *(Figure 9)* have also been studied. Kozak et al. [65] found limit loads considering a bimetallic weld (heterogeneous weld) for SE(B) specimen. From this study, they found that the effect of mismatch within the weld plays a crucial role and has a major influence in the determination of limit load of the fracture toughness specimens.

Hertelé et al. [10] derived an analytical limit load equation for a mismatched SE(T) specimen. They considered several possible combinations of weld geometry, mismatch levels in the weld, and material properties. The outcome of this study showed that simplifying a mismatched weld into configurations such as in *Figure 8* can have a significant effect on limit load estimations and in turn the crack driving forces.

Mismatch in welds not only affects the limit load, crack driving force and fracture toughness of the structure, it also influences the stress-strain distribution around the crack tip. O'Dowd and Shih [66, 67] proposed a method to quantify constraint effects on crack tip stress fields called Q parameter. This method describes the deviation of the stress field from the predicted singularity field (HRR field [68, 69]). This, in turn, illustrates the crack trip stress distribution in terms of the magnitude of the elastic-plastic *J*-parameter [11]. The knowledge of crack tip constraint is important as it affects the apparent fracture toughness and ductile tearing resistance of the material.

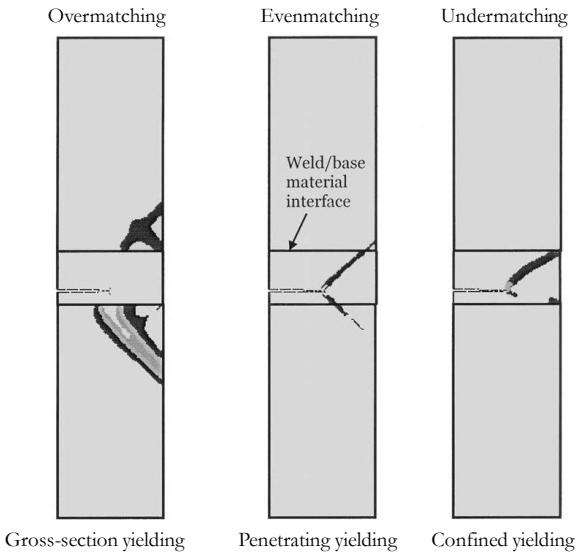

Figure 9: The different types of yielding observed at different levels of mismatch in a center cracked specimen loaded in tension (CCT) [64]

Hao et al. [9] used slip line theory in 1993 to study the constraint conditions of a crack in the mismatched structure. They utilized *J-Q* theory put forward by O'Dowd and Shih [66, 67] and derived an expression for Q involving mismatch term for slightly overmatching and slightly undermatching welds. He showed that the slip lines are altered with the change in yield strength of the regions containing the crack. A constrained plastic flow occurs in undermatched weld while an unconstrained flow was seen in overmatching welds. The level of constraint was measured by estimating the strength of the surrounding base material and the size of the plastic zone. This outcome led Burstow et al. [70] to state that the crack tip constraint increases in undermatching weld and decreases in overmatching weld in SE(B) specimens.

Boothman et al. [71] used a three-dimensional model to understand the implementation of the Q-estimation schemes proposed for homogeneous plates when implemented on mismatched welds containing a semi-elliptical surface defect. They showed that a 30% range of mismatch does not affect the constraint if the crack depth is less than the distance between the crack plane and weld boundary. However, they have acknowledged that the results are confined to rectangular welds and apprehended the validity of the results for complex weld shapes and geometries along with different crack positions. In line with this, several researchers have studied the development of stress fields in mismatched conditions for notched specimens like center cracked panel [9] and single notched [72-74] configurations.

Martin et al. in 1996 [75] presented two-parameter crack tip constraint analysis techniques to analyze stress fields in SE(T) specimens. Graba [76] and Wang [77]

studied the influence of material properties, crack geometry on Q parameter behavior in SE(T) specimens. However, all studies mentioned formerly considered homogeneous weld samples and the conclusions drawn were focussed on the homogeneous weld. Regrettably, the effects of local strength variations in the weld, base, and HAZ are very minimally assessed in specimens having low crack tip constraint conditions. Additionally, the effects of weld heterogeneity variations had been neglected by several standards and it is seen from the literature discussed before that its effect cannot be understated.

1.5. Weld strength heterogeneity in ECA's

Moving forward from the traditional concept of weld mismatch (where the base and weld regions are homogeneous) into the assessment of a defect lying in a heterogeneous weld region, i.e. a region having strength property variations, an improvement of the assessment procedures is needed. The advanced procedures in *Figure 7* involve mismatch criteria to include the complex material properties in the weld region. A flow chart showing the involvement of weld heterogeneity is shown in *Figure 10.*

Additionally, in components subjected to large deformations, the cracks are often at low crack tip constraint conditions. The standardized fracture tests atypically yield highly conservative toughness values resulting in untimely repair of the components. For oil and gas pipes, several researchers have pointed out that the crack tip constraint level for Single Edge notch Tension (SE(T)) specimens closely imitates those defects in pipes rather than other specimen configurations [78-80]. For this reason, the clamped SE(T) configuration is chosen to analyse cracked heterogeneous welds in this research. A flow chart with the methods used in this study is shown in *Figure 11*.

The assessment of defect behavior in a heterogeneous weld region is the major goal of this dissertation. Weld strength heterogeneity and its effects on defect behavior need to be understood by applying analytical concepts, experimental experiences and numerical tools. The research will focus on different levels of material heterogeneity in the weld region and utilize finite element models to simulate complex welds. This will assist in a better understanding of strength characteristics of the weld region, defect behavior in terms of fracture toughness, limit loads, deformation behavior and tearing resistance of a defected weld.

The research approach begins with the consideration of a weld involving strength variations, i.e. material strength heterogeneity within. A defect is placed in a welded specimen according to the SE(T) configuration. With this in hand, several fracture assessment parameters like limit loads, crack driving forces, crack tip constraints and crack tearing resistances are analysed based on the requirement of the standards using numerical and experimental tools with an analytical basis. Each chapter of this

book explains the different effects of heterogeneity on crack behavior of SE(T) specimens. This is outlined in *Section 1.6*.

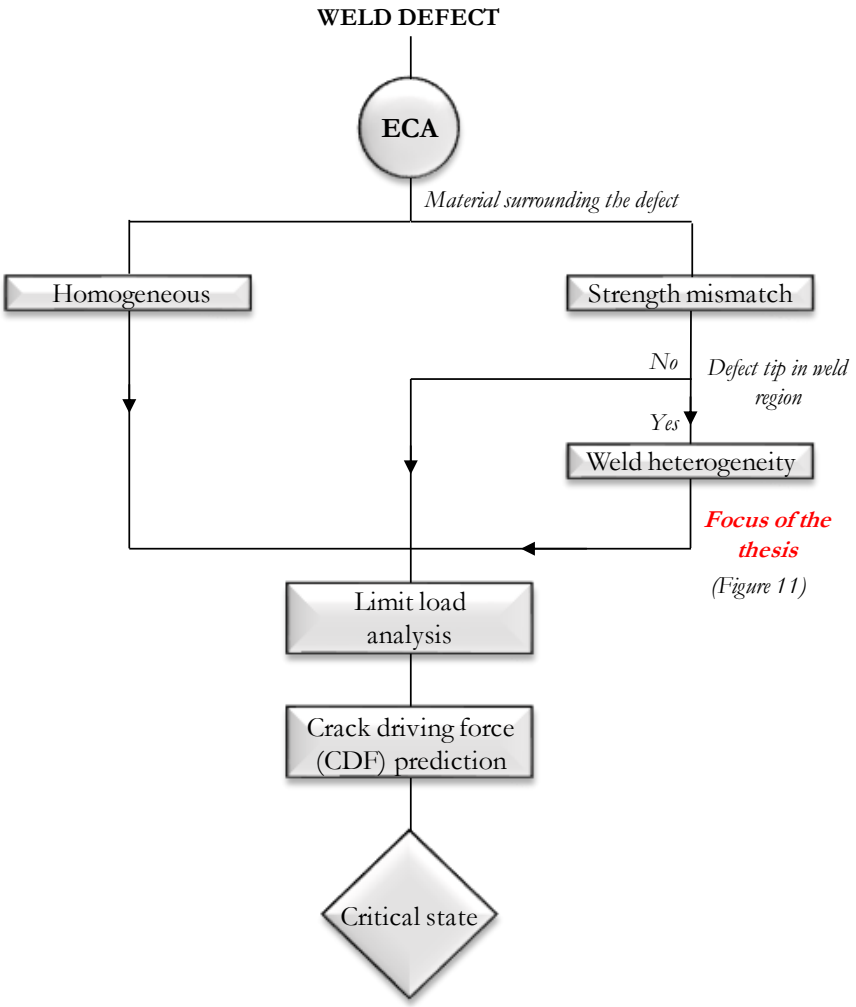

Figure 10: Flow chart of ECA procedure on a defected weld involving weld heterogeneity

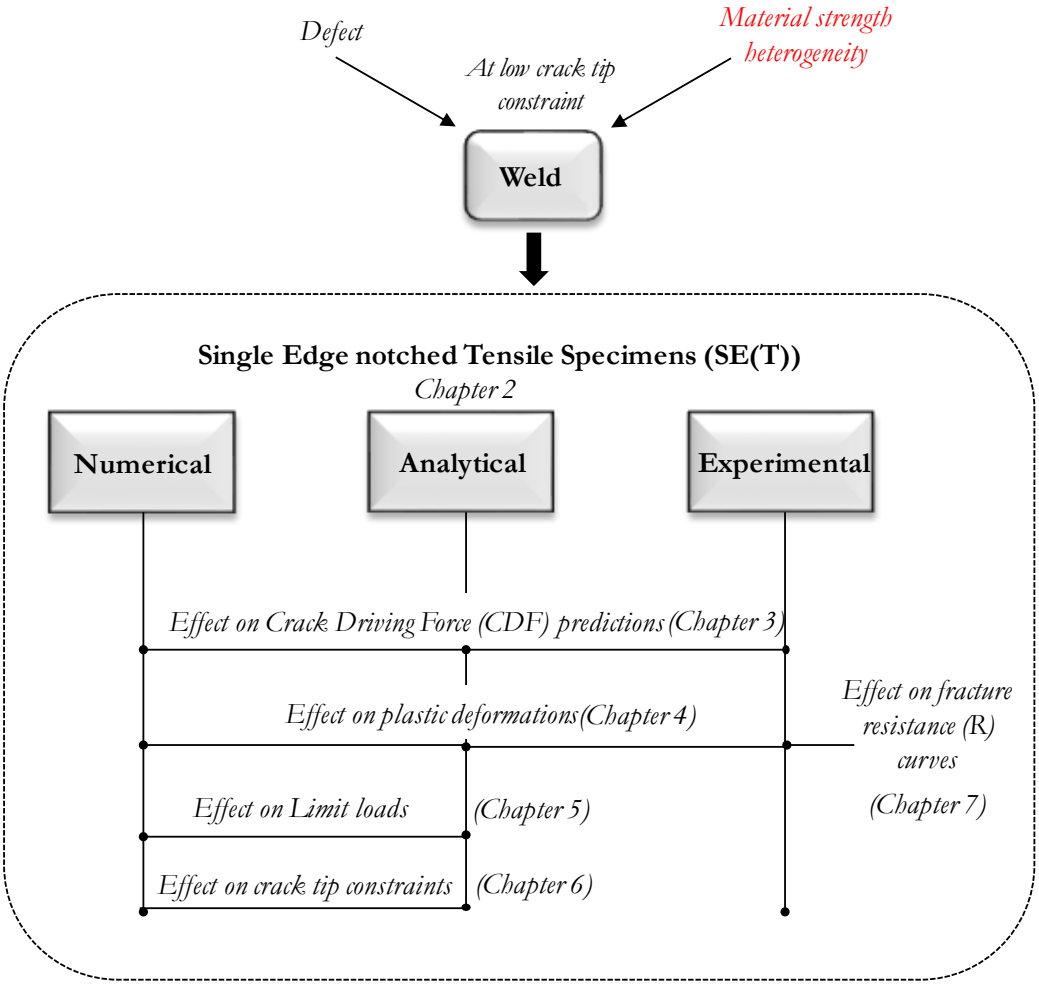

Figure 11: An overall idea of the research conducted in this work to study the effects of weld strength heterogeneity on the behavior of a crack and in turn the structure.

1.6. Summary and conclusions

The issue of heterogeneity in weldments in ECA is not new. Several researchers have pointed out the various challenges of weld structural integrity assessment in the presence of strength variations.

Summarizing the literature, it can be understood that the scientific community considered two or three different materials in a weldment for the assessment of a welded structure. Standards typically provide procedures for bi-materials. Few studies are available to understand the influence of strength variations [10, 48, 81] but the scope of developing a unified approach to deal with more complex local strength variations is still lacking. Therefore, this thesis acts as a platform to understand crack behavior in a heterogeneous weld and the resulting outcome on structural integrity.

The threat of overlooking the strength variations within a weld is pointed out. The analysis of the defect in a weld which is surrounded by heterogeneous material can be a gamble without an appropriate understanding of its properties. This raises several questions related to the mechanical heterogeneity present in the weld region of which few are listed below.

- How can this local strength heterogeneity be quantified?
- Does weld heterogeneity influence crack driving forces in a welded specimen?
- Is the limit load affected by weld heterogeneity?
- What is the influence of weld heterogeneity on crack tip constraint?
- Does weld heterogeneity affect the growth and trajectory of a ductile tear originating from a weld defect?

These questions are analysed in detail and are discussed in the upcoming chapters of this thesis.

Chapter 2

An overview of experimental and numerical methodologies

2.1. Introduction

This chapter expounds on the different methods used in this research. Several analytical concepts have been used which will be introduced in subsequent chapters. Numerical and experimental approaches have been applied to explore, analyze and validate these analytical concepts.

To begin with, the experimental methods used for characterization of weld heterogeneity and crack assessments are explained in *Section 2.2*. A numerical (finite element) model of a SE(T) specimen which has the ability to simulate complex heterogeneous welds is explained in *Section 2.3*.

2.2. Experimental methods and material

Several experimental methods were adopted in this research to characterize and understand the consequences of weld heterogeneity on the fracture toughness and tearing resistance of a defected weld. Two types of weld configurations were used; the first set of specimens was extracted from girth welded pipes (*set A*) and the second set of specimens was extracted from welded plates (*set B*).

Girth weld joints connecting pipes made out of API 5L [82] grade X70 steel (having a specified minimum yield strength of 485 MPa) were considered for crack growth resistance characterization. The girth welds were produced prior to this project within European Union's Research Fund for Coal and Steel (RFCS) research program under grant agreement no. RFSR-CT-2013-00025. Eight different joint configurations were tested. First, two pipes with different diameters and thicknesses (*17.3mm and 19.3mm*) were chosen *(Table 1)*. Welds were produced with a V-bevel preparation, according to two different weld procedures: gas metal arc welding (GMAW) and shielded metal arc welding (SMAW). For each, two different filler metals were adopted to obtain strength properties that were intended to either approximately evenmatch or overmatch the base metal's strength properties along with a pass of Pipliner 6P+ [83] consumable at the bottom of the root.

Additionally, 25 mm thick S690 [84] (structural steel with a minimum yield strength of 690 MPa) welded plates were designed and produced at the *Faculty of Mechanical Engineering, University of Maribor*. The welds are produced in such a way that there is an extreme mismatch between two weld regions *(Figure 15: Figure 12, b; Table 2);* one region being strength overmatching (OM) with respect to the base metal, the other one being strength undermatching (UM). The heterogeneous weld is referred to as OM-UM. Apart from this weld, two additional welded plates each having a fully OM and fully UM configuration was also obtained *(Figure 15: Figure 12, c and d)*. The welding procedure was SMAW, preceded by an X-bevel preparation. The filler metals MIG 90 [85] and VAC 465 [86] were used for the strength overmatching (OM) and undermatching (UM) weld regions, respectively.

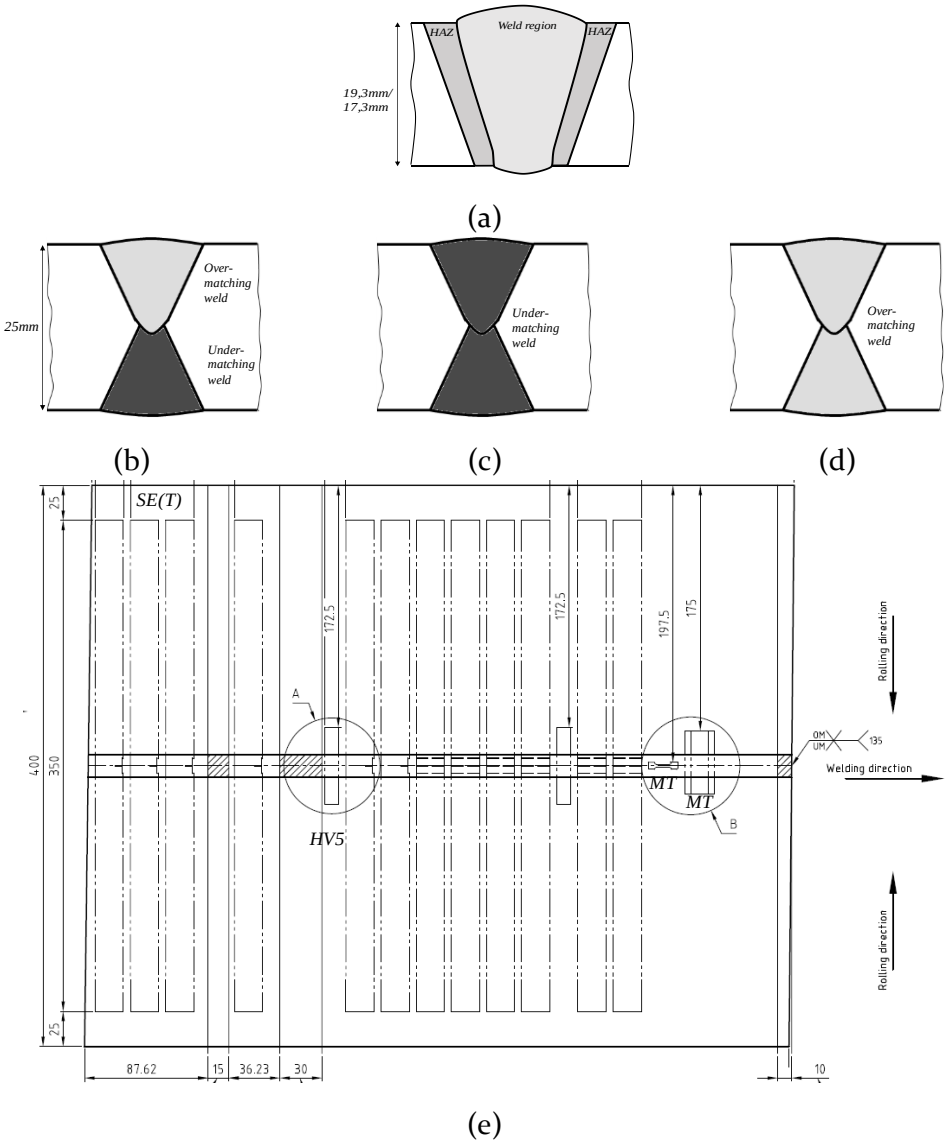

Figure 12: (a) Girth weld with V shaped configuration, (b) test plate having an X shaped weld configuration with OM-UM weld, (c) test plate having an X shaped weld configuration with UM weld (d) test plate having an X shaped weld configuration with OM weld (e) A sample drawing of the extraction of the SE(T), HV5 and MT samples from a welded plate

From the two sets of welded pipes and the plate welds, 11 specimens were extracted on which Vickers macro hardness mapping was performed. The procedure for mapping and the contour plots showing the hardness variations are shown in *Section 2.2.1* Similarly, all weld metal tensile samples of all joints were tested. The yield and ultimate tensile strength values are given in *Section 2.2.2*. Miniature tensile tests were used to validate the hardness calibration equations as further discussed in *Chapter 4*. Here, 14 samples from the OM-UM welded plate (7 from the overmatching region and 7 from the undermatching region) were investigated. Details are provided in *Section 2.2.3*. *Table 3* provides a scheme of all the experiments performed in this thesis.

Base metal geometry (outer diameter × wall thickness)	***Weld procedure***	***Intended weld strength Properties***	***Figure 15***
$48''(1219.2mm) \times 19.3\ mm$	SMAW	Evenmatching	A
		Overmatching	B
	GMAW	Evenmatching	C
		Overmatching	D
$36''(914.4mm) \times 17.1\ mm$	SMAW	Evenmatching	E
		Overmatching	F
	GMAW	Evenmatching	G
		Overmatching	H

Table 1: Material set A: list of API 5L X70 pipe girth weld joints selected for crack growth characterizations

Base metal geometry	***Weld procedure***	***Filler Material***	***Intended weld strength Properties***	***Figure***
$25mm\ S690$ *steel plate*	SMAW	VAC 465 and MIG 90	Overmatching/Undermatching	OM-UM
		VAC 465	Fully undermatching	Fully UM
		MIG 90	Fully undermatching	Fully OM

Table 2: Material set B: welded plate selected for crack growth characterizations

Test performed	***Set A***	***Set B***
Hardness mapping (HV5)	*8*	*3*
All weld metal tensile tests (AWMTT)	*8*	*2*
Miniature Tensile Tests (MTT)	-	*14*
Single edge notched tensile (SE(T)) test	*16*	*12*

Table 3: List of tests and test specimens for the two sets of weld used in this thesis; more details are provided in the following sections.

The consequence of weld heterogeneity on crack tearing behavior was assessed using SE(T) testing of welded specimens. This is explained in *Section* 2.2.4.

2.2.1. *Hardness mapping*

Weld heterogeneity was characterized by means of Vickers hardness (HV) maps [3, 87-89]. Maps of HV indentations with a load of 5kgf or 49N (typically around 1000 per map) were made on polished and etched weld samples. Devoted software allowed to automate the process of hardness mapping. The distance between adjacent indents was kept sufficiently high to avoid interactions, according to ASTM A384-11E1 [89]. The criteria are shown in *Figure 13* and an indented weld is shown in *Figure 14*.

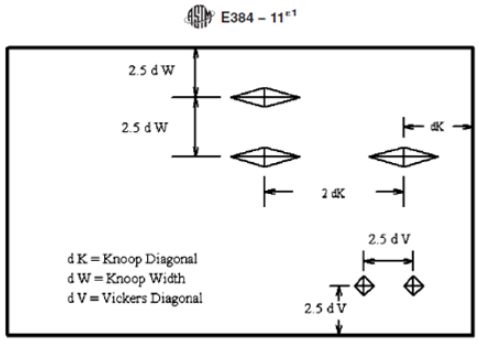

Figure 13: Minimum required indentation spacing according to ASTM E384-11 [89]

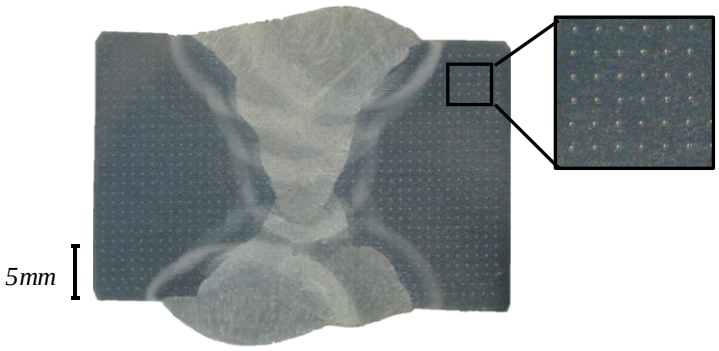

Figure 14: A sample of a set B OM-UM weld after performing hardness mapping

The hardness contour plots for 8 girth welded samples listed in *Table 1* are shown in *Figure 15*. Different observations can be made from a variety of characterized welds. As expected, the presence of multiple weld passes has a pronounced effect on the hardness properties of the weld region. The hardness changes significantly in the welds forming different spatial distributions of hardness from root to cap. Hardness variations may occur due to different weld consumables and/or heat treatments of subsequent weld passes. HAZ softening (observed in specimens A to H) is common for high strength low alloy steels, when weld heat input locally alters the fine grain size that contributes to material strength [90-92].

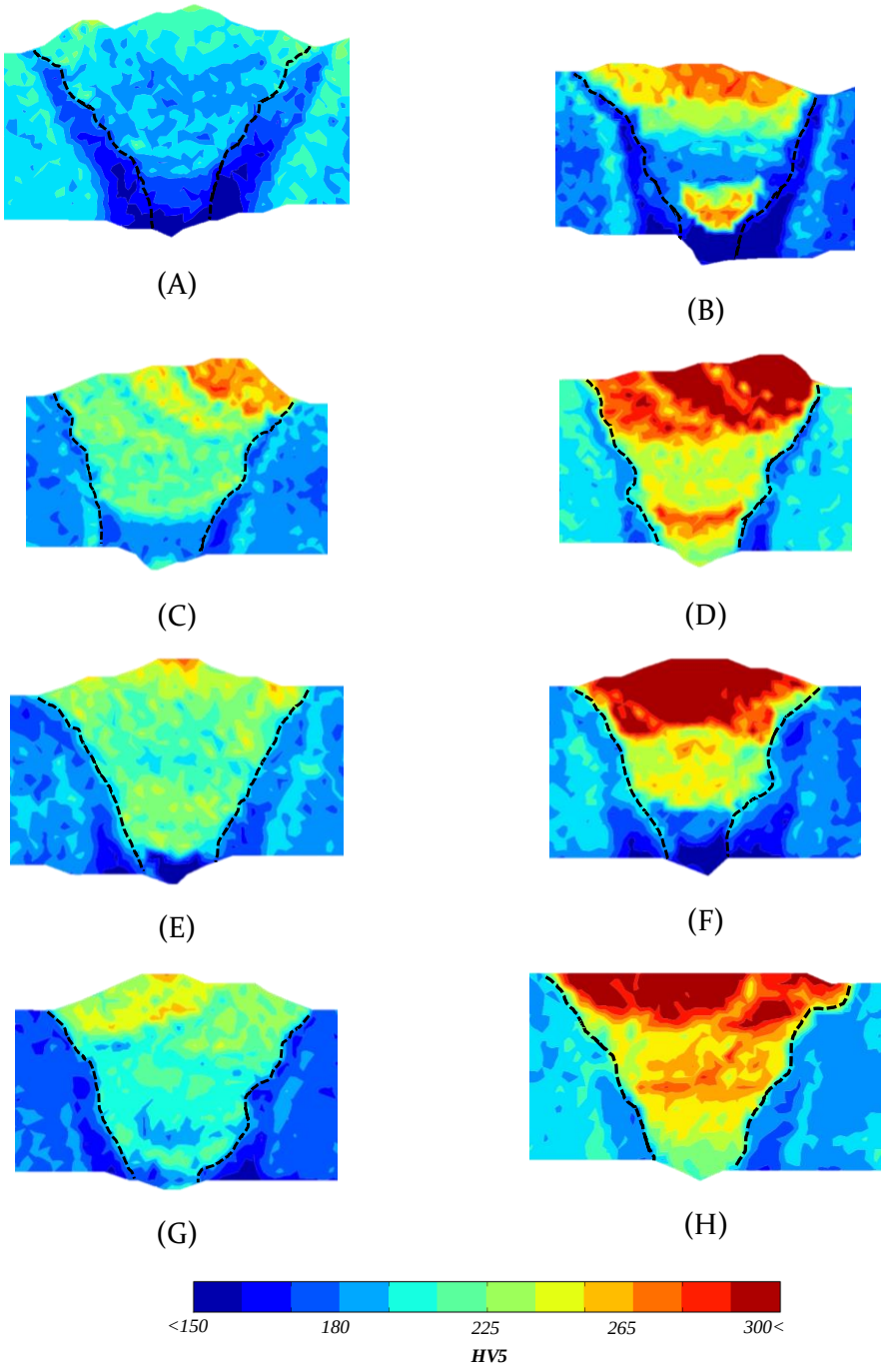

HV5 contour plots of pipe weld samples (A-H)

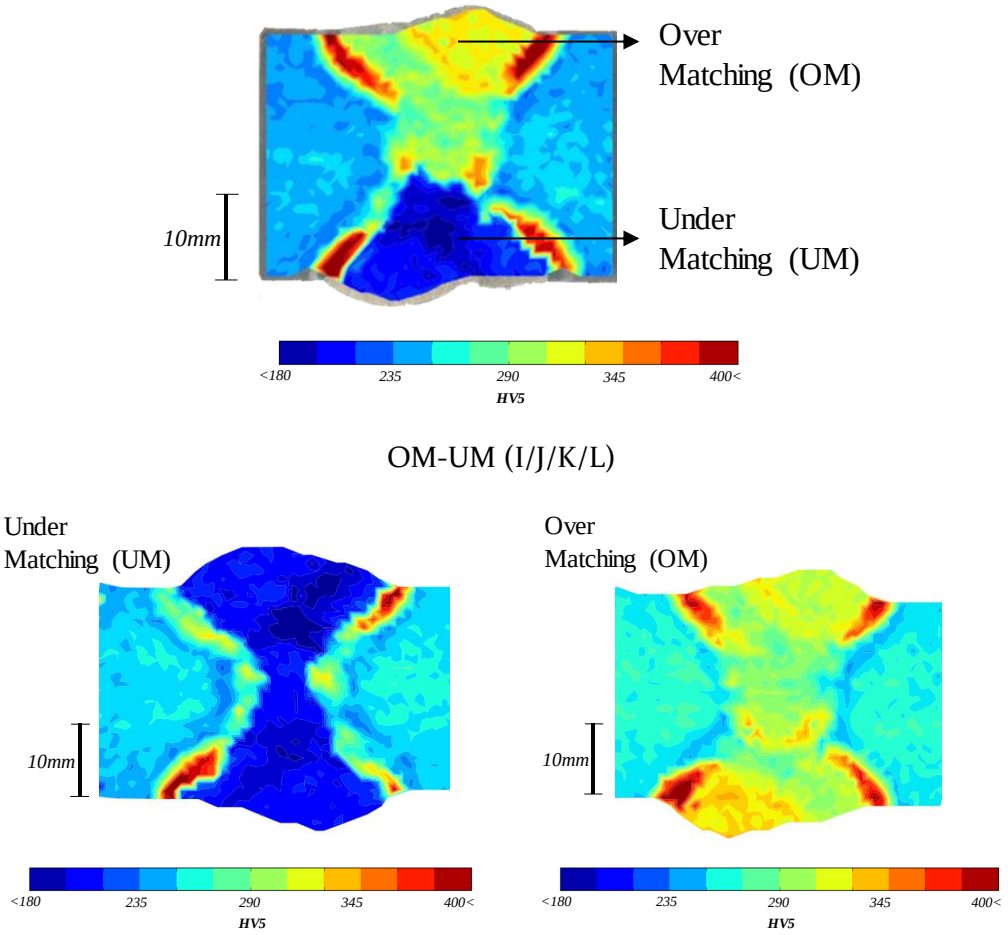

Figure 15: HV5 contour plots of pipe weld samples (A-H) and 25 mm thick S690 plate (OM-UM, fully UM and fully OM) considered for SE(T) testing.

Hardness mapping was also performed on the welded plate and the resulting hardness contour plot (*Figure 15 (OM-UM, fully UM and fully OM)* is shown. Apart from the presence of UM and OM weld regions, *Figure 15* indicates the presence of severely hardened HAZ. HAZ hardening is associated with the creation of hard microstructures due to rapid cooling. As indicated in *Figure 15,* OM-UM weld is assigned with letters I, J, K, L, the fully UM weld as M and the fully OM weld as N. This is useful for further reference to Single edge Notched Tensile (SE(T)) test specimens and is listed in *Table 6*.

The strong variety of heterogeneity patterns demonstrates an excellent basis for the exploration of analytical, numerical and experimental methods covered in this work.

In order to understand the variations of material properties in the welds, hardness traverses were made and plots of HV5 versus distance (*mm*) were obtained. They are shown in *Figure 16*. Three hardness maps from *Figure 15* were chosen, i.e. (A), (B)

and OM-UM welds. Three traverse lines were made, two horizontal ones in cap and root region, *line a* and *line b* respectively, and one vertical along the weld thickness. *Figure 16* includes a 2D contour plot of the HV5 map showing the traverse lines in black. The horizontal lines were plotted from left to right of the specimen and the vertical lines started from the root up to cap region.

Observing the evenmatching weld A on *Figure 16(a) and (b),* it can be seen that the variations in weld and base region are approximately uniform, except that softening is observed in heat-affected zones. The average HV5 value in base and weld was observed to be around 210HV. Due to HAZ softening, the HV5 value dropped to around 190HV along *line a,* while along *line b* it dropped down to 175HV. The effect of softening was also seen in the root to cap traverse line.

In the overmatching weld B of *Figure 16(c) and (d)*, one can observe hard regions in the contour plot. The base material was observed to have around 210HV and HAZ was softened up to 17% with respect to the base material. The hardness at the weld cap (275HV) indicates an overmatching percentage (in terms of hardness) of 30% with respect to the base material and the root hardness came down to 150HV which is a decrease of 28% relative to the base material. Traversing from root to cap in the weld region, one can observe non-uniform variations in hardness.

In the X weld configuration of the OM-UM specimen, the sudden transition of UM to OM region can be seen in *Figure 16 (e) and (f).* An HV5 value of ~170HV was achieved in the UM region whilst an HV5 value of ~320HV was seen in the OM region. HV5 values up to 400HV were measured in the HAZ. Additionally, it can be observed from *Figure 15* that there are sudden changes in material properties within the weld itself as seen in (B) and (F) which can have a severe impact on the crack behavior. The 2D contour plots in *Figure 15* and traverses in *Figure 16* point out the complexities in welds because of material property variations and the importance of including them in defect assessments.

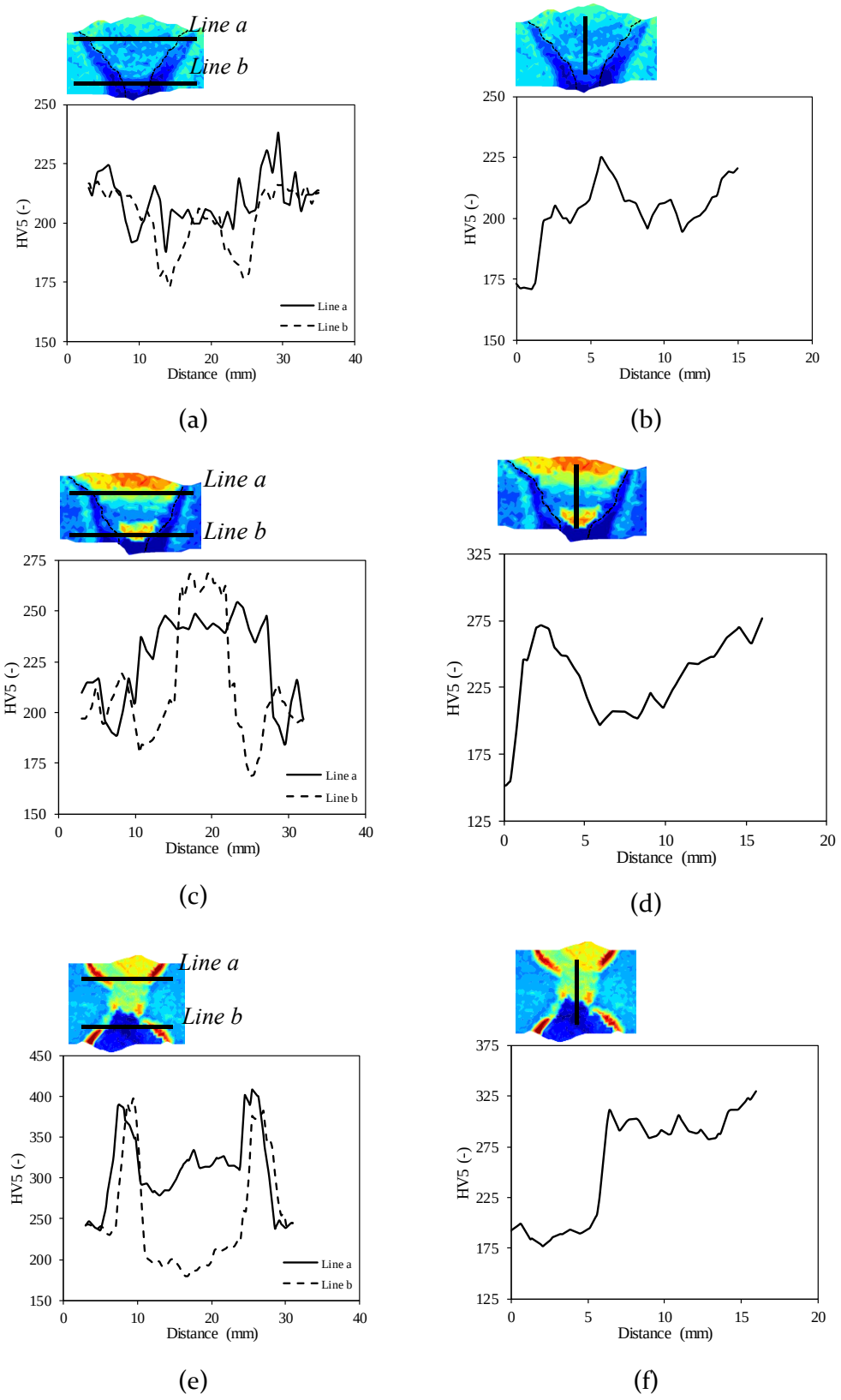

Figure 16: Plots of traverses obtained on different hardness maps: (a) and (b) are from figure 11 (A), (c) and (d) are from figure 11 (B) and (e) and (f) are from figure 11 (OM-UM)

2.2.2. *All Weld Metal Tensile Tests (AWMTT)*

Round bar AWMTT specimens of 5 mm gauge diameter were extracted from each of the girth welded pipes, which constitutes 8 specimens as mentioned in *Table 1*. Additionally, standardized tensile test samples were extracted from OM and UM weld regions of the S690 steel welded test plate. The specimens had a diameter of 6 mm and a gauge length of 30 mm parallel to the welding direction. These specimens were subjected to standard tensile testing to obtain average weld stress-strain properties within the sampled weld region. The results allow calibrating hardness transfer functions according to a procedure which is detailed in *Chapter 4*.

The specimens were extracted near the location of hardness macrographs to minimize the effects of heterogeneity in the welding direction on the AWMTT based transfer functions. *Figure 17* shows the location of extraction of samples in the weld region. The tests were performed in accordance with ASTM E8/E8M-11 [32]. The pipe's tensile test specimens were taken in the central region of the weld and 2/3rd distance from the inner surface of the pipe *(*Figure 17*a)*. For the welded plate *(*Figure 17*b)*, two tensile test samples were extracted from undermatching and overmatching region respectively at 2/3rd distance from the center fusion line. Resulting material properties (averages of three tests each) are summarized in *Table 4* and *Table 5*. In *Table 5*, the values apply for OM-UM welded specimens as well as fully OM and fully UM specimens.

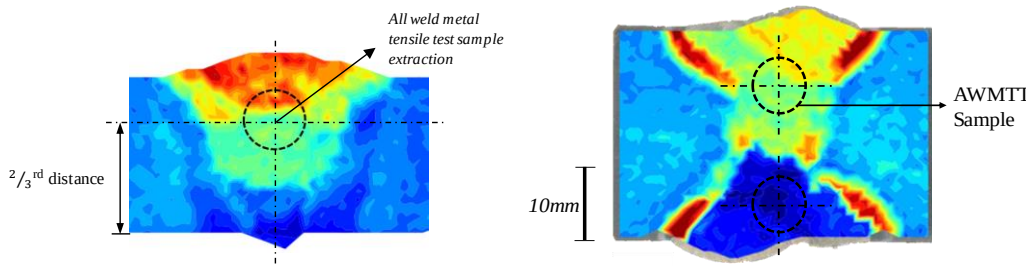

Figure 17: Location of extraction of AWMTT sample from (a) pipe and (b) OM-UM plate

Hardness map *(Figure 15)*	***Yield strength (MPa)***			***Ultimate tensile strength (MPa)***			***Yield to tensile ratio (Y/T) (-)***	
	Weld metal	***Pipe metal***	***Mismatch M_y***	***Weld metal***	***Pipe metal***	***Mismatch M_t***	***Pipe***	***Weld***
A	*579*	*607*	*0.95*	*650*	*660*	*0.98*	*0.92*	*0.89*
B	*620*	*585*	*1.05*	*732*	*637*	*1.14*	*0.92*	*0.85*
C	*641*	*575*	*1.11*	*749*	*626*	*1.19*	*0.92*	*0.86*
D	*711*	*601*	*1.18*	*818*	*655*	*1.24*	*0.92*	*0.87*
E	*616*	*588*	*1.04*	*724*	*660*	*1.09*	*0.89*	*0.85*
F	*674*	*566*	*1.19*	*777*	*639*	*1.21*	*0.89*	*0.87*
G	*630*	*580*	*1.08*	*749*	*647*	*1.15*	*0.9*	*0.84*
H	*752*	*572*	*1.31*	*850*	*643*	*1.32*	*0.89*	*0.88*

Table 4: Average stress properties obtained by all-weld metal tensile testing of the girth welded pipes

Weld regions *(Figure 15)*	***Yield strength (MPa)***			***Ultimate tensile strength (MPa)***			***Yield to tensile ratio (Y/T) (-)***	
	Weld metal	***Base metal***	***Mismatch M_y***	***Weld metal***	***Base metal***	***Mismatch M_t***	***Base***	***Weld***
OM	908	698	1.30	1046	795	1.31	0.87	0.86
UM	635	698	0.90	690	795	0.86	0.87	0.92

Table 5: Average stress properties obtained by all-weld metal tensile testing of the different weld regions in the welded plate specimens

2.2.3. Miniature Tensile Tests (MTT)

MTT specimens were extracted from the weld by means of electrical discharge machining (EDM) *(Figure 18)*. This technique is suitable as no mechanical forces are applied to the vulnerable specimens. Dog bone shaped blocks were taken out in the welding direction, and were divided into 0.7-mm-thick slices (*Figure 19*) [81, 93, 94]. These were then ground on both sides to a final thickness of 0.5 mm, thus removing the brittle heat-affected zone associated with the EDM. The preparation and testing of the specimen were performed at Maribor University during a research visit undertaken in October 2017.

One block was entirely located in the weld and oriented in the through-thickness direction, whereas other blocks sampled base metal, HAZ and weld metals in the welding direction at the OM and UM sides. These different blocks allow to

determine stress-strain curves of different regions of weldment which assists in understanding and analyzing local material property variations in base material (if any), HAZ or in weld material.

For the validation of calibrated hardness transfer functions developed in this thesis (*Chapter 4*) MTT specimens extracted in weld OM and UM region were chosen. Results of 14 specimens in the OM and UM weld regions (7 from each region) of the latter blocks are put forward in *Chapter 4*. The dog bone geometry has a nominal cross-sectional area of 1 mm^2 and was adopted from [93]. Each of the 8 specimens from each configuration is chosen from the region where the AWMTT specimens were extracted from the welded plate. This helps in understanding and accounting the local strength variations ignored by AWMTT experiments used for calibrating hardness transfer functions which are used to obtain material properties from HV5 values. This is further explained in *Chapter 4*.

Digital image correlation was used to measure full-field displacements on MTT specimen surface, out of which the strain was calculated. The specimens were painted white, followed by applying black speckles which were then monitored by cameras that capture images throughout the test, in accordance with reference [81]. These images were then post-processed using devoted software (ARAMIS) for DIC analysis at Maribor University, Slovenia [95].

Additionally, 3 HV5 indents were made on each end of the MTT sample as shown in *Figure 19* (depicted as red diamonds). This will assist in validations of hardness transfer functions which are used to obtain weld material stress-strain properties (*Chapter 4*).

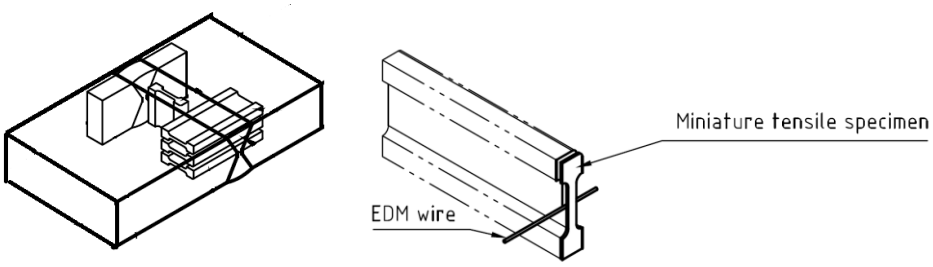

Figure 18: Extraction of micro tensile specimen (image courtesy: P. Štefane, University of Maribor)

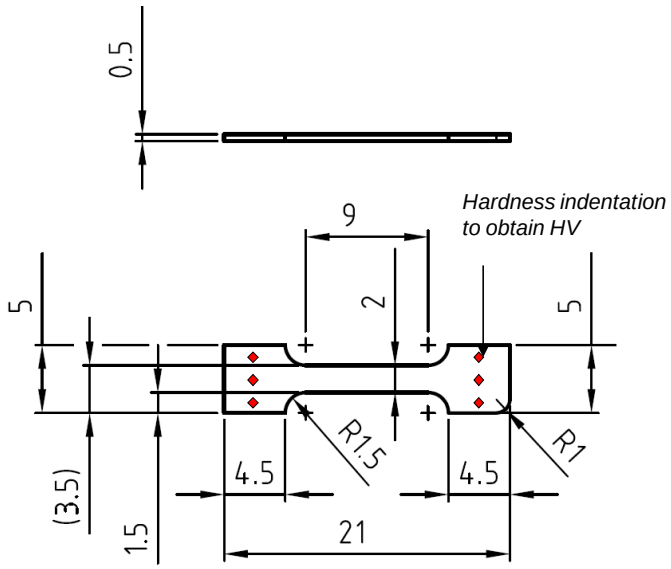

Figure 19: Dimensions of miniature tensile specimens (image courtesy: P. Štefane, University of Maribor)

2.2.4. Single Edge notched Tensile (SE(T)) tests

Twenty-eight SE(T) specimens were extracted from the welded samples mentioned in *section 2*. Two repeat tests were performed for each specimen configuration (8 configurations in pipes and 4 configurations in welded plates). The weld region was located at the center of the specimen. Notch positions were chosen to achieve a maximum variety of results with different possible configurations. The specimens can be classified into two sets:

- *Set A*: 16 specimens extracted from girth welded pipes
- *Set B*: 12 specimens extracted from the welded test plate

The specimens used in this study are summarized in *Table 6*.

Set	*Type*	*Sample Name*	*Tested specimens*	*Side grooves*	*Notch location*	*Fatigue Pre-Crack*
Set A	*Pipe*	A	2	Yes	Root	No
		B	2	Yes	Root	No
		C	2	Yes	Root	No
		D	2	Yes	Root	No
		E	2	Yes	Root	No
		F	2	Yes	Root	No
		G	2	Yes	Root	No
		H	2	Yes	Root	No
Set B	*Plate*	I	2	Yes	OM	No
		J	2	Yes	UM	No
		K	2	No	OM	Yes
		L	2	No	UM	Yes
		M	2	Yes	UM	No
		N	2	Yes	OM	No
Total			**28**			

Table 6: Summary of SE(T) specimens used in this research

Specimens from *set A* had cross-section dimensions $B = W = 15$ mm and a grip daylight distance $L = 200$ mm. They were notched by saw cutting to a targeted depth $a_0/W = 0.3$, producing a notch tip radius of *0.075 mm*, side groove depth equal to 7.5% of B with a root radius of *0.5 mm* and an opening angle of 45^o with the aim to avoid crack tunneling. Fatigue precracking was not carried out. According to different sources, this is not a requirement for sufficiently tough materials, whose failure is preceded by stable ductile tearing [96-98]. The notches were always introduced from the root of the weld (NQ) orientation as per ISO 15653 [33].

In *Set B*, the specimens had dimensions $B = W = 20$ mm and $L = 200$ mm. The notch was located in the OM weld for four specimens and in the UM weld for the other four specimens extracted from OM-UM configuration. Within each of these subsets, four specimens (2 OM and 2 UM notched) had a similar notch and side groove configuration as *Set A* ($a_0/W = 0.3$), without fatigue pre-cracking. The other four specimens (2 OM and 2 UM notched) were not side-grooved and were fatigue pre-cracked in accordance with ASTM E1820:17 [35]. The two fully OM and two fully UM specimens had side grooves and were not fatigue pre-cracked.

The testing was performed at room temperature (23 - 25 ^{O}C). *Figure 20* is a representative image of a not pre-cracked SE(T) specimen showing the notch and side grooves.

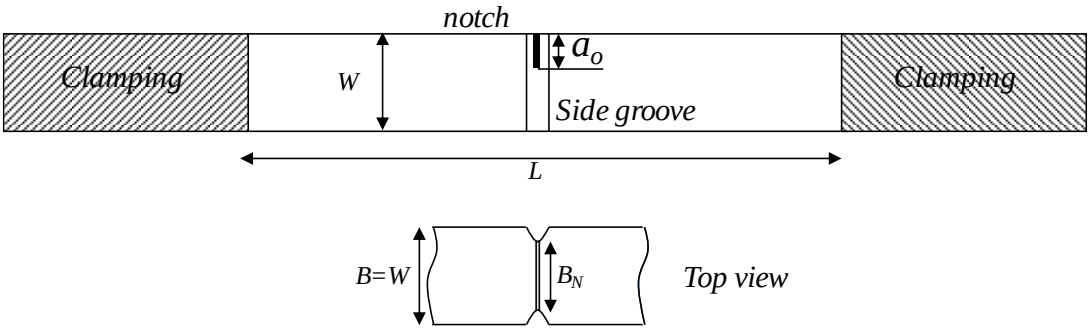

Figure 20: Representation of non fatigue pre-cracked SE(T) specimen with notch and side grooves

The targeted notch depth of the fatigue pre-cracked specimens of *Set B* was 2 mm ahead of the weld interface *(Figure 21)*. Actual a_o/W values were measured post mortem using 9 points (9_{pt}) average method (discussed in *Chapter 3*) and are close to the target (*Table 7*). Nine-point (9_{pt}) measurement is an optical technique that is used to measure initial crack depth and final crack extension of the SE(T) sample. ASTM E1820 [35] suggests measuring the size of the initial and final cracks at nine equally spaced points extending to 0.005W of the surface of the plane sided specimen. The rationale behind the targeted crack position is to stimulate crack extension through the interface between OM and UM regions and check the resulting effect on the tearing resistance curve.

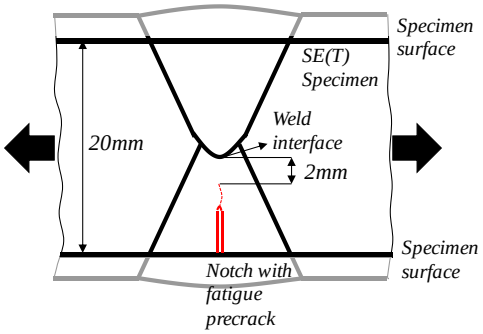

Figure 21: SE(T) specimen extracted from a welded plate and the notch configuration

Specimen *(refer table 5)*	***a_o/W***	***The distance of crack tip to weld interface (mm)***	
		at the surface	***at mid-thickness***
K.1 (crack in OM)	0.55	1.9	1.6
K.2 (crack in OM)	0.61	2.1	1.4
L.1 (crack in UM)	0.39	1.8	1.1
L.2 (crack in UM)	0.32	1.9	1.0

Table 7: Initial fatigue pre-crack positions for specimens of set B without side grooves.

Specimens were tested in universal test rigs having a capacity of 150 kN (for $W = B =$ 15 mm specimens) and 1000 kN (for $W = B =$ 20 mm specimens). Testing was

performed at a fixed displacement rate of 2 mm/min (within the range specified in [55]), using hydraulic clamps that restrained end plane rotations. The displacement was increased until the force dropped down to 75% of its maximum value. CTOD was calculated using a double clip gauge assembly as prescribed by BS 8571:2014 [55]. For the calculation of CTOD, $R_{p0.2}$ is the 0.2% offset yield strength of the base metal or the weld metal depending on the location of the notch (base or weld region) at the temperature of the fracture toughness test.

$$CTOD = \frac{K^2}{1.5\, R_{p0.2} E'} + V_1 - \frac{a_0 + z_1}{z_2 - z_1}(V_2 - V_1) \qquad 2.1$$

The elastic component of CTOD shall be calculated from the elastic stress intensity factor, K. V_1 and V_2 are the plastic parts of the displacements determined from clip gauges mounted at knife heights of z_1 and z_2 respectively in a double clip arrangement as shown in *Figure 22*. In the figure a=a_0 which is the initial crack length.

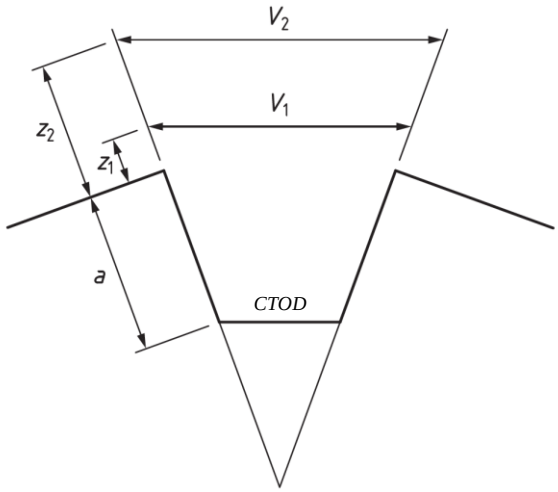

Figure 22: Determination of CTOD from the double clip gauge arrangement [55]

Two clip gauges were mounted at different heights above the specimen (z_1 = 2 mm and z_2 = 8 mm), using devoted knives that were screwed onto the specimen. The specimens were prepared for DCPD measurement – a crack growth measurement technique that uses electric potential to measure crack growth in SE(T) specimens as per the suggestions of [99, 100]. After the tests, specimens were heat tinted at 220°C for two hours. They were then submerged in liquid nitrogen for 10-15 minutes and were broken in a brittle manner in a three-point bending setup. This allowed for the post mortem measurement of crack growth by the 9_{pt} method. The crack measurement procedures using 9_{pt} method, DCPD and Normalization Data Reduction techniques are discussed further.

The crack extension in SE(T) specimens was quantified in three different ways: the 9_{pt} method (for final crack extension), DCPD and NDR. Brief descriptions of the used methods are outlined in the following subsections.

2.2.4.1. Nine-point (9_{pt}) measurement

Nine-point (9pt) measurement is an optical technique that is used to measure initial crack depth and final crack extension of the SE(T) sample. ASTM E1820 [35] suggests measuring the size of the initial and final cracks at nine equally spaced points extending to 0.005W of the surface of the plane sided specimen as shown in *Figure 23*. The initial depth a_o (relating to the initial saw-cut or fatigue pre-crack, if any) and the final crack depth a_f are then calculated using the following equation:

$$a = \frac{1}{8}\left(\frac{a_{(1)} + a_{(9)}}{2} + \sum_{i=2}^{8} a_{(i)}\right) \qquad 2.2$$

where $a_{(i)}$ is the crack length along the lines (1-9) and a is a_o or a_f. Then, the final physical crack extension is calculated by $\Delta a_{9p} = a_f - a_o$.

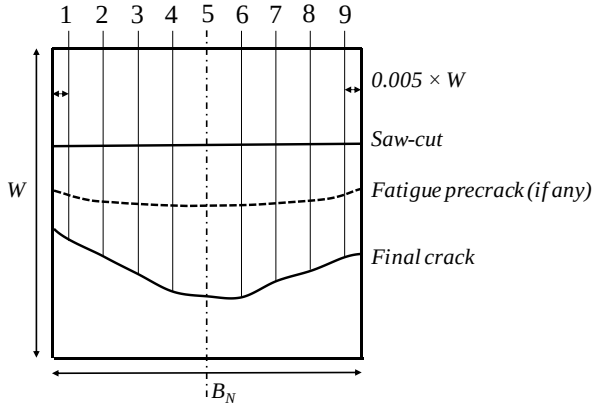

Figure 23: Measurement of the final crack extension on a cross-section of SE(T) sample by the 9_{pt} method.

The initial crack length a_o is obtained from the fatigue pre-crack if present, or the saw-cut in absence of fatigue precracking. The visibility of the final crack for measurement of a_f was increased by heat tinting the specimen prior to forced brittle fracture of the remaining ligament. It is important to note for the following that the 9_{pt} method considers crack extension in the projected through-thickness plane (perpendicular to the tensile loading direction).

2.2.4.2. Direct Current Potential Drop (DCPD) technique

The adopted DCPD technique is explained thoroughly by Verstraete et al. [99] and has been validated on several (welded) specimens by Van Minnebruggen et al. [100]. *Figure 24*. shows a schematic of the experimental setup for DCPD measurements in SE(T) samples adopted in this work. A constant current of 25 A (pipe girth welded specimens) or 50 A (plate butt welded specimens) was supplied depending on the cross-sectional area of the specimen. As the specimens were tensile loaded, the voltage drop V across the notch was measured. The voltage measurement probes were connected to the bolts clamping the knives of a double clip gauge assembly traversing the notch, which was used to calculate CMOD and CTOD by means of trigonometric extrapolation as prescribed by BS8571 [4] . A second reference voltage measurement V_{ref} was taken remote from the notched section, to capture effects of temperature or current leakage through the test setup (by normalizing V against V_{ref}).

A trigger signal was generated every 3 seconds to acquire both voltages i.e. the voltage across the notch and the reference voltage. For each time step, crack growth Δa_{pd} was calculated as $a_{pd} - a_{0,pd}$, using *Equation 2.3* as derived by Johnson [101] to calculate the crack depth from DCPD.

$$a_{pd} = \frac{2W}{\pi} \cos^{-1}\left(\frac{\cosh(\pi\, D_{meas,1}/2W)}{\cosh\left(\frac{v(a_f)}{v(a_0)} \cosh^{-1}\left(\frac{\cosh(\pi D_{meas,1}/2W)}{\cos(\pi a_0/2W)}\right)\right)} \right) \qquad 2.3$$

In *Equation 2.3*, *v(-)* is a normalized value V/V_{ref}. $2D_{meas,1}$ is the distance between two measuring points as shown in *Figure 24*. A crack tip blunting correction was implemented as detailed in [100]. Concretely, a blunting line is fitted through the *v*-CMOD signal by linear regression prior to crack initiation and is then subtracted from the entire curve. The maximum value subtracted was limited to the value of the blunting line at the initiation. In turn, the (minor) crack growth due to blunting was modeled as CTOD/2 up to initiation and added to a_{pd}. Finally, the R-curve was constructed by plotting crack growth against CTOD.

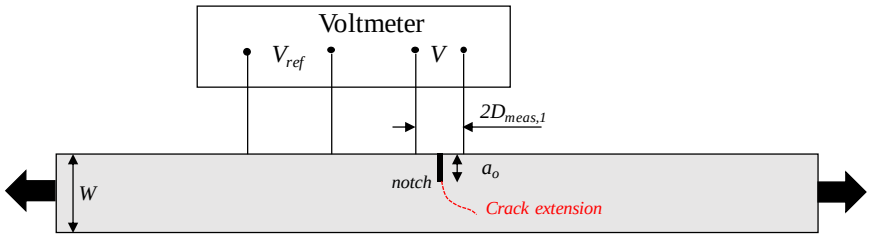

Figure 24: The DCPD setup on a SE(T) specimen

2.2.4.3. *Normalization Data Reduction (NDR) technique*

The third technique used to quantify crack size in this research is Normalization Data Reduction (NDR). ASTM E1820 – 2017 [35] uses force-displacement data together with initial and final crack sizes to obtain a *J* resistance curve (J-R curve) for the specimen types covered by that standard. NDR is not standardized for SE(T) testing but has been explored by Kong et al. [102]. In their work *P*-CMOD data are adopted to achieve normalized force values which are then curve fitted to calculate the CTOD R-curve. The procedure is specifically followed in this research and is briefly discussed hereunder:

- Blunting corrected crack length (a_b) and η_{CMOD} factor along with measured *P* and CMOD values, *J* integral and CTOD [55, 102] values are obtained. For the sake of simplicity, these equations will not be discussed and can be found in [55, 102]. However, the equations to calculate a_b and η_{CMOD} are given.

$$a_b = a_o + \frac{J}{2\sigma_y} \tag{2.4}$$

$$\begin{aligned}\eta_{CMOD} = {} & 1 - 1.089\left({}^{a_o}/_{W}\right) + 9.519.\left({}^{a_o}/_{W}\right)^2 - 48.572\left({}^{a_o}/_{W}\right)^3 + 109.225\left({}^{a_o}/_{W}\right)^4 \\ & - 73.116\left({}^{a_o}/_{W}\right)^5 - 77.984\left({}^{a_o}/_{W}\right)^6 + 38.487\left({}^{a_o}/_{W}\right)^7 \\ & + 101.401\left({}^{a_o}/_{W}\right)^8 + 43.306\left({}^{a_o}/_{W}\right)^9 - 110.77\left({}^{a_o}/_{W}\right)^{10}\end{aligned} \tag{2.5}$$

- Each load value from the initial up to (but excluding) maximum load is normalized to get normalized load P_N:

$$P_N = \frac{P}{BW\sigma_{yw}\left(\frac{W - a_b}{W}\right)^{\eta_{CMOD}}} \tag{2.6}$$

- Similarly, $CMOD_{pl}$ (representing the plastic portion of CMOD) values are also normalized into $CMOD_N$:

$$CMOD_N = \frac{CMOD_{pl}}{W} \tag{2.7}$$

- The normalized load - CMOD (P_N-$CMOD_N$) trajectory is least squares curve fitted. In order to achieve this, $CMOD_N$ values in excess of 0.001 mm and up to maximum load (excluding maximum load value) are used. The fitting equation is:

$$P_{N,F} = \frac{n_1 + n_2 . CMOD_N + n_3 . (CMOD_N)^2}{n_4 + CMOD_N} \quad 2.8$$

  Here, n_1, n_2, n_3, and n_4 are the fitting constants.

- The crack length to thickness ratio is calculated using the equation:

$$a_{NDR}/W = 1 - \left(\frac{P}{P_{N,F}\, W\, B}\right)^{1/\eta_{CMOD}} \quad 2.9$$

- The crack length a_{NDR} obtained from equation 2.9 is further curve fitted against the $CTOD$, which is calculated using the equation in BS8571:2014 [55], using non-linear GRG (Generalized Reduced Gradient) algorithm [103] to find least squares errors [35]. The curve fitted equation is shown in (2.10)

$$\ln CTOD = \ln C_1 + C_2 \ln\left(\frac{a_{NDR}}{k}\right) \quad 2.10$$

  Here, C_1 and C_2 are curve fitting coefficients, k is a fit function parameter and is considered to be *1mm*. This process helps in obtaining the complete R curve (elastic-plastic) as previously, only the plastic part of CMOD and thus CTOD was used to derive a_{NDR} values.

- The fitted curve is extended until the final crack extension value obtained by 9_{pt} method to develop the R curve (CTOD vs crack extension).

In addition to 'conventional' instrumentation, Digital Image Correlation (DIC) was used to depict full-field plastic deformations. The detailed procedure is put forward in [104] and setup is shown in *Figure 25*. In brief, a stereoscopic system consisting of two synchronized monochromatic cameras captures pictures at predefined intervals of time (6 seconds here) during the process of testing. The obtained pictures were correlated using the commercial software package VIC 3D (version 7) to obtain contours of in-plane strain values on the surface of the specimen.

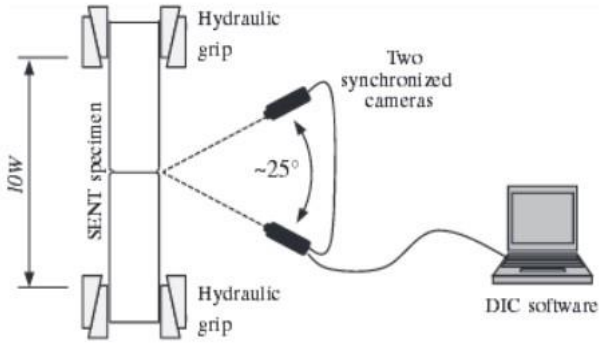

Figure 25: DIC Test setup as shown in Verstraete et al. [104]

2.3. Numerical framework

The numerical model of a SE(T) specimen involved various analysis techniques based on the theoretical and experimental requirements outlined in the following chapters. These different cases are listed as follows:

- Two dimensional SE(T) model
  - Plane strain bi-metallic welds (elastic-perfectly plastic and elastic-plastic with strain hardening);
  - Actual weld based on material behaviour obtained from hardness maps.
- Three dimensional SE(T) model with or without side grooves
  - Actual weld based on material behaviour obtained from hardness maps.

The SE(T) specimen was modeled using the finite element software ABAQUS (version 6.11). The specimen had a width W, crack depth a, and a 'daylight grip length' of $10W$. Three-dimensional, eight-node linear elements with reduced integration have been used. The meshing strategy for this model has been developed in reference [105]. A clamped boundary condition is imposed on one side of the specimen and the other end is displaced in the x-direction over a distance $u_x = W/5$ in order to obtain sufficient crack tip plasticity. Only one half of the specimen was modeled with the introduction of a symmetry boundary condition. A blunt crack was modeled and the crack tip radius, r, was maintained at the value of 0.005 mm.

Small strain assumptions and isotropic $J2$ (von Mises) plasticity have been implemented. For the cases of elastic-perfectly plastic material properties, elastic properties were assigned by Young's modulus E and Poisson's ratio ν. The perfect plasticity was achieved by assigning a constant yield value.

For the simulations including strain hardening, base and weld metals were modeled according to the Ramberg-Osgood model, (*Equation 2.11*), having an equal or different strain hardening exponent n and different yield strength (see *Section 3.1*).

$$\frac{\varepsilon}{\varepsilon_y} = \frac{\sigma}{\sigma_y} + \alpha\left(\frac{\sigma}{\sigma_y}\right)^n \qquad 2.11$$

Here, σ and ε represent true stress and strain while ε_y represents yield strain (equal to σ_y/E). α is a yield offset parameter, where $\alpha\varepsilon_y = 0.002$ to set σ_y as the 0.2% proof stress, and n is the strain hardening exponent.

Incremental plasticity was defined by isotropic hardening and von Mises yield criterion, stress-strain response obeying the Ramberg-Osgood model. Crack initiation and stable ductile tearing were not considered. Crack tip opening displacement (CTOD) was calculated using Rice's 90° intercept method [106] as seen in the *Figure 26*. *J*-integral has been extracted using the domain integral method, considering the 22nd contour of the radial mesh surrounding the crack tip.

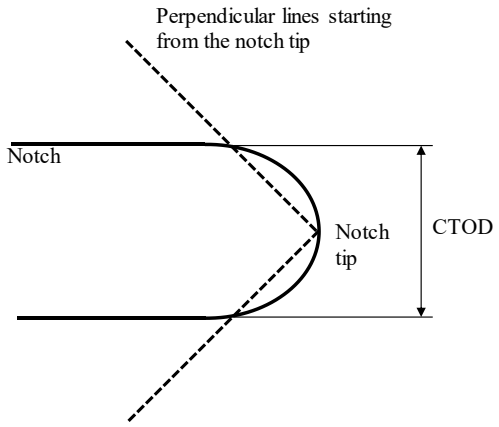

Figure 26: Calculation of CTOD from Rice's 90 degree intercept method [106]

The heterogeneity of the welded connections was introduced by assigning unique stress-strain properties to each element, in accordance with the HV maps of the welds. Hereto, an algorithm developed in reference [48] was adopted. Using the explanation from that reference *(Figure 27)*, a brief procedure for assigning element-specific material properties is explained below.

1. Determination of the centroid of the element (denoted by 'i').
2. Linking (x,z)-coordinates of this centroid with a corresponding position in the hardness map. (Centroids exceeding the boundaries of the hardness map are linked to the nearest point within the hardness map, at the same through-thickness (z) position.)

3. Barycentric interpolation within a triangle (obtained by Delaunay triangulation of the indentation grid) connecting the three nearest hardness indentation points (denoted by I, II and III).
4. Obtaining constitutive properties using hardness transfer equations, to convert HV5 to R_m, $R_{po.2}$ and *n* which will be detailed in *Chapter 4*.

The 2D and the 3D SE(T) specimens have similar material properties in through thickness direction.

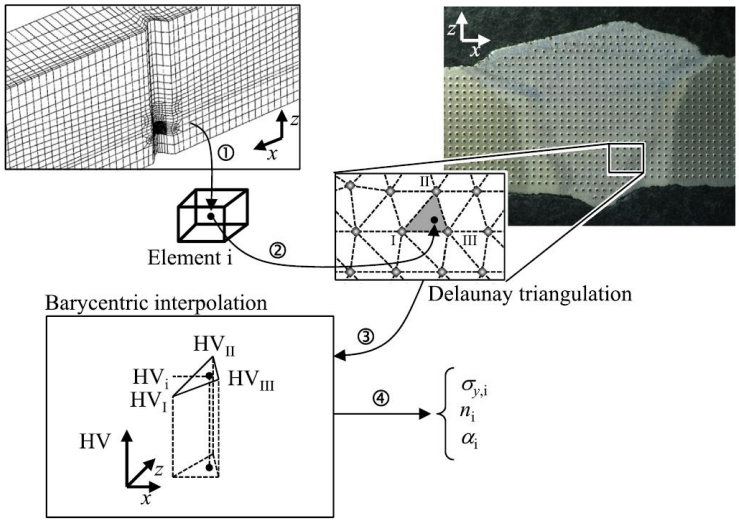

Figure 27: Overview of the approach to assign element-specific material properties in a SE(T) specimen; derived from the reference [48]

An example model is shown in *Figure 28*. *Figure 29* depicts a contour plot of Vickers hardness imported into a SE(T) model. After linking each element to its corresponding HV value, constitutive properties were derived using the different transfer functions which will be discussed in *Chapter 4*. This allowed simulating four different load-CTOD trajectories for each configuration, associated with different treatments of hardness information.

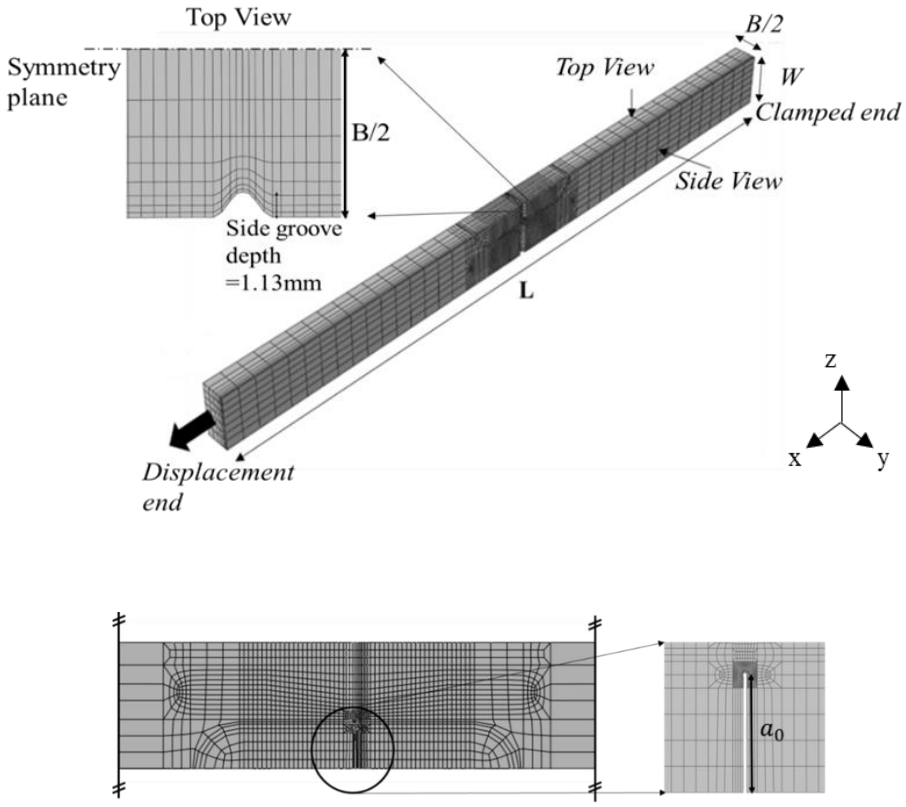

Figure 28: Finite element model of the clamped, side grooved SE(T) specimen

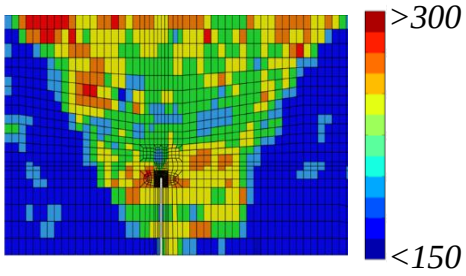

Figure 29: 2D view of the meshed weld region after assigning element-specific strength properties (element color represents local Vickers hardness)

2.4. Summary and conclusions

This chapter has been put forward to show the experimental and numerical methods which will be used in this thesis to assess the mechanical response and tearing resistance behavior in SE(T) specimens

To begin with, Vickers hardness (HV5) measurements were made on several welded samples which were extracted from pipes having V-shaped welds and also welded plates having X-shaped weld configurations. From these measurements, 2D contour

plots and traverses were obtained. This helped in observing the material property variations within the weld and to quantify these variations.

Additional local material properties were obtained through All Weld Metal Tensile Tests (AWMTT) and Miniature Tensile Tests (MTT). These test specimens were extracted from within the weld regions. Fracture toughness and tearing resistance of welded specimens will be assessed using Single edge Notched Tensile (SE(T)) tests. These testing procedures utilized have been explained.

For the numerical SE(T) model, the HV5 values will be utilized to obtain material properties like yield and tensile strength for the weld region. To obtain these material properties, transfer functions have been calibrated and will be validated in *Chapter 4*. Apart from this, a 2D numerical SE(T) model developed in Abaqus has also been explained.

Chapter 3

Tearing resistance of heterogeneous welds in Single Edge notched Tensile (SE(T)) testing

3.1. Introduction

The integrity assessment of welded joints which are subjected to large deformations involves understanding the structural response of its flaws. Flaws accepted by 'good workmanship' rules are considered to be fit for service; the others are potentially unsafe and referred to as defects. Avoiding the repair of defects requires its acceptance through an Engineering Critical Assessment (ECA) procedure, which is based on fracture mechanics. Essential material data input to a detailed assessment is the so-called tearing resistance curve (evolution of ductile crack growth as a function of the applied crack driving force), or simply 'R-curve'. To characterize this curve, a notch is introduced (and possibly fatigue pre-cracked) in a test specimen, which is then loaded to failure. Several specimen configurations are proposed in standards [35, 55, 107, 108]. In the case of thin-walled structures where the load upon a defect is predominantly tensile (such as pipelines), the stress field surrounding the defect is within a state of low crack tip constraint. These conditions are closely replicated in clamped quasi-statically loaded Single Edge notched Tensile (SE(T)) specimens. Several researchers have used SE(T) testing to study toughness properties and crack growth characteristics in both homogeneous and heterogeneous materials including steels [105, 109] and welded joints [48, 52, 79, 100, 110, 111].

Most welded joints characterized in the preceding reference list may be considered fairly homogeneous in nature, implying as a definition in this study that 'weld metal' can be described by one set of strength and toughness properties, distinct from potentially different base metal properties. However, depending on the adopted weld procedure, welds may be heterogeneous in the sense that different properties are observed at different locations within the weld metal region [31].

Weld flaws can arise due to several reasons during welding, repair or operation. As the load acting upon a weld flaw is increased, its tip blunts out and eventually, a ductile crack might initiate (further assuming sufficient toughness to avoid brittle fracture). In heterogeneous welded joints, it is important to understand the influence of the material around the flaw on the crack growth resistance. Defects located in different regions of a weld will respond differently to applied loads. As a crack grows, it may traverse regions of different properties, thus affecting its further growth. In these cases, a well-judged, accurate and accessible technique is required to evaluate crack growth resistance along its entire trajectory. Along with ease of utility and precision, the technique must also have the right balance between conservatism and accuracy.

R-curves can be measured using multiple or single specimen methods. Focusing on the latter, a measurement of the ductile crack extension during testing is required. Several methods to do so have been utilized. Among these, the Direct Current

Potential Drop (DCPD) [99, 100, 112, 113] and Unloading Compliance (UC) [105, 114-116] techniques are the most common. This is reflected in their inclusion in the recent standard BS 8571:2014 for SE(T) testing [55]. The post mortem weighted nine-point average method (9_{pt}), imposed by several standards [33, 35, 117], provides initial and final values of crack extension. These values can be used as a benchmark of the maximum crack extension calculated by the UC or DCPD technique. Both techniques provide comparably accurate results according to a test database reported in [100]. Compared to the UC technique, DCPD involves more extensive instrumentation and sample preparation but consumes less testing time.

An interesting alternative to DCPD and UC is the 'Normalization Data Reduction' or the NDR technique. Researchers have implemented this method to calculate R-curves of many specimen configurations including Compact Tension (C(T)), Single-Edge Notched Bend (SE(B)) and SE(T) [78, 118-120], and it is included in standards ASTM E1820-17 [35] for SE(B) and C(T) testing. Recently, Kong et al. [102] published a modified NDR technique to analyze SE(T) specimens and validated the results using the UC technique. The NDR technique is relatively simple compared to the complexities of DCPD and UC assisted testing, as its analysis is entirely based on the trajectory of tensile load *P* against crack mouth opening displacement (CMOD), and the final crack extension (measured post mortem). However, the investigation in reference [102] was based on homogeneous specimens and, to the authors' knowledge, no work has been performed to evaluate the NDR technique for SE(T) tests of welded (i.e., heterogeneous) joints.

This research work expounds the tearing resistance evaluation of heterogeneous welds under tension loading considering SE(T) specimens, by evaluating three available procedures (9_{pt}, NDR and DCPD) to interpret ductile crack growth. Unloading compliance has not been considered, as previous studies (e.g., [100]) have shown its similar crack sizing abilities to DCPD. Crack tip opening displacement (CTOD) is adopted as a measure of the crack driving force.

3.2. Note on material and methods

Experimental SE(T) tests were performed on the welds shown in *Figure 15*. Two repetitions were performed for each case. The testing procedure and crack measurement techniques are as explained in *Section 2.2.4*. *Table 6* summarized all welds used in these assessments along with the test specimen configurations.

3.3. Tearing resistance analysis

In this section, the outcomes of the experiments are discussed. *Section 3.3.1* is utilized to describe the initial observations of the tests including unstable fractures, crack fronts and shear lips. *Section 3.3.2 and 3.3.3* detail the unstable fracture events and crack fronts respectively. *Section 3.3.6* evaluates the crack extension techniques

used in this study and compares the final crack measurements obtained in *Section 3.3.5*. *Section 3* uses an analytical approach to validate Johnson's equation used in DCPD measurements for a deviating crack front.

3.3.1. Initial observations

Prior to a detailed data analysis, the following observations aid in interpreting the behavior of the SE(T) test specimens.

- Most of the SE(T) specimens underwent stable ductile tearing prior to stopping the test. In some cases, unstable fractures were observed which led to a sudden drop in force. These events are further discussed in *Section 3.3.2*.
- Fracture surface analysis indicated non-straight crack fronts for 11 specimens while others showed straight crack fronts. Crack front uniformity is discussed in *Section 3.3.3*.
- Cracks grew in two directions at the surfaces of non-side grooved specimens due to ductile failure along shear lips (*Figure 30)*. This observation is not related to the crack growth appearance below the surface, where the crack grew in the through-thickness direction for some specimens whilst others demonstrated crack growth at an angle to the pre-crack plane.

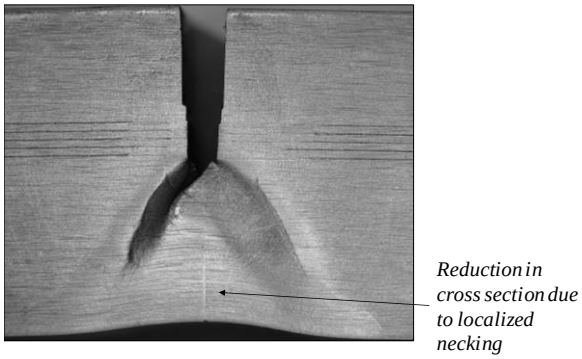

Figure 30: Observation of two angled cracks (the left one being dominant) at the surface of a non-side-grooved specimen, associated with shear lip formation.

3.3.2. Unstable fracture events

Side grooves significantly influenced the crack behavior. In their absence, cracks were unrestrained and could grow in any direction, thus potentially following a deviating path of least resistance (e.g. avoiding regions of stronger material). For side-grooved specimens, however, cracks were forced to grow in the through-thickness direction. At the interface between regions having different material properties (especially traversing from the UM into the OM region), unstable fracture events occurred, i.e. the force dropped significantly and the crack extended extensively. These events are likely attributed to a high level of stress triaxiality

induced by the combined presence of a material property change and side grooves. In such cases, force, CMOD and voltage readings (for DCPD) were considered up to (and excluding) the first point after the unstable event. An example *P*-CTOD curve shown in *Figure 31* displays an unstable fracture event. Notably, it is hard to judge whether this event can be considered as a pop-in (which would imply that the load increases again after the event), as the test was stopped directly afterward.

3.3.3. Crack front analysis

Crack front analysis of tested specimens revealed several different patterns. Out of 24 specimens tested, 11 specimens showed a non-uniform crack front while the others showed uniform fronts. Example specimens having extremely non-uniform final crack extensions are shown in *Figure 32*. The occurrence of non-uniform crack fronts was inconsistent, which makes it hard to pinpoint their exact cause(s). This repercussion affects the measurement of the final crack extension by the 9_{pt} method. As per the standards ISO15653:2010 [33] and BS 8571:2014 [55], the measured individual lengths of a crack at all nine points should not differ more than 20% from its actual length. ASTM E1820:2017 [35] mentions that "none of the nine measurements of original crack size and final physical crack size may differ by more than 0.05*B* from the average physical crack size". *Table 8* shows the validity of the test results based on the ASTM criterion, which is further considered. The table reports maximum differences between the 9_{pt} averaged final crack depth and individual measurement at one of the nine points, expressed as a percentage of *B*. Values below 5% indicate an acceptable crack uniformity and vice versa. Notably, crack sizing was not straightforward for those specimens showing unstable fracture events.

The ASTM E1820 crack uniformity criterion is not met for 13 specimens. As widely discussed in the literature (e.g. [121-123]), plain sided specimens have a tendency towards more non-uniform crack extension. This tendency is confirmed here, since only 1 out of 4 plain sided specimens had an acceptable final crack front, whereas 10 out of 20 side-grooved specimens had acceptable final crack fronts.

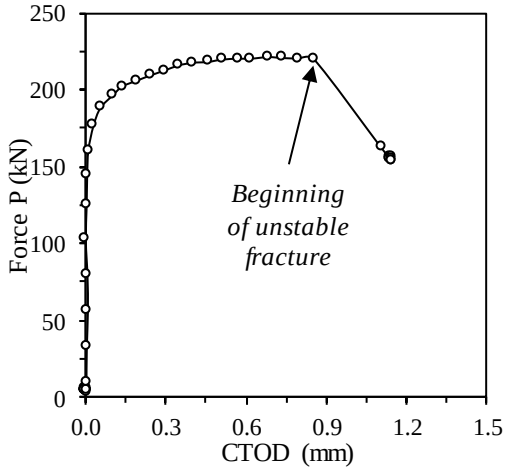

Figure 31: Unstable fracture observed in Set b specimen with side grooves having the notch in UM region

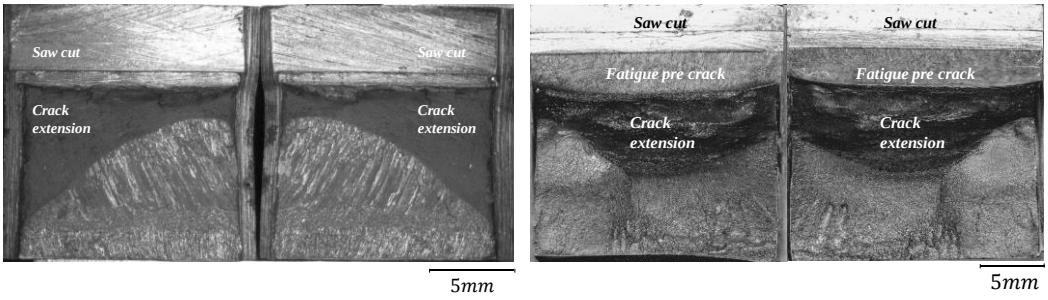

(a) (b)

Figure 32: An example of non-uniform crack extensions observed in (a) side grooved (originates from pipe) (sample E) and (b) no side groove specimens (originates from plate) (Sample L)

The crack extension of the specimens without side grooves extracted from the X-welded plate, and having a starter notch in the UM region, was angular (*Sample L*). This means that the absence of side grooves allowed the crack to extend into the base metal, thus avoiding the OM region (*Figure 32*). As shown in *Figure 15*, this deviation did not require the crack to traverse any of the HAZ regions of very high hardness (dark red regions in the hardness map of *Figure 15*), which would have acted as a barrier for plastic deformation. The crack initially traveled through the HAZ up to the fusion line, which then acted as the weakest link for further crack growth (*Figure 32*). Eventually, it ended up in the base metal. For the two specimens tested in this condition, the deviations of the crack paths were at angles $\theta = 42°$ and $47°$ with respect to the through-thickness direction *(Figure 33 (a))*. As seen in *Figure 33 (b),* a small tear developed from a blunting crack, but then it was rapidly directed towards the fusion line which then acted as the weakest link for crack extension. It is worth to note that, in *Figure 33 (b),* both halves of the specimen were separated (for 9_{pt} measurements) and then the image was captured and recombined.

Set	*Type*	*Sample*	*Tested specimen*	*Validity of final crack front straightness according to ASTM E1820*	*Maximum non-straightness (% of B)*	*Failure mode*	*Angular crack growth (θ)*
Set a	*Pipe material*	A	1	Valid	3.3	Stable ductile tearing	None
			2	Valid	1.5	Stable ductile tearing	None
		B	1	Invalid	18.8	Stable ductile tearing	None
			2	Invalid	7.3	Stable ductile tearing	None
		C	1	Valid	4.9	Stable ductile tearing	None
			2	Valid	1.6	Stable ductile tearing	None
		D	1	Valid	2.8	Stable ductile tearing	None
			2	Invalid	5.4	Unstable fracture	None
		E	1	Invalid	8.3	Unstable fracture	None
			2	Valid	4.5	Unstable fracture	None
		F	1	Invalid	15.3	Unstable fracture	None
			2	Invalid	5.5	Stable ductile tearing	None
		G	1	Invalid	6.1	Unstable fracture	None
			2	Valid	3.6	Unstable fracture	None
		H	1	Valid	4.9	Unstable fracture	None
			2	Invalid	8.2	Unstable fracture	None
Set b	*Test plate*	I	1	Valid	2.5	Stable ductile tearing	None
			2	Invalid	10.9	Stable ductile tearing	None
		J	1	Invalid	5.3	Unstable fracture	None
			2	Valid	1.8	Unstable fracture	None
		K	1	Invalid	5.6	Stable ductile tearing	None
			2	Valid	4.1	Stable ductile tearing	None
		L	1	Invalid	11.4	Stable ductile tearing	42°
			2	Invalid	10.1	Stable ductile tearing	47°

Table 8: Status of the tested specimens measured by 9_{pt} method based on the validity criterion of ASTM E1820 along with failure modes and angles of crack growth (if any).

3.3.4. Evaluation of final DCPD crack extension measurements

In order to obtain a general idea of crack extension accuracy acquired from Direct Current Potential Drop technique (DCPD), its calculated values were compared with the nine-point average measurements. The final crack extension values obtained by DCPD and 9_{pt} are plotted in *Figure 34;* ±15% error lines are drawn in the comparison plot, relating with validity limits for crack sizing accuracy in ASTM E1820:2017. Notwithstanding some outliers, the majority of points lie within the 15% error lines, showing similar trends as in the works of Van Minnebruggen [100] and Verstraete

[99]. The results show that the standard deviation of final DCPD measurement error is 0.15mm, with an average value of -0.03mm. Specimens with final crack extension measurements outside the 15% error line either underwent unstable fracture or had non-uniform crack fronts. The non-straight crack front was observed in the non-side grooved specimens having a notch in the UM region.

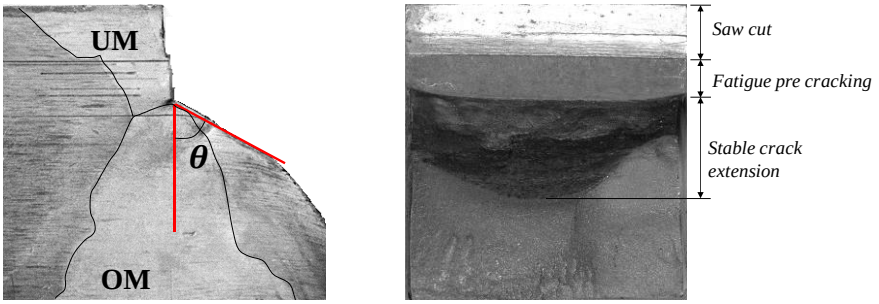

(a)

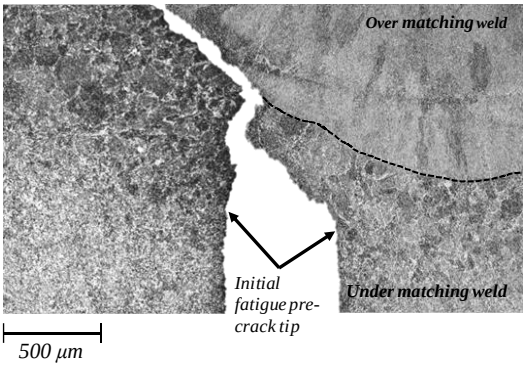

(b)

Figure 33: Crack growth in SE(T) specimen of X-welded plate (without side grooves) notched in the undermatching region. (a) angular crack growth and tunneling (b) crack extension through the HAZ and along the weld fusion line

Most obtained crack extensions lie between 1.5 mm and 3.5 mm, with the exception of the two non-side grooved specimens having a notch in the UM region (around 5 mm). It is recalled from the previous section that these specimens showed significant crack path deviation. Their 9_{pt} values are subject to discussion as the corresponding measurements were made in the projected plane (*Figure 33 (b)*). suggests that DCPD measurements relate with the projected crack extension rather than the physical extension at an angle, which is greater by the inverse cosine of the crack path deviation angle θ.

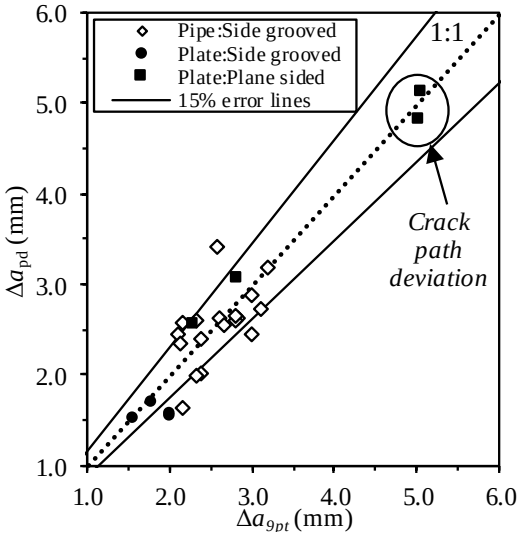

Figure 34: Comparison of maximum crack extension values obtained from DCPD and 9_{pt} methods

3.3.5. Comparison of crack measurements by DCPD and NDR

Based on the above results, 24 samples that had different levels of weld strength heterogeneity were compared for the CTOD R-curves obtained from DCPD and NDR methods. The curves are divided into two sets:

- *Set a*: pipe girth welds (*Figure 35 a-h*)
- *Set b*: plate butt welds (*Figure 36 a-d*)

From *Figure 35* and *Figure 36,* the similarities and differences between the R-curves obtained from DCPD and NDR technique can be observed. Though high differences (up to 30%) at a certain crack extension value can be seen in *Figure 35 (b)* and *(f)* and *Figure 36 (b),* the other plots show limited differences (below 10%). This study indicates a generally fair agreement of DCPD measurements with NDR curves, notwithstanding some exceptions which are further treated.

The point of interest in the R-curves lies in the presence of a kink when there is a transition of the crack from one region of the weld to another. These kinks can be seen prevailingly in *Figure 35 (a), (c), (e), (f), (g) and 94 (c), (d)*. The kinks observed in these plots are attributed to the crossing of cracks through material interfaces. For non-side grooved specimens of the plate butt weld, the kinks are seen at a crack extension Δa of approximately 0.9 mm. Although the target of the notch was to lie within 2 mm distance from the fusion line, the fatigue crack did not have a uniform crack front but rather a curved one. This crack tunneling effect resulted in a closer distance of the crack tip to the weld interface of the specimen mid-thickness. The effects of crack tunneling are discussed in the previous section.

DCPD does not appear to significantly lose accuracy in the presence of crack path deviation even though the analysis leading to the Johnson equation assumed a straight crack. This statement is subject to further attention in *Section 3.3.6.* Also, from *Figure 36 (c) and (d)*, the simplified (power-law) R- curves obtained from the normalization method fail to describe the complexity of the shape of R-curve observed in *Set b* samples.

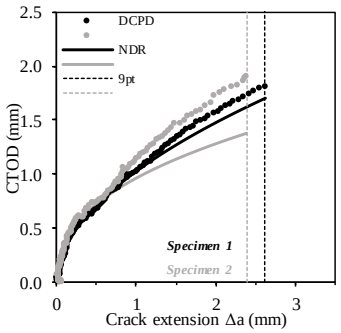

(a) Sample A

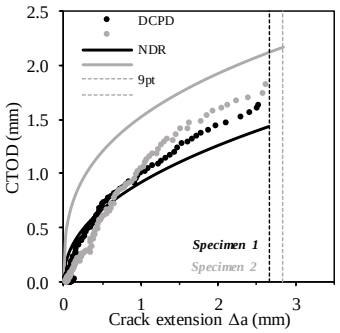

(b) Sample B

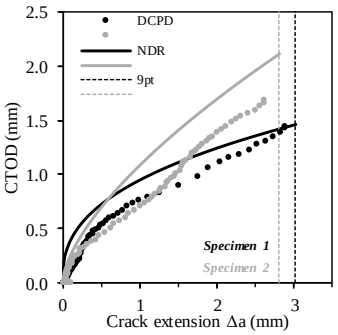

(c) Sample C

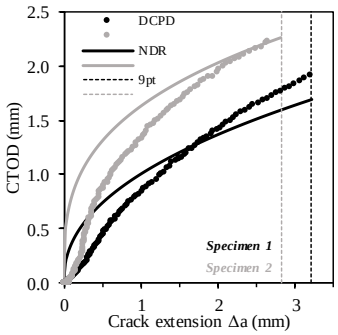

(d) Sample D

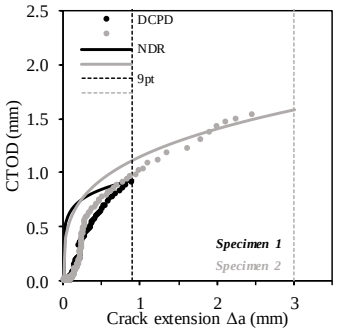

(e) Sample E

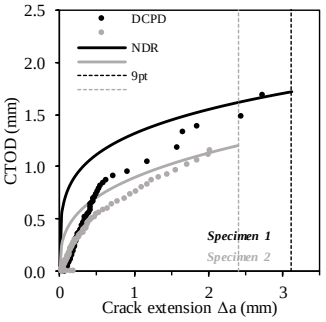

(f) Sample F

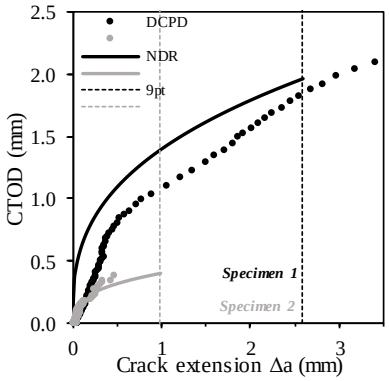

(g) Sample G

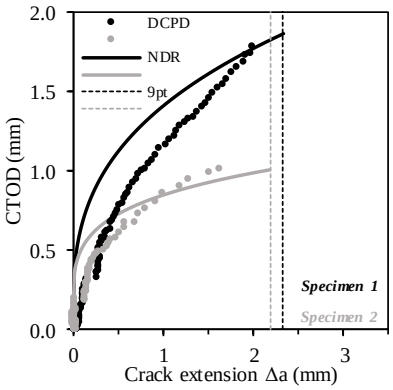

(h) Sample H

Figure 35: The R-curves of SE(T) specimens extracted from pipes obtained from DCPD and NDR technique and compared with 9_{pt} method

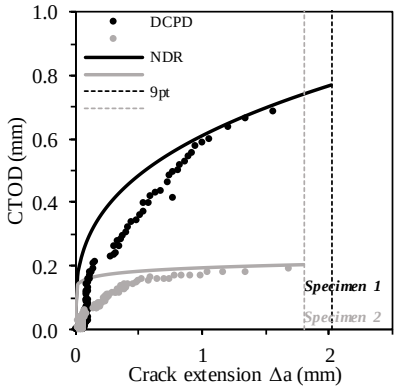

(a) Sample I

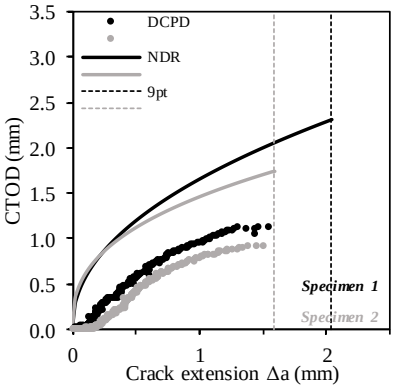

(b) Sample J

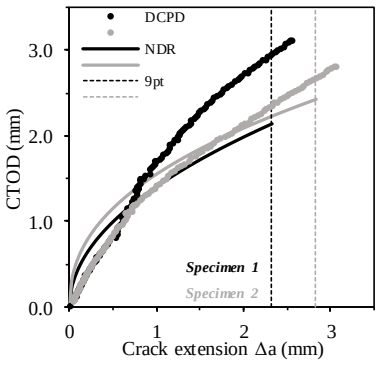

(c) Sample K

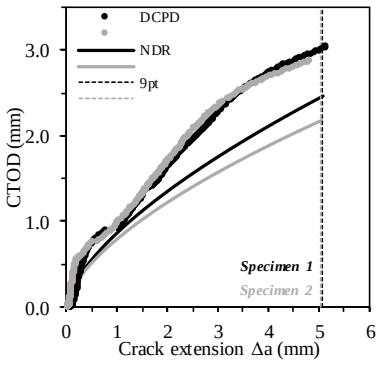

(d) Sample L

Figure 36: The R-curves of SE(T) specimens extracted from butt welded plates as obtained from DCPD and NDR technique and compared with 9_{pt} method. (a) Notch in OM region with side grooves, (b) Notch in UM region with side grooves, (c) Notch in OM region without side grooves, (d) Notch in UM region without side grooves

3.3.6. Analytical study: effect of crack path deviation on crack size prediction using DCPD

In order to assess the effect of crack path deviation on the accuracy of crack sizing using DCPD, a simple calculation scheme is undertaken as follows:

1. A parametric study containing a set of deviating cracks is defined;
2. For each crack, the corresponding potential drop is calculated on the basis of a modified Johnson equation that accounts for crack path deviation;
3. The resulting potential drop value is then fed back into the original, inversed Johnson equation (*Equation 3.3*), to obtain the straight crack growth that would be predicted from this equation. The obtained crack growth values are finally compared against their correct values, that were defined in step 1.

Firstly, the problem is graphically defined in *Figure 37*, showing crack parameters (a_o, a_f, Δa_f, θ), specimen thickness W and DCPD measurement parameters (gauge length $2D_{meas,1}$, asymmetrically divided into $D_{meas,1a}$ and $D_{meas,1b}$). $2D_{meas,1}/W$ was considered to be 1.0 and 0.4, two realistic values that cover different testing conditions. SE(T) test laboratories often choose a fixed value of $2D_{meas,1}$, whereas the specimen thickness W is variable [99]. The following crack configurations were investigated in a full factorial manner:

- a_o/W: 0.2, 0.3, 0.4
- $\Delta a_f/W$: 0.1, 0.2, 0.3
- θ : 0° (no deviation), 10°, 20°, 30°, 40°, 50°

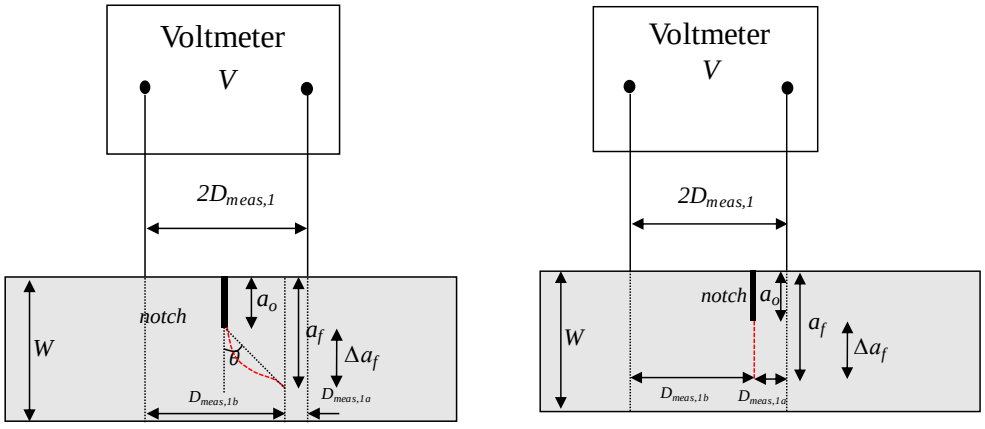

Figure 37: (a) Illustration of the angular crack growth (red dashed line) changing the measurement parameters (b) Configuration assumed for the modified Johnson equation.

Secondly, having defined a set of SE(T) configurations, the corresponding relative potential drop $v(a_f)/v(a_o)$ is predicted through a variation of the Johnson equation.

It is hereby assumed that the true configuration (*Figure 37 (a)*) can be represented by the hypothetical configuration shown in *Figure 37 (b)*. It has a straight crack extension but an asymmetrically positioned voltmeter. *Figure 37 (a) and (b)* are equivalent regarding the position of the voltmeter with respect to the crack tip. First, $D_{meas,1a}$ and $D_{meas,1b}$ are trivially calculated from $D_{meas,1}$, Δa_f (a_f - a_o) and θ based on trigonometry.

$$D_{meas,1a} = D_{meas,1} - \Delta a_f tan\theta \qquad 3.1$$

$$D_{meas,1b} = D_{meas,1} + \Delta a_f tan\theta \qquad 3.2$$

Then, the total relative potential drop $v(a_f)/v(a_o)$ is subdivided into its components left and right of the crack tip. Assuming the model of *Figure 37 (b)*, both can be obtained from a division of the Johnson equation by a factor 2. The resulting relation is:

$$\frac{v(a_f)}{v(a_0)} = \frac{\frac{1}{2}.\left[\cosh^{-1}\left(\frac{\cosh(\pi\, D_{meas,1a}/2W)}{\cos(\pi a_f/2W)}\right) + \cosh^{-1}\left(\frac{\cosh(\pi\, D_{meas,1b}/2W)}{\cos(\pi a_f/2W)}\right)\right]}{\cosh^{-1}\left(\frac{\cosh(\pi\, D_{meas,1}/2W)}{\cos(\pi a_0/2W)}\right)} \qquad 3.3$$

Thirdly, the calculated value for Δa_f is obtained by plugging $v(a_f)/v(a_o)$ into *Equation 3.3*. The final results are shown in *Figure 38* and *Figure 39*. Two $2D_{meas,1}$ values were considered to account for the variability in test procedures. It turns out that DCPD has a good crack sizing ability (given that the data points remain close to the 1:1 line). The agreement remains satisfactory even in scenarios of severe crack path deviation. This result supports the observation that DCPD crack size calculations showed a good correspondence with 9_{pt} measurements (in the projected plane) for those experiments with crack path deviation. Notably, should severe crack path deviation be suspected and of concern prior to testing, one might consider opting for a larger distance $2D_{meas,1}$ between the voltage measurement probes. As *Figure 38* and *Figure 39* show, increasing this distance improves the robustness of the DCPD procedure with respect to crack path deviation.

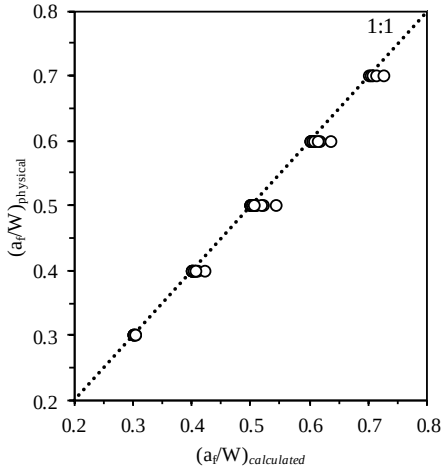

Figure 38: Comparison between theoretical and experimental a/W for $2D_{meas}/W$=1.0

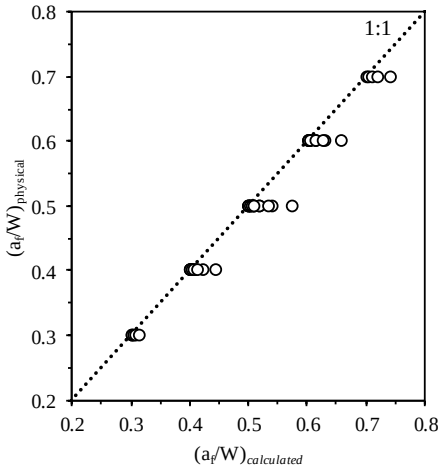

Figure 39: Comparison between theoretical and experimental a/W for $2D_{meas}/W$=0.4

Notably, the specimen design and test analysis of this research were partially based on the 2014 version of BS8571. At the time of publication, a newer version of BS8571 [124] has been released. This version would advise documenting tearing resistance curves of SE(T) tests with crack path deviation in terms of the physical crack extension along the path rather than its projected value in the cross-sectional plane. Since the results of this work indicate that DCPD is related to the projected value of crack growth, its calculated crack growth values should be compensated for by the angle of crack path deviation according to Annex A of BS8571:2018 (thus leading to a reduced tearing resistance).

3.4. Summary and conclusions

The ambition of this research is to understand the crack growth resistance of heterogeneous welds and evaluate available techniques to measure their tearing behavior. Single Edge notched Tension (SE(T)) specimens were considered, the initial notch being located in the weld metal center. Crack growth calculations have been performed in several welds having strength undermatching and overmatching regions. Three crack growth measurement methods were used: the 9 point method, the Direct Current Potential Drop technique and the normalization data reduction technique. Critical observations during the tests were recorded, final crack extensions obtained from DCPD and 9_{pt} method have been compared and R-curves were produced to compare the DCPD and NDR techniques.

The main outcomes of this chapter can be summarized as follows:

- Observations made for different heterogeneous SE(T) specimens with and without side grooves revealed several known phenomena like unstable fractures, crack tunneling and angular crack growth.
- Unstable fracture events were attributed to property changes and the corresponding stress triaxiality present in the weld. Crack tunneling

occurred mainly due to the absence of side grooves. However, it is worthy to note that tunneling and other uneven ductile tearing appearances can also be observed in specimens with side grooves due to heterogeneity effects.

- Angular crack growth was observed in non-side grooved specimens where the region ahead of the crack extended from a softer weld region into a harder weld region. Hereby, crack path deviation is associated with the desire to follow the route of least resistance.
- Differences of final crack extensions calculated by DCPD compared to the 9 point method measurements mostly lie within ±15%, which is within the order of other published test data [99, 100]. This statement holds for severely heterogeneous welds considered in this work.
- Heterogeneous welds show kinks in R-curves as the crack traverses a sudden transition of material properties.
- The effect of angular crack growth on the crack sizing accuracy of DCPD is insignificant. DCPD readings relate to the projected crack extension in the through-thickness direction of the SE(T) specimen.
- DCPD appears to provide an estimate of the projected crack extension (in the through-thickness direction). However, if the crack path deviation angle is constant, the resistance curve could be rescaled using basic trigonometry, and it would lead to a lower tearing resistance

Chapter 4

Characterization of local constitutive properties from macro hardness and its importance for numerical simulations

4.1. Introduction

The measurement of Vickers hardness (HV) is one of the most common techniques to evaluate local strength properties within a weld sample. Hardness mapping may, therefore, serve as a means to quantify the strength heterogeneity within a weld macrograph. Vickers hardness is known to relate to ultimate tensile strength R_m [125] and the equation expressing such relation is referred to as a *'hardness transfer function'* (or simply *'transfer function'*). Conceptually, transfer functions may also be constructed between hardness and yield strength (expressed here as 0.2% proof stress R_{p02}), and strain hardening, thus covering the entire stress-strain behavior. In this chapter, the constitutive law of the weld material is represented by the Ramberg-Osgood (RO) equation [126] and strain hardening is represented by the hardening exponent *n*.

Despite the availability of transfer functions for different steel grades, a generic method to obtain local constitutive property variations in weldments using HV values is lacking. Standards and procedures such as [6, 33, 127] provide equations for conversion of HV to material parameters (R_{p02}, R_m, etc.), which have been derived statistically from a large experimental database. Actual relations between hardness and strength are scattered and can substantially differ from the provided (average) relations.

In this chapter, the ability of standard transfer functions to predict the crack driving force response of cracked specimens based on hardness information is assessed. The study focuses on welds joining high strength low alloy steel components. The method is introduced in *Chapter 2*. Along with this, a technique to bypass HV conversion using standardized ('average') transfer functions has been put forward; an alternative method based on the experimental calibration of the hardness transfer function is proposed. In order to evaluate the approach, a numerical model of a Single Edge notched Tensile (SE(T)) specimen is utilized and validated by means of experiments. To directly validate the soundness of the obtained transfer functions within heterogeneous welds, local strength properties have also been determined by Miniature Tensile Tests (MTT) *(section 2.2.3)*. The material properties obtained from MTT tests have been compared with properties predicted by hardness transfer functions.

This chapter is structured as follows. In *Section 4.2*, a brief background on hardness transfer functions is given. *Section 4.3* puts forward combinations of different transfer functions used to obtain material properties from HV values. *Section 4.4* discusses the accuracy of SE(T) simulations assuming different hardness transfer functions, relative to experimental data. *Section 4.5* validates the calibrated transfer function using miniature tensile tests. *Section 4.6* advises a procedure to use the developed transfer function and *section 4.7* concludes this chapter.

4.2. Background

The early work of Tabor [125] reported on relations between hardness and constitutive properties of metals. Hardness was found to be in relation to the stress at a representative strain level, which is around 0.08 for a Vickers indenter. Given the typical ductility levels and strain hardening characteristics of high strength low alloy steel, this stress is close to the ultimate tensile strength R_m. Therefore, HV has very often been used to estimate R_m. As a conventional HV measurement fails to provide the full range of strain hardening behavior, the approximate nature of these estimates is acknowledged and quantified in the standard ISO 18265 [127]. This standard contains tabulated conversion data between HV, R_m and allows to construct scatter bands for metallic materials. For instance, ISO 18265 mentions that an investigation of about 700 HV-R_m pairs led to a scatter bandwidth of ±85 MPa on ultimate tensile strength, and that systematic deviations from the average transfer function are possible for particular steel groups [127]. A comparison of 250 HV-R_m pairs for high strength low alloy steels and their welds at Soete Laboratory led to a 95%-confidence interval of ±56 MPa with respect to the linear regression fit of the data cloud. Strength variations of these magnitudes are deemed to significantly influence the accuracy of structural calculations using (Vickers) hardness as a material input.

Another relevant international standard is ISO 15653 [33], which mentions HV transfer functions for weld and base metal separately. Unlike ISO 18265, it also mentions relations between hardness and yield strength (additional to ultimate tensile strength). For instance, reported transfer functions for weld metal (estimated for Carbon and C-Mn steels) are:

$$R_{p02} = 2.35\,HV + 62 \tag{4.1}$$

$$R_m = 3.0\,HV + 22.1 \tag{4.2}$$

Researchers have independently constructed hardness transfer functions for their specific purposes. Pavlina et al. [128] assessed the influence of microstructure and yield to tensile (Y/T) ratio using the regression coefficient and regression constant. LaVan [129] plotted conversions only from 180 to 310HV while ISO 18625 [127] validity range is 100 to 350HV. Several other instrumented indentation techniques have been explored by researchers. For example, Midawi et al. [130] characterized material properties using instrumented indentation. However due to availability of excessive research results, ease of implementation and popularity of Vickers hardness measurements in industries, this method has been considered in this thesis.

Recently, Hertelé et al. [48] termed hardness as a tool to produce realistic (but not necessarily the actual) local stress-strain properties of fusion welds with variable yield strength and strain hardening behavior. They considered power law hardening according to the Ramberg-Osgood equation *(Equation 2.11)* and determined its parameters (yield strength σ_y, yield strain ε_y, strain hardening exponent n and yield offset α). Ultimate tensile strength (R_m) was calculated using hardness values according to a linear regression fit of conversion data for steel tabulated in ISO 18265 [127]

$$R_m = 3.21\ HV \tag{4.3}$$

Yield to tensile ratio Y/T is derived from R_m, using a large dataset of stress-strain characteristics of steels [6, 131], i.e.

$$\frac{Y}{T} = \frac{1}{1.07 + (350/R_m)^{2.5}} \tag{4.4}$$

The data set is further referred to as the 'FITNET' dataset as it was also used to calculate an upper bound equation for Y/T in FITNET [6] for welded and non-welded metallic structures. Note that *Equation 4.4* does not represent this upper bound, but rather an average value of Y/T. Notably, the point cloud used to construct the *Equation 4.4* is highly scattered [6].

Yield stress σ_y and strain ε_y are obtained by

$$\sigma_y = R_{p0.2} = R_m . \frac{Y}{T} \text{ and } \varepsilon_y = \frac{\sigma_y}{E} \tag{4.5}$$

where E is considered to be 206.9 GPa in this study. The yield offset α is taken equal to $0.002/\varepsilon_y$. Finally, strain hardening exponent is closely related to Y/T according to Considère's necking criterion $\left(d\sigma/d\varepsilon = \sigma\right)$ [132]. This relation has been curve-fitted into:

$$n = 2.4 + 2.9\ \frac{Y/T}{1 - 0.95\ Y/T} \tag{4.6}$$

Assuming the procedure outlined above, [48] determined the crack driving force response of welds by transferring local weld hardness data into stress-strain input using the above equations within a finite element model. The approximate nature of the above-mentioned hardness transfer functions may influence the fracture mechanics based prediction of weld integrity in the presence of defects. In this chapter, an attempt is made to quantify expectable variations and an experimental

calibration procedure is developed to bypass any variations from scattering with respect to the assumed transfer functions.

4.3. Transfer functions

The standardized transfer functions are considered in this section as they have higher impact in engineering practice. Three combinations of transfer functions were formulated based on available literature to obtain strength and strain hardening properties from HV. They are further termed 'ISO18265+FITNET', 'ISO15653+FITNET' and 'ISO15653' as shown in *Table 9*. The 'ISO18265+FITNET' procedure is adapted from reference [48]; the 'ISO15653' procedure calculates $R_{p0.2}$ and R_m from ISO15653 (*Equations. 4.1, 4.2*), after which Y/T is directly obtained. The 'ISO15653+FITNET' procedure calculates R_m from ISO15653, followed by Y/T calculation from *Equation 4.5* to eventually obtain $R_{p0.2}$. All three procedures finally adopt *Equation 4.6* to obtain n from Y/T. The resulting relations between HV and strength characteristics ($R_{p0.2}$, R_m) are graphically depicted in *figure 19*. Most apparent is the difference between $R_{p0.2}$ calculations using ISO 15653 and using either of the other two procedures.

	ISO18265+FITNET	**ISO15653+FITNET**	**ISO15653**
$\mathbf{R_m}$	$3.21\ HV$	$3.0\ HV + 22.1$	$3.0\ HV + 22.1$
$\mathbf{Y/T}$	$\frac{1}{1.07 + (350/R_m)^{2.5}}$	$\frac{1}{1.07 + (350/R_m)^{2.5}}$	$\frac{R_{p02}}{R_m}$
$\mathbf{R_{p0.2}}$	$R_m * Y/T$	$R_m * Y/T$	$2.35\ HV + 62$

Table 9: Regression based transfer functions to obtain constitutive parameters

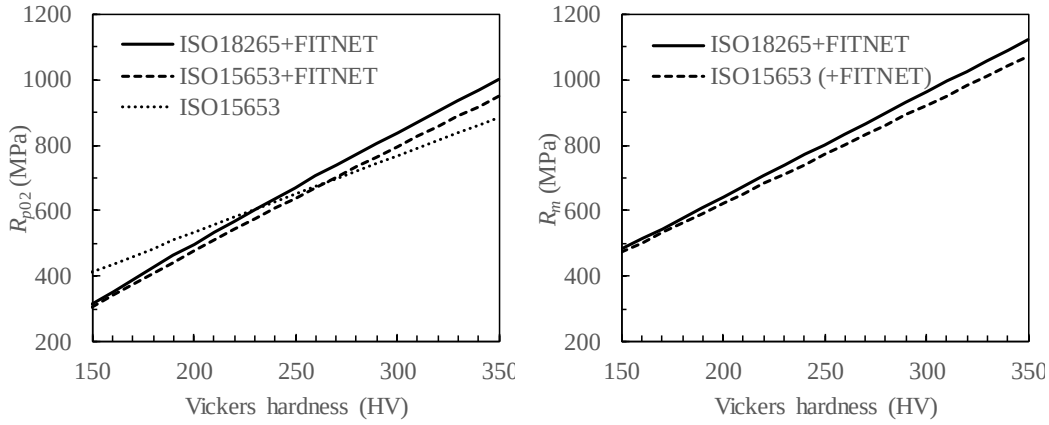

Figure 40: Graphical outcome of three procedures to obtain strength characteristics from HV

Important to recognize is that the above-mentioned hardness transfer functions are based on linear regression, and merely describe a highly scattered point cloud between hardness and constitutive properties. To bypass the scattered nature of hardness-strength relations, a new procedure is proposed in which transfer functions are experimentally calibrated. This set of equations is termed as 'AWMTT', reflecting that the experimental calibration results from a so-called All Weld Metal Tensile Test. The input parameters for these equations are the average hardness of a cross-section of the AWMTT specimen. Locating the AWMTT specimen within a hardness map and using the indentations within this region, i.e. HV_{AWMTT}, yield strength ($R_{p0.2(AWMTT)}$) and ultimate tensile strength ($R_{m(AWMTT)}$) associated with the tensile test detailed in section 2.2.2. *Table 10* gives the associated transfer functions.

	AWMTT
$\mathbf{R_m}$	$R_{m(AWMTT)} * \frac{HV}{HV_{AWMTT}}$
$\mathbf{Y/T}$	$\frac{R_{p02(AWMTT)}}{R_{m(AWMTT)}}$
$\mathbf{R_{p0.2}}$	$R_{p0.2(AWMTT)} * \frac{HV}{HV_{AWMTT}}$

Table 10: Experimentally calibrated transfer function 'AWMTT' to obtain constitutive parameters

4.4. Transfer function validation using SE(T) specimen

Before performing the assessment of the variations in load-CTOD trajectories assuming different HV transfer functions, it is important to validate the FE model's ability to describe experimental SE(T) response with direct stress-strain material input (rather than derived from hardness). Hereto, all-base-metal SE(T) test results have been adopted. This basic validation is provided in *Section 4.4.1.* The comparison of experimental and simulated load-CTOD responses (using different hardness transfer functions) for welded specimens is discussed in *Section 4.4.2.*

4.4.1. Base material SE(T) tests

Base material SE(T) experiments were performed on two specimens made of API grade X70 high strength pipeline steel [82], one (sample 'a') extracted from a 1219 mm (48") × 19.3 mm (outer diameter × wall thickness) pipe and the other (sample 'b') from a 914 mm (36") × 17.1 mm pipe. The numerical study was performed

to evaluate two aspects: (i) the agreement of the numerical model using direct stress-strain input with experiments, and (ii) the implications of assuming power-law strain hardening rather than the actual stress-strain curve.

Regarding the second aspect, there are different ways to infer power-law strain hardening properties from experimental stress-strain data. A first common option is to force the Ramberg-Osgood curve through the experimentally observed yield and ultimate tensile strength. This ensures perfect agreement at these points but may invoke (significant) errors elsewhere (see e.g. reference [133, 134]). A second option is to calculate a "best fitting" Ramberg-Osgood curve by means of least squares curve fitting (e.g. using the Levenberg-Marquardt algorithm [135]). Here, the overall agreement will be better, but the yield and ultimate tensile strength of the power-law approximation may differ from the experimentally recorded values. *Figure 41* compares the experimental *P*-CTOD trajectories against three simulated responses for each base material SE(T) specimen, based on (i) actual pointwise stress-strain input, (ii) an RO curve forced through the experimental yield and tensile strength ("RO Curve forced"), and (iii) a least squares curve fitted RO curve ("RO Curve fit"). The corresponding stress-strain data are depicted in *Figure 42*. The comparison between simulated and experimental P-CTOD curves for sample 'a' yields consistently small errors for all three simulations. The close agreement between all three simulated curves resembles the fact that the pointwise stress-strain data of material 'a' can be well represented by a power-law hardening curve. Notably, the curve-fitted RO material yields a closer correspondence to experimental behavior (average error of 2.1 % on load in the CTOD interval between 0.1 and 0.5 mm) than the forced RO material description.

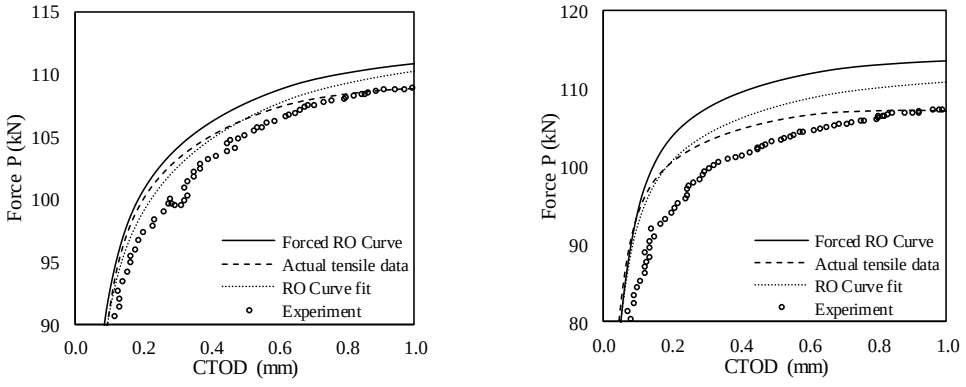

Figure 41: Numerical and experimental force versus CTOD plots for 2 base material SE(T) speicmens (a) and (b)

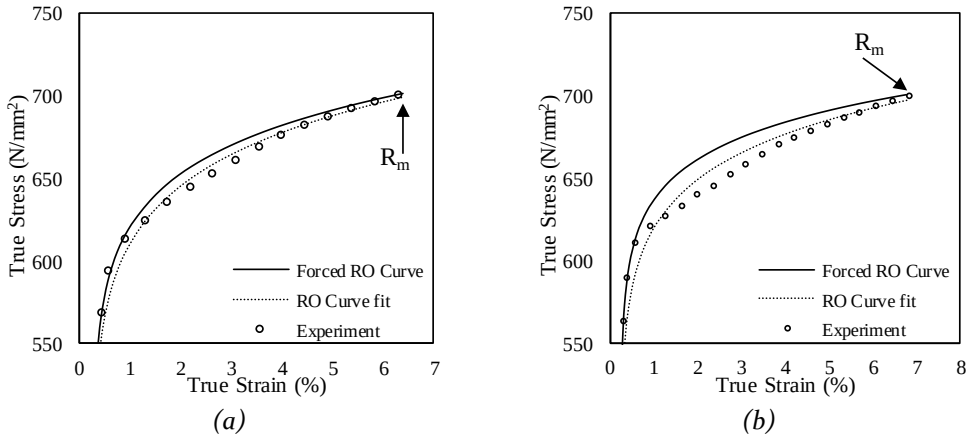

Figure 42: Pointwise $\sigma - \varepsilon$ curves of two base material samples (a) and (b), along with different RO curve approximations

Simulated CTOD responses of sample 'b' show a slightly higher error with respect to the experimental output. Here, actual stress-strain input yields the highest accuracy (average error of 5.2% on load in the CTOD interval 0.1-0.5 mm). The difference between simulated load-CTOD trajectories is larger compared to sample 'a'. This reflects the observation that the stress-strain data of sample 'b' agree to a lesser extent with their associated RO curves (*figure 21b*). Nonetheless, comparing both RO curve approximations, least squares curve fitting provides the best agreement (average relative error of 0.8% on load). This agreement is considered satisfactory. Summarizing this validation study, it is concluded that the finite element model of a SE(T) specimen provides satisfactory numerical predictions of CTOD response, provided proper stress-strain input is used. Hence it is sound to use this model in the follow-up sections related to heterogeneous welds. Supported by the analysis above, it can also be concluded that the curve-fitted Ramberg-Osgood material input yields higher accuracy than a Ramberg-Osgood model forced through the experimental points of yield and ultimate tensile strength.

Given the second conclusion, it was decided to calibrate the "AWMTT" hardness transfer procedure *(table 8)* based on yield and ultimate tensile strength values corresponding to a curve-fitted RO model of the all-weld metal tensile test rather than the 'actual' values corresponding to pointwise stress-strain behavior.

4.4.2. Weld metal SE(T) tests

The relations mentioned in *Table 9* and *Table 10* were adopted to obtain local Ramberg-Osgood parameters from HV5 values in SE(T) models containing hardness maps as a material input. Corresponding load-CTOD predictions are then compared with experimental output up to the point of crack initiation. The process of determining crack initiation using the blunting line obtained from Direct Current Potential Drop is mentioned in *Chapter 3*. As the crack initiation is taken just as a

reference point, it will not be discussed in this chapter. The chronology of the validation procedure is as follows:

1. *SE(T) tests were conducted and P-CTOD plots were obtained.*
2. *Transfer functions from* Table 9 and *Table 10 were used to obtain Ramberg-Osgood (RO) parameters from HV5 values to facilitate simulations. Three of these are purely analytical and based on standard guidelines, the fourth has an experimental calibration basis from AWMTT testing. Hereby, the AWMTT stress-strain curve was approximated by a best-fitting Ramberg-Osgood curve, whose yield and ultimate tensile strength was used in the equations of Table 10.*
3. *Obtained RO parameters were assigned to each element in the SE(T) finite element model, based on their local HV value.*
4. *P-CTOD plots from the simulations were obtained, allowing to compare numerical predictions (assuming different hardness transfer procedures) with experimental results (Figure 43 and Figure 44).*

Figure 43 shows *P-CTOD* curves for 10 specimen configurations, obtained using all four transfer functions and also includes experimental results. A first look at the plots shows a sizeable amount (around 10-20 kN) of load variations between each transfer function. Regarding transfer functions, the procedure based on All Weld Metal Tensile Test data ("AWMTT") generally shows the best agreement to the experiments while the other transfer functions deviate. This should not surprise, given the experimental nature of its calibration. Remarkably, analytical transfer functions consistently led to an overestimation of load-bearing capacity. In contrast, the AWMTT based procedure yields more balanced predictions including overestimations and underestimations of experimental behavior.

Focussing on the analytical transfer functions of *Table 9*, the ISO18265+FITNET transfer procedure provides the largest errors, followed by ISO15653+FITNET and ISO15653. This may be understood from the following:

- ISO 18265 [127] mentions that systematic deviations may occur for specific materials. To the author's knowledge, hardness data of welds have not been considered in this standard. Hence it is viable that the equations from ISO 18265 yield the largest deviations among the transfer functions.
- ISO 15653 [33] explicitly provides transfer equations for weld metal, for both yield and ultimate tensile strength. Given the specific nature of these equations, they may be expected to provide higher accuracy with respect to the experimental data.
- Noting the above, the "ISO15653+FITNET" procedure is hard to motivate, given that *Equation 4.5* is based on a highly scattered dataset involving a wide variation of different steels (including weld but also base metal).

In order to quantify the observed deviations from the simulations with the experiments, errors at three fixed CTOD values (0.10, 0.15 and 0.20 mm) are considered (*Figure 44* - *Figure 46*). These three values of CTOD are chosen as the values lie in the plastic region of *P*-CTOD curve, at equal intervals and within the region before crack initiation. Hereby, error (%) is defined as the deviation between simulated and experimental load at the considered CTOD level, relative to the experimental load. A positive error implies that the simulation overestimates the experimental load and vice versa. Along with estimations based on the transfer functions, it was attempted to construct statistical error bars relating to the scattered nature of the accuracy in hardness-strength relations in *Table 9*.

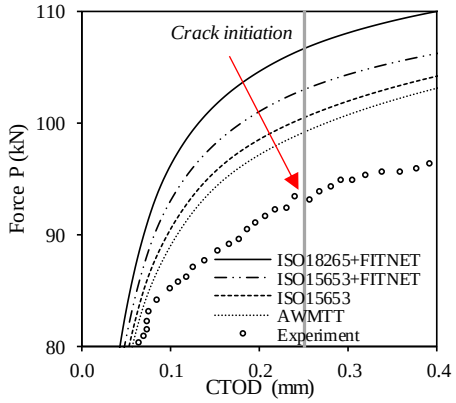

(A)

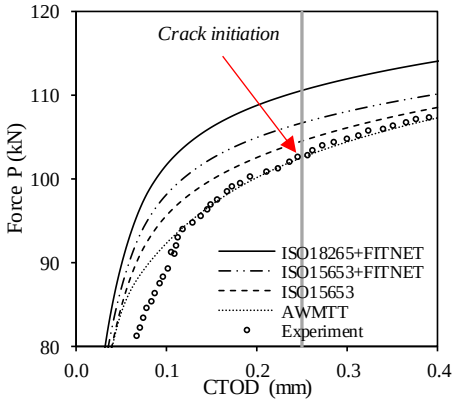

(B)

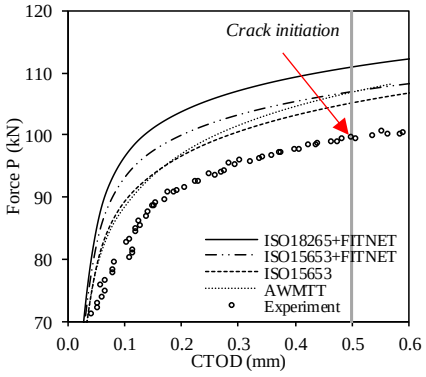

(C)

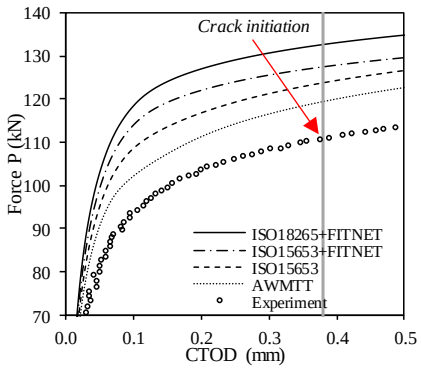

(D)

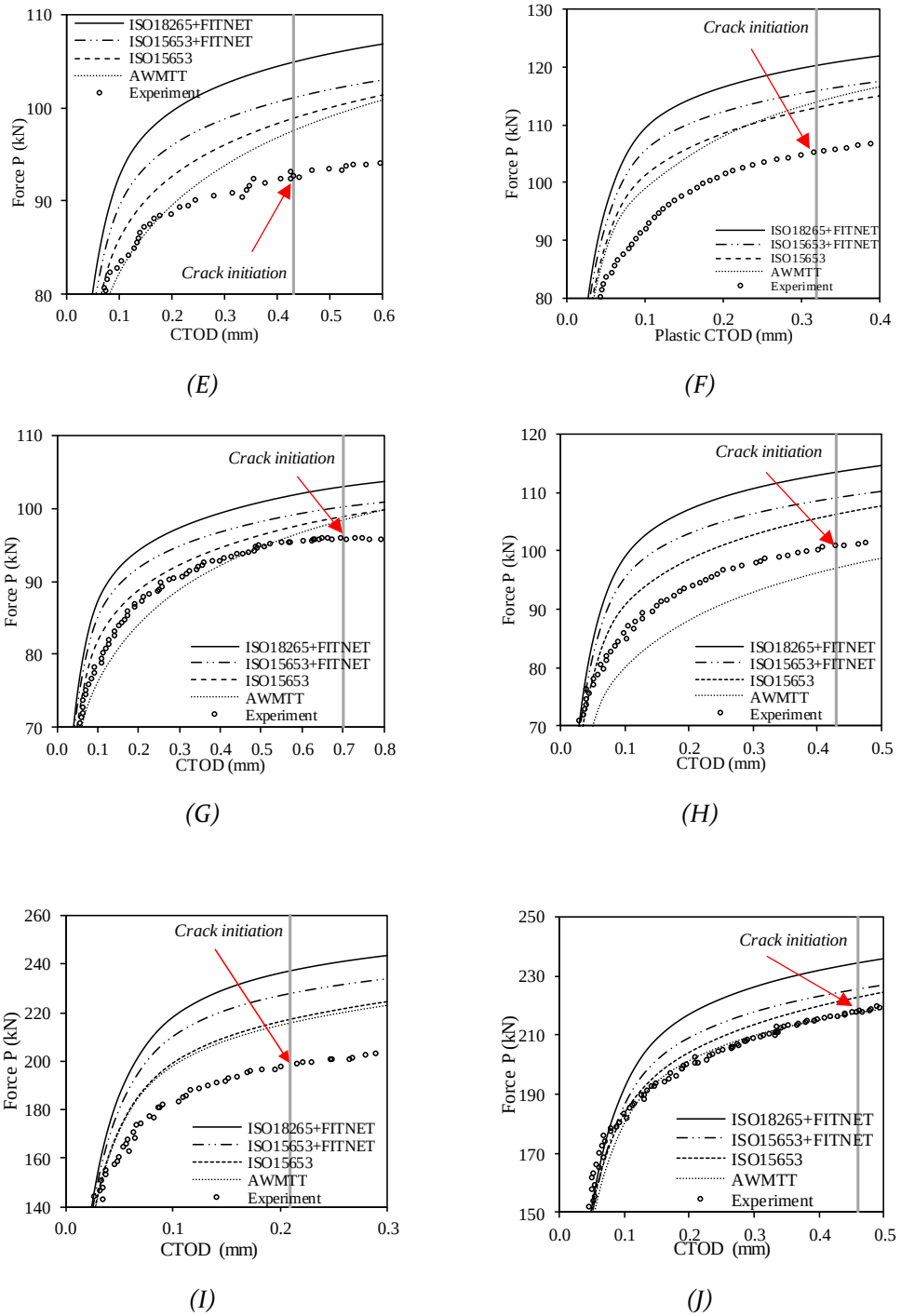

Figure 43: The plots of P versus CTOD for different samples (A-J) shows the agreement/disagreement of results obtained from simulations based on transfer functions with experimental results

The following observations are made from *Figure 44* - *Figure 46*. As apparent *Figure 44*, a wide range of weld heterogeneity patterns was covered to examine the predictive ability of the SE(T) model under various circumstances. Closer analysis of

Figure 46 does not allow to reveal any trends of simulation error in relation to the nature of weld heterogeneity. In other words, simulation error is related to the transfer of hardness to strength values rather than the complex heterogeneous nature of the welds.

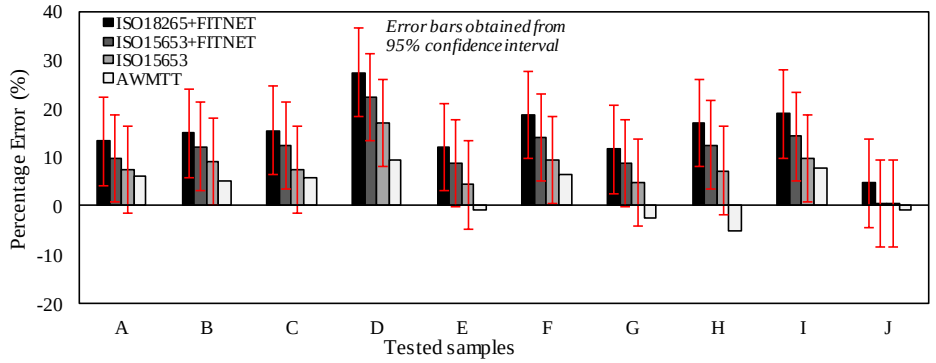

Transfer Function	*ISO18265+FITNET*	*ISO15653+FITNET*	*ISO15653*	*AWMTT*
Average error (%)	15.43	11.56	7.67	3.13

Figure 44: The percentage error on forces at the CTOD value of 0.1mm in numerical simulations compared with experiments shows that the transfer function obtained from AWMTT has the best agreement with experiments.

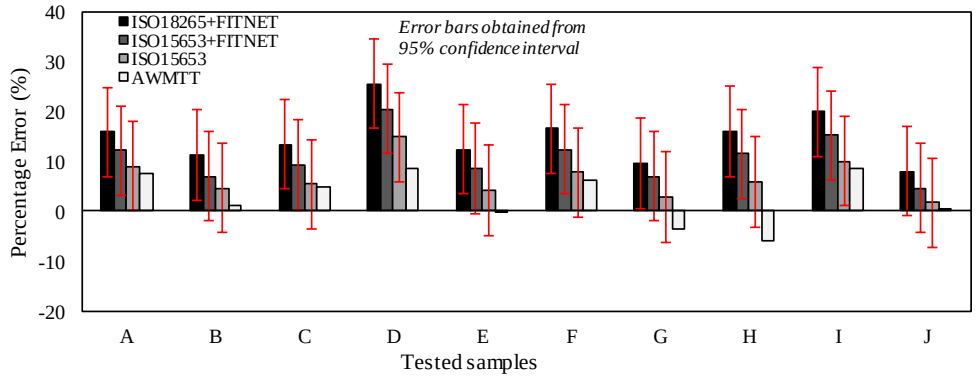

Transfer Function	*ISO18265+FITNET*	*ISO15653+FITNET*	*ISO15653*	*AWMTT*
Average error (%)	14.85	10.82	6.64	2.78

Figure 45: The agreement between numerical simulations (at P-CTOD of 0.15mm) and experimental values using AWMTT transfer function

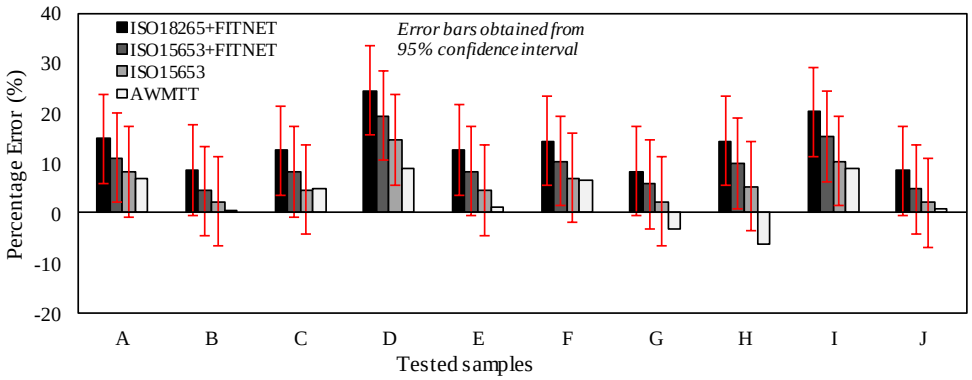

Transfer Function	*ISO18265+FITNET*	*ISO15653+FITNET*	*ISO15653*	*AWMTT*
Average error (%)	13.91	9.77	6.15	2.89

Figure 46: The fact that AWMTT equations are the best transfer function has been reiterated in this plot showing the errors at CTOD value of 0.20mm

The implementation of hardness transfer functions in a SE(T) model is equally performant in the simulation of homogeneous welds (such as specimen A) and strongly heterogeneous welds (such as specimen F). Analytical hardness transfer procedures without an experimental calibration basis can overestimate the load-bearing capacity up to 25% (specimen D, ISO18265+FITNET). The maximum and minimum percentages of load overestimation when using the AWMTT transfer function are 9% and -6%, respectively. Hence, the degrees of over- and underestimation using this procedure are similar. Average predictive errors using the AWMTT procedure are close to zero (around 3%).

4.5. Transfer function validation using micro tensile tests

Supported by experimental and numerical SE(T) results, the work in the previous section serves as an evaluation of the accuracy of the experimental procedure to calibrate hardness transfer functions. In this section, the strength properties i.e. yield strength ($R_{p0.2}$) and tensile strength (R_m) values obtained from AWMTT and MTT specimens, along with Vickers hardness maps, are utilized to directly validate the equations put forward in *Table 10*. Using the values obtained from the above tests, plots were created comparing MTT results against corresponding HV values. The data points are then compared against different HV transfer functions (*Figure 47* and *Figure 48*). The equations are derived from ISO 18265 (linear regression of tabulated data), ISO 15653 and FITNET. These are shown in *Table 9*. Notably, ISO 18265 provides a transfer function for R_m only, whereas ISO 15653 additionally informs how to calculate R_{p02} from HV. Along with these lines, strength properties ($R_{p0.2}$ and R_m) acquired from MTT tests are plotted against hardness values from the same samples as MTT(OM) and MTT(UM).

The following can be observed in *Figure 47* and *Figure 48*.

- The hardness and strength values of the MTT specimens confirm the very strong differences in properties between the UM and OM weld regions.
- The equations given in *Table 10* predict lower values of R_m when compared with the standard equations as seen in *Table 9*. For instance, the ultimate tensile strength predicted from the AWMTT data of the undermatching region is ~5% lower than that given by ISO 18265 (*Figure 47*). In *Figure 48*, a similar deviation is observed for yield stress.
- AWMTT analysis of the UM and OM regions yields different hardness transfer functions. This highlights the material-specific character of the relation between hardness and strength properties and confirms that the generic nature of standardized HV transfer functions may invoke errors. The FE model used in the simulations requires one specific transfer function.
- Focusing on $R_{p0.2}$ (*Figure 48*), the differences between different transfer functions are subtle compared to the scatter in data points obtained from the MTT test data. This relates to the knowledge that HV is theoretically stronger related to R_m [125]. The scatter in the $R_{p0.2}$ dataset, also seen in several other researches likely results from local variations in strain hardening behavior which are not captured by the transfer functions as seen in the references [3, 93, 136]. In contrast, experimental scatter is limited for R_m and there the AWMTT based transfer function appears to better represent the average of the MTT datasets. Notwithstanding the higher scatter for the $R_{p0.2}$ plot, the corresponding HV transfer functions manage to capture the general trend and to quantify the large differences between the yield strengths of UM and OM weld metal.
- Averaging all specimens and configurations, the differences obtained between AWMTT based calibrated transfer functions and MTT results are 3.2% for R_m and 5.2% for $R_{p0.2}$. This is less than the deviations when using standard transfer functions which show average differences of ~11% for R_m (ISO 18265); and ~7% for R_m and ~18% for $R_{p0.2}$ (ISO 15653).

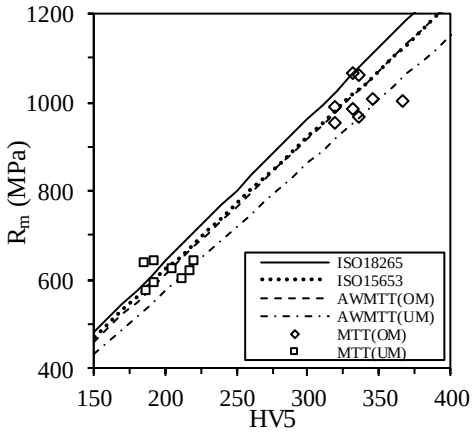

Figure 47: Hardness values (HV5) against tensile strength (R_m) from different transfer functions and experimental data

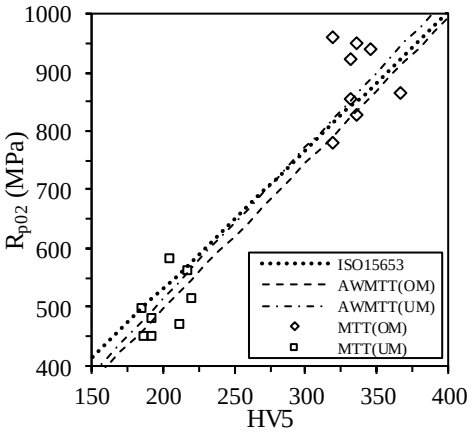

Figure 48: Hardness values (HV5) against yield strength (R_{p02}) from different transfer functions and experimental data

With these observations, it turns out that experimentally calibrated transfer functions (based on HV mapping and a simple standard AWMTT test) agree with actual HV-strength relations obtained from (more challenging) micro tensile tests. Moreover, the correspondence of the outcome between MTT and HV-transferred material strength properties are less compelling than the agreement between simulated and tested SE(T)s. This is logical because of the much higher sensitivity to local variations. SE(T) results are rather governed by average properties in the weakest section.

4.6. Advised procedure

This chapter has presented an updated approach to estimate local material properties, i.e. yield and ultimate tensile strength of welds. A step by step procedure is summarized in this section to assess the crack driving force response of welded joints using transfer functions with a minimum (but sufficient) experimental input. It goes as follows:

1. Extract a weld macrograph and an all weld metal tensile sample. The sample sizes are drawn out according to standards like ASTM E8 / E8M-16a and ASTM E384-11e1 [32, 89]. Multiple specimens can be extracted and tested to characterize (and account for) the natural scatter of weld properties.
2. Hardness maps of the weld region or a hardness map obtained from a cross-section of the failed AWMTT specimen (which did not plastically deform) are obtained through Vickers hardness (HV5) testing on the macrograph.
3. AWMTT related yield ($R_{p0.2(AWMTT)}$) and ultimate tensile strength values ($R_{m(AWMTT)}$) are obtained from a least squares curve fitted Ramberg-Osgood

curve relating to the all weld metal tensile test. These values are not necessarily equal to the actual $R_{p0.2}$ and R_m values of the pointwise stress-strain curve.

4. An average hardness value (HV_{AWMTT}) is obtained from the weld macrograph, focussing on the (circular) region demarcating the cross-section of the (round) tensile test sample at its location of extraction.
5. Local HV5 values, and $R_{p0.2(AWMTT)}$ and $R_{m(AWMTT)}$ are used to calculate local R_m and $R_{p0.2}$ using the equations of *Table 9*.

Since numerical predictions using the AWMTT based procedure may lead to either underestimations or overestimations of structural response, it is recommended to reduce the obtained load-bearing capacity by a safety factor for the sake of conservatism. For the cases considered in this thesis, a reduction of the simulated load-bearing capacity of SE(T) specimens by 10% would lead to safe predictions, compared to the experimental values.

4.7. Summary and conclusions

A combined experimental-numerical analysis has been performed to investigate the ability to predict crack driving force in (heterogeneous) welded structures on the basis of Vickers hardness maps. Single Edge notched Tension (SE(T)) specimens were utilized for this study, comprising ten different weld/notch configurations. Finite element analyses of an experimentally validated model were performed with local (element-specific) properties derived from hardness maps by means of different procedures to link hardness with stress-strain behavior. Three of these are based on published equations, whereas a fourth procedure is experimentally calibrated by means of an all weld metal tensile test (AWMTT). Simulated crack driving force response (*P*-CTOD) were compared against experimental test output. Additionally, Micro Tensile Tests (MT) and All Weld Metal Tensile Tests (AWMTT) were utilized to calibrate transfer functions to obtain material properties like yield strength ($R_{p0.2}$) and tensile strength (R_m) from HV5 values. The calibrated equation results which give global behavior were compared with MT results which give local material properties to assess the robustness of transfer functions.

The following is concluded from the presented study:

- The predictive accuracy of the model using the AWMTT based procedure is consistent for ten different configurations comprising various heterogeneity patterns, and including heat-affected zone softening and hardening. This indicates high robustness of the procedure with respect to the degree and complexity of weld heterogeneity. In other words, complex heterogeneous welds can be simulated with similar accuracy as more straightforward homogeneous welds.
- The natural scatter associated with the hardness-strength relation of materials may significantly alter the predictive accuracy of computational fracture

mechanics, when material input adopts regression-based (standardized) hardness transfer functions. In this study, varying the hardness transfer function according to an experimentally obtained 95% confidence interval on R_m led to changes in simulated load around ±10%.

- This chapter advises a procedure to experimentally calibrate the hardness-strength relation of a weld region by means of all weld metal tensile test (AWMTT) data. Compared with regression-based transfer functions, this procedure provides more accurate predictions of crack driving force response with less systematic error (on average 3% on load for the investigated data). In practical terms, the required material input is easy to obtain. The procedure is entirely based on a weld hardness map and stress-strain output of an AWMTT extracted at a known location.
- There is a significant variation in crack driving force curves predicted by the finite model using different regression-based transfer functions. Hereby, transfer functions for specific material categories such as welds (e.g. given by ISO15653) appear to provide a better agreement with experimental data than more generic functions (e.g. tabulated in ISO18265).
- This comparison was performed on MTT and AWMTT specimens which were extracted from undermatching and overmatching regions. The outcome by comparing the results of yield strength ($R_{p0.2}$) and tensile strength (R_m) showed a good understanding between two test methods with differences around 5%. The results show a promising trend that motivates the usage the calibrated transfer functions.

The modeling concept put forward in this thesis will support the development and evaluation of approaches to translate complex heterogeneous welds into idealized welds with a similar crack driving force response, whose characteristics can be readily inputted to existing ECA frameworks.

Chapter 5

Deformation analysis of flawed heterogeneous welds

5.1. Introduction

The understanding of the deformation behavior of a flawed structure plays a major role in assessing its integrity. Evaluating the tearing resistance of the material or its fracture toughness to estimate structural failure, necessitates knowledge of its deformation behavior. Welds with heterogeneous constitutive properties show a complex deformation behavior which is challenging to predict. When a crack is surrounded by an inhomogeneous material, the resulting deformations are heterogeneous too. Welds which have different constitutive properties within show variable deformation behavior. Zerbst et al. [31] point out that the plastic strain concentration is high around the flaw surface at a sufficiently high load. This plastic strain concentration influences the growth of the crack.

The slip mechanism is the most important plastic deformation mechanism in metallic structures. Even if the loading is purely tensile, shear stresses exist in a plane under 45°. These shear stresses are termed as 'resolved shear stress'. Based on this concept, a theory was utilized by Hill [137] to define plastic deformation patterns and stress fields, which is called the '*slip line field theory*'. This theory became popular for explaining deformation problems in metal forming and machining processes [138, 139]. Further, it was expanded to assess the limit loads in cracked structures [58, 60] and mismatched welds [8, 9, 140]. Thus this theory gains prominence in this thesis.

This chapter aims at providing a brief background of '*slip line field theory*', which helps in comprehending *Chapter 6* discussing the limit load estimations of SE(T) specimens using slip line field theory and *Chapter 7* where the relation between crack tip constraint and slip lines is drawn. Additionally, this chapter is utilized to explain the need to study deformations of SE(T) specimens including a weld and their relation with the shear stresses on which slip line theory is based.

The chapter is structured by giving a brief background on relevant plasticity concepts in *Section 5.2* and introducing the slip line theory, the assumptions behind the theory and the drawbacks in *Section 5.3*. In *Section 5.4* the deformation analysis of SE(T) specimens is made by addressing the drawbacks mentioned in *Section 5.3*.

5.2. Plasticity concepts

In order to understand the deformation analysis, bounding theorems *(chapter 6)* and the concept of limit loads, the essentials of plasticity theory are explained in this section. The calculation of limit loads requires a yield criterion based upon which plastic flow is predicted to occur. The two common yield criteria are Tresca and von Mises. They are briefly explained based on principal stresses σ_1, σ_2 and σ_3.

- *Tresca yield criterion*

This criterion states that yielding occurs when

$$\max\left(\frac{|\sigma_1-\sigma_2|}{2},\frac{|\sigma_2-\sigma_3|}{2},\frac{|\sigma_3-\sigma_1|}{2}\right)=k \qquad 5.1$$

where k is the shear yield stress.

For uniaxial loading,

$\sigma_1=\sigma_y\,,\quad \sigma_2=\sigma_3=0\ \Rightarrow\quad \sigma_y=\ 2k$

In case of plane strain (in the 3rd direction), it can be shown that $\sigma_3=\frac{\sigma_1+\sigma_2}{2}$,

$$\sigma_y=\ 2k=\ \sigma_1-\sigma_2 \qquad 5.2$$

- *Von Mises yield criterion*

This criterion states that yielding occurs when

$$\frac{1}{\sqrt{2}}\sqrt{(\sigma_1-\sigma_2)^2+(\sigma_2-\sigma_3)^2+(\sigma_3-\sigma_1)^2}=\ \sigma_y \qquad 5.3$$

when expressed in principal stresses. In the case of plane strain (in the 3rd direction),

$$\sigma_y=\ \sqrt{3}k\ (uniaxial)\Rightarrow\ \sigma_1-\sigma_2=\frac{2\sigma_y}{\sqrt{3}}=2k \qquad 5.4$$

The common expression in the above cases is that yielding occurs when $\sigma_1-\sigma_2=2k$

5.3. Slip line field theory

5.3.1. Definition

Slip line field theory is an analytical and graphical method to represent and understand plastic flow patterns in a rigid - perfectly plastic material. Graphical representations can be obtained, showing the directions of the maximum shear stress (slip lines) in a rigid plastic continuum body deforming in 2D plane strain conditions [141, 142].

This theory was initially based on uniaxial compression assessed in 2D plane strain conditions. Based on this case, it was formulated that there are two orthogonal directions of slip lines that appear during deformation. These are termed as *α-lines*

and *β-lines* and shown in *Figure 49*. In the figure, the compression loads are applied in 2D plane strain conditions. The velocity distribution and stress state in the solid can be determined from the geometrical pattern of the *α-lines* and *β-lines*. These slip lines are expressed through hydrostatic stress σ_m using Hencky equations, as follows:

$$-\sigma_m + 2k\theta = constant \text{ for } \alpha\text{-lines} \quad 5.5$$

$$-\sigma_m - 2k\theta = constant \text{ for } \beta\text{-lines} \quad 5.6$$

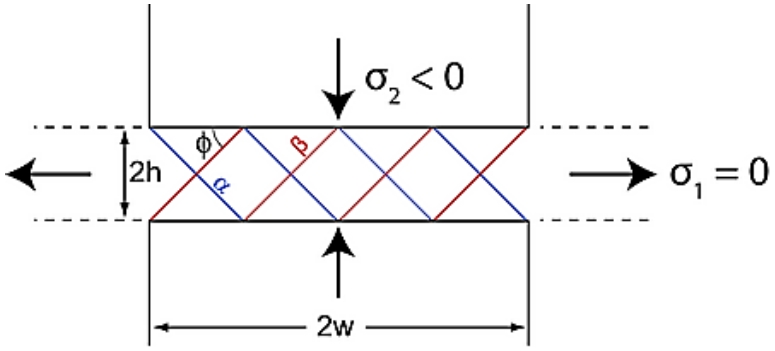

Figure 49: The development of α-lines and β-lines during compression of a body in plane strain conditions [141]

Both the stress and velocity boundary conditions must be used to obtain a slip line [137, 143]. Slip line trajectories should respect `kinematic compatibility' as illustrated in *Figure 50* for a tensile loaded component. The assumption of perfectly plastic material behavior implies that there is no further resistance against plastic flow in the collapsing section when the collapse occurs. The plastic collapse is the relative movement of rigid bodies (regions left and right of the notch) touching each other in a slip line. There cannot be any separation between them.

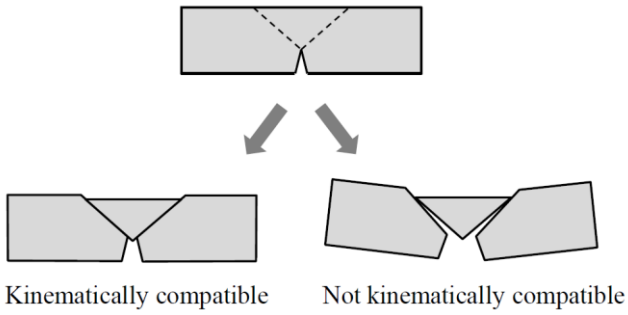

Figure 50: The principle of kinematic compatibility [143]

In other words, at both sides of a slip line the velocity component normal to the slip line should be equal because otherwise both sides would be moving away from/towards each other instead of just sliding. This puts mathematical restrictions

on the geometry of a slip line, which are essential equations to solve the slip line fields.

In order to understand the simplifications seen in slip line theory, the next subsection describes the assumptions involved.

5.3.2. Assumptions

Classical slip line field theory is built upon many assumptions, which are required to keep the problem complexity within acceptable limits.

- *Perfectly plastic material response*

A rigid perfectly plastic material involves no elastic deformations and just plastic deformation without strain hardening. The stress-strain curve of rigid perfectly plastic material is shown in *Figure 51*

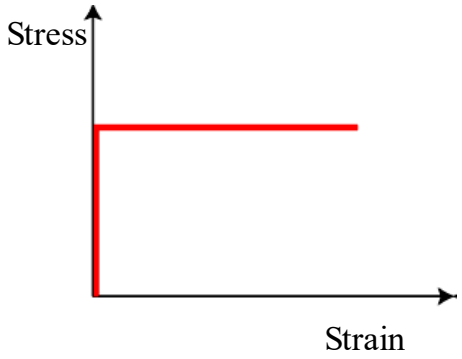

Figure 51: Material response of a rigid perfectly plastic material

- *Isotropic material*

Isotropic materials exhibit the same properties in all directions. Thus, choosing a different coordinate system does not influence the material properties.

- *Quasi-static loading without temperature effects and body forces*

Slip line field theory applies to continuous processes that are slow enough to neglect inertial effects.

- *Plane strain conditions*

Plastic deformation in 2D plane strain conditions involves deformation where one of the three principal strains is zero. Very often, the solution of a slip line field starts at the boundary conditions. Particularly,

- *The stress normal to a free surface is principal stress, so the α and β lines must meet the surface at 45°.*
- *The α and β -lines must meet a frictionless contact surface at 45°*
- *The α and β -lines meet surfaces of sticking friction at 0° and 90°*

5.3.3. *Limitations*

It can be observed from the assumptions of slip line theory that both the material properties and the loading conditions are extensively simplified. The basic equations do not include material property variations nor other complications such as material strain hardening or three-dimensional specimens. Its applicability to fracture mechanics analysis of heterogeneous defected welds may be questioned and will be investigated further on; particularly in *Chapter 7*.

5.4. Deformation analysis of heterogeneous welded SE(T) specimens

Despite its severe assumptions, *'slip line theory'* has been utilized by researchers to obtain analytical equations for different weld configurations. Joch et al. [60] put forward limit load solutions considering the mismatch between welds for plane strain problems. They obtained solutions assuming a perfectly plastic mismatch problem and a straight-line deformation mechanism. They showed that the simplification of deformation bands to straight lines results in over-estimation of limit loads as it follows from an upper bound theorem of limit load theory (discussed in *chapter 5*). Similar development of limit load solutions followed by considering different crack geometries using plane strain conditions.

Hao et al. [9] constructed slip line fields for Center Cracked Tensile (CC(T)) loaded panels with a mismatched joint, including an analytical methodology to estimate slip line deviations at bi-material interfaces. To a certain extent, CC(T) specimens can be considered similar to SE(T) specimens, given that their central symmetry plane cuts the CC(T) specimen into two SE(T) configurations. They considered cases of weld strength undermatching and overmatching, showing different slip line patterns arising from these configurations and showing that the slip lines which arise from the notch tips indeed meet the surface of the specimen at 45°, in line with the theoretical boundary condition of slip line field theory discussed above. However, they pointed out that there could be a discontinuity in slip line orientation along the interface of two materials. The slip line field solution depicting the probable change of angle at the interface is shown in *Figure 52*. In the figure, r_1 and r_2 are the radii formed by the slip line due to the discontinuity and B_s is the thickness of the slip line. This was constructed by applying equilibrium conditions to both normal and shear stress. Hao et al. suggested that, with the assumption of 45° slip lines touching the surface, the slip line orientation at the crack tip can be back calculated. These equations are not elaborated here but it is important to understand that slip line deviations have been recognized for a simple bi-material

interface. For more complex material heterogeneities, other deviations of slip line trajectories from theoretical straight lines under 45° are to be expected.

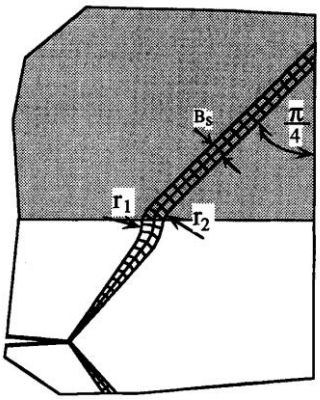

Figure 52: A general solution of the slip line field as represented by Hao et al. [9]

An analysis of plastic deformations in complex heterogeneous welds (including strain hardening) was performed by Hertelé et al. [144]. They considered a welded SE(T) specimen under uniaxial tension loading. Strain concentration bands originating from the defect tip were simplified into slip lines, defined as trajectories of maximum equivalent (plastic) strain. Based on Digital Image Correlation (DIC), non-linear slip line trajectories deviating from straight lines at 45° were observed, and this was attributed to weld heterogeneity. This observation acts as a motivation to further investigate the validity of slip line theory in complex heterogeneous welds. *Section 5.4.1* explains the methodology for conducting a deformation analysis of SE(T) specimens and *5.4.2* gives results and discussions of deformation analysis performed on welded SE(T) specimens.

5.4.1. Methodology

Welded SE(T) specimens shown in *Figure 15(OM-UM)* were considered for this analysis. Experiments were performed on such specimens in accordance with the procedure outlined in *Chapter 2* [99, 145]. Two notch locations were considered: one in the OM region and the other in the UM region. CMOD and CTOD were measured using double clip gauges as per BS 8571:2014 [55]. The clip gauges were located 2 mm and 8 mm above the specimen surface. Digital Image Correlation (DIC) was used to depict full-field plastic deformations as detailed in *Section 2.2.4*.

Similar to the experiments, two three-dimensional sides grooved SE(T) specimens were modeled using the commercial finite element software package Abaqus® (version 6.11) as explained in *section 2.3*. Modeled specimens were given the same dimensions (overall, notch tip radius, side groove geometry) as those used in

experiments. The specimen had length *L=200mm*, in accordance with the daylight length between the grips of the experimental tests and width *W* and thickness *B* equal to *20mm*. *Figure 28* shows the detailed FE model with *B* the thickness and *W* the width of the specimen. Isotropic *J2* type plasticity obeying Ramberg-Osgood (RO) strain hardening with finite strain assumptions was implemented. This FE model is shown again in *Figure 53,* together with the geometry of the applied side grooves and the notch. *Figure 53* shows the outcome of using experimentally determined hardness values and assigning them to an individual element in FE model. The complex weld properties were incorporated in the finite element model by assigning element-specific properties using hardness values as input and converting them to material properties (R_{p02}, R_m *and* n) using AWMTT based transfer function calibrated in *Chapter 4*.

The analysis of plastic deformations is the initial step to extract slip lines originating from the crack tip. In this study, plastic deformations are expressed in terms of equivalent plastic strain ($\varepsilon_{eq,pl}$). Strain values are obtained at the nodes in the FE model and using DIC in experiments. The experimental technique is based on equivalent elastic-plastic strains rather than equivalent plastic strains as DIC cannot differentiate between them. The full-field strain distributions are obtained at the surface of the specimen, making it a 2D analysis on a 3D model.

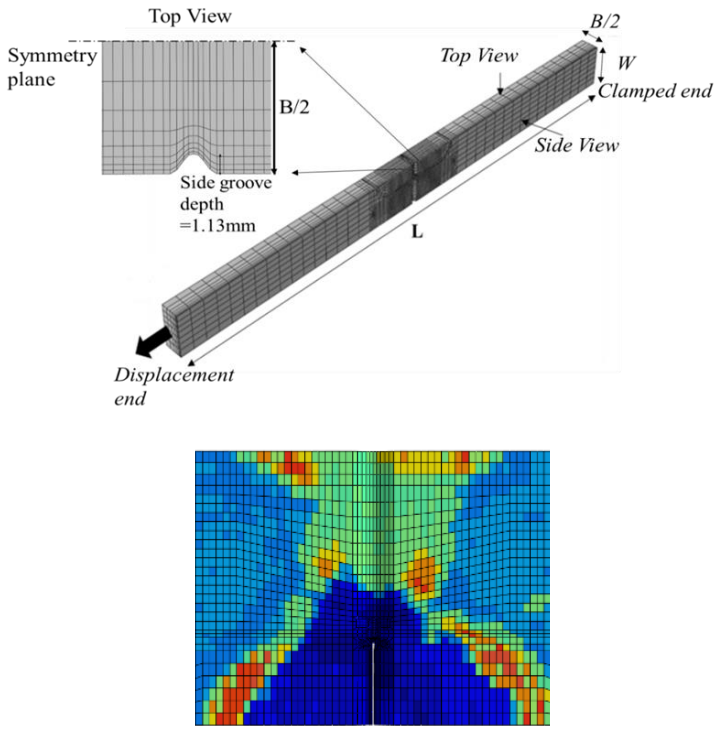

Figure 53: Views of the numerical SE(T) model and outcome after the assignment of element-specific properties

The maximum strains in experiments and simulations are subsequently mapped for a series of grid points parallel to the notch at the surface of the specimen. The maximum values are extracted from lines within this grid and connecting these points between adjacent lines eventually yields a slip line trajectory (*Figure 54)*. As explained in [146], the starting point in the determination of the slip lines is the evaluation of all plastic strains in a specific section of the specimen. This section can be an outer edge, but also an inner plane of the specimen (in case of simulations). If the surface under investigation is designated as the XY-plane, the following true strains have to be known in that section: ε_{xx} , ε_{yy}, ε_{xy}. With these strains, the in-plane principal strains ε_1 and ε_2 and thus ε_{eq} can be calculated as follows:

$$\varepsilon_1 = \frac{\varepsilon_{xx} + \varepsilon_{yy}}{2} + \sqrt{\left(\frac{\varepsilon_{xx} - \varepsilon_{yy}}{2}\right)^2 + \left(\frac{\varepsilon_{xy}}{2}\right)^2} \qquad 5.7$$

$$\varepsilon_2 = \frac{\varepsilon_{xx} + \varepsilon_{yy}}{2} - \sqrt{\left(\frac{\varepsilon_{xx} - \varepsilon_{yy}}{2}\right)^2 + \left(\frac{\varepsilon_{xy}}{2}\right)^2} \qquad 5.8$$

$$\varepsilon_{eq} = \frac{2}{\sqrt{3}} \sqrt{{\varepsilon_1}^2 + {\varepsilon_2}^2 + \varepsilon_1 \varepsilon_2} \qquad 5.9$$

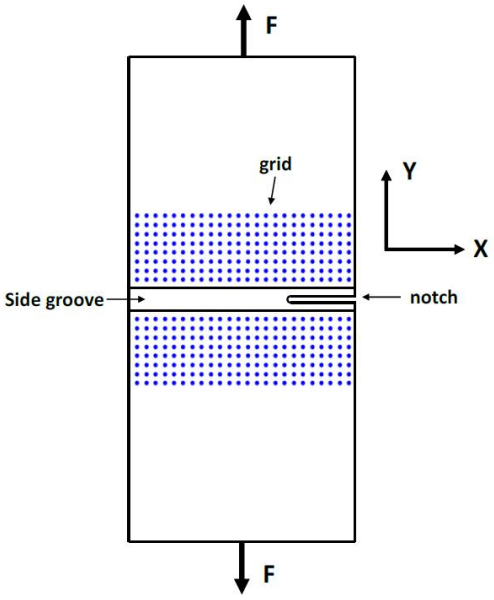

Figure 54: Grid pattern used in SE(T) specimen (experimental and numerical) to determine equivalent plastic strains [146]

The grid lines were chosen based on a convergence study performed in [146]. Based on this study, 40 grid lines (20 on each side of the notch) with a distance of 1mm are chosen for the extraction of $\varepsilon_{eq,pl-max}$ and τ_{max} points in this work.

It should be noted that the theoretical slip line analysis relates to Tresca's criterion for plastic flow upon attainment of a critical value of maximum shear stresses, in an isotropic 2D elastic-perfectly plastic material [137]. Instead, equivalent plastic strain $\varepsilon_{eq,pl}$ rather relates to von Mises' plasticity criterion. $\varepsilon_{eq,pl}$ relates to the von Mises equivalent stress through the material's uniaxial true stress-true strain behavior (assuming isotropic material). The link between theoretical slip lines (trajectories of maximum shear stress) and observed ones through strain analysis will be evaluated in the next sub-section. Along with this assessment, the pattern of slip lines are studied in experiments on heterogeneous welded SE(T) specimens.

5.4.2. Results and discussions

The starting point of this section is a finite element analysis based evaluation of the relevance of maximum strain analysis with respect to slip line field theory, as questioned in the previous paragraph. Points of maximum shear stress τ_{max} (related to Tresca's criterion) and of maximum equivalent plastic strain $\varepsilon_{eq,pl-max}$ (related to von Mises' criterion) were extracted from the analysis grid (refer *section 5.4.1*) at a limit load value extracted from the Twice Elastic Slope (TES) method. ASME Section III [147] recommends the use of TES method to determine limit load for simulations using the force-displacement plot [148, 149] as shown in *Figure 55*. Trajectories of τ_{max} and $\varepsilon_{eq,pl,max}$ originating from the notch are shown in *Figure 56*. *Figure 56* (a) shows the points of τ_{max} and $\varepsilon_{eq,pl,max}$ for the specimen having the notch located in the OM region and *Figure 56* (b) shows the points for the notch located in UM region. Shown as a reference are 45° oriented straight lines, predicted to act as slip lines within the severe assumptions of slip line field theory.

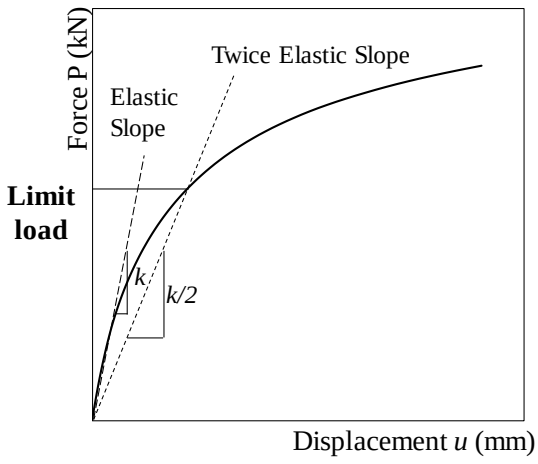

Figure 55: Limit load estimation using Twice Elastic Slope (TES) method

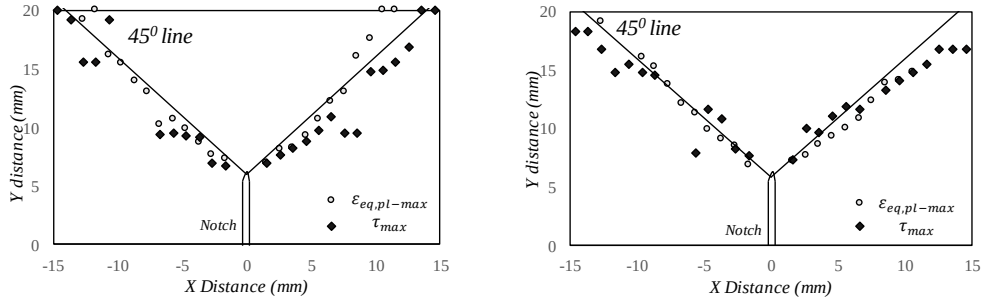

(a) *(b)*

Figure 56: The comparison between $\varepsilon_{eq,pl-max}$ and τ_{max} obtained from simulations of two configurations, i.e. notch located in OM (a) and notch located in UM (b)

Two observations are made from *Figure 56*:

- Omitting marginal differences, trajectories of τ_{max} and $\varepsilon_{eq,pl,max}$ are overall similar. This confirms that strain analysis (e.g. facilitated by means of DIC) may serve to investigate the influence of weld heterogeneity on the development of (shear stress based) slip lines.
- Slip line trajectories agree to a fair extent with the theoretically predicted 45° lines for homogeneous bodies (as in literature mentioned in previous sections). Nonetheless, the trajectories show notable irregularities. The cause and implications of these irregularities deserve further investigation, as discussed further in this sub-section.

The discussion above relies on the validity of the finite element model. Therefore, numerically predicted slip line trajectories are evaluated by comparison with experiments. Hereto, SE(T) tests indicated as I and J in *Table 6* were adopted. *Figure 57(a)* shows the points of $\varepsilon_{eq,pl,max}$ when the notch is in the OM region. *Figure 57(b)* shows the points of $\varepsilon_{eq,pl,max}$ for a notch located in the UM region. The experimental points (obtained from DIC measurements) are shown by a black line and the points from the simulation are shown as diamond markers. Obtained trajectories are depicted in conjunction with the hardness distribution.

A first evaluation of the trend of deformation patterns indicates a satisfactory agreement between numerical simulations and experiments. The extracted locations of $\varepsilon_{eq,pl,max}$ show a similar tendency in experiments and numerical study. The small variations observed between the two methods can be attributed to a variety of reasons, being either numerical (accuracy of the finite element model, transfer of hardness values to constitutive properties), experimental (scatter in optical strain measurement, variability of hardness map along the direction of welding) or analytical (significance of difference between total and plastic equivalent strain). Considering this last aspect, it seems that the disagreement between experimental and numerical slip lines can (at least partially) be attributed to the magnitude of strain since, as the strain level decreases further away from the

notch tip, the difference between total and plastic strain becomes more significant, and the agreement between experimental (based on total strain) and numerical (based on plastic strain) slip lines decreases.

Additionally, the deformation bands obtained from DIC analysis are shown in *Figure 58* and simulation results are shown in *Figure 59*. These figures help in gaining insight into the non-uniform deformation bands observed in the material due to heterogeneities. In these figures, one can observe the non-uniform distribution of the plastic deformations in contrast with the homogeneous specimens [104, 150]. Regarding the development of slip lines, *Figure 57* shows the $\varepsilon_{eq,pl,max}$ points at limit loads. It turns out that bands of maximum strain are fairly invariable as the deformation of the specimen is increased, and the discussions above do not merely apply to the particular load level investigated.

The material heterogeneity tends to affect regions of smaller strains to a stronger extent. Related hereto, Ewing et al. [151] showed that the applicability of slip line theory is strongest around the notch tip where the highest degree of plasticity occurs. Likewise, we can see that the $\varepsilon_{eq,pl,max}$ points invariably make an angle of 45° orientation around the notch tip and the deviations begin away from the notch as the influence of heterogeneity comes in to play. To confirm this observation, points were extracted at the initiation of plasticity and at maximum deformation from simulations and experiments.

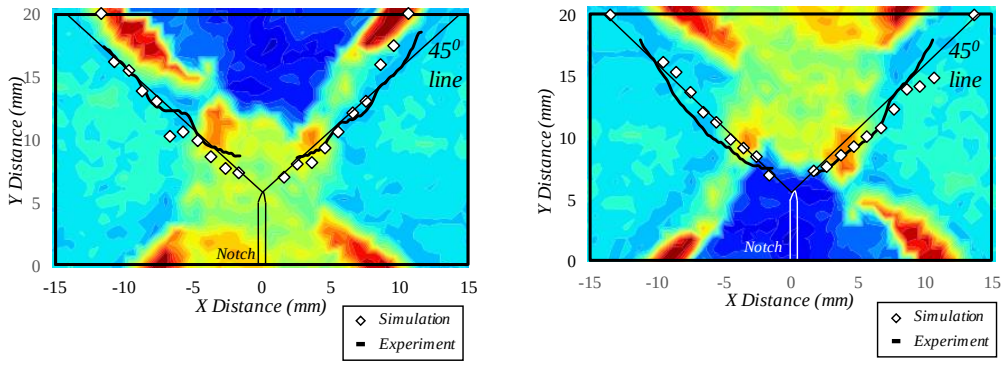

Figure 57: The points of $\varepsilon_{eq,pl,max}$ on SE(T) specimen surface at maximum applied deformation (a) deformation pattern for a notch located in the strength overmatching (OM) weld region and (b) deformation pattern for the notch in the strength undermatching (UM) region

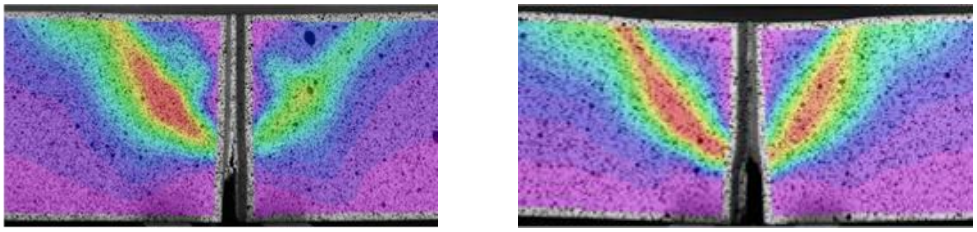

(a) (b)

Figure 58: Strain patterns obtained through DIC on speicmens with (a) notch located in OM region and (b) notch located in UM region

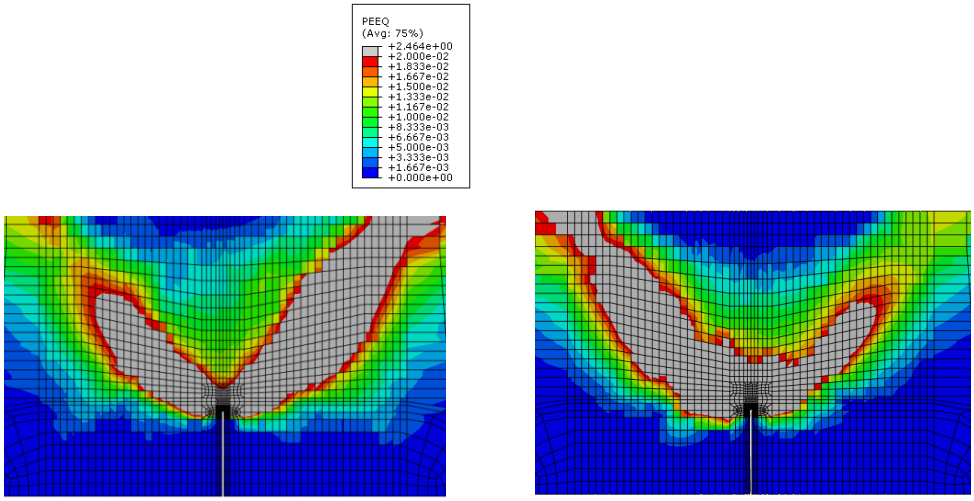

(a) (b)

Figure 59: Strain patterns obtained through numerical simulations on speicmens with (a) notch located in OM region and (b) notch located in UM region

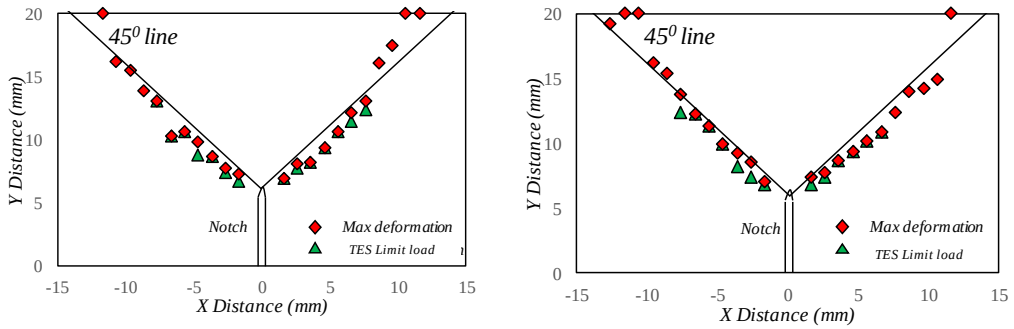

(a) (b)

Figure 60: The trajectories of $\varepsilon_{eq,pl,max}$ obtained from simulations at the onset of plasticity and at limit load for the specimens having the notch located in (a) OM region and (b) in UM region

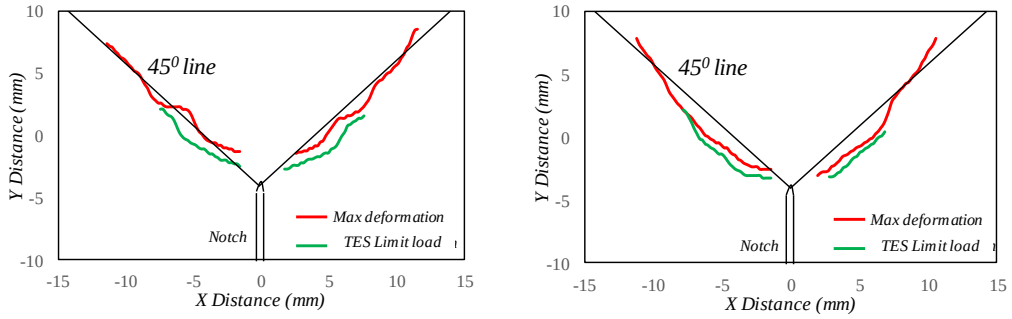

(a) *(b)*

Figure 61: The experimental trajectories of $\varepsilon_{eq,pl,max}$ obtained from DIC analysis at the onset of plasticity and at TES limit load for the specimens having the notch located in (a) OM region and (b) in UM region

5.5. Summary and Conclusions

This chapter describes the importance of deformation analysis of heterogeneous welds.

Slip line field theory depicts plastic deformations in a loaded continuum, in terms of lines along with maximum shear stress occurs. This theory is limited by severe assumptions for simplicity in calculations. These have been pointed out through experimental and numerical analysis in this chapter.

SE(T) specimens were considered to determine deformation bands and in turn slip lines through experimental Digital Image Correlation (DIC) analysis. Simulations were performed in similar conditions as the experiments to compare experimental and numerical outcomes. By inspecting the maximum equivalent (plastic) strain values and maximum shear stress values, it is shown that the consideration of plastic equivalent strain or shear stress does not affect observed slip line trajectories significantly. Consequently, from this analysis, it was seen that the optical deformation measurement techniques can be used to analyze slip line fields.

The simulation model was validated by the experiments, paving the way to in-depth parametric studies using the finite element model. Additionally, the angle of slip lines starting from the flaw tip was found to be approximately 45° around the notch tip and tends to deviate as it moves away from the notch. Slip lines may be attracted by regions of minimum resistance to plastic deformation, i.e. softened regions. These observations act as a motivation to further explore the feasibility of applying slip line field theory for the evaluation of material heterogeneity.

Chapter 6

Limit load predictions for heterogeneous and simplified welds

6.1. Introduction

Estimation of the load-carrying capacity of a structure plays a pivotal role in its integrity assessment. In order to predict the load-carrying capacity, a limit analysis is performed. Limit analysis is the estimation of a critical load at which the plastic region has extended over the entire cross-section and unconstrained plastic flow occurs. Beyond this point, the load does not further increase assuming a perfectly plastic material. This critical load is termed as 'limit load'. Estimation of limit load requires a detailed understanding of the material's constitutive behavior, which can become very difficult in the presence of strength heterogeneity. Thereto several assumptions like homogeneity, isotropy, small strains, absence of strain hardening, no temperature dependence, etc. are included in the limit analysis of the structure. These assumptions led to limit load values different from the actual value.

Prediction of lower values of the limit load as compared to the actual one gives conservative values from a structural integrity point of view. These values can be obtained using a *'lower bound limit load theorem'*. It is the basis of most limit load estimates used in structural analysis. Conversely, higher values of the limit load as compared to the actual one can be determined using an *'upper bound theorem'*. A schematic plot of upper, lower and actual limit load values is shown in *Figure 62*.

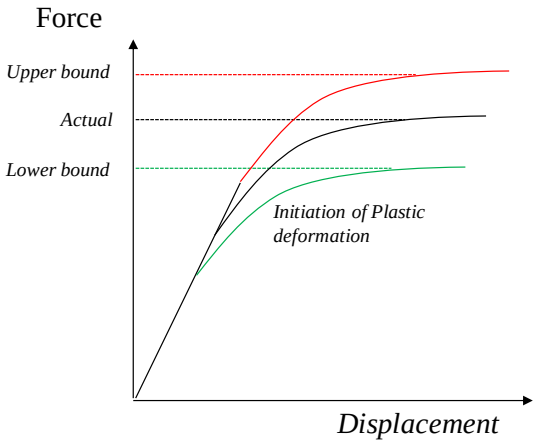

Figure 62: Force-displacement plot showing the actual, upper bound and lower bound limit loads.

Analytical limit theorems for plasticity provide relatively easier estimations of upper and lower bound limit loads without any complexities of experiments and simulations. These theorems are however based on severe assumptions and may become difficult to apply in case of heterogeneous connections.

Several researchers have developed analytical limit load solutions for a notched weld subjected to tension or bending load. Lower bound limit load solutions for several

notched specimen configurations are presented in [21], [152] and [153]. A detailed review of limit load solutions has been put forward by Miller [58]. He evaluated different cases of two-dimensional specimen configurations derived from plane strain, plane stress and thin shell assumptions. Because limit analysis ignores the strain hardening of the material, a choice must be made as to what value of yield strength to use in the limit solution. Miller recommends the use of 0.2% proof stress.

References [60] and [9] considered deformation fields of notched welded panels to derive upper bound limit load solutions. Weld strength mismatch effects were included in upper bound limit load equations developed by several researchers [63] [65] [8]. Hao et al. [9] established the limit load of a mismatched center cracked plate by integrating principal stresses along the assumed slip lines. Kim et al. [8] utilized the slip line field theory and numerical simulations to put forward different limit load equations for different specimen configurations. They also predicted different paths of slip lines for different cases of strength mismatch. The slip lines predicted by Kim et al. [8] are shown in *Figure 63*; they considered different values of mismatch ratio (M) and normalized remaining ligament $\psi = (W - a)/H$ where $(W - a)$ represents the crack ligament and H the half weld width.

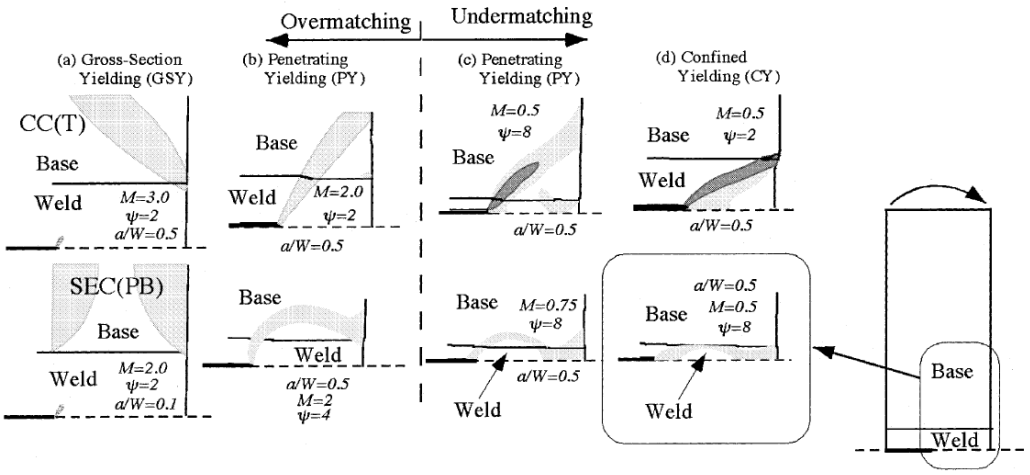

Figure 63: Possible plastic deformation patterns for mismatched plates with interface cracks, extracted from the FE limit analyses based on non-hardening assumptions [8]

It is important to note that in all these solutions the welds are idealized, i.e. analytical limit load solutions that incorporate material property variations within a weld are lacking. The simplified weld is termed as the 'idealization' when it involves simplifying the complex geometry of the weld fusion line to a straight line and heterogeneous strength properties to a homogenous weld region. It is evident from previous work ([48], [31] and [154]) that the heterogeneity within a weld affects the flawed behavior, which in turn affects the limit load of the structure. *Figure 63* acted as a motivation for involving heterogeneous properties within a weldment by considering base metal and a bi-material weld by splitting it into root and cap

regions [10]. Although the intrinsic complexity of the heterogeneity in welds is much larger than in bi-material welds, the introduction of different properties in the weld root and cap led to observations that deviated from idealized welds.

In this work, a lower bound limit load equation which is based on homogeneous material will be updated for a weld having different root and cap properties (bi-material weld) in a SE(T) specimen. Along with lower bound equations, upper bound equations developed for mismatched welds are utilized to assess the limit loads of SE(T) specimens. Particularly, the predictive ability of upper bound limit load equations developed in reference [10] for perfectly plastic material behaviour is explored for welds with strain hardening. The analytical predictions will be compared with limit loads obtained from finite element simulations.

Apart from analyzing the limit loads of actual welds, it is important to investigate how the estimated limit loads of simplified welds compare to those of actual, heterogeneous welds. As mentioned previously, complex heterogeneous welds are usually simplified to single weld material, differentiating base and weld regions only, prior to further assessments using an ECA standard. The local variations of strength are simplified and the weld region is considered to be a homogeneous body (eg. *Figure 63)*. This process of simplification is referred to as '*weld idealization*'.

Another approach involves a simplification where the weld is assigned with strength properties extracted from All Weld Material Tensile Tests (AWMTT) [155]. Also, several standards and codes used for ECA included the concept of mismatch by distinguishing between Base Material (BM) and Weld Material (WM)[6, 21, 62]. These different regions of weldment were categorized based on their constitutive properties. The complex fusion line profiles of butt welds are simplified as straight lines. Idealization allows the safety assessment of a welded structure with less difficulty. On the other hand, it overlooks the presence of local variations in mechanical properties in the weld region and the presence of HAZ requiring conservative safety factors leading to unnecessary repair.

Thus this chapter is utilized to perform two sets of analyses

(a) Analytical estimations of upper and lower bound limit loads in bi-metallic welded 2D elastic-perfectly plastic SE(T) specimens and validating them using numerical FE simulations assuming several simplifications. This analysis aims to provide an analytical method to predict limit loads.
(b) Simplifying an actual weld into an idealized weld and determining limit loads of 2D elastic-plastic SE(T) specimens through numerical FE simulations. This analysis aims to achieve simplification of an actual weld to the nearest possible extent and understand how the limit load of the simplified weld compares to that of the actual heterogeneous weld.

In line with the two analyses, *Section 6.2* first describes the analytical lower and upper bound equations for bi-material welds and results obtained from numerical simulations are evaluated using analytical equations. Secondly, in *Section* 6.3 the standardized Twice Elastic Slope (TES) method is used to obtain a limit load of complex heterogeneous and simplified SE(T) specimens and a detailed comparison is made between the outcomes. *Section 6.4* summarizes and concludes.

6.2. Bounded limit load estimations for bi-material welds

6.2.1. Lower bound limit load

The lower bound theorem states that '*In an elastic-fully plastic body when the stresses are in equilibrium with the boundary conditions and the equivalent stress does not exceed yield stresses, then the maximum load estimated will be lower than the actual load required to cause plastic collapse*' ([137], [156]). Accordingly, for the homogeneous SE(T) specimen shown in *Figure 64,* the specimen collapses when the stress σ_1 at the ligament reaches twice the elastic shear stress, $2k$. This stress level is equal to $c\sigma_y$, where $c = 2/\sqrt{3} = 1.155$ when assuming the von Mises yield criterion (Recall *Equation 5.4*). Then, the limit load P_{LB} of a homogeneous plain sided SE(T) sample can be defined as follows: :

$$P_{LB} = c.\sigma_y.A = c.\sigma_y.B.b \qquad 6.1$$

B is considered to be unity (assuming 2D plane strain conditions). Similarly, for a welded SE(T) specimen *(Figure 65)* having different material properties in the root and the cap region, the equation for the lower bound limit load when assuming collapse in the ligament can be modified as:

$$P_{LB} = c.B.(\sigma_{y1}.b_1 + \sigma_{y2}.b_2) \qquad 6.2$$

where, b_1 and b_2 are the ligament lengths of the cap and root regions of the weld as shown in *Figure 65* and σ_{y1} and σ_{y2} are the yield strengths of the cap and the root of the weld respectively.

It is important to realize that heterogeneous welds may show different locations of failure, depending on crack dimensions and weld strength mismatch ratios. Three cases of collapse are considered.

- The first case considers the collapse in base material away from the notch as seen in *Figure 66.* A strongly overmatching weld metal might lead to a collapse in the base metal. The equivalent mismatch for this failure can be denoted as *W/W-a.*

- The second case considers collapse in the weld region as shown in *Figure 65*. The collapse occurs in both root and cap regions where M_r and M_c are considered for the calculation of the equivalent mismatch M_{eq} which is given by $\frac{b_2}{b_1+b_2} M_r + \frac{b_1}{b_1+b_2} M_c$.
- In *Figure 67* the third case of collapse is observed in root and in base material only. The collapse does not occur in the cap region at all. In this case, it corresponds to M_c=1 for the cap region. Thus M_{eq} is given by $\frac{b_2}{b_1+b_2} M_r + \frac{b_1}{b_1+b_2}$.

The three cases are incorporated in *Equation 6.3*. The lower bound limit load is calculated by taking the minimum of the three cases of collapse.

Theoretically, the lower bound limit load should be defined as the minimum of lower bounds associated with each of these failure cases. However, the lower bound limit load in *Equation 6.2* merely considers failure along the smallest cross-section which is the crack ligament as seen in *Figure 65, Figure 66 and Figure 67*. The limit load of a welded connection is often expressed relative with respect to the base metal limit load.

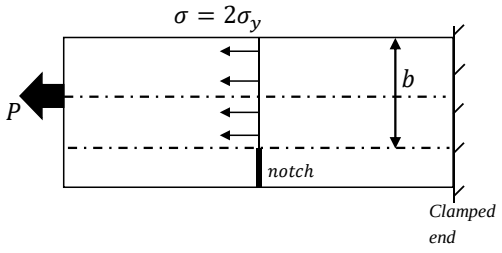

Figure 64: Statically admissible stress field in homogeneous SE(T) specimen

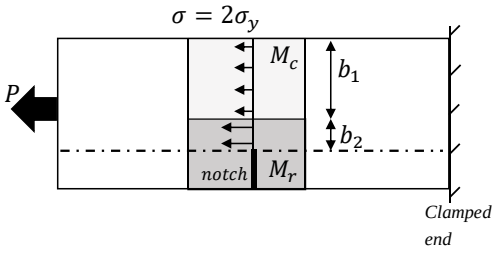

Figure 65: Statically admissible stress field in heterogeneous SE(T) specimen with the collapse occurring in the weld material

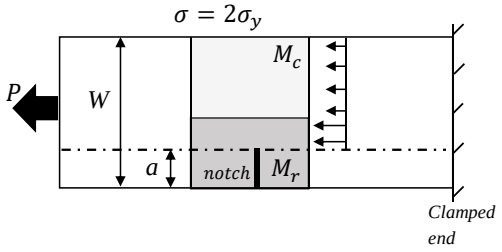

Figure 66: Statically admissible stress field in heterogeneous SE(T) specimen with the collapse occurring in the base material

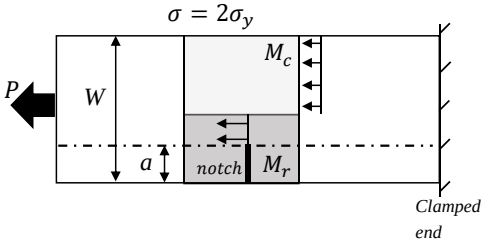

Figure 67: Statically admissible stress field in heterogeneous SE(T) specimen with the collapse occurring in the root of the weld and in the base material

Expressing the minimum of the limit loads (in base and weld) (including *equation 6.1*) in terms of equivalent mismatch (M_{eq}) eventually leads to the expression:

$$M_{eq} = \frac{P_{LBm}}{P_{LBb}} = \min\left(\frac{W}{W-a};\ \frac{b_2}{b_1+b_2}\ M_r + \frac{b_1}{b_1+b_2}\min(1, M_c)\right) \qquad 6.3$$

P_{LBm} and P_{LBb} are the lower bound limit loads of mismatched weld region and base material (σ_{yb} as base material yield strength) respectively. M_r and M_c are the mismatch ratios of root and cap with respect to base material respectively.

The material properties σ_{y1} in cap and σ_{y2} in root along with the SE(T) thickness, crack depth, and location of the root-to-cap interface will have an effect on the lower bound limit load estimate.

6.2.2. Upper bound limit load

The upper bound limit load theorem states that '*In an elastic-perfectly plastic body having a kinematically admissible velocity field, the maximum load estimated will be higher than the actual load required to cause plastic collapse*' [137]. Implementing slip line field theory is a common approach used to determine upper bound limit load solutions. The upper bound theorem tends to be less relevant for engineering applications as it creates non-conservative estimates of the load-bearing capacity of a structure. Nevertheless, if the slip line trajectory is not exactly known but can be estimated with reasonable accuracy, the application of the upper bound theorem on this estimated trajectory can lead to approximations that are very close to the actual limit load [9, 60]. Also, obtaining a close agreement between lower bound and upper bound limit loads indicates that both values are at the proximity of actual limit loads which is in between.

Bimetallic welded samples are considered to make an assessment of the upper bound limit loads. It is assumed that straight slip lines originate from the crack tip at an angle of 45° with respect to the loading direction as set forward in slip line field theory for a fully homogeneous SE(T) specimen. It needs not necessarily be the correct slip line for a heterogeneous connection. Similar to lower bound analysis elaborated in the previous section, upper bound limit load is determined in terms of equivalent mismatch (M_{eq}) i.e. the ratio of mismatched limit load of SE(T) specimen to the limit load of the welded SE(T) specimen with the homogeneous base metal, which is as expressed in lower bound solutions in *Section 6.2.1*. The equivalent mismatch is calculated by *Equation 6.4*. This equation was put forward by taking motivation from reference [10] where the strength mismatch integration along the whole 45° lines is performed up to the surface to obtain an equivalent mismatch of the SE(T) specimen. In this study, the weighted averages follow from the integration of the weld strength mismatch level of each section of the weldment (i.e. the root, the cap, and the base material) along the portion of the slip line lengths $l_{(.)}$ of each of the regions. M_r and M_c are the mismatch ratios of the root and cap material with respect to base material, respectively. $f_{(.)}$ represents normalized lengths, for which $f_b + f_c + f_r = 1$.

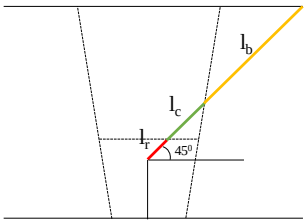

Figure 68: The slip line originating from the notch tip is shown and the equation to calculate equivalent mismatch (M_{eq}) is given ([10], [48])

$$M_{eq} = \frac{P_{UBm}}{P_{UBb}} = f_b + f_c . M_c + f_r . M_r \qquad 6.4$$

$$f_{(.)} = \frac{l_{(.)}}{l_{(b)} + l_{(c)} + l_{(r)}}$$

$$M_{(.)} = \frac{\sigma_{y(.)}}{\sigma_{yb}}$$

In this chapter, analytical limit load predictions are made on bimetallic welds and are compared to simulated values with the exclusion of strain hardening in the numerical model. This will give a better insight into the bounding theorems which consider the assumptions mentioned in S*ection 5.3.2.* The comparison of upper bound and lower bound values is performed on the same set of welds having the same set of assumptions.

6.2.3. Weld configurations

The weld configurations chosen in this study are similar to the welds chosen by Hertelé et al. [10] in an earlier study of weld heterogeneity effects. This selection was based on several actual weld configurations and further simplified to a weld containing two distinct layers, root and cap. The root and cap are assigned with different material properties and the notch is always located in the root of the weld. The weld is V-shaped, having a fusion line angle β with respect to the through-thickness direction.
Assumptions of the weld configurations considered in this chapter are as follows,

- The materials are elastic-perfectly plastic (no strain hardening) and isotropic
- 2D plane strain conditions

Weld strength has been varied between root to cap separated by an interface where strength properties show a discontinuous jump. This represents an extreme condition of local weld heterogeneity. The height of the weld root is given by W_r, thus introducing an additional geometric parameter into the analysis.

Narrow (β = 10°) and wider welds (β = 30°) are considered. Root width $2H_r$ is taken to be constant ($2H_r/W = 0.3$). Two values have been considered for W_r: $W_r/W = 0.3$ and $W_r/W = 0.6$. Two crack depth levels ($a/W = 0.2$ and 0.4) have been simulated. The crack is positioned in the weld metal center.

Eight combinations of weld geometry are considered, as illustrated in *Figure 69*. Using this collection of geometries ensures that all possible slip line trajectories from the crack tip to the crack surface are covered, as illustrated by the 45° diagonal lines in the figure: root-cap-base metal (geometries i, iv, v, vii), root-base metal (geometry iii), cap-base metal (geometry ii), root-cap (geometry viii), cap only (geometry vi). This allows accounting for different levels and configurations of weld heterogeneity.

All materials were given a constant Young's modulus $E = 200000\ MPa$, with $E/\sigma_{yb} = 400$ since σ_{yb} was kept constant at 500 MPa. Weld root and cap metal are characterized by mismatch levels M_r and M_c, respectively (both with respect to the base metal yield strength σ_{yb}). M_r has been given three values: 0.85 (undermatching), 1.00 (evenmatching) and 1.15 (overmatching). Weld root-to-cap heterogeneity is characterized on the basis of $\Delta M_{cr} = M_c - M_r$. Given that cap material tends to be harder and a hardness difference of 30% is realistic as one can observe in the hardness maps of *Chapter 2* and in the explanation of *Section 1.3*, the following heterogeneity levels have been considered: ΔM_{cr} = 0.00, 0.15, 0.30. ΔM_{cr} = 0.00 corresponds to a homogeneous weld mismatching with the base material (undermatch, evenmatch or overmatch). The other two values yield a bi-material weld. This results in 5 different yield strength or mismatch M_r values of the cap region. In total, 120 simulations were performed.

The limit load from simulations is obtained at the load value obtained using Twice Elastic Slope (TES) method used in *Section 5.4.2* in the elastic-perfectly plastic simulations with small strain assumptions as shown in *Figure 70*. The TES method was chosen as it is a standardized method [147]. Another method to obtain a limit load is to consider the maximum load from the load-displacement plots. This consideration would result in increased limit load values up to 3% compared to the limit load obtained from the TES method. Additionally, considering the limit load as the value at the point of yielding leads to a decreased limit load value of approximately 3%.

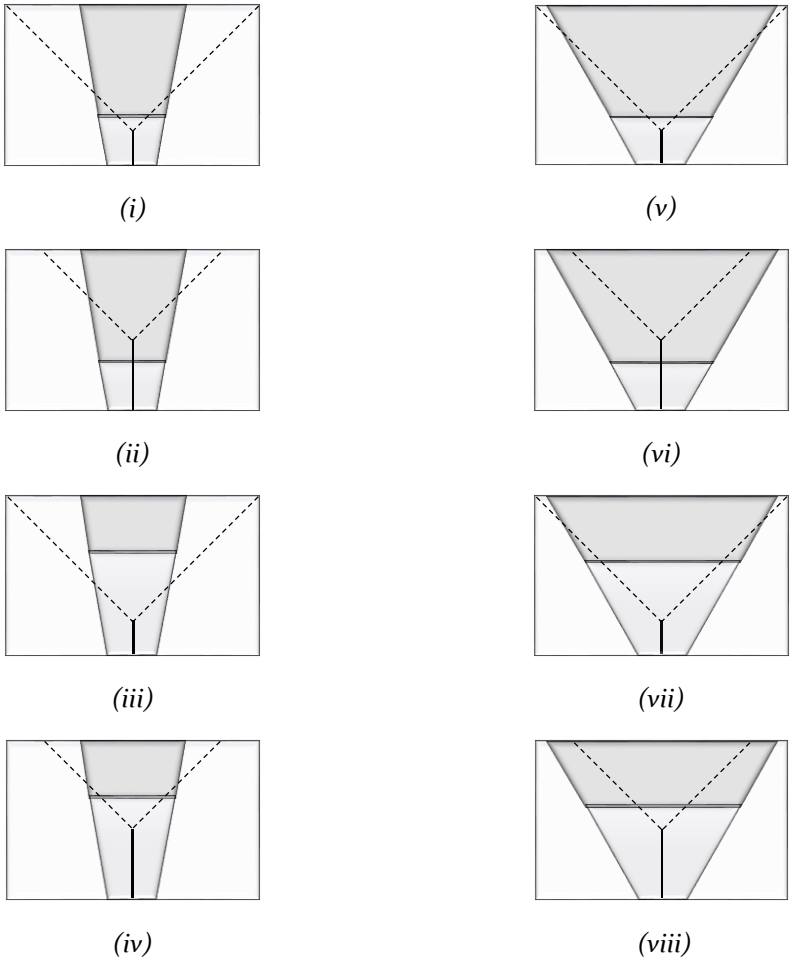

Figure 69: Eight weld configurations used in this study of limit load predictions

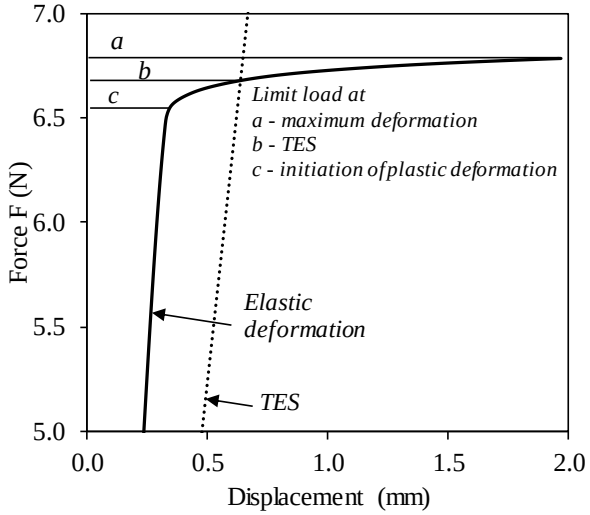

Figure 70: Theoretical estimation of limit load through elastic-perfectly plastic simulations

6.2.4. Results and discussions

Firstly, the **lower bound** limit load analysis is evaluated for the eight weld configurations. *Figure 71* compares the results of analytical lower bound and numerically simulated limit loads. The results show that the analytical limit load points mostly lie in that region of the plot corresponding to an underestimation of the limit loads obtained from the simulations. Additionally, 15 out of 120 points are slightly overestimating the limit load. These results are discussed further. However, this analysis generally produced lower bound estimates in accordance with the theorem as put forward in section *5.2.1*. For different weld configurations with various properties, the limit load estimations were conservative and the results provide safe projections.

Additionally, in *Figure 71,* differentiation is made between fusion line angles 10° and 30°. In order to compare the analytically and numerically obtained limit loads, a percentage difference between both limit load values:

$$\%\, diff = \frac{P_{LB\,(an)} - P_{LB\,(FE)}}{P_{LB\,(FE)}} \times 100 \qquad 6.5$$

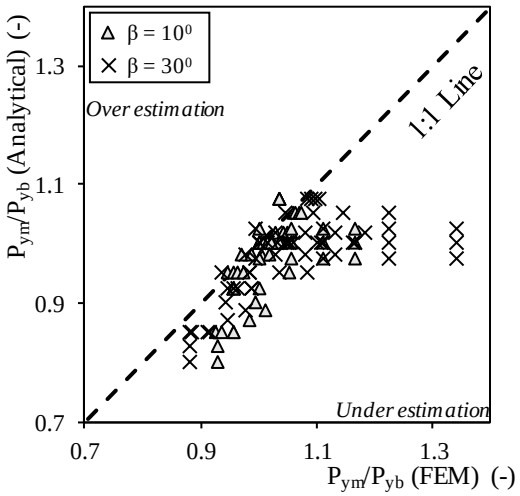

Figure 71: Lower bound predictions in bi-metallic welds

As mentioned, for a limited number of cases the analytical solutions were overestimating the FE determined limit loads. The overestimations were limited to less than 3%, which is very low from an engineering point of view. Yet, it is interesting to examine why a theoretically intended lower bound equation may produce overestimations of limit load. The overestimated cases were assessed individually to get a thorough understanding of the behavior of welds with different configurations. The limit loads deviating from expected patterns (lower bound) are considered in the following, and the cause of the deviations is assessed by studying

the plastic deformations observed in the simulations, weld configurations and the consequences of using the considered analytical equations.

Figure 72 is used to discuss the results of *Figure 71* in detail. Different cases of mismatch of the root *(M_r<1* and *M_r≥1)* and cap (*M_c<1* and *M_c≥1)* are dissected from *Figure 71* from each configuration with different fusion line angles. The main outcomes of the plot are summarized:

- *M_c<1* always produced lower bound solutions while the other cases of mismatching *M_r<1, M_r≥1* and *M_c≥1*, few estimations deviated but as a whole, they were lower bound estimates.
- For configurations *i-iv (β=10°)*, the estimates were mostly lower bound and the extent of conservatism was up to a value of 0.84 (-16% difference). Few values overestimated the limit loads giving non-lower bound estimates. Among 60 results, 6 analytical values over-estimated the simulated load by 4%. This shows that the predicted non-lower bound values differ by a small margin.
- Configurations *v-viii (β=30°)* showed a greater range of deviations in analytical predictions compared to the actual limit load (obtained from numerical simulations). This can be seen through the lines of the two plots in *Figure 71 (a) and (b).* The conservatism was up to a value of 0.73 (-27% difference). 4 values out of 60 produced non-conservative estimates and the highest deviation from the actual limit load is 3%.
- Lower bound equations fail to account for the beneficial effects of *M_c>1*. This could result in extreme conservatism of the limit load values and the estimations are more scattered which can be seen in *Figure 71*.

For the configurations where the cap was wider and the deformation bands did not pass through the cap region, the estimated limit loads were either on the 1:1 line or were overestimated. The deformation bands are shown in *Figure 73*. The configurations shown in (a) and (b) had the highest cap strength and lowest root strength; configuration (c) had the highest root strength and lowest cap strength. From these figures, it can be observed that the variations in the angle of the slip line or the deformation band were not significant due to the assumption of non-strain hardening materials.

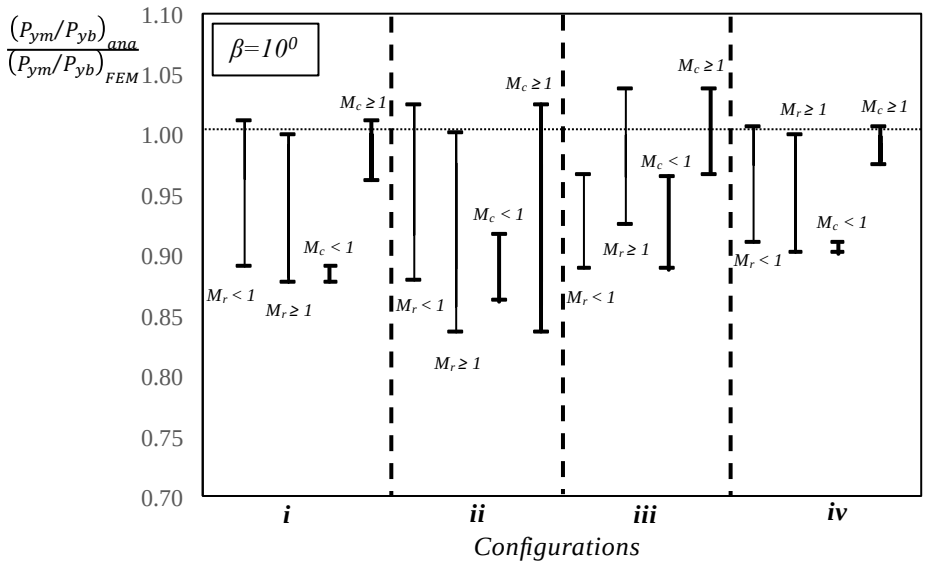

(a)

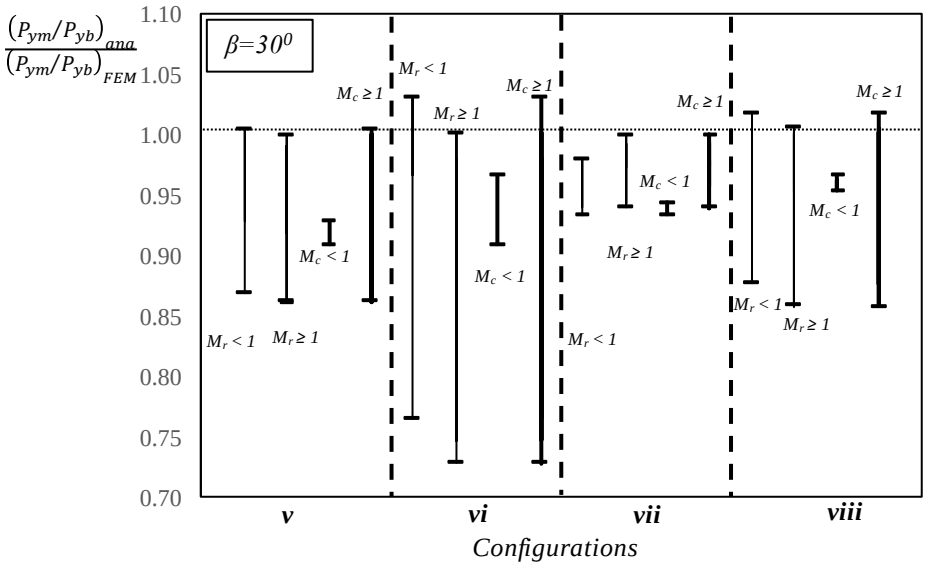

(b)

Figure 72: Lower bound estimations for different cases of root and cap mismatch for each configuration of the weld geometry (a) β=10° and (b) β=30°

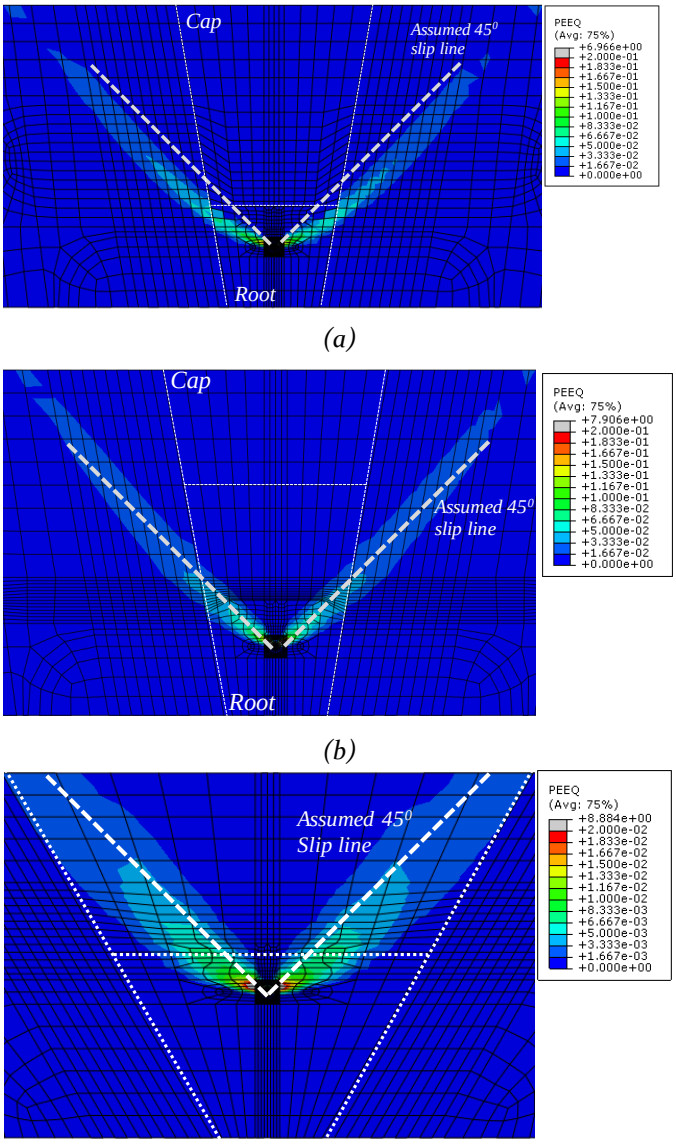

Figure 73: Deformation bands originating for different configurations in a bimetallic weld

Secondly, the **upper bound** limit analysis was performed on the same eight weld configurations and the corresponding limit load predictions are shown in *Figure 74*. The procedure used here is as described in *Section 6.2.2*. It is evident from this study that the upper bound limit load estimation procedure [10] is also applicable for elastic-perfectly plastic materials. In order to quantify the differences, an equation equivalent to *Equation 6.4* for lower bound analysis is used.

The differences were within 5% for most of the welded specimens. For a few cases, there were higher differences above 5% (up to 10% overestimations of FE simulated limit load using the analytical equation). As seen in lower bound predictions, the wider cap limit loads produced higher upper bound predictions than the narrower

welds which has its data points located near the 1:1 line. However, as the predictions are upper bound as required by the study, it can be tolerated.

Remarkably, certain analytical limit load predictions are non-upper bound i.e. less than the simulated limit loads even though the equation should theoretically provide upper bound values. A close investigation of these estimates did not reveal a pattern and also, as explained in previous sections, the deformation bands did not deviate from a particular angle. It is assumed that this discrepancy is the (possibly combined) result of numerical inaccuracies and/or the adopted definition of limit load (arbitrarily based on the twice elastic slope method). Nonetheless, overall, fairly accurate solutions are predicted using the upper bound method, which shows that the technique may be a suitable ingredient within ECA procedures that account for the strength heterogeneity of welds.

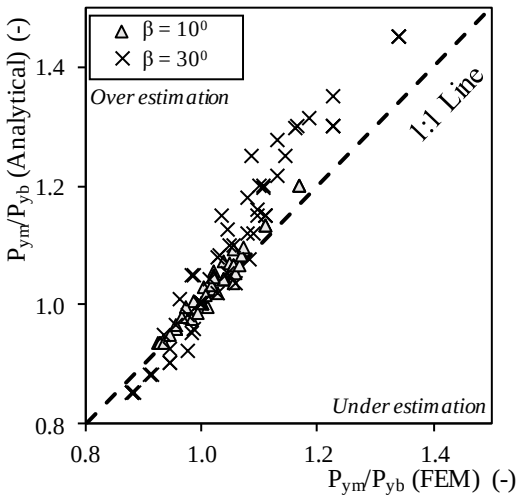

Figure 74: Upper bound predictions in bimetallic welds

A detailed analysis of *Figure 74* is undertaken in line with the analysis of lower bound results. Different cases of mismatch of the root ($M_r<1$ and $M_r\geq1$) and cap ($M_c<1$ and $M_c\geq1$) are considered to assess the outcome. It is displayed in *Figure 75* in which (a) shows the analysis for the configurations *i-iv* and (b) shows the analysis for the configurations *v-viii*. The plots are analyzed as follows:

- It can be seen that a general trend of the upper bound predictions could not be observed and is configuration dependent. This is due to the sophistication of the analytical upper bound equation where the material properties are integrated along the 45° line. This leads to the configuration dependent analytical prediction.
- Configurations *iii, v* and *viii* all produced upper bound solutions. However, for other configurations, there were certain values that were underestimating the simulated limit loads.

- For configuration *i-iv,* only 9 out of 60 simulations produced non-upper bound estimates, with the maximum underestimation equal to 6%. Out of 9, 6 values were obtained in configurations having undermatching or evenmatching cap. Incidentally, not all values in this configuration were underestimating the simulated limit loads and thus did not lead to a concrete statement about the outcome.
- In configurations v-vii, 15 out of 60 analytical predictions provided lower estimates compared to simulations. In these cases, the minimum estimate was 0.83. The value 0.83 was obtained for configuration vi and vii for an undermatching cap region. Besides this case, other underestimations were less than 10%.
- It can be seen that when the fusion line angle β is 30° the range of the minimum to maximum limit load is higher as compared to 10°. This means that the range of M_{eq} is larger in configurations having β=30° than in the configurations having β=10°.
- In *Figure 74,* the data points obtained from the analysis of configurations having β=30° tend to show higher deviations from the 1:1 line while the dataset obtained from analysis of the configurations with β=10° lie near to 1:1 line. It is difficult to draw a consensus regarding this result based on the analysis in this research. A possible reason could be the result of the local variation in angle as the deformation band reaches the fusion line. This is further explained i*n Chapter 7*. These angle changes are not accounted for in the analytical upper bound limit load estimation scheme.

Thus, based on results from the assumed set of weld analysis, general guidance is put forward for the user to obtain upper and lower bound estimates in bimetallic welds. For lower bound analysis, *Equation 6.3* can be utilized for an analytical estimation when knowing the weld geometry with the dimensions of the cap and root regions along with the material properties of each region. To avoid the non-lower bound estimates, a reduction of up to 4% in the obtained limit load value would achieve completely lower bound estimations. For upper bound analysis, the procedure shown in *Figure* 68 can be utilized to obtain upper bound limit load estimates with an increase of 13% to achieve all upper bound estimates as few results were underestimating up to 13%. From the outcome of this chapter, it is difficult to put forward a generic correction factor. However, these estimates will serve for analytical predictions in the situation where there is a non-availability of numerical or experimental facilities. An improvement of these predictions could be achieved through a better understanding of slip lines and deformation bands.

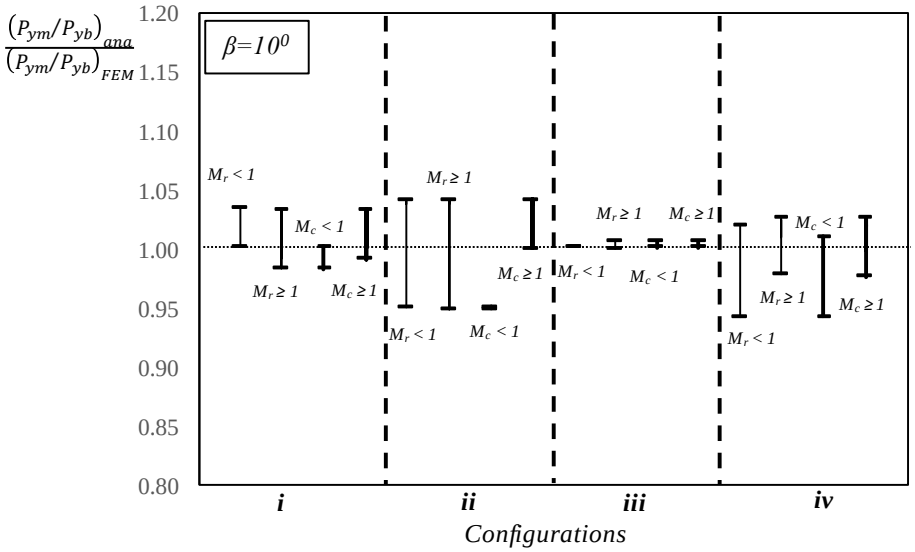

(a)

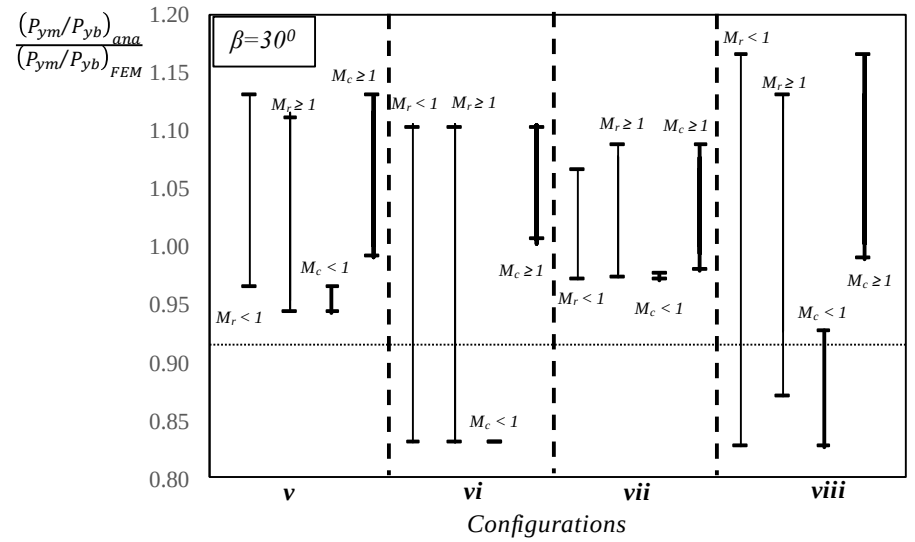

(b)

Figure 75: Upper bound estimations for different cases of root and cap mismatch for each configuration for the weld geometry (a) β=10° and (b) β=30°

The application of the lower bound approach for a heterogeneous weld as used in Chapter 4 would be difficult. Conversely, the upper bound approach could be used for the determination of limit loads in a complex heterogeneous weld. The numerical estimations can be utilized to predict the actual limit load based on the assumptions made in this section and a safety factor can be applied on the acquired limit load based on the requirement of an upper or lower bound limit load. A database could be established considering several welds with different geometries and material properties which helps in a ready-made solution for limit load assessments in welds.

6.3. Limit load estimations of heterogeneous welds and corresponding idealized welds

The previous section focused on a fairly simplistic category of heterogeneous welds, i.e. bi-material welds of which root and cap have distinct but different properties. The simplicity of those welds allowed to directly apply simplified bounding theorems. The applicability of these theorems may be impractical for actual welds with more complex heterogeneity patterns.

When actual welds are to be assessed, current ECA practice suggests treating welds as "idealized", i.e. having straight fusion lines and homogeneous properties. Therefore, the current section focuses on how to translate ("idealize") complex heterogeneous welds into idealized welds having a similar limit load, which can then be further used within the standardized ECA.

6.3.1. Material and methods

Two weld idealization schemes are explored in this chapter. The methods used for weld idealizations are compared with the actual weld on the basis of their accuracy in predicting limit loads through numerical simulations.

The **first** and the most widely used technique to obtain average weld constitutive properties is to extract an AWMTT specimen from the weld region. The obtained stress-strain curve is then assigned to the whole weld region. This is the simplest method to idealize a weld, but does not include the material heterogeneities present in the weld and also the HAZ is not considered in this method. There is no particular method to define how the fusion line geometry should be simplified or how to deal with the HAZ. Therefore in this research, 45° slip lines are considered from the crack tip up to the fusion line with the base material and the corresponding thickness is assigned to the idealized weld. The process of weld simplification is performed as explained in *Figure 77* and $2H_{eq}$ is considered as the thickness of the weld.

The **second** technique used to simplify a weld was developed by Hertelé et al.[10, 48]. Weld strength mismatch is governed by average strength properties along the slip line originating from the crack tip assumed to be in 45° orientation for the case of uniaxial load perpendicular to the crack. The procedure to simplify a weld from a hardness contour plot is as follows:

- The average hardness of the weld (HV_{WM}) is calculated along the slip line originating from the crack tip and the average hardness of the base is taken on the left and right side of the weld region including the HAZ.

$$HV_{WM} = \frac{l_1}{l_1 + l_2} HV^{WM}_{avg\ left} + \frac{l_2}{l_1 + l_2} HV^{WM}_{avg\ right}$$

$$HV_{BM} = < HV^{BM}_{avg\ left}, HV^{BM}_{avg\ right} >$$

where $l_{(.)}$ is the length of the slip line originating from the crack tip up to the base material interface at an angle of 45°.

- From HV_{WM} and HV_{BM}, yield strength R_{p02}, ultimate tensile strength R_m, yield to tensile ratio R_{p02}/R_m and strain hardening exponent n are calculated from transfer functions using AWMTT and base metal tensile tests respectively. These equations have been experimentally calibrated and validated in *Chapter 4*.
- The obtained material properties are assigned to the weld region (homogeneous weld)

The equivalent width of the weld ($2H_{eq}$) is determined to perform its idealization *(Figure 78).*

The base material is assigned with the material properties which are obtained from all weld metal tensile tests. This was assumed after the assessment of the stress-strain properties of the base material which were obtained from two methods – (a) converting *HV5* to $R_{po.2}$ and R_m using the standardized equation from ISO15653 [33] (formulated for *HV5* values with RO strain hardening (*Equation 2.11*) as in *Section 4.3*) and (b) obtaining $R_{po.2}$ and R_m through tensile tests of the base material. The stress-strain curves obtained from these two methods for three considered specimens are shown in *Figure 76*. For both techniques, the $R_{po.2}$ values showed differences up to 50MPa. With this result in hand, the material strength values of $R_{po.2}$, R_m and n for the base material simulations were taken from tensile test results as they produce the complete stress-strain curve rather than using transfer equation using *HV5* measurements. They also acted as a basis for the standards [33, 127] to obtain a transfer function that allows to convert *HV5* to material properties.

Two weld idealization techniques are evaluated using numerical models based on actual and idealized welds. The FE model simulates a SE(T) specimen under 2D plane strain with clamped boundary conditions. The daylight length *(L)* of the specimen is 200mm and its thickness *(W)* is 15mm. Three notch depths were considered for the study i.e. a/W = 0.2, 0.3 and 0.4, with a being the depth of the notch. A first notch was located in the root, and a second one in the cap of the weld; both were introduced at the weld metal center. The notch tip radius (ρ) was chosen to be 0.075mm. The other details of the simulations are explained in *Section 2.3*. The three welds considered in this assessment are B, D, and F of *Figure 15*. Their hardness contour plots are shown in *Figure 79.* These welds show a high degree of strength variation from root to cap and additionally involve wider heat-affected zones.

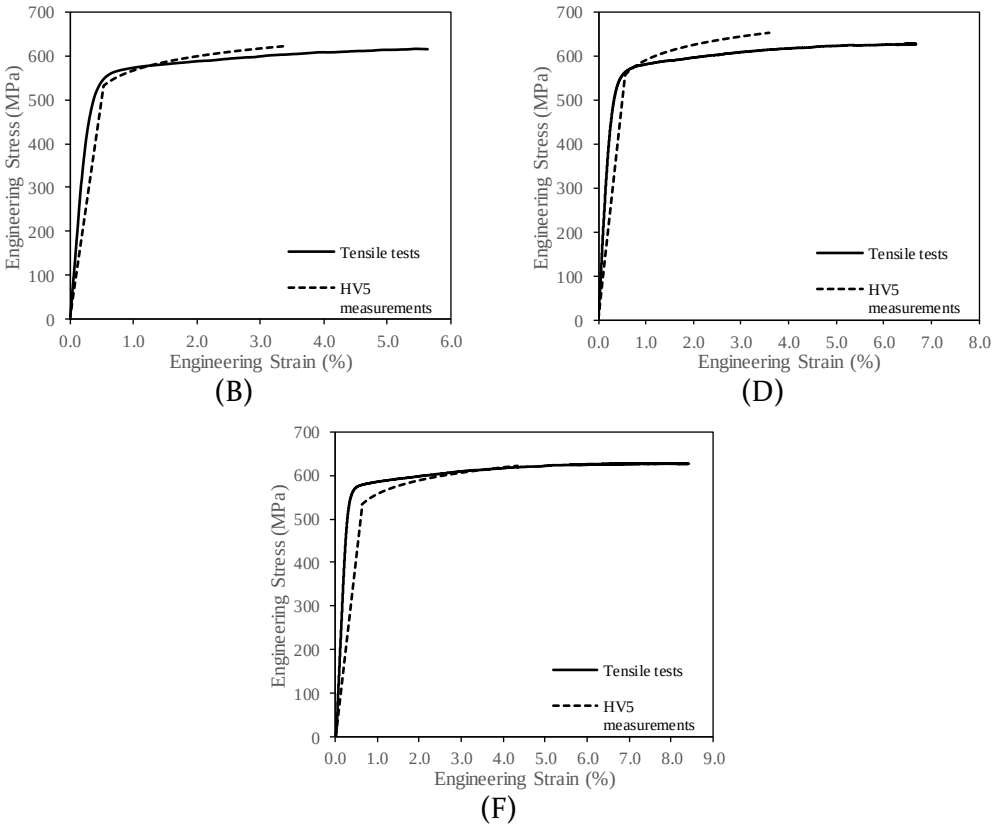

Figure 76: The stress-strain curves obtained for the base material of the three specimens B, D, and F using tensile test results and converting HV5 values into material strength properties.

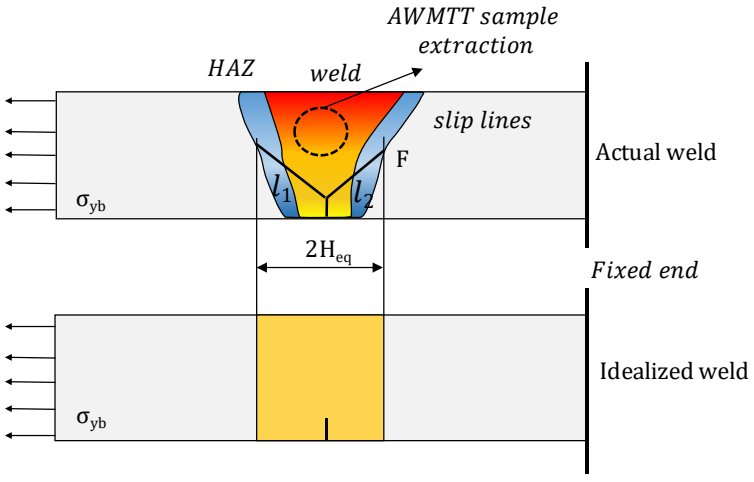

Figure 77: Procedure to idealize a weld using all weld metal tensile test and slip line assumption

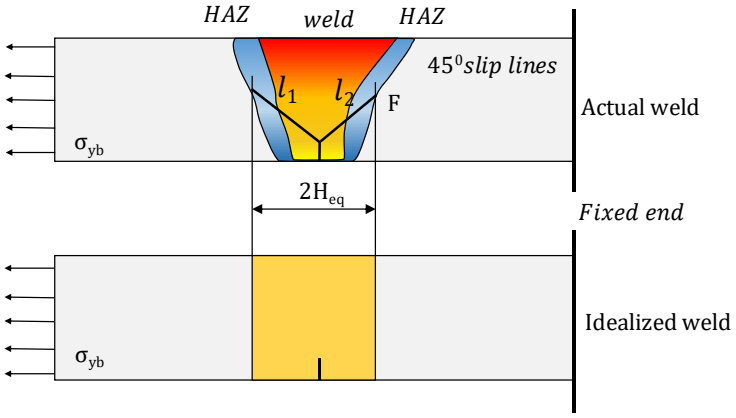

Figure 78: Procedure to idealize a weld using the concept of slip lines.

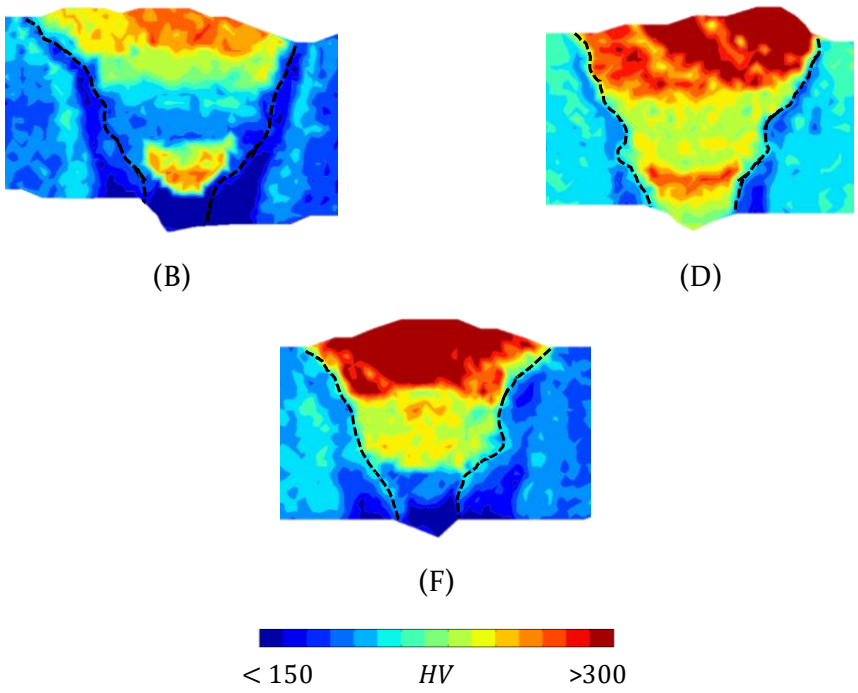

Figure 79: Hardness contour plots of the weld samples used for weld idealization analysis chosen from Figure 15.

6.3.2. *Results and discussions*

In the **first method** of idealization using AWMTT results, yield strength R_{p02}, ultimate tensile strength R_m, yield to tensile ratio $R_{p0.2}/R_m$ and strain hardening exponent n of the three samples (B, D, and F) were obtained from All Weld Metal Tensile Tests (AWMTT). *Table 11* summarizes the data obtained from the experiments.

Sample	*Average Hardness*	*Yield Strength* (N/mm^2)	*Ultimate tensile strength* (N/mm^2)	*Yield to tensile ratio*	*Strain hardening exponent*
	HV_{avg}	$R_{p0.2}$	R_m		n
B	240.23	674.66	777.8	0.87	16.96
D	260.62	752.94	850.3	0.89	18.61
F	217.79	621.08	731.6	0.85	15.27

Table 11: Constitutive properties of weld metal obtained from all weld metal tensile tests.

The weld properties were assigned to the finite element model based on the values from *Table 11*. The thickness of the weld $2H_{eq}$ was different for each specimen as it was determined based on the method shown in *Figure 77*. Limit loads obtained from the TES method suggest an average difference of ~8% between idealized and actual weld results. The results of the limit loads between idealized and actual welds had differences varying from 0.9% to -15% (the difference is calculated as the ratio of limit load obtained from the actual and idealized weld). A positive difference suggests a conservative result and a negative difference an overestimation of limit load compared to the actual weld. *Figure 80* plots the comparison. The variability of differences was quantified using standard deviation which was found to be ~4.5%. In all cases, the idealization process leads to over-estimation of limit loads.

The **second method**, which considers the slip lines originating from the crack tip to obtain constitutive properties, includes more parameters in order to simplify a weld. As per this technique, the average hardness calculated was based on notch depth and location. The results are given in *Table 12*. The variability in average hardness values depending on the location and depth of the notch can be seen. One observation from *Table 12* is that hardness increases with the increase in notch depth from the root whilst it shows a decreasing trend at the cap. This is due to the fact of having a harder region in the cap and a comparatively softer region in the root. The slip line method takes varying hardness into account, whilst the AWMTT method is based on constant stress-strain properties irrespective of notch position and depth. The hardness values from *Table 12* were used to obtain material parameters. Yield strength $R_{p0.2}$, ultimate tensile strength R_m, yield to tensile ratio $R_{p0.2}/R_m$ and strain hardening exponent n were calculated using the AWMTT transfer function as explained in *Chapter 4*. With material parameters in hand, the SE(T) simulations for the idealized weld were performed. The average differences between actual and idealized weld limit loads were ~2%. The deviations of simulated results from actual loads range from 8% to -10%.
The standard deviation of differences between numerical simulations was ~6%. This technique (second method) resulted in improved predictions owing to its ability to involve more parameters. The results comparing the limit loads of actual and

idealized welds using the two methods are shown in *Figure 80*. In the case of sample B, the limit loads were underestimated leading to conservative results and samples D and F had differences which are less than the AWMTT technique of idealization though the limit loads are overestimated.

Notch depth (a/W)	***Notch location***	***Hardness (HV_{avg}) of weld***		
		Sample B	***Sample D***	***Sample F***
0.2		*238.92*	*263.32*	*219.78*
0.3	*Root*	*240.46*	*272.62*	*226.42*
0.4		*247.67*	*276.66*	*230.77*
0.2		*215.49*	*259.65*	*208.87*
0.3	*Cap*	*211.96*	*256.4*	*202.42*
0.4		*209.97*	*258.81*	*198.99*

Table 12: Results of average hardness taken along the slip lines originating from the crack tip in SE(T) samples

Three important observations can be made from this plot. Firstly, there is a significant variation of limit load values which reconfirms the effect of weld heterogeneity on load-bearing capacity. Secondly, the difference in the limit load between the two schemes of idealization has high variations. In certain cases, there is a noticeable difference (~8%). But in most cases, it is less than 2%. A third and most important observation is that the limit load suggested by idealization schemes is often higher than the actual limit load of the considered welds (except sample B - idealization using slip line method). This means that the actual structure reaches its plasticity limit sooner than the predicted limit load of a simplified weld. The standard deviations on the % differences between idealized and actual welds showed a variation of 0.7% between slip line and AWMTT method. In case D, the deviations are higher in AWMTT than in slip line method.

The investigation of limit loads of actual and idealized welds shows the discrepancy in currently used techniques to analyze a weld defect. The variations observed in the limit load predictions deserve consideration in ECA methods. In order to understand these variations, a detailed analysis based on slip lines through deformation bands observed in numerical simulations is conducted. Thus, an analysis of the deformation plots considering equivalent plastic strains (PEEQ) was performed.

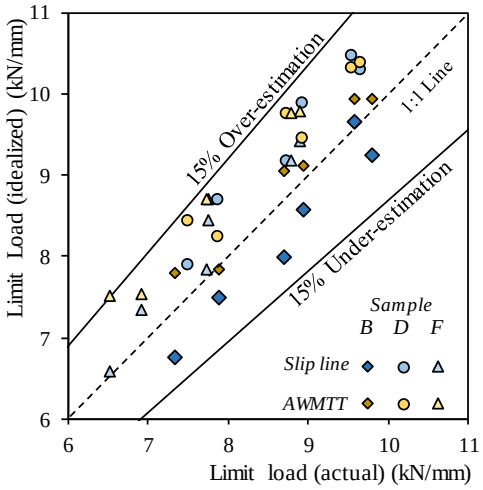

σ (% difference)	B	D	F
Slip line	-2.76	+2.43	+2.92
AWMTT	+2.02	+2.82	+2.23

Figure 80: Limit load comparison between the actual and idealized weld and the values of standard deviations between the % difference of actual and idealized limit loads (+ denotes over estimation and – denotes under estimation)

Researchers [8-10, 59, 60] typically assumed that the slip line pattern obtained from a notched weld is a straight line, mostly 45°. This consideration was based on a homogeneous body or a mismatched weld. But an inconsistent strength variation inside the weld region was not considered in such assessment. Observations regarding the effects of strength variations on equivalent plastic strain (PEEQ) are made in this numerical study. *Figure 81* shows strain concentration bands originating from the notch tip in a homogeneous weld performed on the idealized weld of *Figure 79(D)*. From these, deformation bands have been derived as a trajectory of maximum PEEQ towards root/cap. Similar slip line patterns were observed in idealized specimens (using both homogenization schemes) of other samples. The uneven distribution of the deformation bands at both sides of the notch depended on the H_{eq} length on both sides. As seen in *Figure 81, the* left part of the notch is having a longer deformation line when compared to the right side as the fusion line is farther away from the notch on the left side. This was observed in other configurations too.

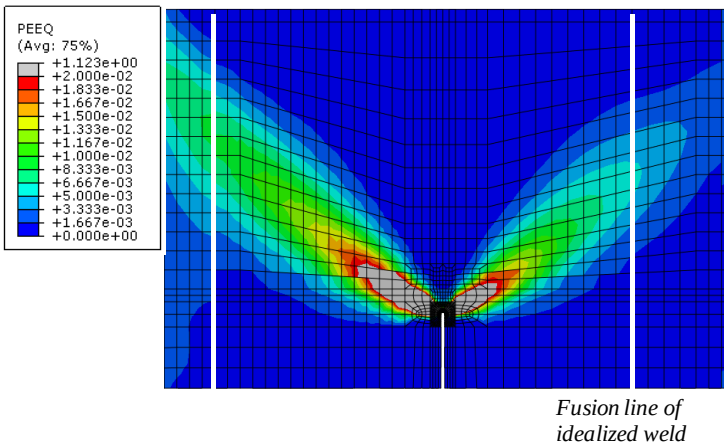

Figure 81: Deformation bands in an idealized weld from sample D

The assumption of straight 45° slip lines becomes doubtful when considering actual welds. The high strain regions in actual and homogenized welds are incomparable. Two examples from different sets of simulations were chosen to analyze the slip lines in actual welds, i.e. (i) notch located in root and a/W=0.2 of sample D (*Figure 82*(a) illustrating the case of crack tip in soft region) and (ii) notch located in cap and a/W=0.3 of Sample B (*Figure 82*(b)) illustrating the case of notch tip located in harder region). This also shows that the width of the assumed deformation band (assumed to be infinitely narrow) for the weld idealization is also not comparable to the deformation bands in actual welds.

The strain concentration bands arising from the notch tip tend to flow to the region having low hardness. This means that the harder region resists deformation creating a non-straight slip front. The bands concentrate inside the material at the fusion line on the right side and flow to the base material and HAZ on the left side.

As deformation is applied, secondary branches of slip lines were observed to originate in low strength material. Referring to *Figure 82*(b) on the left-hand side and right-hand side, it can be observed that there is a sudden transition from hard weld metal to a soft HAZ. This transition affects the angle of flow as the deformation tends to be higher in the HAZ. This invalidates the assumption of 45° slip line homogenization. By observing the strain concentrations from the notch located in the cap of sample B (*Figure 82*(b)), the region of the notch resists deformation and hence slip line flow in upward direction, showing a uniform slip line front. The primary slip line flows towards the root of the weld and the secondary slip line which begins in the region of the fusion line flows towards the cap of the weld. At higher deformation, the slip line runs parallel to the fusion line.

Similar slip line bands were obtained in other actual welds simulations and are confirmed by experimental results in *Chapter 5*. This shows that the prediction of slip lines in complex welds is challenging. This hampers the predictive accuracy of

slip line based methods of limit load estimations, such as the averaging of weld metal properties along 45° lines.

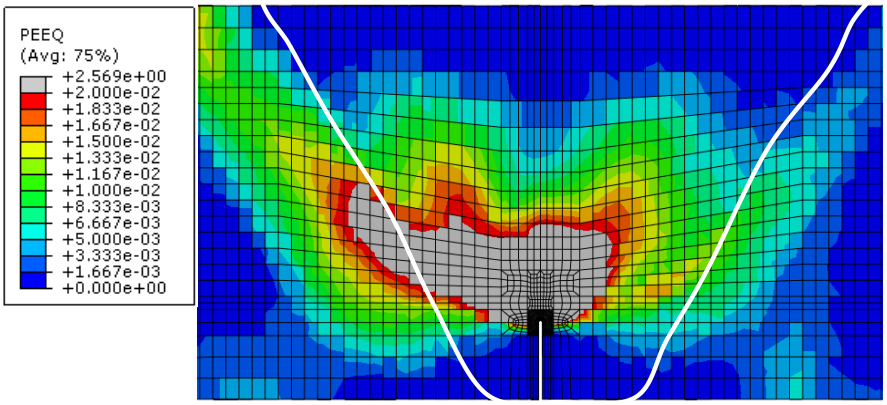

(a)

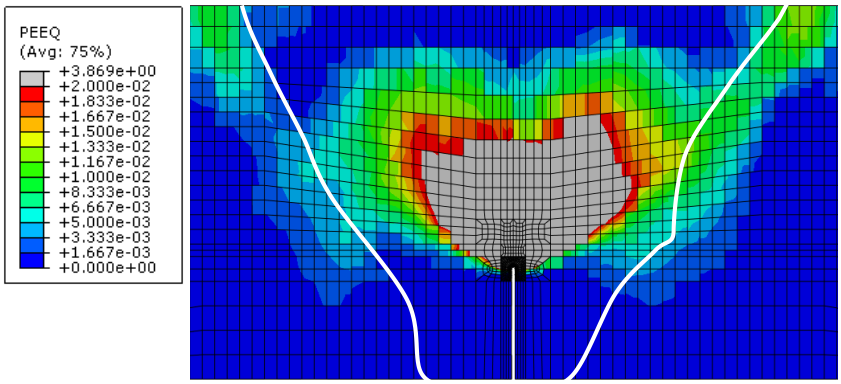

(b)

Figure 82: Deformation bands of the samples D (a) and B (b) showing a clear deviation from 45° and additionally showing non-uniform deformation bands.

6.4. Summary and conclusions

Two investigations on the limit load analysis of heterogeneous welded joints have been demonstrated in this chapter.

Firstly, the lower and upper bound analysis was performed on bi-material welds. Modified limit load estimation schemes that take into account the strength properties in bi-material welds were put forward. A lower bound estimation scheme is advantageous as it provides safe estimates of the SE(T) specimens but it could be extremely conservative for cases where M_c>1. The implementation of this estimation scheme in heterogeneous welds could also be a challenge. The upper bound limit load estimation scheme provides a suitable method to implement the procedure in heterogeneous welds. By knowing the analytical upper and lower bound limit loads, the actual limit load could be established.

Secondly, two weld simplification techniques have been analyzed involving homogenization and geometry idealization methods. The two techniques of simplification, one using all weld metal tensile test data and the other using slip line concept proved to be competent techniques to simplify a weld based on error analysis. The variations (standard deviations) were higher in the slip line method (standard deviations up to 2.9) than in the AWMTT method as the slip line method takes into account the material properties where the deformation bands tend to flow. AWMTT assumes the material properties only the weld region where the tensile samples were extracted.

Chapter 7

Crack tip constraint behavior in heterogeneous welds and its relation with slip line formation

7.1. Introduction

In order to undertake an effective failure assessment of a specimen or a structure, the knowledge of fracture toughness plays an important role. Traditional single parameter fracture mechanics (based on *K*, J-integral or CTOD) will not be applicable when excessive plasticity is present in the material. These theories are only valid for geometries under high constraint conditions and can then be used as a geometry independent failure criterion. High constraint on the crack tip to contract/expand during loading arises due to the resistance offered by the surrounding material resulting in a triaxial state of stresses near the crack tip. These theories will be rendered invalid when the specimen undergoes excessive plasticity, i.e. when the fracture toughness becomes dependent on the size and geometry of the test specimen.

SE(T) specimens have been designed to have low crack tip constraint and single parameter fracture mechanics would strongly overestimate the crack tip stresses. Due to this, several researchers attempted to describe the crack tip stress fields using a second parameter representing the crack tip constraint. It is expressed in various forms such as *T*-stress [157], *Q* and Q_m parameters [66, 67], A_2 parameter [158] and other quantities. The *T*-stress calculation assumes elastic material properties [159, 160] and the parameters *Q* and A_2 are applicable for elastic-plastic analysis.

The Hutchinson-Rice-Rosengren (HRR)[68, 69] solution can be used to theoretically describe the crack tip stress singularities in the plastic zone under small scale yielding conditions. This solution accounts for the first-order term of the stress field. This consideration is however not sufficient for describing stress fields around the crack tip that are under low constraint conditions (eg. SE(T) specimen) for which higher-order terms have to be considered. The first higher-order term represents a spatially uniform hydrostatic shift at the crack tip stress field [66, 67]. This hydrostatic shift can be characterized by a single parameter *Q*. *Equation 7.1* shows the influence of the *Q* factor in determining crack tip stresses.

$$\sigma_{ij} = (\sigma_{ij})_{HRR} + Q\,\sigma_y \delta_{ij} \qquad 7.1$$

This hydrostatic shift is valid in a range of radial distances (*r* from *Figure 83)* ahead of the crack tip between $J/\sigma_0 < r < 5\,J/\sigma_0$ [66, 67]. Additionally, the *Q* parameter is conventionally determined at a distance $r = 2\,J/\sigma_0$ which represents ductile or cleavage fracture.

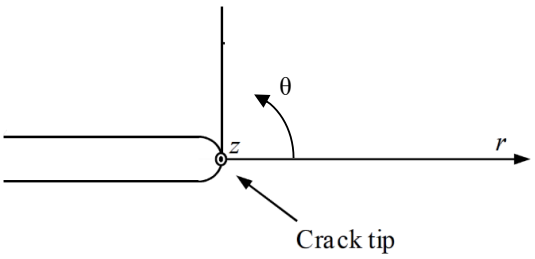

Figure 83: Crack tip showing the axes and references where the Q parameter is determined

Based on *Equation 7.1*, the Q parameter is often practically obtained from the crack governing stress $\sigma_{\theta\theta}$ at $\theta = 0$.

$$Q = \frac{\sigma_{\theta\theta} - \sigma_{\theta\theta;MBL}}{\sigma_y} \text{ at } \theta = 0 \qquad 7.2$$

Here the reference stress field $\sigma_{\theta\theta;MBL}$ is obtained from a Modified Boundary Layer (MBL) model which is in plane strain conditions representing small scale yielding (SSY). The MBL solution offers a good correspondence with the HRR solution but is more realistic for the analysis of elastic-plastic conditions since the HRR solution assumes fully plastic material behavior.

Along with the Q parameter, the hydrostatic stress ahead of the crack tip can be determined using the additional Q_m parameter. Verstraete et al. [161] have reported that Q and Q_m yield similar values though Q_m is believed to capture out of plane constraint effectively. This is also pointed out in [162]. Neimitz et al. [163] explain that during cleavage and/or ductile failures, in-plane constraint is of major importance while the out-of-plane constraint is significant during ductile failure only. The parameter Q_m is calculated as follows:

$$Q_m = \frac{\sigma_m - \sigma_{m;MBL}}{\sigma_y} \text{ at } \theta = 0 \qquad 7.3$$

Researchers have assessed crack tip stress fields and their effect on crack tip constraint in mismatched welds. Burstow et al. [140, 164] have assessed the effect of material mismatch on crack tip stress fields by modifying the *T*-stress parameter around the crack tip. They found that there is a significant effect of weld strength mismatch. The effect of level of mismatch, the width of the weld and applied load has been accounted for. Similar assessment of crack tip stresses and quantification of constraint was performed by Verstraete et al. [161] utilizing *J-Q* theory and stress triaxiality parameter h which acts as an alternative to Q_m. The correlation between Q and h can be found in [165].

In spite of these assessments, there is a lack of understanding of the stress fields arising due to weld heterogeneity or mismatch at low crack tip constraint conditions. This understanding will be crucial to further investigate the plastic deformations in a welded specimen. Štefane et al. [95] have studied the effect of weld heterogeneity on the crack tip constraint and in turn toughness, and the effect of mismatch on crack tip constraint. This assessment was performed for high constraint conditions in SE(B) specimens.

Hao et al. [9] used the analytical slip line solutions to determine the crack tip constraint in undermatching and overmatching welds. They used a *Q* parameter to describe the effect of mismatching on the stress fields around the crack tip within a Center Cracked Tension (CCT) loaded panel. They utilized a CCT specimen to perform this analysis because its crack tip is at high constraint condition. Using fully plastic conditions, they estimated the *Q* constraint factor near the crack tip using slip line solutions. They pointed out that the mismatched cases result in altering of fracture toughness and deformation capacity of the material.

BS 7910 [21] mentions the importance of invoking the constraint analysis to determine the optimal fracture toughness at low crack tip constraint conditions. The standard also acknowledges the difficulty in ascertaining the level of crack tip constraint effects. One of the reasons for this difficulty is strength mismatch which leads to changes in plastic deformations resulting in ineffective estimations of crack behavior. However, the influence of weld material heterogeneity on plastic deformations and crack tip effects are unavailable and the effect is not quantified.

Given the known effects of weld strength mismatch on crack tip constraint, it is reasonable to assume that there is a lack of assessments on stress-strain variations at the crack tip for different weld geometries. An understanding of the relation between the stresses around the crack tip with the global behavior (plastic deformations and/or collapse which can be explained using the concept of slip line field theory) of a weld would aid in establishing fracture toughness of an heterogeneous welded connections more effectively. This understanding would facilitate the determination of crack tip stresses through experimental methods like Digital Image Correlation (DIC) or the numerical models involving heterogeneous material properties as seen in *Section 5.4* without the need for any additional constraint analysis. Thus, the heterogeneity effects for fracture toughness can be observed on welds with minimum assumptions and simplifications.

This chapter is aimed at understanding two aspects of a SE(T) specimen behavior:

- The relation between *Q* parameter (crack tip constraint) with respect to the crack driving force (J integral) in a bi-metallic weld. This assessment shows the influence of varying material properties (of root and cap) on crack tip constraint behavior which relates to the fracture toughness. This will be

achieved through the analysis of J-Q curves obtained through numerical simulations of the welded SE(T) configurations.

- Establishing the relation between the global plastic deformations and the crack tip stresses starting with the considered bi-material weld configurations. This aids in the establishment of a unified procedure to understand fracture toughness at the crack tip using the Q parameter and global plastic collapse in a bi-metallic weld using slip line field theory. A theoretical relation is obtained to relate slip lines with the crack tip constraint parameter. This relation is further assessed through numerical simulations.

In this chapter, *Section 7.2* explains the theory behind the analysis of crack tip constraint and its relation with slip lines originating from the crack tip. *Section 7.3* describes the methodology used in this research. The details of the weld configurations used for the study and its importance are explained. The results are discussed in *Section 7.4* and the chapter is concluded in *Section 7.5*.

7.2. The relation between slip line and crack tip constraint

The fundamental theory for analyzing the stress-strain state around the crack tip is taken from O'Dowd and Shih [66, 67] as explained in *Equations 7.1 and 7.2*. The theory was briefly outlined in the previous section. In this section, the focus is on understanding the relationship between the *Q* parameter and the slip line angle.

Based on the explanations of slip lines and *J-Q* theory from Hao et al. [9], the procedure (for extreme undermatching) to obtain limit loads and stress distribution analytically was obtained using the Prandtl stress field. Slip lines were determined for Center Cracked Tensile (CCT) specimens as shown in *Figure 84*. They consider a case of extreme undermatching $((W-a) > (3.88+2\pi+\sqrt{2})H)$ to obtain an expression for the stress state at the crack tip. The region OBCD consists of α and β categories of slip lines (recall *Section 5.3*) which are further considered to derive the limit load. This basis has been used by several researchers to describe stresses around the crack tip and relate to slip line field theory [70, 72, 164, 166].

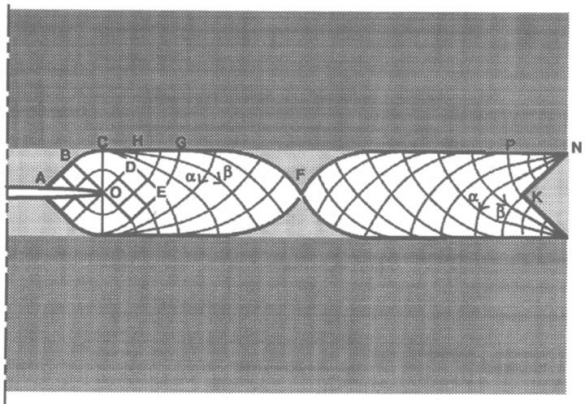

Figure 84: Slip line fields for undermatching cases as seen in Hao et al. [9] which is an example to derive stress distribution using the Prandtl field.

Here SE(T) specimens are considered for understanding the stress fields arising from the crack tip at low constraint conditions and the effect of weld heterogeneity. The heterogeneity in the weld is applied in the form of a bi-material weld, which has two different regions in root and cap. The question arises about the suitability of the methods formerly discussed to describe the effect of crack tip stresses on the deformation patterns and slip line angle in an SE(T) specimen having a bi-material weld. This is due to the fact that the slip lines are very narrow as can be seen in *Figure 73*, and the deformation is not confined in the weld metal itself as shown in *Figure 84*.

The investigations in this chapter are based on a simplified case of a heterogeneous weld i.e. bi-material; the motivation for which is drawn from reference [9]. Hao et al. [9] recognized the deviations of slip lines as they cross the interface between two materials as shown in *Figure 85 (a).* This figure shows the α and β slip lines in two different surfaces represented by + and -, deviating as they hit the interface L at the points A and b. Using the stress components along the slip line, they deduced a general solution that resulted in a slip line field as shown in *Figure 85 (b).* Parameters r_1 and r_2 are the radii of the slip lines at the interface resulting from the material changes. In this thesis, this solution is not explained further and only the concept of discontinuities is taken to examine this discontinuity numerically and to find the slip line angle θ_{tip} as shown in *Figure 86*.

Hertelé utilized the concept of the slip line angle deviation from Hao et al. [9] and plasticity concepts to describe the relation between crack-tip stresses and the slip line angle. A homogeneous weld is assumed having a strength mismatch with respect to the base material. This assumption is made to reduce the complexity of the bimetallic weld initially and to understand the *J-Q* relation of a homogeneous weld. Validation of this relation will act as a motivation to extend this analysis towards bi-metallic welds.

To begin with, the slip line trajectory is plotted in *Figure 86*. An α slip line originating from the crack tip at an angle θ_{tip} with respect to the x-axis passes through the fusion line making two arcs with radii r_1 and r_2 as in *Figure 85 (b)*. This gives rise to angle θ_w for the weld region and θ_b as it enters the base material and then goes up to the surface of the specimen at an angle θ_c (*Figure 86)*

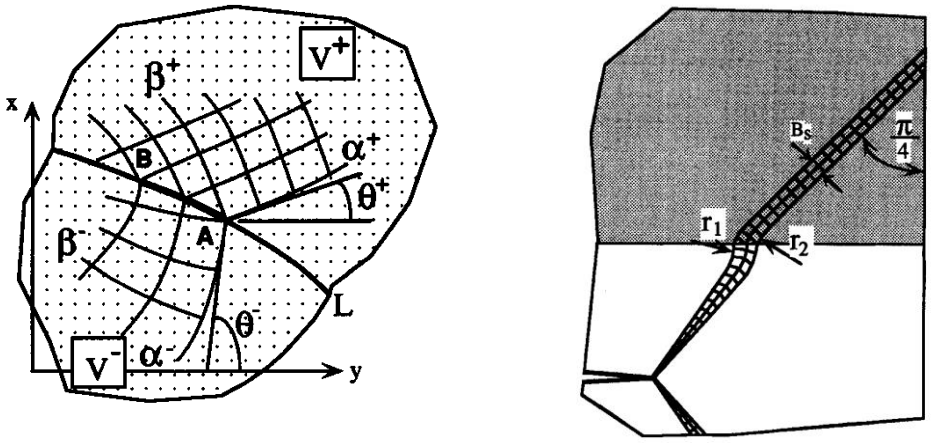

(a) (b)

Figure 85: Hao et al. [9] show (a) a graphical explanation of the slip line discontinuity at an interface and (b) general solution of the slip-line field for over- or undermatching welds.

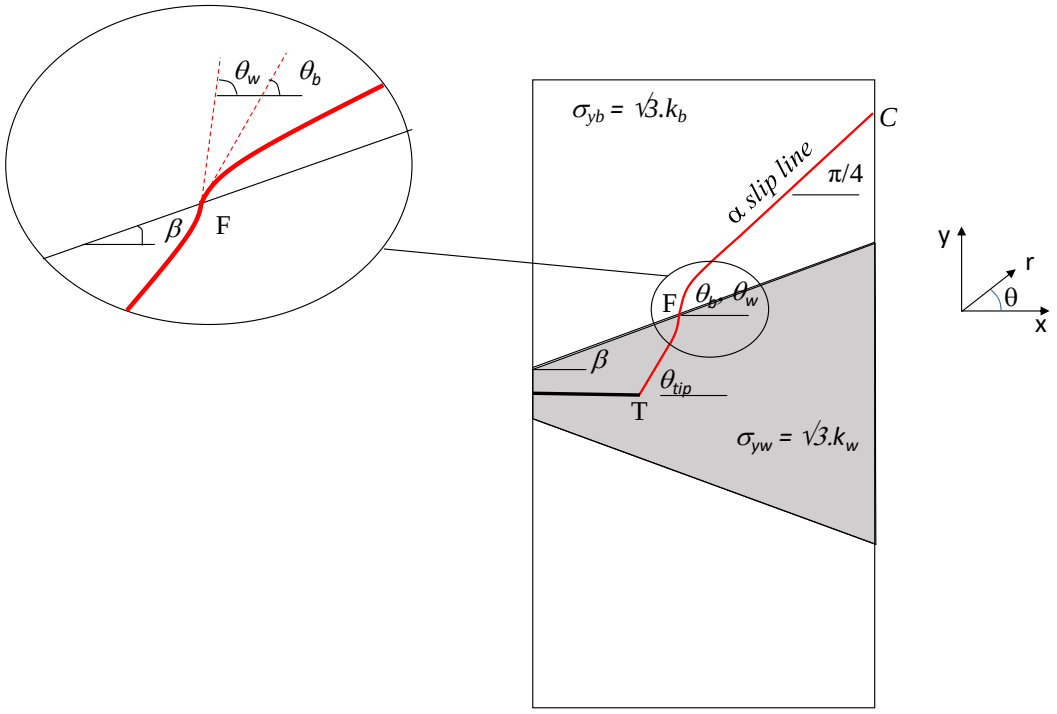

Figure 86: Slip line trajectory in a bi-material SE(T) specimen

It is known that the slip lines are parallel to the axes of the principal stress in a solid. In 2D plane strain conditions, the Lévy-Mises criterion implies that hydrostatic stress σ_m is equal to $(\sigma_1 + \sigma_2)/2$, the average of both in-plane principal stress components.

The relation governing the hydrostatic stresses can be explained through Hencky equation for a α-slip line, which is as follows,

$$-\sigma_m + 2k\theta = constant \tag{7.4}$$

with k the local shear yield strength (k_b for base material and k_w for weld material) and θ the angle of the slip line with respect to the x-axis.

It is known that the slip line is always at 45° at a free surface boundary, i.e. point C of *Figure 86.* This results in

$$\theta_c = \frac{\pi}{4} \tag{7.5}$$

Referring back to *Section 5.2*, $\sigma_1^C = 2k_b$ and $\sigma_2^C = 0$, thus $\sigma_m^C = k_b$.

Two relations between distinct slip line angles and hydrostatic stresses can be put forward, based on *Equation 7.4*:

$$\sigma_m^{F,b} - k_b = 2k_b\left(\theta_{F,b} - \frac{\pi}{4}\right) \tag{7.6}$$

$$\sigma_m^{F,w} - \sigma_m^T = 2k_w\left(\theta_{F,w} - \theta_{tip}\right) \tag{7.7}$$

Where $\theta_{F,w}$ and $\theta_{F,b}$ are slip line angles in base and weld regions and $\sigma_m^{F,w}$ and $\sigma_m^{F,b}$ are hydrostatic stresses in base and weld regions respectively. Further, $\theta_{F,w}$, $\theta_{F,b}$, $\sigma_m^{F,w}$ and $\sigma_m^{F,b}$ are related through relations for a slip line crossing a material interface developed by Hao et al. [9]. This relation can be expressed as follows for a specific use of *Figure 86*:

$$\sigma_m^{F,b} - k_b \sin 2\left(\theta_{F,b} - \beta\right) = \sigma_m^{F,w} - k_w \sin 2\left(\theta_{F,w} - \beta\right) \tag{7.8}$$

$$k_b \cos 2\left(\theta_{F,b} - \beta\right) = k_w \cos 2\left(\theta_{F,w} - \beta\right) \tag{7.9}$$

with β the fusion line angle.

It is clear that finding an analytical solution for the equations above is highly challenging, due to the non-linear nature of *Equations 7.7 and 7.8*. Since the main goal of this derivation is to indicate a qualitative (rather than quantitative) influence

of slip line angle on crack tip constraint, it is assumed for the following that the slip lines (deformation bands) traverse through the fusion line from both sides at an angle of around 45°:

$$\theta_{F,b} - \beta \approx \theta_{F,W} - \beta \approx \frac{\pi}{4}. \quad 7.10$$

In such case, a Taylor series development indicates that the sines in *Equation 7.8* are roughly one and the cosines in *Equations 7.9* reduce to $\cos x \approx -x$. Then *Equations 7.8 and 7.9* respectively become:

$$\sigma_m^{F,b} - k_b \approx \sigma_m^{F,w} - k_w \quad 7.11$$

$$k_b(\theta_{F,b} - \beta) \approx k_w(\theta_{F,w} - \beta) \quad 7.12$$

or, by restructuring *Equation 7.12*:

$$k_b\theta_{F,b} - k_w\theta_{F,w} \approx \beta(k_b - k_w) \quad 7.13$$

Substituting $\sigma_m^{F,b}$ and $\sigma_m^{F,w}$ in *Equation 7.11* using *Equations 7.6 and 7.7* yields:

$$2k_b\left(\theta_{F,b} - \frac{\pi}{4}\right) \approx \sigma_m^T + 2k_w\left(\theta_{F,w} - \theta_{tip} - \frac{1}{2}\right) \quad 7.14$$

which, using *Equation 7.13*, leads to:

$$\sigma_m^T \approx k_w - 2k_b\left(\frac{\pi}{4} - \beta\right) + 2k_w(\theta_{tip} - \beta) \quad 7.15$$

Equation 7.15 predicts that, as the slip line angle θ_{tip} increases, the hydrostatic stress increases linearly. Note that for homogeneous SE(T) specimens $k_b = k_w$ and $\beta = 0$, and since θ_{tip} would be 45°, *Equation 7.13* would indicate that $\sigma_m^T \approx k_w$ as expected from the analytical solution for a homogeneous specimen.

From *Equation 7.1* it can also be seen that σ_m^T is linearly proportional to $Q_m\,\sigma_{yw}$. According to von Mises criterion, critical shear stress can be expressed as $k_w = \sigma_{yw}/\sqrt{3}$. Based on these assumptions, the value Q_m is directly proportional to $2/\sqrt{3}$ times the angle θ_{tip} expressed in radians. The above is further analyzed using numerical simulations. The Q_m the parameter is compared with the angle $\theta = \theta_{tip}$ for different weld configurations and the outcome is analyzed for its compatibility with the analytical formulation. As mentioned in the previous section, Verstraete et al. [161] and others have reported that the parameters Q and Q_m yield similar values although Q_m is believed to capture out of plane constraint effectively. Based on these assumptions the relation between Q and θ is also assessed.

7.3. Analysis methodology

The bi-metallic welds considered for the analysis in this chapter are the same 8 configurations introduced in *Section 6.2.3*, as illustrated and reiterated in *Figure 87*. The material properties in the base, cap, and root of the weld are also identical to *Section 6.2.3*. The notch is assumed to be positioned in the weld metal center. Additionally, a strain hardening exponent *n* having 3 different values *10, 15 and 20* was introduced for root and cap material. Introducing strain hardening exponent *n* will have a further realistic effect on material behavior which helps in better understanding of the *J-Q* parameters and its effect on deformation bands. Also, from the results in *6.2.4,* for different material configurations, it was seen that the deviations of the slip line angle θ away from 45° were not evident in elastic-perfectly plastic material.

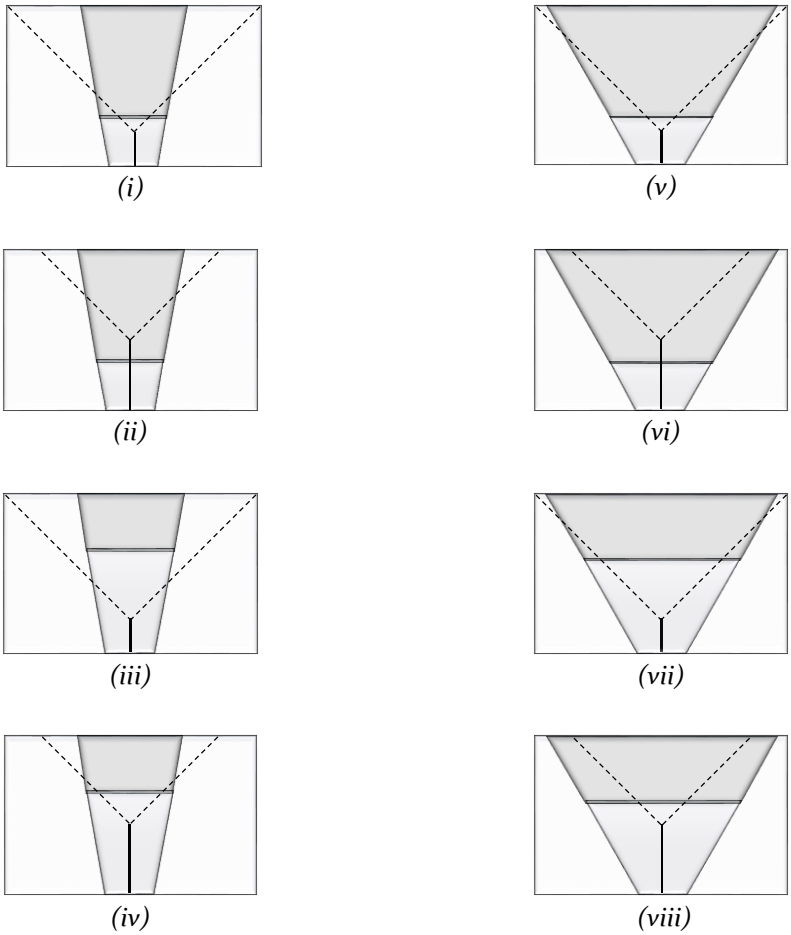

Figure 87: 8 weld configurations used in this study

The methodology to determine the *J-Q* curves is mentioned in *Section 7.3.1* and *Section 7.3.2* explains the method of determining slip line angle θ to plot against the *Q*-parameter.

7.3.1. Determination of J-Q curves

For the analysis of *J-Q* curves, *Q* is determined using *Equation 7.2.* In this equation, $\sigma_{\theta\theta}$, $\sigma_{\theta\theta,MBL}$ and σ_y are required parameters to find Q.

2D SE(T) simulations are post-processed to obtain the crack tip opening stress $\sigma_{\theta\theta}$. Small scale yielding (SSY) conditions are used to calculate the *Q* parameter. This method has good correspondence with the HRR solution [161] and has been frequently done using a Modified Boundary Layer (MBL) model in-plane strain conditions having a similar mesh around the crack tip as in the SE(T) model. This model as shown in *Figure 88* was used to obtain $\sigma_{\theta\theta,MBL}$; the details of the MBL model have been explained in reference [161]. The material (stress-strain) properties of the MBL model are equal to those of the material surrounding the notch tip of the SE(T) configuration. An initially blunted crack is modeled with a notch tip radius of 2.5 μm. The outer radius is 10^6 times the notch tip radius. This large outer radius prevents the interaction of plasticity effects with the applied linear elastic boundary conditions. The FE model is a 2D model that consists of plane strain linear elements with reduced integration (CPE4R).

The validity of the *Q* calculations is evaluated by comparing the reference stress field obtained from an MBL model and the actual crack tip stress field obtained from the SE(T) model. This is commonly performed through a comparison of the *Q*-parameters calculated at normalized distances ahead of the crack tip [167, 168], which is given by

$$\Delta Q = \frac{|Q_{r=1} - Q_{r=5}|}{4} \qquad 6.16$$

Published results indicate that the difference must be smaller than 0.1 to obtain a description that is sufficiently independent of the radial distance from the crack tip [161].

Crack driving force in terms of J-integral was extracted using the domain integral method, considering the 22nd contour of the radial mesh surrounding the crack tip. The standard deviation between values of the last ten contours did not exceed 1.5% of their average, indicating a path (domain) independent J value[10]. Using the values of Q and J, graphs are plotted with J on the ordinate and Q on the absissa.

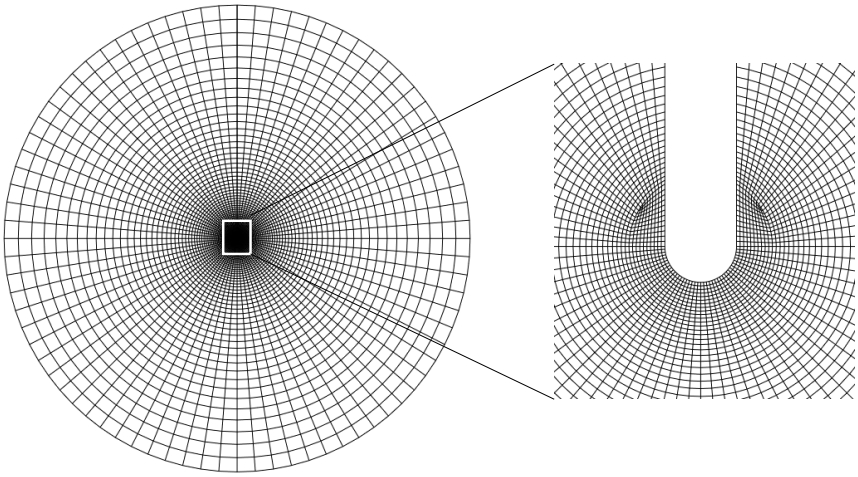

Figure 88: Mesh configuration of Modified Boundary Layer (MBL) model

7.3.2. Determination of slip line angle

The slip lines are assessed based on the deformations bands obtained in the numerical simulations. The procedure to determine these deformation bands is explained in *Chapter 5*. In addition to the determination of the points of maximum equivalent plastic strain (PEEQ) which depict the deformation bands, the angle of these bands is calculated as per the plot is shown in *Figure 89*. A linear regression line was plotted along with the maximum equivalent plastic strain (PEEQ) points that lie within the weld region. The angle between this linear regression line and the vertical is the slip line angle θ.

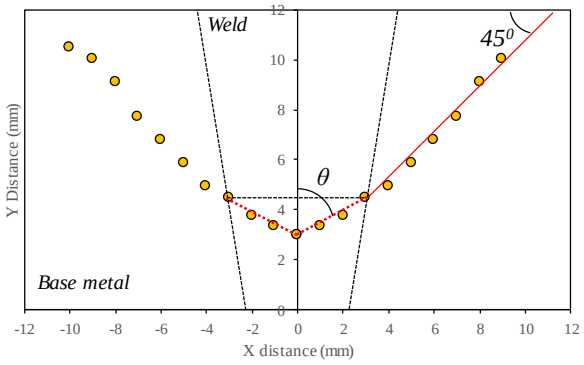

Figure 89: Determination of slip line angle θ for understanding its relation with the Q parameter.

This calculation method is in line with the theory proposed by Hao et al. [9] showing the discontinuity of slip lines crossing the interface. After obtaining θ and Q for all considered SE(T) specimen configurations, a Q - θ scatter plot is obtained to assess the hypothesized relation between Q and slip line angle θ numerically and according to the theory explained in *Section 7.2*.

7.4. Results and discussions

7.4.1. Analysis of J-Q curves

The *J-Q* curves obtained for the 8 configurations with each having 45 variations (in yield strength of cap and root, strain hardening exponent) have been scrutinized. This assessment resulted in 72 *J-Q* plots and not all of them are shown in this chapter for the sake of brevity but an explanation of the trends is explained in detail by utilizing representative plots.

For configurations *ii* and *iv*, σ_y represents the yield strength of the weld cap and for the other configurations σ_y represents root yield strength.

Each plot is shown in *Figure 90 and Figure 91* represents the different variations in the yield strength of root and cap, and strain hardening exponent of the simulated SE(T) specimens. Each plot has 5 different variations of cap yield strength denoted by (.)1, (.)2, (.)3, (.)4, (.)5 for 425, 500, 575, 650 and 725 N/mm² respectively while the root yield strength and strain hardening exponent is maintained constant as mentioned in the previous section. The yield strength of the root (425 N/mm², 500 N/mm², and 575 N/mm²) is given by the letters *a, b and c* for a strain hardening exponent *n=10*. For *n=15*, it is denoted by *d, e, and f* while for *n=20*, it is denoted by *g, h and i*.

To begin with, the effect of strain hardening is studied for all configurations. This analysis mostly showed that there is a reduction in the *Q* parameter with an increase in strain hardening exponent. Additionally, with an increase in strain hardening, the sensitivity of *J-Q* curves to cap yield strength increases. The J-Q curves are shown for the range up to 350 N/mm². This range was chosen so that all the curves lie within the validity conditions used to calculate Q values. This also facilitates in choosing a J value for assessing the influence of strain hardening, fusion line angles and later the slip line angles on the Q parameter. The analysis of the effects of strain hardening is made in two parts – fusion line angles $\beta=10^o$ and $\beta=30^o$. The plots in *Figure 90 and Figure 91* show the results of the SE(T) simulations for $\beta=10^o$ and $\beta=30^o$. These results had a root yield strength of 425N/mm² and a varying cap yield strength as explained before. *Figure 90* shows three plots for the same *configuration i* with three strain hardening exponents 10, 15 and 20, while the other plots show the cases for *n* equal to 10 and 20 for configurations *ii, iii, and iv*. *Figure 91* shows *J-Q* plots for different strain hardening values of 10 and 20 for configurations *v-viii.*

From the *J* versus *Q* plots obtained from all simulations, the initial observation shows that the *Q* values tend to become more negative with an increase in strain hardening exponent. This was clearly evident in *Figure 90* and *Figure 91.* However, the amount of change of the *J-Q* curve due to change in strain hardening exponent is configuration dependent. For the five different variations of cap yield strength and

constant root yield strength, the change in strain hardening exponent resulted in a shift of Q value from -0.3 to -0.6. These values were obtained for a range of J values from 100-200N/mm. This range was chosen as it was within the validity criteria for the J-Q curve when $r/(J/\sigma_0) = 2$ for all chosen configurations. As expected, for $n=15$, the shift in Q values was half of the shift observed when $n=20$.

Configurations *i-iv* had a cap width of $2H_c = 9mm$ while the configuration *v-viii* had cap size of $2H_c = 18mm$. As the area of the cap of a weld increases, the stresses in the global model $\sigma_{\theta\theta}$ the increase compared to the MBL model stresses $\sigma_{\theta\theta;\,MBL}$. This leads to an increase in Q values for different levels of yield strength in the cap region. However, the Q values were reduced as the root yield strength increased whilst maintaining the cap and strain hardening exponent. The effect of material variations in the root region is observed in the MBL model and also in the global level of SE(T) specimen. In the case of configurations *ii* and *vi,* the root yield strength variations did not have any influence on the Q parameter as the notch tip lies in the cap region. Certain discontinuities can be observed from the J-Q plots. Q sometimes becomes more negative and then increases again and then decreases again like in the plots of *configuration v and viii*. Kinks are observed in the plot of *configuration iii*. These variations can be attributed to the change of stress from the root of the weld to the cap. This is a direct consequence of having a different material in root and cap regions. From this analysis, the effect of changes in Q due to strain hardening variations is further studied in the slip line angle θ in the next section.

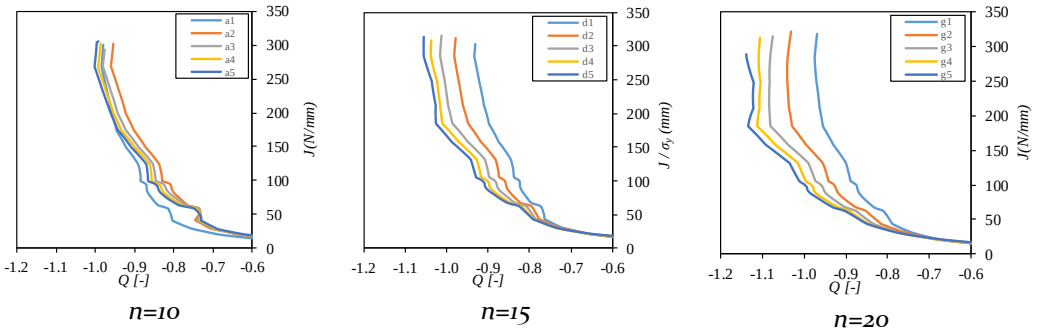

n=10

n=15

n=20

Configuration i

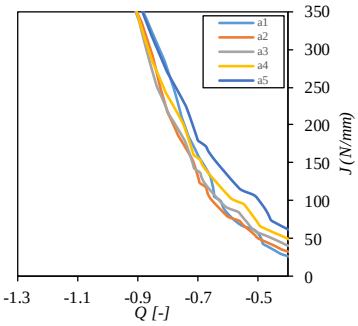

n=10

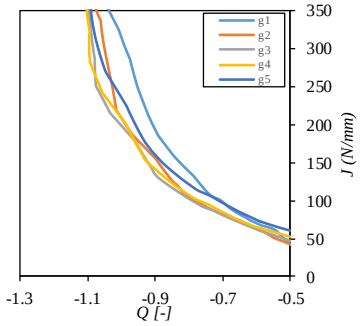

n=20

Configuration ii

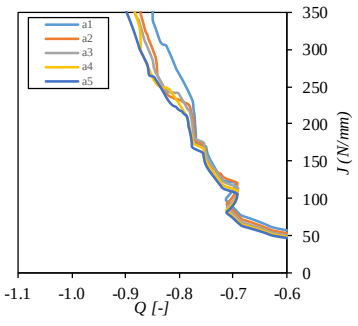

n=10

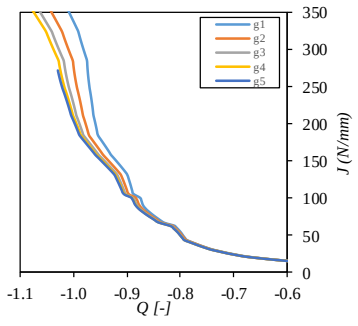

n=20

Configuration iii

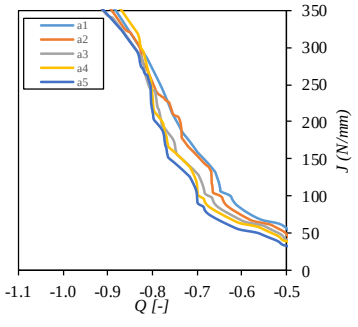

n=10

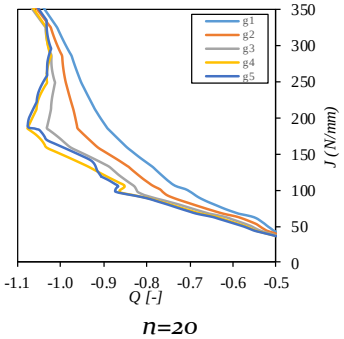

n=20

Configuration iv

Figure 90: J-Q plots for ***configurations i-iv*** *showing strain hardening variations for a root yield stress of 425N/mm²* while cap yield stress varied from 425 to 725 N/mm² in steps of 75N/mm² denoted by (.)1, (.)2… (.)5.

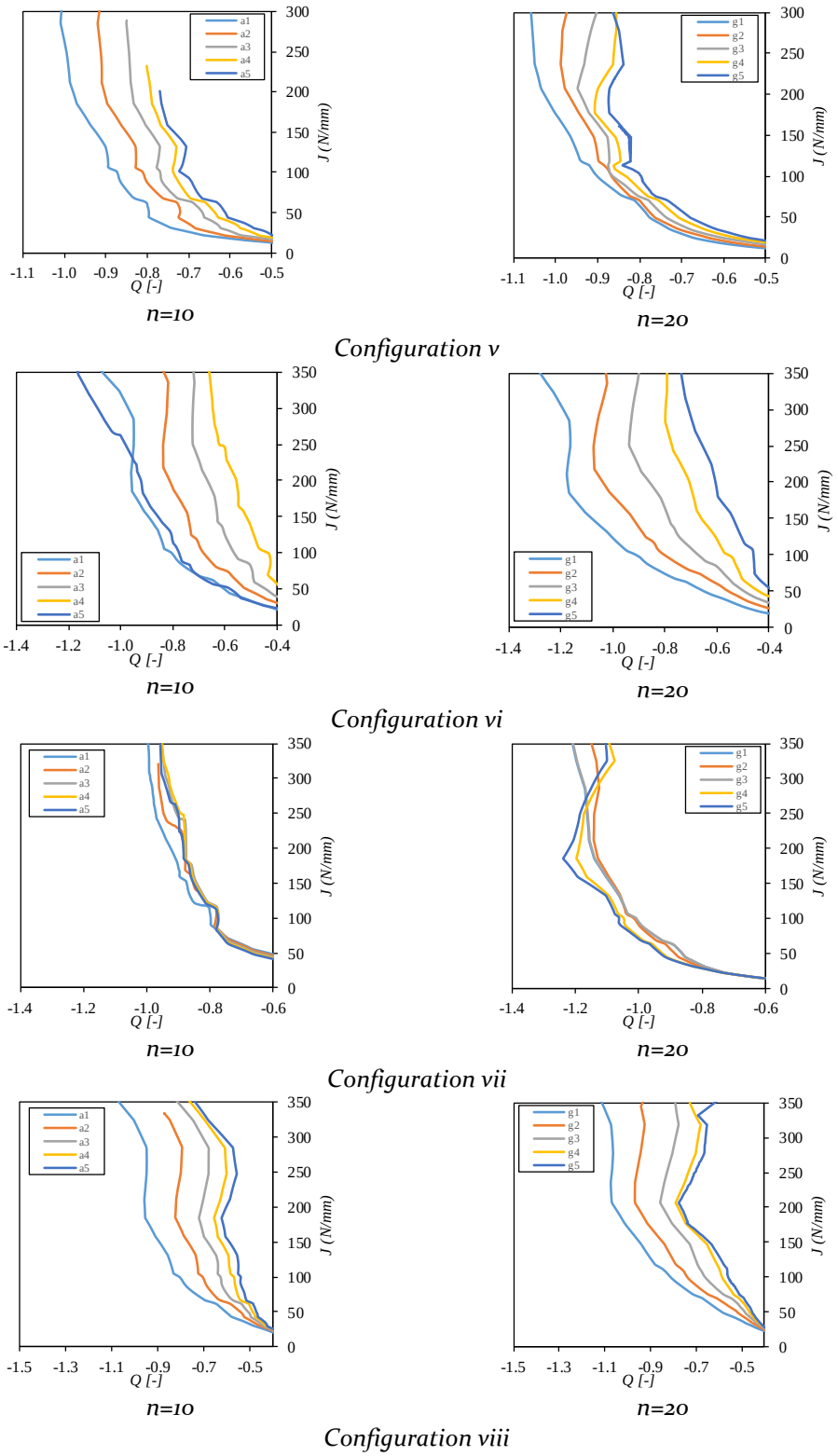

Figure 91: J-Q plots for ***configurations v-viii*** *showing strain hardening variations for a root yield stress of 425N/mm²* while cap yield stress varied from 425 to 725 N/mm² in steps of 75N/mm² denoted by (.)1, (.)2… (.)5.

7.4.2. The relation between slip lines and Q parameter

After analyzing the *J-Q* behavior of the SE(T) model with different weld configurations used in this chapter, the coupling of the *J-Q* theory and the slip line angle originating from the crack tip is assessed in this section.

The simulations performed for the assessments of the *J-Q* curve were utilized to understand the relation between the deformation bands and in turn slip lines with the *Q* parameter. As described in Section 5.4.1, the $\varepsilon_{eq,pl-max}$ points were obtained for all 8 configurations at a value *J* = 200N/mm. The reason for choosing this value of *J* is to set a constant position where the comparison could be made for all eight weld configurations without moving into the invalid region (when $r/(J/\sigma_0) = 2$) of the $J - Q$ curve. Setting *J* = 200N/mm² keeps the analysis within the validity conditions. At this value of *J, Q* values were chosen and at that increment of displacement in SE(T) simulations, the $\varepsilon_{eq,pl-max}$ points were extracted. The angle of the slip line θ was determined by selecting the points up to the weld fusion line as explained in *Section 7.2* and shown in *Figure 89*. This was chosen in accordance with the theory explained in.

Among 8 configurations, configurations *i, v,* and *viii* are chosen to display the evolution of the slip line angle and observe the pattern of change due to the influence of yield strength variations in root and cap. The plots are shown for three different root yield stress values (named (a), (b) and (c)) in *Figure 92, Figure 93* and *Figure 94*. Each plot contains curves corresponding to 5 different variations of cap yield stress. From *Figure 92, Figure 93* and *Figure 94*, the variation in cap yield strength has a quantifiable effect on the deformation patterns in SE(T) specimens. The plastic collapse occurs in the weaker section of the specimen. As the yield strength of the cap increases, resistance is offered towards the deformation band forcing it to flow in the weaker root region and then to the base material. In other words, the angle θ increases with an increase in weld cap strength.

A plot of θ versus *Q* is obtained for all 8 configurations considered in this chapter. As seen in the previous section in *Figure 90* and *Figure 91, Q* is influenced by strain hardening. Thus two sets of *Q*-θ plots were obtained for strain hardening values 10 and 20. Plots shown in *Figure 95(a)* are for a fusion line angle β = 10°, i.e the configurations *i-iv and Figure 95 (b)* corresponds to an angle β = 30° for configurations *v-viii* at strain hardening value of 10.

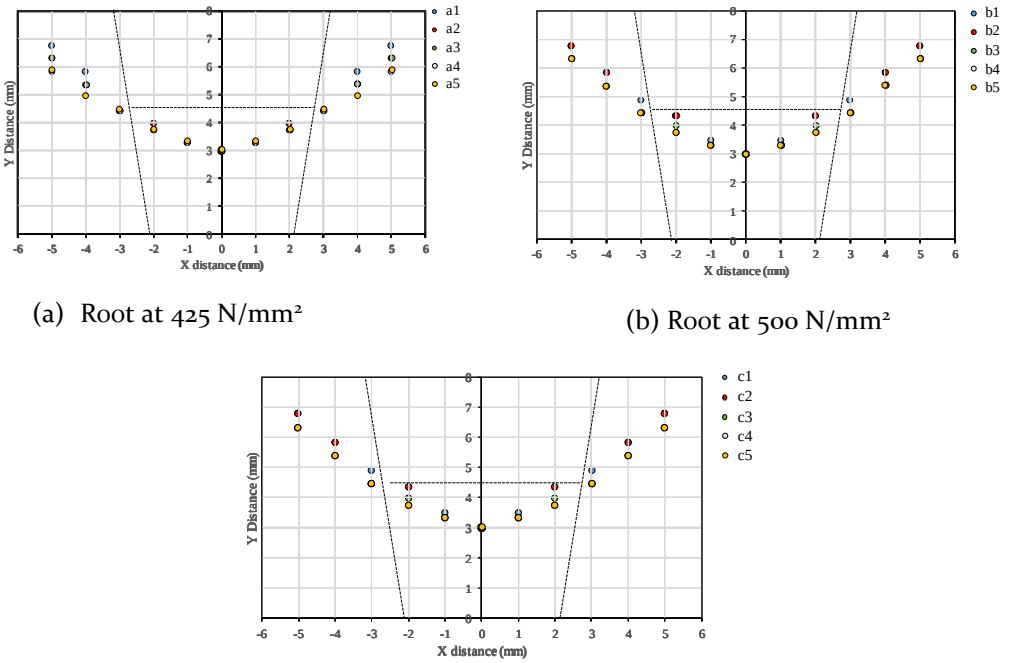

(a) Root at 425 N/mm²

(b) Root at 500 N/mm²

(c) Root at 575 N/mm²

Figure 92: The points of $\varepsilon_{eq,pl-max}$ depicting slip lines are shown for configuration i. The dotted lines show the boundary of the fusion line and the region of the cap and root.

For the fusion line angle β = 10°, slip line angles are influenced by the changes in material properties in the root and cap region. However, the variations in Q for the chosen set of J-values and that particular increment of displacement did not yield high variations; the maximum change is limited to 0.01. Due to this result, a direct relationship of the slip line angle with Q could not be observed. Thus, the theoretical outcome of this section could not be explained through the numerical simulations. In order to further assess the configurations where β = 10°, Q and θ at J=300N/mm and 400N/mm were additionally obtained. The outcome showed similar trends as seen in *Figure 95(a)*. However, the angle θ was taken at a higher interval of deformations applied during simulations 94but this did not result in a change in angle. The Q value was 0.2 lower than in *Figure 95(a)* but no change in the general trend of the plot could be observed. A similar observation was made for configurations *i-iv* when *n=20 Figure 96(a).* The points shifted to a more negative Q value but the trends did not show a larger change which could explain the trend as per theory put forward in *Section 7.2.*

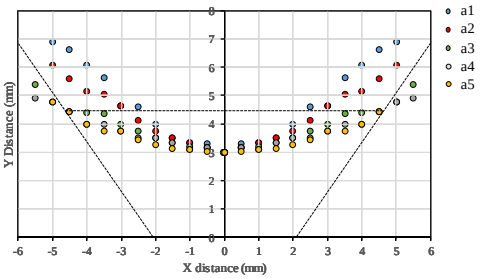

(a) Root at 425 N/mm²

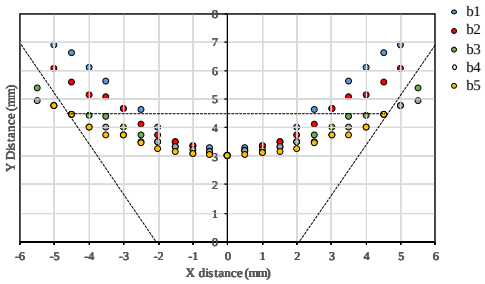

(b) Root at 500 N/mm²

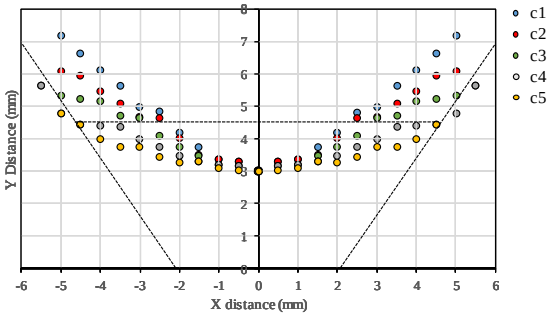

(c) Root at 575 N/mm²

Figure 93: The points of $\varepsilon_{eq,pl-max}$ depicting slip lines are shown for configuration v. The dotted lines show the boundary of the fusion line and the region of the cap and root.

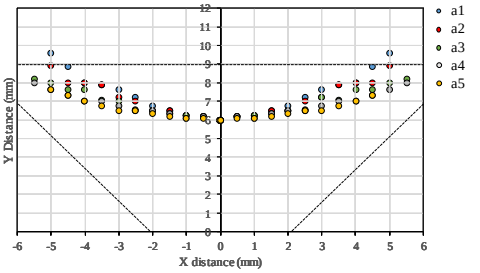

(a) Root at 425 N/mm²

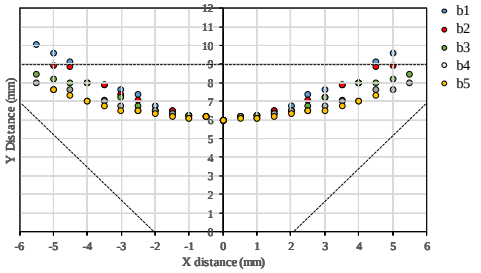

(b) Root at 500 N/mm²

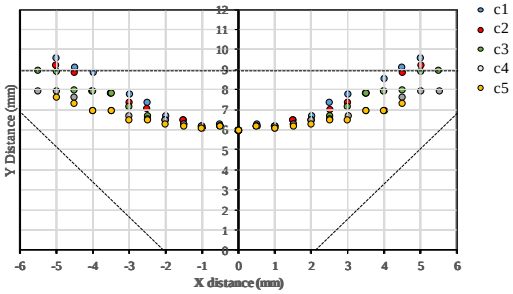

(c) Root at 575 N/mm²

Figure 94: The points of $\varepsilon_{eq,pl-max}$ depicting slip lines are shown for configuration viii. The dotted lines show the boundary of the fusion line and the region of the cap and root.

However, for the fusion line angle $\beta = 30^{o}$, a general trend of increasing slip line angle θ with increasing Q could be observed. According to the theoretical derivation, the Q value should increase with a value -0.2 for every 10^{o} change in slip line angle β. In *Figure 95(b),* this analytical prediction is more evident. In configuration *v* and the angles between 60^{o}-70^{o}, the Q value varied up to -0.16. For angles between 65^{o} to 75^{o}, Q changed 0.1. In configuration *vi*, a change of 10^{o} resulted in a range of Q values starting from -0.12 to -0.19 for different values of the weld material properties. In configuration *vii,* the change of Q was up to -0.08 while for the configuration *viii*, for 10^{o} change in slip line angle, there was an increase in the Q value of -0.4. A similar trend was observed in *Figure 96(b)* for the simulations having a strain hardening exponent $n=20$. For a 10^{o} change in angle (from 60^{o} to 70^{o}), the change of Q was 0.08. For slip line angles greater than 70^{o} there was a variation in Q from -0.3 up to -0.6 for different configurations and a 10^{o} change in slip line angle.

One of the reasons for the discrepancies between the results obtained from the numerical and theoretical approaches could arise due to the assumptions made in the theoretical derivations. The assumption of single material property in the weld region in which the simulations had a bimetallic weld could have an influence on Q parameter predictions. Another could be due to the fact that the fusion line angle was not accounted for theoretical calculations which clearly had influence in numerical simulations. Other reasons which contribute to deviations are the method involved in measuring slip line angle in simulations which could be enhanced by creating a finer grid to extract maximum equivalent plastic strain points and finer mish density around the crack tip.

This analysis further motivates us to study the relationship between the fusion angle β with the Q parameter (crack tip constraint) when the slip line angle is constant. From the considered set of configurations where only the fusion line angle was increased and all other geometric parameters were similar (comparison made between the sets *i-v, ii-vi, iii-vii, and iv-viii*), *i* and *v* had a common θ of 67^{o} for a case of undermatching root (425 N/mm^2) and overmatching cap (500 N/mm^2). At this angle, the Q parameter decreased by 11% when there is an increase of 20^{o} in fusion line angle β. This analysis is based on a small set (3 comparisons) and requires further analysis to validate this outcome by considering different cases of weld geometries other than the ones considered in this thesis.

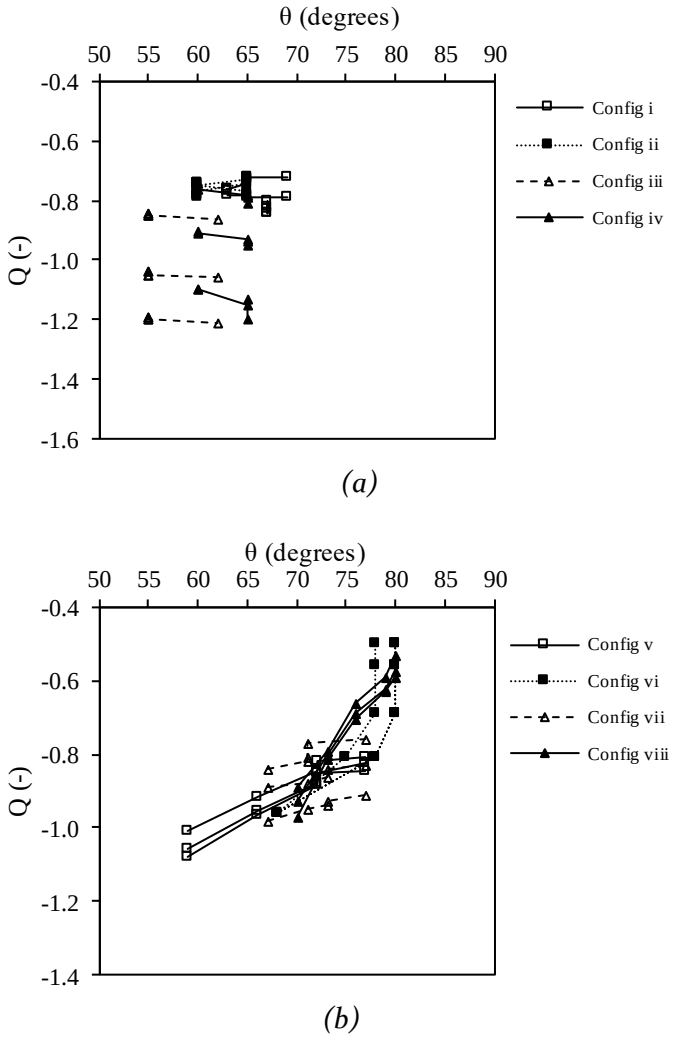

Figure 95: The values of the Q parameter and slip line angle θ during deformations extracted at $J = 200\ N/mm^2$ (a) $\beta = 10^o$ (b) $\beta = 30^o$ for strain hardening exponent of 10.

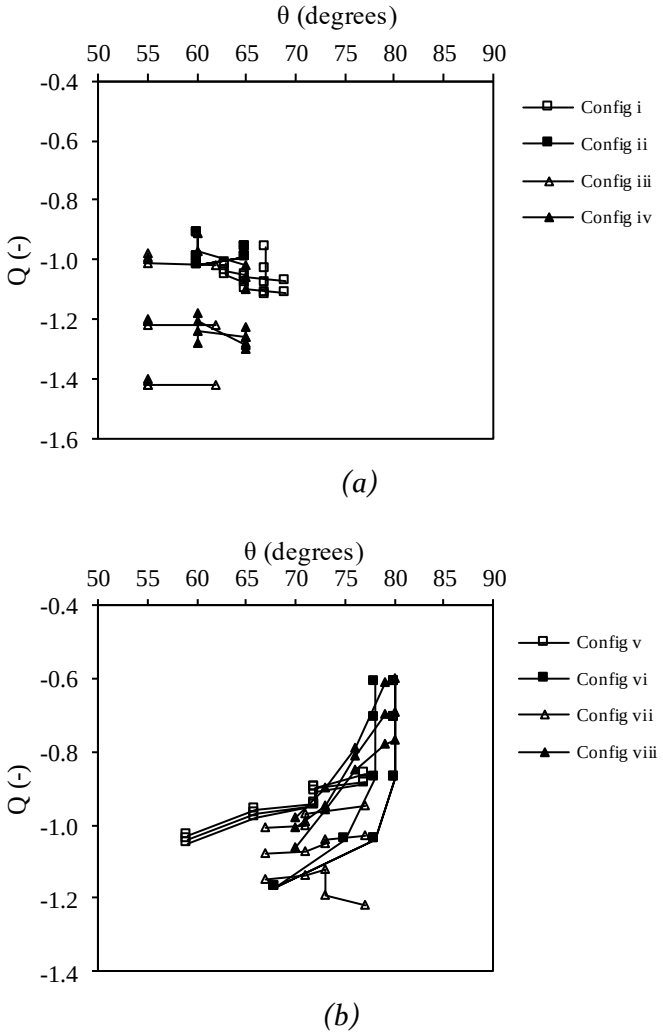

Figure 96: The values of the Q parameter and slip line angle θ during deformations extracted at $J = 200$ N/mm² (a) $\beta = 10^{o}$ (b) $\beta = 30^{o}$ for strain hardening exponent of 20.

In order to assist the assessment of the change in θ during the deformation for the changes in root and cap yield stress values, deformation plots are utilized for all 8 configurations. Here, in *Figure 97,* 16 contour plots (2 for each configuration) are shown, the yield stress of the root was 425 N/mm² and n=10. One plot is shown for the lowest cap yield stress at 425 N/mm² and one for the highest at 725 N/mm² for each configuration. From the plots, it can be understood that the θ points of all configurations having a soft weld region compared to the base material (i.e. yield strengths of root, cap, and base materials were 425 N/mm², 425 N/mm²,, and 500 N/mm² respectively) showed a slip line angle of approximately 45°. The case was similar in the evenmatching welds too (i.e. yield strengths of root, cap, and base materials were 500 N/mm²). As the yield strength of the cap increases, the effect on the deformation pattern is seen, especially for configurations *v* and *viii* and not so much for configurations where $\beta = 10^{o}$

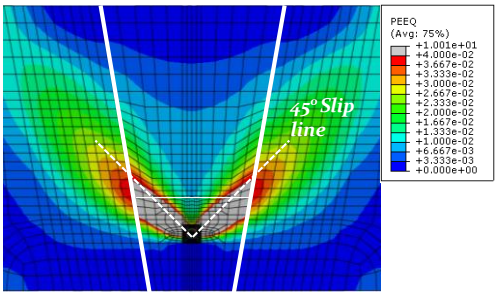

Configuration i – a1

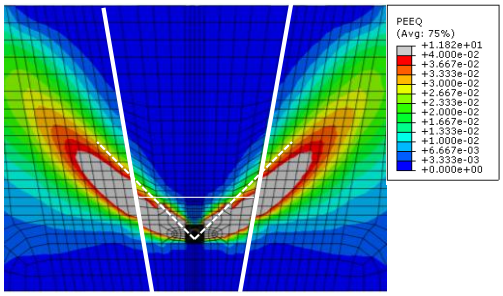

Configuration i – a5

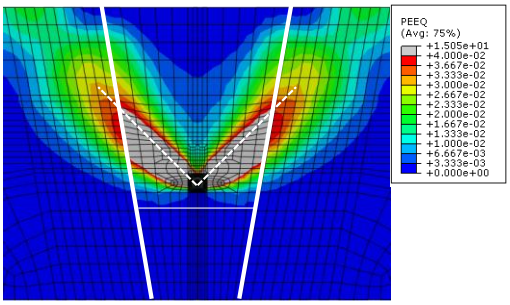

Configuration ii – a1

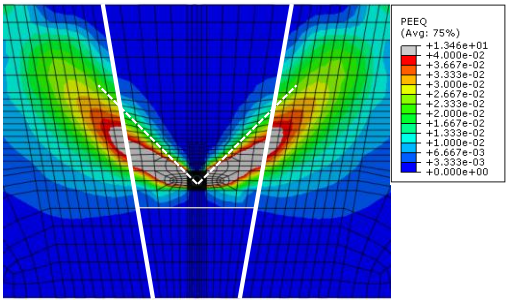

Configuration ii – a5

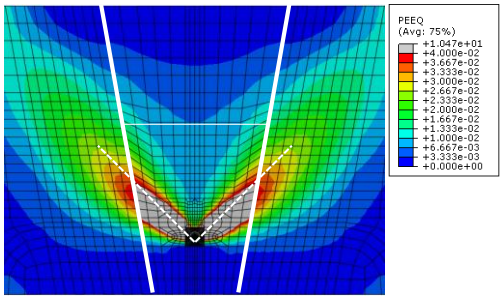

Configuration iii – a1

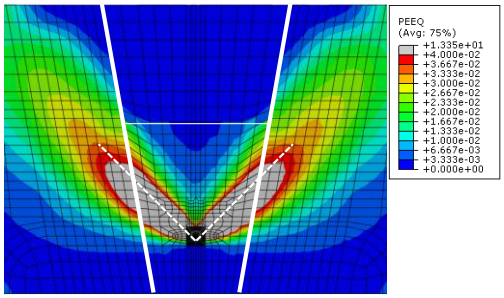

Configuration iii – a5

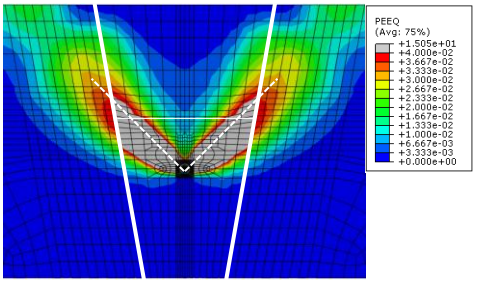

Configuration iv – a1

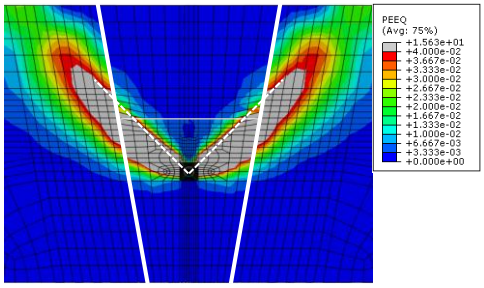

Configuration iv – a5

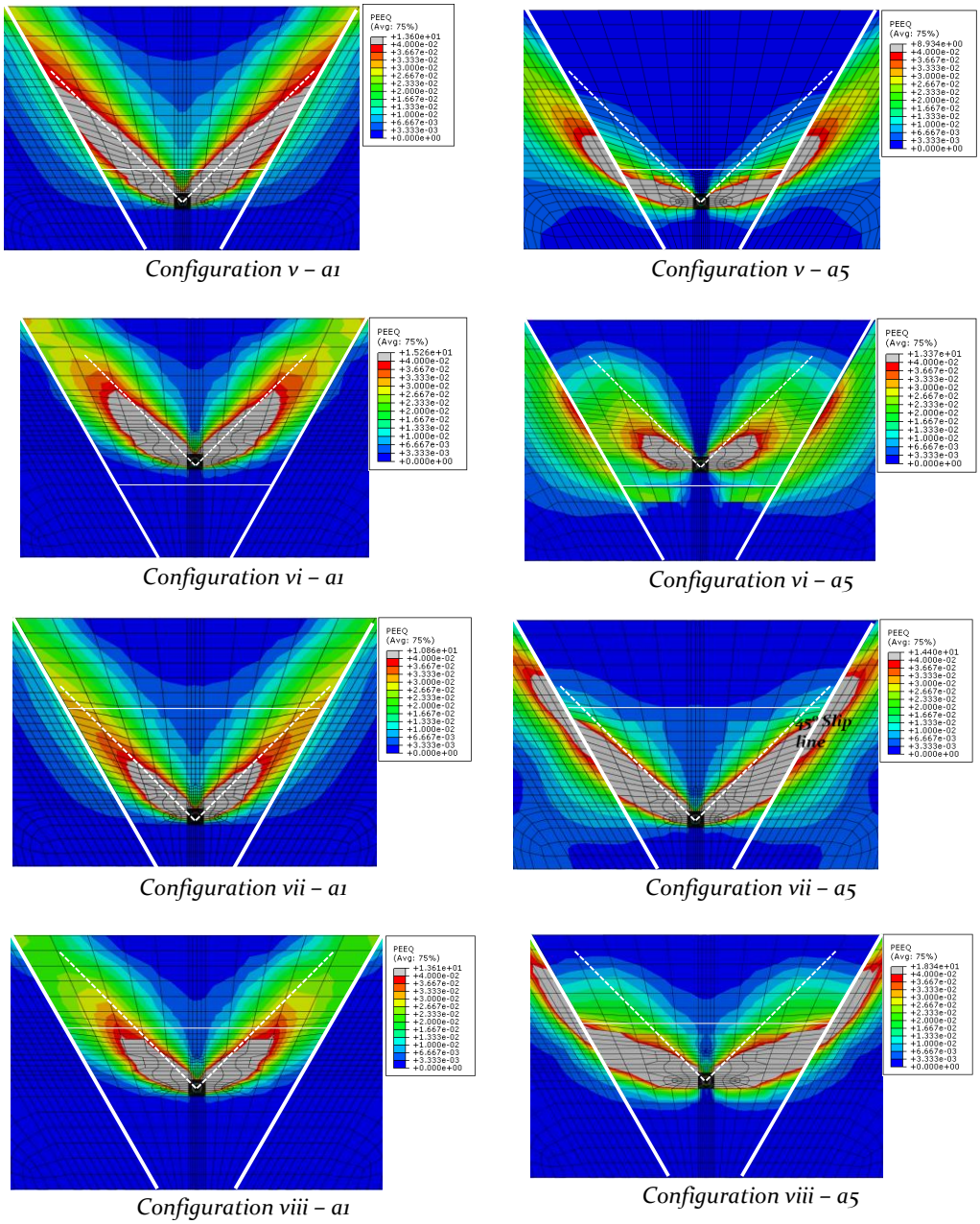

Figure 97: Contour plots showing deformation bands for 8 weld configurations

In configurations *v-viii*, the largest change in θ was observed. The wider cap has a greater influence on the deformation pattern and as the cap becomes stronger than the base material, the deformation flow chooses the closest path towards the base material resulting in θ=75°. For configuration *vi*, when the cap is the hardest, the collapse already begins in the base material before the cap region collapses, which is a direct consequence of weaker base material compared to the cap. However, this effect was not seen in configuration *ii* as the cap area was smaller.

7.5. Summary and conclusions

A thorough analysis of the *J-Q* behavior of bi-metallic welds was performed in this chapter. Eight different weld configurations were considered and different yield stress values for root and cap region of the weld, strain hardening exponent and weld geometries were chosen. From these configurations, a detailed account of the *J-Q* behavior was made and it was adopted to analyze the relation between Q and slip line angle θ. A theoretical relationship between Q parameter and slip line angle θ was developed and subsequently assessed using the numerical SE(T) model.

The results showed that the *J-Q* curves behave differently and are unique for each configuration of weld geometry and material parameters. However, a trend was established and the quantification was made based on the change in Q parameter for a chosen value of J.

For the assessment of slip lines, a hypothesis was derived from numerous simulations that the change in Q parameter is directly proportional to the change in slip line angle θ at the crack tip. A fusion line having angle $\beta = 10^{o}$ leads to changes in the Q value at a fixed value of J which could not lead to a consensus on the relation between Q and θ. However, for a fusion line angle $\beta = 30^{o}$, the analytical predictions which suggest an increase in Q value of 0.02 per degree change in slip line angle can generally be observed. Along with this result, it was also seen from the deformation contour plots that the deformation bands do not always follow a 45^{o} path as assumed in several theories but depend on the root and cap material properties.

The conducted analysis shows the relationship between the crack tip stresses and the deformation bands, and additionally the slip lines. This shows that there is a direct relationship between crack tip stresses and the global plastic deformations for particular geometric and material configurations of bi-material welds. However, a better understanding is required to establish a concrete relationship. An enhancement of the theoretical derivation by involving the material complexities or improving the capabilities of the numerical model to predict/calculate slip line angles in a more effective way could improve the correspondence. This assessment will lead the way forward in the understanding effect of material heterogeneity on crack tip constraint and plastic deformations in the material with a theoretical relationship. Additionally, the experimental approach like DIC could be used to predict crack tip constraint behavior in a welded specimen. This will further enhance the capability to determine the fracture toughness of the welded specimen having material heterogeneity which in turn assists in the utilization of ECA procedures effectively.

Chapter 8

Conclusions and future work

8.1. The main outcomes

8.1.1. Challenges for a higher level ECA of a heterogeneous weld

Out of several challenges during Engineering Critical Assessments (ECA) of welded structures, weld strength heterogeneity is an important aspect that requires good understanding. The presence of a defect in a weld adds to this complexity. This challenge is recognized in this thesis.

Chapter 1 gives a brief introduction to the issues of weld failures, challenges faced during ECA of a defected weld because of strength heterogeneity and summarizes the effort undertaken by researchers to involve weld heterogeneity during defect assessments.

From the literature study, it was seen that a better understanding of the effects of strength variations within a weld is required to contribute towards a better estimation of the ability of the welded structure to perform its operation. In order to achieve this, a combination of analytical, numerical and experimental tools was considered in this thesis allowing to assess the fracture behavior of a defect present in a weld.

8.1.2. Appraisal of strength heterogeneity in welds

Characterization of strength heterogeneity is an initial step to get an insight into the level of strength variations present in a weld. Vickers's hardness mapping provided detailed information about the local hardness variations present in a weld. It was seen clearly from the 2D hardness contour plots that the weld involves hardness (HV5) variations up to 50% from one region to another.

Tearing resistance behavior of a defect located in heterogeneous weld was analyzed using experiments performed on welded SE(T) specimens. The crack growth and ductile tearing in a heterogeneous were measured using Direct Current Potential Drop (DCPD) technique and Normalization Data Reduction. The outcome of the results showed that the DCPD method has better capability to describe crack behavior through different stages of crack tearing and produce the variations in the crack resistance curve due to strength heterogeneity. Crack path deviations were observed during ductile tearing which shows that material heterogeneity has an influence on the crack path and must not be ignored. This is further explained in *Chapter 3*.

Importing hardness indentation values in the numerical Single Edge notched Tension SE(T) model has been achieved previously at Soete Laboratory by assigning HV5 values to each element in a mesh based on hardness map. The main challenge is to convert (using transfer functions) HV5 into material properties like

yield strength *($R_{p0.2}$),* ultimate tensile strength *(R_m)* and strain hardening *(n)* values. In this work, using All Weld Metal Tensile Tests (AWMTT) extracted from the weld region and HV5 maps were used to calibrate an *AWMTT transfer function* for the numerical model of a SE(T) specimen containing a heterogeneous weld. The difference between numerical force-CTOD results with experimental ones is within 5%. The standardized transfer functions gave the performance of 10% difference. This calibrated transfer function was further evaluated using Minature tensile testing (MTT). *Chapter 2* details the procedure. The outcome of this evaluation showed the validity of the *AWMTT transfer function* to determine material properties more efficiently.

8.1.3. Accounting for the effects of heterogeneity in weld assessments

Analysis of deformations in experiments and FE simulations on welded SE(T) specimens showed the complexities in deformation patterns due to the presence of weld heterogeneity. Digital Image Correlation (DIC) was used to obtain experimental deformation patterns while the heterogeneous SE(T) finite element model yielded numerical deformation plots. The deformation patterns, which are linked to the analytical slip line theory, were used to determine the loads at which the specimen fails which is termed as *'limit load'*. This is explained in *Chapter 5*.

Bounded limit load theorems, that provide limit load values of a specimen, were considered to analyze the plastic collapse of a welded SE(T) specimen. Two theorems providing lower bound and the upper bound limit load was performed on eight different weld configurations having two distinct weld regions (cap and root) with different geometry. 2D numerical simulations of a SE(T) model were utilized to compare the limit load results with analytical equations. From this analysis, an understanding of the performance of available equations was studied. Lower bound equations provide excessive conservatism resulting from the necessity to differentiate between different possible collapse mechanisms in heterogeneous welds. Instead, the upper bound equations provide near to actual or upper bound estimates which were not excessively upper bound due to consideration of deformation patterns during calculations. Additionally, the eight considered configurations were simplified to have a single material in the weld region using two different techniques. The limit load (determined using the Twice Elastic Slope (TES) method) of the simplified welds and the complex welds were compared to assess the outcome. The advantages and limitations of the methods are put forward in *Chapter 6,*

Crack tip constraint analysis was performed on eight weld configurations considered previously for bounded limit load analysis. *J*-integrals and *Q* parameter values were obtained to assess the stress concentrations around the crack tip due to the influence of varying material parameters in the welded region. This study was extended to analyze the influence of crack tip constraint on the deformation

behavior of the SE(T) specimens. The theoretical derivation which shows that the *Q* parameter is related to the angle of slip lines was also observed through simulations. Though this was not proved outright, the outcome of a couple of specimens opens the door for further reconsideration of the theoretical assumptions by pointing out the challenges. These findings and shortcomings of the analysis are discussed in *Chapter 7*. A better understanding of the crack tip constraint behavior and it's relating to deformation behavior aids in the better assessment of the fracture toughness of heterogeneous welds.

8.1.4. Significance of collaboration with Maribor University, Slovenia

For this thesis, the contribution of the University of Maribor has played a crucial role in acquiring double V-shaped welds for assessing fracture behavior and tearing resistance in SE(T) specimens. Additionally, MTT tests were conducted at Maribor University. Maribor Univerisity utilized DCPD setup at Ghent University to obtain crack growth information in SE(B) specimens. Along with this, they conducted Medium Wide Plate (MWP) tests for the Failure Assessment Diagrams (FAD).

For the evaluation of weld heterogeneity effects in fracture assessments, Maribor University has performed constraint and fracture toughness analysis on SE(B) specimens which possessed double V-shaped welds [95]. Different cases of mismatch levels were used in the double V-shaped weld which is similar to the double V-shaped welds used in this thesis. They have reported the outcome of each of the weld configurations and pointed out the behavior of a crack for different levels of mismatch. As in *Chapter 3* where crack path deviations were discussed for SE(T) specimens, it was also observed in the case of SE(B) specimens because of the same reasons. They observed crack path deviations when the growing crack reaches the OM-UM interface. This particularly shows the importance of understanding material heterogeneity with the presence of the crack.

Their work on failure assessment diagram is in progress and will allow an improved insight in crack behavior in larger-scale specimens with the presence of weld heterogeneity.

8.1.5. Framework for weld heterogeneity assessment in ECA

The framework for defect assessment as mentioned in ECA was briefly explained in *Chapter 1*. The procedure/flowchart is recalled in *Figure 98*. It includes an additional step for involving weld heterogeneity. Based on the outcome of the thesis, the recommended procedure is outlined in *Figure 99*. This flowchart is explained as follows:

- Weld heterogeneity needs to be quantified. This can be achieved using hardness indentations combined with AWMTT testing or miniature tensile

testing. Hardness indentations and AWMTT testing are recommended in this work. The basis of this recommendation is explained in *Chapters 2 and 4.*

- After strength characterizations, it is important to choose the level of flaw assessment complexity. Based on the requirement, the following two choices are available: to simplify the complex weld or to use the heterogeneous properties of the weld.
- If the requirement is to predict the defect behavior as precisely as possible, the heterogeneous strength properties of the weld have to be fully considered. The consequence of involving weld strength heterogeneity in defect assessment procedures can be seen in *Chapters 4* where the weld heterogeneity influenced P-CTOD plots, *Chapter 5* where weld heterogeneity influenced deformation bands and *Chapter 3,* where the influence of weld heterogeneity was seen during crack growth. Considering a fully heterogeneous weld for numerical simulations gives possibly the best estimations of crack behavior but is computationally intensive. Additionally, to determine the material properties, different experimental setups are required.
- If the requirement is to conduct defect analysis in a simplified manner, then the welds must be simplified which can be done in two different ways
    - Idealized weld: Bimetallic weldment having 2 materials, one in the base and one in the weld region with a straight fusion line (*Chapter 6).* This results in a strength mismatched weld as considered in standards.
    - Homogenized weld: retaining the geometry of the fusion line of the actual weld but representing the weld as a bimetallic region similar to the idealized weld [10]

  The simplified weld offers an easier procedure to obtain a numerical model. The determination of material properties does not require extensive experiments and is computationally simpler than the heterogeneous weld models. Simplified welds are used to determine limit loads which are in turn can be used to predict crack driving forces using established methods like reference stress approach.
- The type of weld (heterogeneous or simplified) could be chosen based on the requirements and available resources. The most precise fracture toughness estimations require a heterogeneous weld. The simplified weld allows providing reasonable approximations.
- Once the type of weld is chosen, further ECA procedures can be followed to perform defect assessments.

These recommendations require further validations and there is scope for improvements in several aspects which are explained in the next section. However, this is a step forward in achieving better, safer and accurate assessments of defect behavior during Engineering Critical Assessments of welded connections.

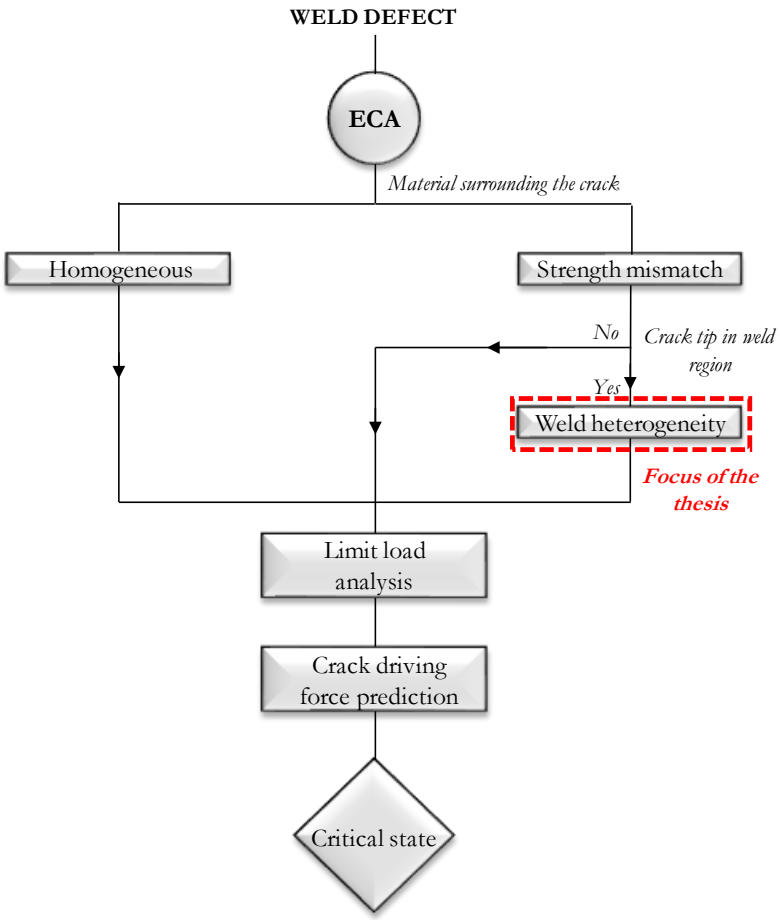

Figure 98: Flow chart of ECA procedure on a defected weld involving weld heterogeneity

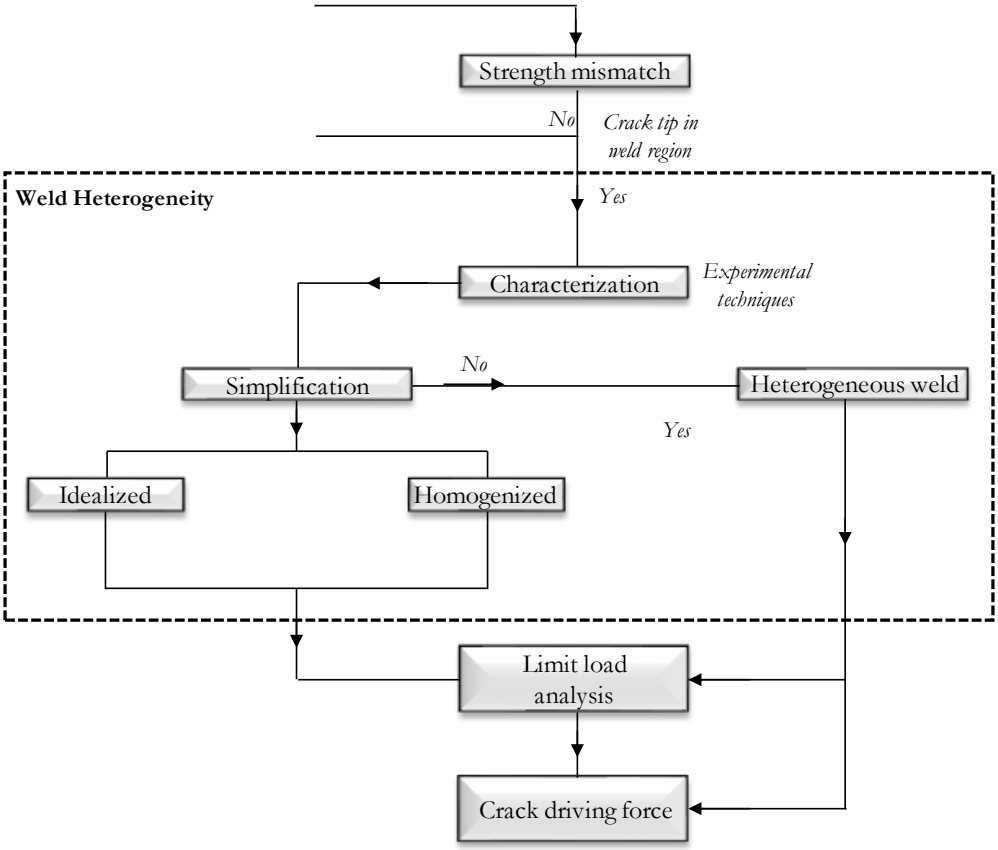

Figure 99: Flow chart for the assessment weld heterogeneity within the framework of ECA

8.2. The outlook

This thesis has presented many interesting aspects for involving weld strength heterogeneity in the structural integrity assessments of a defected weld. This outcome also presents challenges and future opportunities to explore, improve and understand further the aspects of effects of heterogeneity in weldments during structural integrity assessments. The recommendations for future work based on this thesis is provided further.

8.2.1. Characterization of weld strength heterogeneity

Results from *Chapter 4* indicate that hardness mapping is an efficient approach to characterize weld strength heterogeneity. However, there are other approaches all weld metal tensile tests and miniature tensile tests mentioned in literature to characterize material strength variations. These approaches need to be thoroughly analyzed for their robustness to characterize weld strength heterogeneity and methods in involving those variations into the numerical model. There is always scope for finding easier weld heterogeneity characterization techniques. The developed transfer functions can be further used for different applications involving

local mechanical property variations such as castings, additively manufactured components, etc.

8.2.2. Assessment of welds involving strength heterogeneity

Bounded limit load analysis was performed on a bi-metallic weld considering elastic-perfectly plastic analysis. Crack tip constraint (*J-Q*) analysis and its relationship with deformation bands and slip lines were assessed on similar welds. These assessments can be extended towards heterogeneous welds using the numerical model which involves varying material properties used in *Chapter 4*. This direction leads towards the assessment of actual welded SE(T) specimens. Updating the numerical model with different mesh densities to suit the analysis of deformations near the crack tip could yield better assessments of slip line patterns and its relation with the *Q* parameter.

A brief study of weld simplifications schemes as performed in *Chapter 6* with complex heterogeneous welds and its effect on crack driving forces and in turn fracture toughness must be explored. This simplification scheme, if conservative enough, would lead to a simplified approach towards estimating limit loads.

In this thesis, all assessments were made on SE(T) specimens. This analysis should be extended to different specimen configurations and loading conditions and eventually to components and structures.

Another important aspect that was not analyzed in this thesis is the fracture toughness behaviour of the material based on the sizes of the specimens. Analyses involving different scales of specimens should be considered to understand the size effect involved in the integrity of heterogeneous welds.

The study of tearing resistance in *Chapter 3* showed that the material strength variations have an influence on the ductile tearing, resistance curves and tearing trajectories which in turn provides a strong indication that the heterogeneity must not be ignored. This outcome can be further investigated for different weld configurations.

The inclusion and utilization of Continuum Damage Mechanics (CDM) concepts will aid in the further development of Fitness For Service (FFS) and Engineering Critical Analysis (ECA) procedures. The mechanism of nucleation, growth and coalescence could be explained better and thus will give an in-depth understanding of the crack extensions in heterogeneous welded structures.

Additionally, several parametric analyses can be performed using the tools used in this research. They are listed below keeping SE(T) specimen in focus.

- Bounded limit analysis involving HAZ region along with the weld
- Constraint analysis involving HAZ region along with weld
- Assessment of HAZ hardening and softening on defect behaviour
- Effect of crack depths on constraints and limit loads
- Different simplification schemes for different geometries

8.2.3. Broad perspective

Researchers and engineers are striving hard for constant improvement in standards, codes and techniques to enhance the prediction capabilities of failures in pipelines which results in economic and environmental safety. This thesis is a small step towards the establishment of a unified defect assessment approach during *FFS* analysis. Still, several aspects in determining material properties, loading effects and defect geometry characteristics need to be considered and analyzed for the betterment of *FFS* standards.

References

[1] N. K. Simha, F. D. Fischer, O. Kolednik, and C. R. Chen, "Inhomogeneity effects on the crack driving force in elastic and elastic–plastic materials," *Journal of the Mechanics and Physics of Solids,* vol. 51, no. 1, pp. 209-240, 2003/01/01/ 2003.
[2] U. Zerbst, R. A. Ainsworth, and K. H. Schwalbe, "Basic principles of analytical flaw assessment methods," *International Journal of Pressure Vessels and Piping,* vol. 77, no. 14, pp. 855-867, 2000/12/01/ 2000.
[3] S. Hertelé, N. Gubeljak, and W. De Waele, "Advanced characterization of heterogeneous arc welds using micro tensile tests and a two-stage strain hardening ('UGent') model," *International Journal of Pressure Vessels and Piping,* vol. 119, no. Supplement C, pp. 87-94, 2014/07/01/ 2014.
[4] J. Predan, N. Gubeljak, and O. Kolednik, "On the local variation of the crack driving force in a double mismatched weld," *Engineering Fracture Mechanics,* vol. 74, no. 11, pp. 1739-1757, 2007/07/01/ 2007.
[5] E. Østby, Z. L. Zhang, and C. Thaulow, "Constraint effect on the near tip stress fields due to difference in plastic work hardening for bi-material interface cracks in small scale yielding," *International Journal of Fracture,* vol. 111, no. 1, pp. 87-103, 2001/09/01 2001.
[6] D. M. Koçak, "FITNET - EUROPEAN FITNESS FOR SERVICE NETWORK," GKSS Forschungszentrum Geesthacht GmbH (GKSS)GTC1 – 2001 – 43049, 2006.
[7] P. J. Budden, J. K. Sharples, and A. R. Dowling, "The R6 procedure: recent developments and comparison with alternative approaches," *International Journal of Pressure Vessels and Piping,* vol. 77, no. 14, pp. 895-903, 2000/12/01/ 2000.
[8] Y.-J. Kim and K.-H. Schwalbe, "Mismatch effect on plastic yield loads in idealised weldments: I. Weld centre cracks," *Engineering Fracture Mechanics,* vol. 68, no. 2, pp. 163-182, 2001/02/01/ 2001.
[9] S. Hao, A. Cornec, and K. H. Schwalbe, "Plastic stress-strain fields and limit loads of a plane strain cracked tensile panel with a mismatched welded joint," *International Journal of Solids and Structures,* vol. 34, no. 3, pp. 297-326, 1997/01/01/ 1997.
[10] S. Hertelé, W. De Waele, M. Verstraete, R. Denys, and N. O'Dowd, "J-integral analysis of heterogeneous mismatched girth welds in clamped single-edge notched tension specimens," *International Journal of Pressure Vessels and Piping,* vol. 119, pp. 95-107, 2014/07/01/ 2014.
[11] T. L. Anderson, *Fracture Mechanics: Fundamentals and Applications, Third Edition*. CRC Press, 2005.
[12] C. J. Tassava, "Launching a Thousand Ships: Entrepreneurs, War Workers, and the State in American Shipbuilding, 1940—1945," *Enterprise & Society,* vol. 6, no. 4, pp. 588-600, 2005.
[13] N. Y. Schlager, *When Technology Fails - Significant technological disasters, accidents, and failures of the twentieth century*. Gale Research, 1994.
[14] CIA. (2019). *CIA World Factbook - Oil and gas consumption*. Available: https://www.cia.gov/library/publications/the-world-factbook/geos/xx.html
[15] CIA. (2019). *The World Factbook - Pipeline network*. Available: https://www.cia.gov/library/publications/the-world-factbook/fields/383.html
[16] N. Newman. *Virtual Pipelines*. Available: https://www.eniday.com/en/technology_en/virtual-pipelines-lng/
[17] *Countries of the world*. Available: https://theodora.com/pipelines/france_and_belgium_pipelines.html
[18] I. Milne, R. Ritchie, and B. L. Karihaloo, *Comprehensive Structural Integrity*. Elsevier Science, 2003.
[19] "BP Statistical Review of World Energy," BPJune, 2018 2018, Available: https://www.bp.com/content/dam/bp/business-

sites/en/global/corporate/pdfs/energy-economics/statistical-review/bp-stats-review-2018-full-report.pdf.
[20] *API 1104 - Welding of Pipelines and Related Facilities* 1999.
[21] *BS 7910:2013+A1:2015 - Guide to methods for assessing the acceptability of flaws in metallic structures*, 2015.
[22] T. L. Anderson and D. A. Osage, "API 579: a comprehensive fitness-for-service guide," *International Journal of Pressure Vessels and Piping,* vol. 77, no. 14, pp. 953-963, 2000/12/01/ 2000.
[23] R. A. Ainsworth and D. G. Hooton, "R6 and R5 procedures: The way forward," *International Journal of Pressure Vessels and Piping,* vol. 85, no. 3, pp. 175-182, 2008/03/01/ 2008.
[24] *BS EN ISO 17637:2016 - Non-destructive testing of welds. Visual testing of fusion-welded joints*, 978 0 580 87798 8, 2016.
[25] *BS EN 1370:2011 - Founding. Examination of surface condition*, 978 0 580 71102 2, 2011.
[26] *ISO 3452-1:2013 - Non-destructive testing -- Penetrant testing -- Part 1: General principles*, 2013.
[27] *BS EN ISO 23277:2015 - Non-destructive testing of welds. Penetrant testing. Acceptance levels*, 978 0 580 80883 8, 2015.
[28] *BS EN ISO 15548-3:2008 - Non-destructive testing. Equipment for eddy current examination. System characteristics and verification*, 978 0 580 55890 0, 2008.
[29] *BS EN ISO 15549:2010 - Non-destructive testing. Eddy current testing. General principles*, 978 0 580 72199 1, 2010.
[30] *ISO 5817:2014 - Welding -- Fusion-welded joints in steel, nickel, titanium and their alloys (beam welding excluded) -- Quality levels for imperfections*, 2014.
[31] U. Zerbst *et al.*, "Review on fracture and crack propagation in weldments – A fracture mechanics perspective," *Engineering Fracture Mechanics,* vol. 132, no. Supplement C, pp. 200-276, 2014/12/01/ 2014.
[32] *ASTM E8 / E8M-16a, Standard Test Methods for Tension Testing of Metallic Materials, ASTM International, West Conshohocken, PA*, 2016.
[33] *ISO 15653:2010 - Metallic materials -- Method of test for the determination of quasistatic fracture toughness of welds*, 2010.
[34] *BS 7448-1:1991 - Fracture mechanics toughness tests. Method for determination of KIc, critical CTOD and critical J values of metallic materials*, 1991.
[35] *ASTM E1820-18, Standard Test Method for Measurement of Fracture Toughness, ASTM International, West Conshohocken, PA*, 2017.
[36] K. Satoh and M. Toyoda, "Fracture toughness evaluation of welds with mechanical heterogeneity," *Transactions of Japan welding society,* vol. 13, no. 1, 1982.
[37] K. Satoh and M. Toyoda, "The incidence of mechanical heterogeneity on fracture toughness evaluation of welds," *IIW,* vol. DGC. X-1031-83, 1983.
[38] K. Seo, F. Nogata, and M. Kusaka, L. Karlsson, L. Lindgren, and M. Jonsson, Eds. *Effect of Mechanical Heterogeneity on the Absorbed Energy of Welded Joint*, Mechanical Effects of Welding ed. (International Union of Theoretical and Applied Mechanics). Springer, Berlin, Heidelberg, 1992.
[39] D. Qiao, W. Zhang, T. Y. Pan, P. Crooker, S. David, and Z. Feng, "Evaluation of residual plastic strain distribution in dissimilar metal weld by hardness mapping," *Science and Technology of Welding and Joining,* vol. 18, no. 7, pp. 624-630, 2013/10/01 2013.
[40] P. Yayla, E. Kaluc, and K. Ural, "Effects of welding processes on the mechanical properties of HY 80 steel weldments," *Materials & Design,* vol. 28, no. 6, pp. 1898-1906, 2007/01/01/ 2007.
[41] K. Prasad and D. K. Dwivedi, "Some investigations on microstructure and mechanical properties of submerged arc welded HSLA steel joints," *The*

International Journal of Advanced Manufacturing Technology, vol. 36, no. 5, pp. 475-483, 2008/03/01 2008.

[42] R. Mittal and B. S. Sidhu, "Microstructures and mechanical properties of dissimilar T91/347H steel weldments," *Journal of Materials Processing Technology,* vol. 220, pp. 76-86, 2015/06/01/ 2015.

[43] M.-L. Zhu and F.-Z. Xuan, "Correlation between microstructure, hardness and strength in HAZ of dissimilar welds of rotor steels," *Materials Science and Engineering: A,* vol. 527, no. 16, pp. 4035-4042, 2010/06/25/ 2010.

[44] S. A. David, S. S. Babu, and J. M. Vitek, "Welding: Solidification and microstructure," *JOM,* vol. 55, no. 6, pp. 14-20, 2003/06/01 2003.

[45] M. Eroğlu, M. Aksoy, and N. Orhan, "Effect of coarse initial grain size on microstructure and mechanical properties of weld metal and HAZ of a low carbon steel," *Materials Science and Engineering: A,* vol. 269, no. 1, pp. 59-66, 1999/08/30/ 1999.

[46] K. H. Schwalbe and U. Zerbst, "The Engineering Treatment Model," *International Journal of Pressure Vessels and Piping,* vol. 77, no. 14, pp. 905-918, 2000/12/01/ 2000.

[47] Y.-J. Kim, M. Koçak, R. A. Ainsworth, and U. Zerbst, "SINTAP defect assessment procedure for strength mis-matched structures," *Engineering Fracture Mechanics,* vol. 67, no. 6, pp. 529-546, 2000/12/01/ 2000.

[48] S. Hertelé, N. O'Dowd, K. Van Minnebruggen, M. Verstraete, and W. De Waele, "Fracture mechanics analysis of heterogeneous welds: Numerical case studies involving experimental heterogeneity patterns," *Engineering Failure Analysis,* vol. 58, no. Part 2, pp. 336-350, 2015/12/01/ 2015.

[49] K. H. Schwalbe, S. Hao, and A. Cornec, "ETM-MM - The engineering treatment model for mis-matched welded joints," 1994, pp. 539-560: Mechanical Engineering Publications, London.

[50] R. A. Ainsworth, F. Gutierrez-Solana, and J. R. Ocejo, "Analysis levels within the SINTAP defect assessment procedures," *Engineering Fracture Mechanics,* vol. 67, no. 6, pp. 515-527, 2000/12/01/ 2000.

[51] R. A. Ainsworth, A. C. Bannister, and U. Zerbst, "An overview of the European flaw assessment procedure SINTAP and its validation," *International Journal of Pressure Vessels and Piping,* vol. 77, no. 14, pp. 869-876, 2000/12/01/ 2000.

[52] *DNVGL-RP-F108 - Assessment of flaws in pipeline and riser girth welds*, 2017.

[53] M. Toyoda, C. Thaulow, and J. G. Blauel, "Strength mis-matching and its influence on performance of welded structures," 1994, pp. 335-350: Mechanical Engineering Publications, London.

[54] J. R. Gordon and Y. Y. Wang, "The effect of weld metal mis-match on fracture toughness testing and analysis procedures," 1994, pp. 351-368: Mechanical Engineering Publications, London.

[55] *BS 8571:2014 - Method of test for determination of fracture toughness in metallic materials using single edge notched tension (SENT) specimens*, 2014.

[56] K.-H. Schwalbe and A. Cornec, "THE ENGINEERING TREATMENT MODEL (ETM) AND ITS PRACTICAL APPLICATION," *Fatigue & Fracture of Engineering Materials & Structures,* vol. 14, no. 4, pp. 405-412, 1991.

[57] R. A. Ainsworth, "The assessment of defects in structures of strain hardening material," *Engineering Fracture Mechanics,* vol. 19, no. 4, pp. 633-642, 1984/01/01/ 1984.

[58] A. G. Miller, "Review of limit loads of structures containing defects," *International Journal of Pressure Vessels and Piping,* vol. 32, no. 1, pp. 197-327, 1988/01/01/ 1988.

[59] Y. Lei, J. Tao, and P. N. Li, "Limit load and J estimates of a centre cracked plate with an asymmetric crack in a mismatched weld," *International Journal of Pressure Vessels and Piping,* vol. 76, no. 11, pp. 747-757, 1999/09/01/ 1999.

[60] J. Joch, R. A. Ainsworth, and T. H. Hyde, "Limit load and J-estimates for idealised problems of deeply cracked welded joints in plane-strain bending and tension " *Fatigue & Fracture of Engineering Materials & Structures,* vol. 16, no. 10, pp. 1061-1079, 1993.

[61] Y.-J. Kim and K.-H. Schwalbe, "Mismatch effect on plastic yield loads in idealised weldments: II. Heat affected zone cracks," *Engineering Fracture Mechanics,* vol. 68, no. 2, pp. 183-199, 2001/02/01/ 2001.

[62] Schwalbe, Zerbst, Brocks, Cornec, Heerens, and Amstutz, "The ETM method for assessing the significance of crack-like defects in engineering structures," *Fatigue & Fracture of Engineering Materials & Structures,* vol. 21, no. 10, pp. 1215-1231, 1998.

[63] S. Alexandrov, N. Chicanova, and M. Kocak, "Analytical yield load solution for overmatched center cracked tension specimen," *Engineering Fracture Mechanics,* vol. 64, no. 4, pp. 383-399, 1999/11/01/ 1999.

[64] A. Kotousov and M. F. Mohmed Jaffar, "Collapse load for a crack in a plate with a mismatched welded joint," *Engineering Failure Analysis,* vol. 13, no. 7, pp. 1065-1075, 2006/10/01/ 2006.

[65] D. Kozak, N. Gubeljak, P. Konjatić, and J. Sertić, "Yield load solutions of heterogeneous welded joints," *International Journal of Pressure Vessels and Piping,* vol. 86, no. 12, pp. 807-812, 2009/12/01/ 2009.

[66] N. P. O'Dowd and C. F. Shih, "Family of crack-tip fields characterized by a triaxiality parameter—I. Structure of fields," *Journal of the Mechanics and Physics of Solids,* vol. 39, no. 8, pp. 989-1015, 1991/01/01/ 1991.

[67] N. P. O'Dowd and C. F. Shih, "Family of crack-tip fields characterized by a triaxiality parameter—II. Fracture applications," *Journal of the Mechanics and Physics of Solids,* vol. 40, no. 5, pp. 939-963, 1992/07/01/ 1992.

[68] J. R. Rice and G. F. Rosengren, "Plane strain deformation near a crack tip in a power-law hardening material," *Journal of the Mechanics and Physics of Solids,* vol. 16, no. 1, pp. 1-12, 1968/01/01/ 1968.

[69] J. W. Hutchinson, "Singular behaviour at the end of a tensile crack in a hardening material," *Journal of the Mechanics and Physics of Solids,* vol. 16, no. 1, pp. 13-31, 1968/01/01/ 1968.

[70] M. C. Burstow and I. C. Howard, "Constraint effects on crack growth resistance curves of strength mismatched welded bend specimens," in *Mis-Matching of Intefaces and Welds*, Geesthacht, FRG, 1997, pp. 357-369: GKSS Research Center Publications.

[71] D. P. Boothman, M. M. K. Lee, and A. R. Luxmoore, "The effects of weld mismatch on J-integrals and Q-values for semi-elliptical surface flaws," *Engineering Fracture Mechanics,* vol. 64, no. 4, pp. 433-458, 1999/11/01/ 1999.

[72] C. Betegón and I. Peñuelas, "A constraint based parameter for quantifying the crack tip stress fields in welded joints," *Engineering Fracture Mechanics,* vol. 73, no. 13, pp. 1865-1877, 2006/09/01/ 2006.

[73] E. Østby, C. Thaulow, and Z. L. Zhang, "Numerical simulations of specimen size and mismatch effects in ductile crack growth – Part II: Near-tip stress fields," *Engineering Fracture Mechanics,* vol. 74, no. 11, pp. 1793-1809, 2007/07/01/ 2007.

[74] T. Nishioka, Y. Kobayashi, T. Fujimoto, and J. S. Epstein, "Finite element analyses of near-tip deformation in inhomogeneous elastic-plastic fracture specimens," *International Journal of Pressure Vessels and Piping,* vol. 63, no. 3, pp. 277-291, 1995/01/01/ 1995.

[75] J. T. Martin and S. B. Lambert, "Analysis of constraint in single edge notch tension specimens using the T-stress," *International Journal of Pressure Vessels and Piping,* vol. 65, no. 1, pp. 13-19, 1996/01/01/ 1996.

[76] M. Graba, "The influence of material properties and crack length on the Q-stress value near the crack tip for elastic-plastic materials for single edge notch plate in tension," *Archives of Civil and Mechanical Engineering,* vol. 11, no. 2, pp. 301-319, 2011/01/01/ 2011.

[77] E. Wang, W. Zhou, and G. Shen, "Three-dimensional finite element analysis of crack-tip fields of clamped single-edge tension specimens – Part II: Crack-tip constraints," *Engineering Fracture Mechanics,* vol. 116, pp. 144-157, 2014/01/01/ 2014.

[78] X.-K. Zhu, S. Cravero, and C. Ruggieri, "Determination of J-R Curve for X60 Pipeline Steel Using SENT Specimens and Normalization Method," presented at the ASME 2009 Pressure Vessels and Piping Conference, 2009. Available: http://dx.doi.org/10.1115/PVP2009-78089

[79] B. Nyhus, M. L. Polanco, and O. Ørjasæther, "SENT Specimens an Alternative to SENB Specimens for Fracture Mechanics Testing of Pipelines," presented at the ASME 2003 22nd International Conference on Offshore Mechanics and Arctic Engineering, 2003. Available: http://dx.doi.org/10.1115/OMAE2003-37370

[80] M. Chiesa, B. Nyhus, B. Skallerud, and C. Thaulow, "Efficient fracture assessment of pipelines. A constraint-corrected SENT specimen approach," *Engineering Fracture Mechanics,* vol. 68, no. 5, pp. 527-547, 2001/03/01/ 2001.

[81] S. Hertelé, J. Bally, N. Gubeljak, P. Štefane, P. Verleysen, and W. De Waele, "Characterization of heterogeneous arc welds through minature tensile testing and vickers hardness mapping," (in English), *Materiali in Tehnologije,* Article vol. 50, no. 4, pp. 571-574, Jul-Aug 2016.

[82] *API Specifications 5L (Specifications for line pipe), 43rd ed.*, 2004.

[83] *A5.1/A5.1M:2004 SPECIFICATION FOR CARBON STEEL ELECTRODES FOR SHIELDED METAL ARC WELDING (HISTORICAL)*, ISBN 0-87171-642-9, 2004.

[84] *BS EN 10025-6:2019 - Hot rolled products of structural steels. Technical delivery conditions for flat products of high yield strength structural steels in the quenched and tempered condition*, ISBN 978 0 580 73970 5, 2019.

[85] *ISO 16834:2012 - Welding consumables -- Wire electrodes, wires, rods and deposits for gas shielded arc welding of high strength steels -- Classification*, 2012.

[86] *ISO 14341:2010 - Welding consumables -- Wire electrodes and weld deposits for gas shielded metal arc welding of non alloy and fine grain steels -- Classification*, 2010.

[87] B. C. Hornbuckle *et al.*, "Property mapping of friction stir welded Al-2139 T8 plate using site specific shear punch testing," *Materials Science and Engineering: A,* vol. 682, no. Supplement C, pp. 192-201, 2017/01/13/ 2017.

[88] E. L. Stevens, J. Toman, A. C. To, and M. Chmielus, "Variation of hardness, microstructure, and Laves phase distribution in direct laser deposited alloy 718 cuboids," *Materials & Design,* vol. 119, no. Supplement C, pp. 188-198, 2017/04/05/ 2017.

[89] *ASTM E384-11e1, Standard Test Method for Knoop and Vickers Hardness of Materials, ASTM International, West Conshohocken, PA*, 2011.

[90] R. Denys, "The effect of HAZ softening on the fracture characteristics of modern weldments and the practical integrity of marine structures made by TMCP steels," presented at the EVALMAT 89, Kobe, Japan, Nov, 1989.

[91] T. Mohandas, G. Madhusudan Reddy, and B. Satish Kumar, "Heat-affected zone softening in high-strength low-alloy steels," *Journal of Materials Processing Technology,* vol. 88, no. 1, pp. 284-294, 1999/04/15/ 1999.

[92] V. H. Baltazar Hernandez, S. K. Panda, Y. Okita, and N. Y. Zhou, "A study on heat affected zone softening in resistance spot welded dual phase steel by nanoindentation," *Journal of Materials Science,* journal article vol. 45, no. 6, pp. 1638-1647, March 01 2010.

[93] M. Koçak, "Structural integrity of welded structures: process-property-performance (3P) relationship," presented at the 63rd Annual Assembly & International Conference of the International Institute of Welding, Istanbul, Turkey, July, 2010.
[94] U. Ceyhan, M. Horstmann, and B. Dogan, "High temperature cross-weld characterisation of steel weldments by microtensile testing," *Materials at High Temperatures,* vol. 23, no. 3-4, pp. 233-243, 2006/01/01 2006.
[95] P. Štefane, S. Naib, S. Hertelé, W. De Waele, and N. Gubeljak, "Crack tip constraint analysis in welded joints with pronounced strength and toughness heterogeneity," *Theoretical and Applied Fracture Mechanics,* vol. 103, p. 102293, 2019/10/01/ 2019.
[96] O. Akourri, M. Louah, A. Kifani, G. Gilgert, and G. Pluvinage, "The effect of notch radius on fracture toughness JIc," *Engineering Fracture Mechanics,* vol. 65, no. 4, pp. 491-505, 2000/03/01/ 2000.
[97] *Measurement of crack tip opening displacement (CTOD) – fracture resistance curves using single-edge notched tension (SENT) specimens*, 2010.
[98] M. A. Verstraete, W. De Waele, K. Van Minnebruggen, and S. Hertelé, "Single-specimen evaluation of tearing resistance in SENT testing," *Engineering Fracture Mechanics,* vol. 148, pp. 324-336, 2015/11/01/ 2015.
[99] M. Verstraete, K. V. Minnebruggen, S. Hertelé, R. Denys, and W. D. Waele, "Determination of tearing resistance in SENT and CWP specimens using direct current potential drop measurements," presented at the 6th International Pipeline Technology Conference, Proceedings, Ostend, Belgium, 2013.
[100] K. Van Minnebruggen, S. Hertelé, M. A. Verstraete, and W. De Waele, "Crack growth characterization in single-edge notched tension testing by means of direct current potential drop measurement," *International Journal of Pressure Vessels and Piping,* vol. 156, no. Supplement C, pp. 68-78, 2017/09/01/ 2017.
[101] H. Johnson, "Calibrating the Electric Potential Method for Studying Slow Crack Growth," *Materials Research & Standards,* pp. 442-445, 1965.
[102] L. Z. Kong, X. Y. Zhou, L. Q. Chen, K. Huang, and H. T. Peng, "CTOD-R Curve Tests of API 5L X90 By SENT Specimen Using a Modified Normalization Method," *Fatigue & Fracture of Engineering Materials & Structures,* vol. 40, no. 2, pp. 288-299, 2017.
[103] L. S. F. Lasdon, Richard L. ; Ratner, Margery W., "Nonlinear optimization using the generalized reduced gradient method," *RAIRO - Operations Research - Recherche Opérationnelle,* vol. 8, no. V3, pp. 73-103, 1973.
[104] M. A. Verstraete, R. M. Denys, K. Van Minnebruggen, S. Hertelé, and W. De Waele, "Determination of CTOD resistance curves in side-grooved Single-Edge Notched Tensile specimens using full field deformation measurements," *Engineering Fracture Mechanics,* vol. 110, pp. 12-22, 2013/09/01/ 2013.
[105] M. A. Verstraete, S. Hertelé, R. M. Denys, K. Van Minnebruggen, and W. De Waele, "Evaluation and interpretation of ductile crack extension in SENT specimens using unloading compliance technique," *Engineering Fracture Mechanics,* vol. 115, no. Supplement C, pp. 190-203, 2014/01/01/ 2014.
[106] J. R. Rice, "A Path Independent Integral and the Approximate Analysis of Strain Concentration by Notches and Cracks," *Journal of Applied Mechanics,* vol. 35, no. 2, pp. 379-386, 1968.
[107] *ASTM E23-16b, Standard Test Methods for Notched Bar Impact Testing of Metallic Materials, ASTM International, West Conshohocken, PA*, 2016.
[108] *ASTM E2298-15, Standard Test Method for Instrumented Impact Testing of Metallic Materials, ASTM International, West Conshohocken, PA*, 2015.
[109] D. W. Zhou, "Measurement and modelling of R-curves for low-constraint specimens," *Engineering Fracture Mechanics,* vol. 78, no. 3, pp. 605-622, 2011/02/01/ 2011.

[110] X.-K. Zhu, "Review of fracture toughness test methods for ductile materials in low-constraint conditions," *International Journal of Pressure Vessels and Piping,* vol. 139-140, pp. 173-183, 2016/03/01/ 2016.
[111] X.-K. Zhu, "Progress in development of fracture toughness test methods for SENT specimens," *International Journal of Pressure Vessels and Piping,* vol. 156, pp. 40-58, 2017/09/01/ 2017.
[112] N. Okumura, T. V. Venkatasubramanian, B. A. Unvala, and T. J. Baker, "Application of the ac potential drop technique to the determination of R curves of tough ferritic steels," *Engineering Fracture Mechanics,* vol. 14, no. 3, pp. 617-625, 1981/01/01/ 1981.
[113] Y. Hioe, S. Kalyanam, and G. M. Wilkowski, "Comparison of Calculated Crack Growth Values Using Unloading Compliance and d-c EP During SENT Testing," in *2016 11th International Pipeline Conference*, 2016, no. 50266, p. 9.
[114] S. Cravero and C. Ruggieri, "Estimation procedure of J-resistance curves for SE(T) fracture specimens using unloading compliance," *Engineering Fracture Mechanics,* vol. 74, no. 17, pp. 2735-2757, 2007/11/01/ 2007.
[115] D.-Y. Park, W. R. Tyson, and J.-P. Gravel, "CANMET SENT test method, updates and applications," *International Journal of Pressure Vessels and Piping,* vol. 156, pp. 8-16, 2017/09/01/ 2017.
[116] G. Shen and W. Tyson, "Crack Size Evaluation Using Unloading Compliance in Single-Specimen Single-Edge-Notched Tension Fracture Toughness Testing," *Journal of Testing and Evaluation,* vol. 37, no. 4, pp. 347-357, 2009.
[117] *ISO 12135:2016 - Metallic materials -- Unified method of test for the determination of quasistatic fracture toughness*, 2016.
[118] J. Landes, Z. Zhou, K. Lee, and R. Herrera, "Normalization Method for Developing J-R Curves with the LMN Function," *Journal of Testing and Evaluation,* vol. 19, no. No. 2, pp. 305-311, 1991.
[119] M. Scibetta, E. Lucon, J. Schuurmans, and E. van Walle, "Numerical simulations to support the normalization data reduction technique," *Engineering Fracture Mechanics,* vol. 73, no. 4, pp. 524-534, 2006/03/01/ 2006.
[120] G. Shen, J. A. Gianetto, and W. R. Tyson, "Measurement of J-R Curves Using Single-Specimen Technique On Clamped SE(T) Specimens," presented at the The Nineteenth International Offshore and Polar Engineering Conference, Osaka, Japan, 2009/1/1/, 2009.
[121] W. Lan, X. Deng, and M. A. Sutton, "Investigation of crack tunneling in ductile materials," *Engineering Fracture Mechanics,* vol. 77, no. 14, pp. 2800-2812, 2010/09/01/ 2010.
[122] M. A. James and J. C. Newman, "The effect of crack tunneling on crack growth: experiments and CTOA analyses," *Engineering Fracture Mechanics,* vol. 70, no. 3, pp. 457-468, 2003/02/01/ 2003.
[123] D. K. Mahanty and S. K. Maiti, "Experimental and finite element studies on mode I and mixed mode (I and II) stable crack growth—I. Experimental," *Engineering Fracture Mechanics,* vol. 37, no. 6, pp. 1237-1250, 1990/01/01/ 1990.
[124] *BS 8571:2018 - Method of test for determination of fracture toughness in metallic materials using single edge notched tension (SENT) specimens*, 2018.
[125] D. Tabor, *The Hardness of Metals*. Oxford: Clarendon, 1951.
[126] W. Ramberg and W. Osgood, R., "Description of stress-strain curves by three parameters," National Advisory Committee for Aeronautics; Washington, DC, United StatesNACA-TN-902, Jul 01, 1943 1943.
[127] *ISO 18265:2013 - Metallic materials -- Conversion of hardness values*, 2013.
[128] E. J. Pavlina and C. J. Van Tyne, "Correlation of Yield Strength and Tensile Strength with Hardness for Steels," *Journal of Materials Engineering and Performance,* journal article vol. 17, no. 6, pp. 888-893, December 01 2008.

[129] D. A. LaVan and W. N. Sharpe, "Tensile testing of microsamples," *Experimental Mechanics,* journal article vol. 39, no. 3, pp. 210-216, September 01 1999.
[130] A. R. H. Midawi, Y. Kisaka, E. B. F. Santos, and A. P. Gerlich, "Characterization of Local Mechanical Properties of X80 Pipeline Girth Welds Using Advanced Techniques," in *2016 11th International Pipeline Conference*, 2016, vol. Volume 3: Operations, Monitoring and Maintenance; Materials and Joining, V003T05A042.
[131] A. C. Bannister, J. Ruiz Ocejo, and F. Gutierrez-Solana, "Implications of the yield stress/tensile stress ratio to the SINTAP failure assessment diagrams for homogeneous materials," *Engineering Fracture Mechanics,* vol. 67, no. 6, pp. 547-562, 2000/12/01/ 2000.
[132] A. Considère, "Annales des Ponts et Chaussées 9," pp. 574-775, 1885.
[133] S. Hertelé, W. De Waele, R. Denys, and M. Verstraete, "Full-range stress–strain behaviour of contemporary pipeline steels: Part I. Model description," *International Journal of Pressure Vessels and Piping,* vol. 92, pp. 34-40, 2012/04/01/ 2012.
[134] S. Hertelé, W. De Waele, R. Denys, and M. Verstraete, "Full-range stress–strain behaviour of contemporary pipeline steels: Part II. Estimation of model parameters," *International Journal of Pressure Vessels and Piping,* vol. 92, no. Supplement C, pp. 27-33, 2012/04/01/ 2012.
[135] K. Levenberg, "A METHOD FOR THE SOLUTION OF CERTAIN NON-LINEAR PROBLEMS IN LEAST SQUARES," *Quarterly of Applied Mathematics,* vol. 2, no. 2, pp. 164-168, 1944.
[136] W. K. Wang, Y. Liu, Q. B. Zhang, L. J. Zhang, and J. X. Zhang, "Microstructure and local mechanical properties of a dissimilar metal welded joint with buttering layer in steam turbine rotor," *Materials Science and Engineering: A,* vol. 747, pp. 244-254, 2019/02/18/ 2019.
[137] R. Hill, "LXXXVIII. On the state of stress in a plastic-rigid body at the yield point," *The London, Edinburgh, and Dublin Philosophical Magazine and Journal of Science,* vol. 42, no. 331, pp. 868-875, 1951/08/01 1951.
[138] W. Johnson, "Some slip-line fields for swaging or expanding, indenting, extruding and machining for tools with curved dies," *International Journal of Mechanical Sciences,* vol. 4, no. 4, pp. 323-347, 1962/07/01/ 1962.
[139] H. Kudo, "Some new slip-line solutions for two-dimensional steady-state machining," *International Journal of Mechanical Sciences,* vol. 7, no. 1, pp. 43-55, 1965/01/01/ 1965.
[140] M. C. Burstow, I. C. Howard, and R. A. Ainsworth, "The Effect of Material Strength Mismatching on Constraint at the Limit Load of Welded Three-Point Bend Specimens," *International Journal of Fracture,* vol. 89, no. 2, pp. 117-142, 1998/01/01 1998.
[141] U. o. Cambridge, "Slip Line Field Theory," DoITPoMS, Ed., ed.
[142] A. F. Bower, "Chapter 6 - Analytical techniques and solutions for plastic solids," ed.
[143] S. Hertelé, "A course on Fracture Mechanics," 2015.
[144] S. Hertelé, F. Van Gerven, S. Naib, N. Gubeljak, and W. De Waele, "Experimental and numerical slip line analysis of welded single-edge notched tension specimens," *Procedia Structural Integrity,* vol. 2, pp. 1763-1770, 2016/01/01/ 2016.
[145] K. Van Minnebruggen, M. Verstraete, S. Hertelé, and W. De Waele, "Evaluation and Comparison of Double Clip Gauge Method and Delta 5 Method for CTOD Measurement in SE(T) Specimens," *Journal of Testing and Evaluation,* vol. 44, no. 6, pp. 2414-2423, 2016.
[146] F. V. Gerven, "Slip line analysis of heterogeneous flawed welds loaded in tension," MSc., Ghent University, 2015.

[147] ASME. (2019). *Boiler and Pressure Vessel Code, 2019 Edition*. Available: https://www.asme.org/shop/standards/new-releases/boiler-pressure-vessel-code-2013

[148] M. G. Kirkwood and D. G. Moffat, "Plastic Loads for Piping Branch Junctions Subjected to Combined Pressure and In-Plane Moment Loads," *Proceedings of the Institution of Mechanical Engineers, Part E: Journal of Process Mechanical Engineering,* vol. 208, no. 1, pp. 31-43, 1994/02/01 1994.

[149] D. G. Moffat, M. F. Hsieh, and M. Lynch, "An assessment of ASME III and CEN TC54 methods of determining plastic and limit loads for pressure system components," *The Journal of Strain Analysis for Engineering Design,* vol. 36, no. 3, pp. 301-312, 2001/04/01 2001.

[150] K. Samadian, S. Hertelé, and W. De Waele, "A novel flaw alignment approach based on the analysis of bands of maximum strain using full-field deformation measurements," *Procedia Structural Integrity,* vol. 5, pp. 1245-1252, 2017/01/01/ 2017.

[151] D. J. F. Ewing and J. R. Griffiths, "The applicability of slip-line field theory to contained elastic-plastic flow around a notch," *Journal of the Mechanics and Physics of Solids,* vol. 19, no. 6, pp. 389-394, 1971/11/01/ 1971.

[152] V. Kumar, M. D. German, and C. F. Shih, "An Engineering Approach for Elastic-Piastic Fracture Analysis," in "NP-1931, Research Project 1237-1," EPRI report1981.

[153] I. Milne, R. A. Ainsworth, A. R. Dowling, and A. T. Stewart, "Assessment of the integrity of structures containing defects," *International Journal of Pressure Vessels and Piping,* vol. 32, no. 1, pp. 3-104, 1988/01/01/ 1988.

[154] S. Naib, W. De Waele, P. Štefane, N. Gubeljak, and S. Hertelé, "Crack driving force prediction in heterogeneous welds using Vickers hardness maps and hardness transfer functions," *Engineering Fracture Mechanics,* 2018/07/18/ 2018.

[155] R. Denys, "Testing for weld metal yield strength," presented at the Mismatching of welds. ESIS 17, 1994.

[156] D. C. Drucker, W. Prager, and N. J. Greenberg, "Extended limit design theorems for continuous media," *Quarterly of Applied Mathematics,* vol. 9, no. 4, pp. 381-389, 1952.

[157] M. L. Williams, "On the Stress Distribution at the Base of a Stationary Crack," *Journal of Applied Mechanics,* vol. 24, pp. 109-114, 1957.

[158] Y. J. Chao, S. Yang, and M. A. Sutton, "On the fracture of solids characterized by one or two parameters: Theory and practice," *Journal of the Mechanics and Physics of Solids,* vol. 42, no. 4, pp. 629-647, 1994/04/01/ 1994.

[159] S. Cravero, R. E. Bravo, and H. A. Ernst, "Constraint Evaluation And Effects On J-R Resistance Curves For Pipes Under Combined Load Conditions," presented at the The Eighteenth International Offshore and Polar Engineering Conference, Vancouver, Canada, 2008/1/1/, 2008. Available: https://doi.org/

[160] R. H. Dodds, C. Fong Shih, and T. L. Anderson, "Continuum and micromechanics treatment of constraint in fracture," *International Journal of Fracture,* vol. 64, no. 2, pp. 101-133, 1993/11/01 1993.

[161] M. A. Verstraete, W. De Waele, R. M. Denys, K. Van Minnebruggen, and S. Hertelé, "Constraint analysis of defects in strength mismatched girth welds of (pressurized) pipe and Curved Wide Plate tensile test specimens," *Engineering Fracture Mechanics,* vol. 131, pp. 128-141, 2014/11/01/ 2014.

[162] R. A. Ainsworth, I. Sattari-Far, A. H. Sherry, D. G. Hooton, and I. Hadley, "Methods for including constraint effects within the SINTAP procedures," *Engineering Fracture Mechanics,* vol. 67, no. 6, pp. 563-571, 2000/12/01/ 2000.

[163] A. Neimitz and J. Galkiewicz, "Fracture toughness of structural components: influence of constraint," *International Journal of Pressure Vessels and Piping,* vol. 83, no. 1, pp. 42-54, 2006/01/01/ 2006.

[164] M. C. Burstow, I. C. Howard, and R. A. Ainsworth, "The influence of constraint on crack tip stress fields in strength mismatched welded joints," *Journal of the Mechanics and Physics of Solids,* vol. 46, no. 5, pp. 845-872, 1998/05/01/ 1998.

[165] B. S. Henry and A. R. Luxmoore, "The stress triaxiality constraint and the Q-value as a ductile fracture parameter," *Engineering Fracture Mechanics,* vol. 57, no. 4, pp. 375-390, 1997/07/01/ 1997.

[166] S. Hao, K. H. Schwalbe, and A. Cornec, "The effect of yield strength mis-match on the fracture analysis of welded joints: slip-line field solutions for pure bending," *International Journal of Solids and Structures,* vol. 37, no. 39, pp. 5385-5411, 2000/09/25/ 2000.

[167] O. Ranestad, Z. L. Zhang, and C. Thaulow, "Quantification of Geometry and Material Mismatch Constraint in Steel Weldments with Fusion Line Cracks," *International Journal of Fracture,* vol. 99, no. 4, pp. 211-237, 1999/10/01 1999.

[168] T. V. Pavankumar, J. Chattopadhyay, B. K. Dutta, and H. S. Kushwaha, "Numerical investigations of crack-tip constraint parameters in two-dimensional geometries," *International Journal of Pressure Vessels and Piping,* vol. 77, no. 6, pp. 345-355, 2000/05/01/ 2000.

Publications

A1 - Peer reviewed journal publications included in Science Citation Index

1. Crack driving force prediction in heterogeneous welds using Vickers hardness maps and hardness transfer functions
   ***Sameera Naib**, Wim De Waele, Primož Štefane, Nenad Gubeljak and Stijn Hertelé, Engineering Fracture Mechanics, vol. 201, p. 322-335, 2018.*

2. Tearing resistance of heterogeneous welds in Single Edge notched Tensile (SE(T)) testing
   ***Sameera Naib**, Wim De Waele, Primož Štefane, Nenad Gubeljak and Stijn Hertelé, Engineering fracture mechanics, vol. 214, p. 194-211, 2019*

3. Crack tip constraint analysis in welded joints with pronounced strength and toughness heterogeneity
   *Primož Štefane, **Sameera Naib**, Stijn Hertelé, Wim De Waele, and Nenad Gubeljak, Theoretical and Applied Fracture Mechanics, vol. 103, p. 102293, 2019.*

A2 - Peer reviewed journal publications not included in Science Citation Index

1. Evaluation of a finite element model for SENT testing of welded connections"
   *Matthijs De Visschere, **Sameera Naib**, Wim De Waele and Stijn Hertelé, (2016) INTERNATIONAL JOURNAL OF SUSTAINABLE CONSTRUCTION AND DESIGN. 7(1).*

2. Experimental and numerical analysis of deformation patterns in notched heterogeneous welds"
   *Marc Giménez Avalos, Florence Keppens, **Sameera Naib**, Wim De Waele and Stijn Hertelé, (2017) INTERNATIONAL JOURNAL OF SUSTAINABLE CONSTRUCTION AND DESIGN. 8(1).*

C1 - Publications in conference proceedings

1. "Sensitivity study of crack driving force predictions in heterogeneous welds using Vickers hardness maps"
   ***Sameera Naib**, Koen Van Minnebruggen, Wim De Waele and Stijn Hertelé, (2016) International NAFEMS Conference on Engineering Analysis, Modelling, Simulation and 3D-Printing.*

2. Evaluation of weld homogenization schemes based on plastic loading of single edge notched tension (SE(T)) tests
   ***Sameera Naib**, Wim De Waele and Stijn Hertelé, (2017) PROCEEDINGS OF THE ASME PRESSURE VESSELS AND PIPING CONFERENCE, 2017, VOL 5*

3. Evaluation of slip line theory assumptions for integrity assessment of defected welds loaded in tension"
   ***Sameera Naib**, Wim De Waele, Primož Štefane, Nenad Gubeljak and Stijn Hertelé, (2017) 2ND INTERNATIONAL CONFERENCE ON STRUCTURAL INTEGRITY, ICSI 2017. In Procedia Structural Integrity 5. p.1417-1424*

4. Characterization of crack growth in heterogeneous welds using Single Edge notched Tension (SE(T)) specimens
   ***Sameera Naib**, Primož Štefane, Wim De Waele, Nenad Gubeljak and Stijn Hertelé, (2018), Technology for future and ageing pipeline conference, TFAP 2018*

5. Calibration of hardness transfer functions based in micro tensile and all weld metal tensile tests for heterogeneous welds
   ***Sameera Naib**, Primož Štefane, Wim De Waele, Nenad Gubeljak and Stijn Hertelé, (2018), Presented at 13th International conference on Experimental mechanics, Brussels, Belgium, Proceedings 2018, 2(8), 468*

6. Analytical limit load predictions in heterogeneous welded Single Edge notched Tension (SE(T)) specimens"
   ***Sameera Naib**, Wim De Waele, Primož Štefane, Nenad Gubeljak and Stijn Hertelé, (2018) 22ST EUROPEAN CONFERENCE ON FRACTURE, (ECF22) . Procedia Structural Integrity, vol. 13, pp. 1725-1730, 2018.*

7. Experimental and numerical slip line analysis of welded single-edge notched tension specimens"
   *Stijn Hertelé, Filip Van Gerven, **Sameera Naib**, Nenad Gubeljak and Wim De Waele, (2016) 21ST EUROPEAN CONFERENCE ON FRACTURE, (ECF21) . In Procedia Structural Integrity 2. p.1763-1770*

8. *E*ffect of crack length on fracture toughness of welded joints with pronounced strength heterogeneity
   *Primoz Štefane, **Sameera Naib**, S. Hertelé, W. De Waele, and N. Gubeljak, Procedia Structural Integrity, vol. 13, pp. 1895-1900, 2018.*

C3 – Conference abstracts and posters

1. Hardness mapping – A tool to evaluate integrity of heterogeneous welds
   Sameera Naib, Wim De Waele, Primož Štefane, Nenad Gubeljak and Stijn Hertelé, (2018) Colloque Indentation 2018, 11 – 14 Septembre 2018 Liège, Groupe d'Indentation Multi Echelle